Trapped Antihydrogen in Its Ground State

Thesis advisor

Gerald Gabrielse

Author

Philip John Richerme

Trapped Antihydrogen in Its Ground State

Abstract

Antihydrogen atoms ($\overline{\mathrm{H}}$) are confined in a magnetic quadrupole trap for 15 to 1000 s - long enough to ensure that they reach their ground state. This milestone brings us closer to the long-term goal of precise spectroscopic comparisons of $\overline{\mathrm{H}}$ and H for tests of CPT and Lorentz invariance. Realizing trapped $\overline{\mathrm{H}}$ requires characterization and control of the number, geometry, and temperature of the antiproton ($\overline{\mathrm{p}}$) and positron (e^+) plasmas from which $\overline{\mathrm{H}}$ is formed. An improved apparatus and implementation of plasma measurement and control techniques make available 10^7 $\overline{\mathrm{p}}$ and 4×10^9 e^+ for $\overline{\mathrm{H}}$ experiments - an increase of over an order of magnitude. For the first time, $\overline{\mathrm{p}}$ are observed to be centrifugally separated from the electrons that cool them, indicating a low-temperature, high-density $\overline{\mathrm{p}}$ plasma. Determination of the $\overline{\mathrm{p}}$ temperature is achieved through measurement of the $\overline{\mathrm{p}}$ evaporation rate as their confining well is reduced, with corrections given by a particle-in-cell plasma simulation. New applications of electron and adiabatic cooling allow for the lossless reduction in $\overline{\mathrm{p}}$ temperature from thousands of Kelvin to 3.5 K or colder, the lowest ever reported. The sum of the 20 trials performed in 2011 in which $\overline{\mathrm{p}}$ and e^+ mix to form $\overline{\mathrm{H}}$ in the presence of a magnetic quadrupole trap reveals a total of 105 ± 21 trapped $\overline{\mathrm{H}}$, or 5 ± 1 per trial on average. This result paves the way towards the large numbers of simultaneously trapped $\overline{\mathrm{H}}$ that will be necessary for laser spectroscopy.

Contents

Papers and Publications

1. **Efficient transfer of positrons from a buffer-gas-cooled accumulator into an orthogonally oriented superconducting solenoid for antihydrogen studies**
   D. Comeau, A. Dror, D. W. Fitzakerley, M. C. George, E. A. Hessels, C. H. Storry, M. Weel, D. Grzonka, W. Oelert, G. Gabrielse, R. Kalra, W. S. Kolthammer, R. McConnell, P. Richerme, A. Müllers, and J. Walz. *New J. Phys.* **12**, 045006 (2012).

2. **Trapped Antihydrogen in Its Ground State**
   G. Gabrielse, R. Kalra, W. S. Kolthammer, R. McConnell, P. Richerme, D. Grzonka, W. Oelert, T. Sefzick, M. Zielinski, D. W. Fitzakerley, M. C. George, E. A. Hessels, C. H. Storry, M. Weel, A. Müllers, and J. Walz. *Phys. Rev. Lett.* **108**, 113002 (2012).

3. **Adiabatic Cooling of Antiprotons**
   G. Gabrielse, W.S. Kolthammer, R. McConnell, P. Richerme, R. Kalra, E. Novitski, D. Grzonka, W. Oelert, T. Sefzick, M. Zielinski, D. Fitzakerley, M.C. George, E.A. Hessels, C.H. Storry, M. Weel, A. Müllers, and J. Walz. *Phys. Rev. Lett.* **105**, 073002 (2011).

4. **Pumped Helium System for Producing 1.2 K Positrons and Electrons**
   J. Wrubel, G. Gabrielse, W.S. Kolthammer, P. Larochelle, R. McConnell, P. Richerme, D. Grzonka, W. Oelert, T. Sefzick, M. Zielinski, J.S. Borbely, M.C. George, E.A. Hessels, C.H. Storry, M. Weel, A. Müllers, J. Walz, and A. Speck. *Nuclear Instruments and Methods in Physics Research* **640**, 232 (2011).

5. **Centrifugal Separation of Antiprotons and Electrons**
   G. Gabrielse, W.S. Kolthammer, R. McConnell, P. Richerme, J. Wrubel, R. Kalra, E. Novitski, D. Grzonka, W. Oelert, T. Sefzick, J.S. Borbely, D. Fitzakerley, M.C. George, E.A. Hessels, C.H. Storry, M. Weel, A. Müllers, J. Walz, and A. Speck. *Phys. Rev. Lett.* **105**, 213002 (2010).

6. **Antihydrogen Production Within a Penning-Ioffe Trap**
   G. Gabrielse, P. Larochelle, D. Le Sage, B. Levitt, W.S. Kolthammer, R. McConnell, P. Richerme, J. Wrubel, A. Speck, M.C. George, D. Grzonka, W. Oelert, T. Sefzick, Z. Zhang, A. Carew, D. Comeau, E.A. Hessels, C.H. Storry, M. Weel, and J. Walz. *Phys. Rev. Lett.* **100**, 113001 (2008).

Acknowledgments

I am grateful to the many people who have supported, encouraged, and collaborated with me over the course of my graduate career. I have grown tremendously under the guidance of Prof. Jerry Gabrielse, for which I will always remain appreciative. I am continually impressed by his dedication to the ATRAP experiment. Whether it be by flying out to CERN on short notice to discuss important matters, calling during morning, afternoon, and night shifts to talk, chairing weekly collaboration meetings, commenting on the lablog, or sending emails at all times of the day, his constant support was evident.

During my first summer at CERN, I was fortunate to have a seasoned crew show me the ropes. Jonathan Wrubel and Ben Levitt were particularly patient teachers, and were both willing to help even after moving on from ATRAP. David Le Sage and Phil Larochelle, in addition to letting me sleep on their couch for several weeks, introduced me to the intricacies of taking beam while keeping the long shifts in the AD entertaining.

I worked closely with a number of excellent colleagues these past few years at CERN. Robert McConnell and Steve Kolthammer, whether they knew it or not, served as excellent role models for me. Both were integral to rounding out my knowledge of the experiment, and both were always happy to talk about physics, life, Shakespeare, Frisbee, or anything else that might come up in the RF cabin. Dan Fitzakerley is a reasonable guy, and could always be relied upon to tame the positrons or help with anything else as needed. Andi Müllers kept our laser systems in excellent working order, and his masterful grilling skills will be missed dearly. Rita Kalra and Stephan Ettenauer will be carrying the ATRAP torch forward next year, and I

enjoyed the challenging questions and good ideas posed by both of them.

It is hardly a unique opinion around the ATRAP barracks that Walter Oelert is amazing. His good nature and obvious enthusiasm, as well as his hosting of group dinners and chocolate encouragement at 3am, were all thoroughly appreciated. Along with Walter, Dieter Grzonka kept our detector system running with hardly any failures during the several years I was at CERN.

Our collaborators from York University also deserve my gratitude. Eric Hessels was a fountain of excellent ideas, and I am especially thankful for his assistance with the analysis performed at the end of 2011. Matt Weel and Matt George did an excellent job building and setting up the positron accumulator and continue to be helpful with their comments and hands-on contributions. Cody Storry and his can-do attitude have been responsible for a surprisingly large number of major installations in and around the ATRAP experiment.

Back at Harvard, Jan Ragusa worked tirelessly to keep the group running smoothly, and I am confident that there is no problem too small or too large for her to handle. Stan Cotreau has taught me nearly everything I know about machining, and Jim MacArthur greatly improved my electronics knowledge (in addition to patiently fielding emergency phone calls from CERN).

Though they both work on the $g-2$ experiment, Elise Novitski designed the majority of the CTRAP quench protection system and along with Josh Dorr often performs the thankless chore of shipping equipment to CERN. I am thankful for their efforts and friendship. In addition, I have enjoyed learning from and working with the other members of the Gabrielse lab - Jack DiSciacca, Josh Goldman, David Hanneke,

Shannon Fogwell, Nick Guise, Yulia Gurevich, Paul Hess, and Ben Spaun.

Lastly, my incredible wife Lauren has been an unwavering source of support, encouragement, and love these past few years. More than anyone else, she knows the struggles, successes, disconsolations, and exhilarations intertwined with this work, since she has been there with me through all of them.

For my father

Chapter 1

Introduction

Antihydrogen ($\overline{\mathrm{H}}$), the bound state of an antiproton ($\overline{\mathrm{p}}$) and a positron (e^+), provides a compelling system for studying the fundamental laws of physics. As the complement to the well-understood Hydrogen atom, $\overline{\mathrm{H}}$ serves as a natural candidate for investigating symmetries and asymmetries between matter and antimatter. $\overline{\mathrm{H}}$ may hold the key to answering some of the most important questions in physics today: is CPT an exact symmetry of nature? Why is there vastly more matter than antimatter in the universe? Does antimatter fall under the influence of gravity in the same way as matter, or does it violate the weak equivalence principle?

To address such questions, it was proposed long ago by Gabrielse [1] to create and trap $\overline{\mathrm{H}}$ for precision studies:

> For me, the most attractive way ... would be to capture the antihydrogen in a neutral particle trap such as has been used for neutrons and neutral atoms. The objective would be to then study the properties of a small number of [antihydrogen] atoms confined in the neutral trap for a long time.

Creation of $\overline{\mathrm{H}}$ was achieved for the first time in 1996 [2], with 9 atoms produced at

relativistic speeds. Six years later, the ATRAP [3, 4] and ATHENA [5] collaborations observed orders of magnitude more $\overline{\mathrm{H}}$ atoms at orders of magnitude lower temperatures. This thesis reports the simultaneous trapping of multiple $\overline{\mathrm{H}}$ atoms for long enough to ensure they are in their ground state, an important step towards realization of the long-term goal of $\overline{\mathrm{H}}$ studies.

1.1 Precision Measurements with Trapped Antihydrogen

Precision measurements of fundamental physics will become possible once significant numbers of $\overline{\mathrm{H}}$ atoms are trapped. As described in the original proposals for $\overline{\mathrm{H}}$ experiments at CERN [1, 6, 7], stringent tests of CPT symmetry and Lorentz invariance may be performed on trapped $\overline{\mathrm{H}}$ atoms by comparing their internal laser and microwave transitions to those in H. In addition, the inherent neutrality of $\overline{\mathrm{H}}$ atoms could permit sensitive comparisons of gravitational forces on matter and antimatter.

1.1.1 Tests of CPT Symmetry

The CPT theorem is one of the most fundamental in physics, underlying quantum field theories such as the Standard Model. Starting from only a few basic assumptions (like Lorentz invariance and locality), the CPT theorem for quantum electrodynamics states that the combined effect of Charge conjugation (turning a particle into its antiparticle), Parity inversion (flipping coordinate locations from $\vec{r} \rightarrow -\vec{r}$), and Time reversal (setting $t \rightarrow -t$) is an exact symmetry of nature [8]. Precision tests of CPT

symmetry are a prime motivation for this work.

It had been long believed that reality was invariant under C, P, and T transformations separately. In 1956, however, Lee and Wang noted that while experimental evidence existed for parity invariance in electromagnetic and strong interactions, P invariance had not been tested for weak interactions [9]. Later that year, Wu *et al.* observed the first experimental evidence of parity violation during the β decay of spin-polarized ^{60}Co, where electrons were preferentially emitted anti-parallel to the direction of the nuclear spin. Under a P transformation, this decay would not be symmetric since the nuclear magnetic moment of ^{60}Co would remain oriented in the same direction, but the momentum of the emitted electrons would be reversed; their emitted direction would then be parallel to the nuclear spin rather than anti-parallel. P violation was also seen to accompany other weak interactions soon afterwards [10, 11], and it is now established as a signature of the weak force [12].

After the observation of P violation, proposals that reality was always invariant under CP transformations [13] were quickly disproven by experiments performed in the mid 1960s. Gell-Mann and Pais showed that decays of the long-lived neutral kaon K_L^0 into two pions would be evidence of CP violation [14], and such decays were later observed by Cronin and Fitch [15]. Further confirmation of CP violation came in later kaon decay experiments [16, 17] as well as in experiments measuring decay rates in B^0-$\overline{\mathrm{B}}^0$ pairs [18, 19].

The current widespread belief that reality is invariant under CPT transformations is supported by the success of quantum field theories, as well as a number of precision experimental measurements. One consequence of the CPT theorem is that particle-

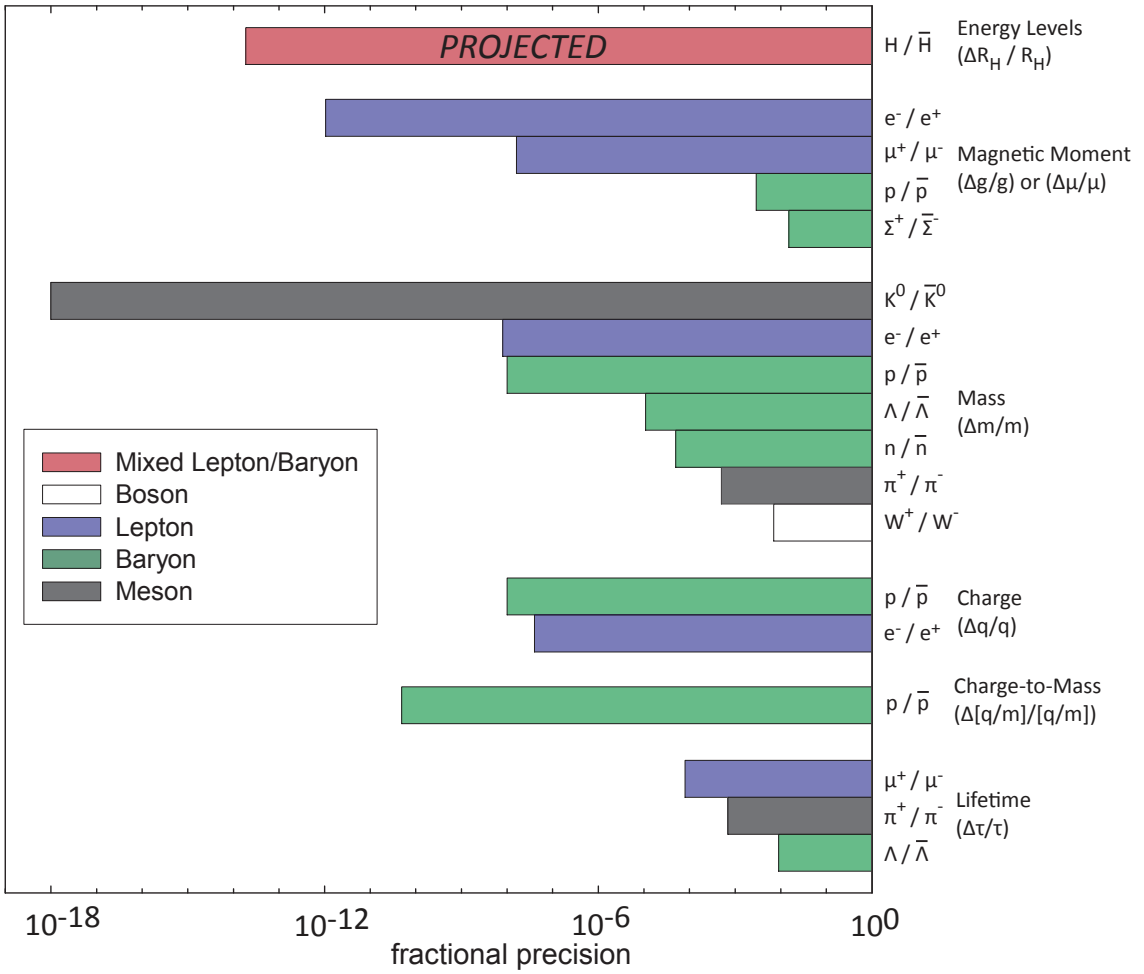

Figure 1.1: Comparison of the projected fractional precision achievable with a 1S-2S measurement in $\overline{\mathrm{H}}$ to existing tests of CPT. Values taken from the best measurement of the 1S-2S line in H [20] and tables compiled by the particle data group [21].

antiparticle pairs should have the same mass, g-value, and lifetime, and opposite charge, while atom-antiatom pairs should have the same internal structure. Sensitive measurements of these quantities therefore test CPT invariance. As shown in Fig. 1.1, highly accurate comparisons between matter and antimatter leptons, baryons, and mesons have been performed.

For leptons, the most accurate CPT test is a comparison of the e^- and e^+ magnetic

moments measured in a Penning trap [22], while measurement of the p and $\overline{\mathrm{p}}$ charge-to-mass ratios (via their cyclotron frequencies) yields the best baryon comparison [23]. In the mesonic sector, a delicate mass balance in neutral kaon systems allows a measurement of $m_{\mathrm{K}^0}/m_{\overline{\mathrm{K}}0}$ to a fractional precision of 5×10^{-18} [24].

Whether CPT symmetry is an exact symmetry of nature is an experimental question. Despite the high precision to which CPT has already been tested, its fundamental importance to our understanding of reality is an enticement to perform even more accurate experiments. There are good reasons to suspect violations. One of the large unsolved mysteries in physics is why the universe is made of matter (as opposed to antimatter). Sakharov proposed an explanation at odds with several deeply held ideas in physics: baryon number violation, C and CP violation (more than currently observed), and thermal non-equilibrium [25]. However, if CPT is violated, then the matter-antimatter asymmetry in the universe may be explained by assuming only baryon number violation [26, 27]. Additionally, the Standard Model is incomplete insofar as it does not include gravity, and a quantum theory of gravity has yet to be formulated.

Since we do not know *a priori* where violations in CPT may occur, it is important to look for them in systems that differ in significant ways. Comparisons of the energy level structures of H and $\overline{\mathrm{H}}$ could significantly improve upon existing tests of CPT symmetry with leptons and baryons (see Fig. 1.1). Laser spectroscopy of the $1S - 2S$ line presents an attractive option, for example, since this transition has been measured in H to an accuracy of 1.8 parts in 10^{14} [20]. Although this measurement was performed using a cold atomic beam (not possible for $\overline{\mathrm{H}}$ due to the vastly smaller

flux), measurements of the H $1S-2S$ line have also been performed in a neutral particle trap with a relative uncertainty of 1.2×10^{-12} [28]. With improved laser stability (a limiting factor in both experiments), achieving a fractional uncertainty equal to the natural linewidth of 1.3 Hz (constituting a 5×10^{-16} measurement) seems plausible.

The relative dearth of $\overline{\mathrm{H}}$ atoms available for study presents a challenge for precision spectroscopy. To wit, the number of H atoms used in any single spectroscopy measurement above exceeds the total number of $\overline{\mathrm{H}}$ atoms that have ever been created by many orders of magnitude. Nevertheless, it may be possible to make a 1 part in 10^{12} measurement of the $\overline{\mathrm{H}}$ $1S-2S$ transition frequency using only 1000 trapped atoms [29]. It may even be possible to improve upon standard schemes by destructively photoionizing an $\overline{\mathrm{H}}$ atom with three 243 nm photons, ejecting it from the trap, and exploiting the high-efficiency detection of the annihilation that follows.

In addition to being the first CPT test in a combined lepton-baryon system, $1S-2S$ spectroscopy in $\overline{\mathrm{H}}$ could also improve lepton and baryon measurements individually. Comparison of the $1S-2S$ line in H and $\overline{\mathrm{H}}$ directly compares the Rydberg constants for both systems

$$\frac{R_{\overline{\mathrm{H}}}}{R_{\mathrm{H}}}=\left(\frac{m_{\mathrm{e}^+}}{m_{\mathrm{e}^-}}\right)\left(\frac{q_{\mathrm{e}^+}}{q_{\mathrm{e}^-}}\right)^2\left(\frac{q_{\overline{\mathrm{p}}}}{q_{\mathrm{p}}}\right)^2\left(\frac{1+m_{\mathrm{e}^-}/m_{\mathrm{p}}}{1+m_{\mathrm{e}^+}/m_{\overline{\mathrm{p}}}}\right) \tag{1.1}$$

Measurements of $R_{\overline{\mathrm{H}}}$ at the 1 part in 10^{12} level would already improve the accuracy to which the e^- and e^+ mass ratio is known [22] by a factor of 10000, while improving the p to $\overline{\mathrm{p}}$ mass ratio measurement [23] by an order of magnitude.

The Standard Model Extension [30], a theoretical framework that parameterizes Lorentz-violating additions to the Standard Model, makes predictions of the sensi-

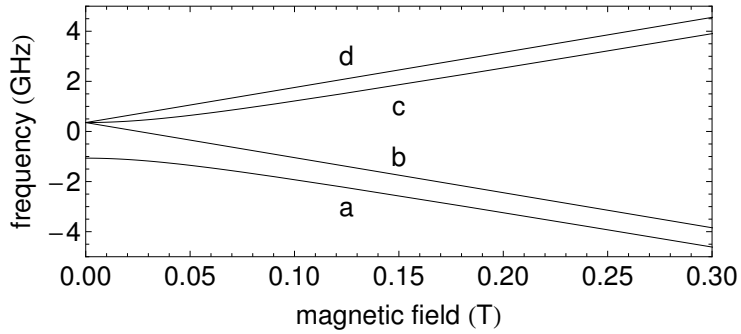

Figure 1.2: Energy level diagram for the H $1S$ hyperfine levels in a magnetic field.

tivity of various physical constants to CPT violating effects. This model predicts the possibility of improved CPT tests via $1S - 2S$ laser spectroscopy in $\overline{\mathrm{H}}$ [31], and predicts even more sensitive coupling (by a factor of $1/\alpha^2 \sim 10^4$) of the $\overline{\mathrm{H}}$ hyperfine transitions to CPT violating terms. Thus, microwave spectroscopy of the $\overline{\mathrm{H}}$ hyperfine splittings is an alternative test of CPT symmetry.

Independently of any model, microwave spectroscopy of $\overline{\mathrm{H}}$ could also improve direct comparisons of particle-antiparticle properties. Consider the hyperfine energy levels of H in a magnetic field, as shown in Fig. 1.2. For a given magnetic field B, the two transition frequencies ν_{da} and ν_{cb} are given (in the strong-field limit) by

$$2\pi\nu_{da} = \frac{\mathcal{A}\hbar}{2} + \frac{\mu_B g_{\mathrm{e}^-}}{\hbar} B \tag{1.2}$$

$$2\pi\nu_{cb} = -\frac{\mathcal{A}\hbar}{2} + \frac{\mu_B g_{\mathrm{e}^-}}{\hbar} B \tag{1.3}$$

where μ_B is the Bohr magneton, g_{e^-} is the electron g value, and $\mathcal{A}$ is the zero-field hyperfine splitting, given by

$$\mathcal{A} = \frac{2}{3} \frac{g_{\mathrm{p}} g_{\mathrm{e}^-} m_{\mathrm{e}^-} c^2 \alpha^4}{\hbar^2} \left(\frac{m_{\mathrm{e}^-}}{m_{\mathrm{p}}}\right) \left(1 + \frac{m_{\mathrm{e}^-}}{m_{\mathrm{p}}}\right)^{-3} \tag{1.4}$$

The frequency difference between these two hyperfine transitions, $\nu_{da} - \nu_{cb} =$

$\mathcal{A}\hbar/(2\pi)$, gives a direct measurement of the hyperfine splitting $\mathcal{A}$ for a hydrogen atom in any strong B field. Comparison of the hyperfine splitting (Eqn. 1.4) in H and $\overline{\mathrm{H}}$ would then yield

$$\frac{\mathcal{A}^{\overline{\mathrm{H}}}}{\mathcal{A}^{\mathrm{H}}} = \left(\frac{q_{\mathrm{e}^+}}{q_{\mathrm{e}^-}}\right)^4 \left(\frac{q_{\overline{\mathrm{p}}}}{q_{\mathrm{p}}}\right)^4 \left(\frac{m_{\mathrm{e}^+}}{m_{\mathrm{e}^-}}\right)^2 \left(\frac{m_{\mathrm{p}}}{m_{\overline{\mathrm{p}}}}\right) \left(\frac{g_{\mathrm{e}^+}}{g_{\mathrm{e}^-}}\right) \left(\frac{g_{\overline{\mathrm{p}}}}{g_{\mathrm{p}}}\right) \left(\frac{1 + m_{\mathrm{e}^-}/m_{\mathrm{p}}}{1 + m_{\mathrm{e}^+}/m_{\overline{\mathrm{p}}}}\right)^3 \tag{1.5}$$

Of particular interest is that this expression varies linearly with the ratio of the $\overline{\mathrm{p}}$ and p g factors - a quantity currently known to only 0.3%. Measurement of ν_{da} and ν_{cb} in $\overline{\mathrm{H}}$ to a precision of better than 1 MHz would already lead to an improved measurement of $g_{\overline{\mathrm{p}}}/g_{\mathrm{p}}$. However, if proposed experiments to measure $g_{\overline{\mathrm{p}}}$ through the same spin-flip method as g_{p} [32, 33] are successful, a sub-kHz measurement of the $\overline{\mathrm{H}}$ hyperfine splitting would then be required to decrease the uncertainty in $g_{\overline{\mathrm{p}}}$.

1.1.2 Gravitational Studies

Large numbers of trapped $\overline{\mathrm{H}}$ atoms may also permit a test of the weak equivalence principle for antimatter. The neutrality of $\overline{\mathrm{H}}$ is critical for such measurements, since the gravitational force between a bare $\overline{\mathrm{p}}$ and the entire Earth can be overcome by a single stray charge anywhere within a 12 cm radius of the $\overline{\mathrm{p}}$. Tests of interactions between $\overline{\mathrm{H}}$ atoms and gravity had been suggested long ago [34], while a proposal to measure the effect of gravity on $\overline{\mathrm{H}}$ atoms in a beam has been recently approved at CERN [35].

In a trap, the spatial distribution of $\overline{\mathrm{H}}$ atoms will be altered under the effect of gravity, with the density along the vertical axis proportional to $\exp(-m_{\overline{\mathrm{p}}}\overline{g}h/k_BT)$, where $\overline{g}$ is the gravitational acceleration for antimatter, h is the height along the vertical axis, k_B is Boltzmann's constant, and T is the $\overline{\mathrm{p}}$ temperature [36]. For a

1 m tall trap, the thermal and gravitational potential energies are matched when $T \approx 1$ mK, which is relatively close to the 2.5 mK Doppler cooling limit in H. For these parameters, the density of trapped $\overline{\mathrm{H}}$ should be a factor of 3 different at the top and bottom of the trap. Given enough $\overline{\mathrm{H}}$, measurement of the density profile would be sufficient at least to determine the sign of $\overline{g}$. However, for sensitive tests of the absolute magnitude $|\overline{g}/g - 1|$, it will be difficult for this method to surpass the 1×10^{-6} accuracy determined by comparisons of the p and $\overline{\mathrm{p}}$ cyclotron frequencies in a Penning trap [23, 37].

1.2 A Brief Summary of Antihydrogen Research

Though their existence was first proposed in 1931 [38], and their first observation followed in 1955 [39], $\overline{\mathrm{p}}$ were not successfully trapped until 1986 [40]. Following this accomplishment, the TRAP collaboration (the predecessor to ATRAP) launched the field of antihydrogen physics with proposals to create [41] and trap [1] $\overline{\mathrm{H}}$ for precision spectroscopy and gravitation studies [34]. Today, five international collaborations make use of a dedicated facility at CERN, the Antiproton Decelerator, for $\overline{\mathrm{p}}$ and $\overline{\mathrm{H}}$ experiments.

Since the late 1980s, numerous milestones have been reached in pursuit of the stated long-term goal. Techniques to slow $\overline{\mathrm{p}}$ in a matter degrader [42] enabled reduction of $\overline{\mathrm{p}}$ energies from several MeV to several keV and optimization of the trappable fraction. Further work investigated the electron cooling of $\overline{\mathrm{p}}$ [43], allowing for at least another 4 orders of magnitude reduction in $\overline{\mathrm{p}}$ energy to the sub-eV level.

The creation of hot $\overline{\mathrm{H}}$ atoms at CERN [2], then at Fermilab [44], generated

widespread interest in $\overline{\mathrm{H}}$ physics in the mid-1990s. However, these atoms were much too energetic to be conceivably confined in a trap for precision studies. Significant progress towards the synthesis of cold antihydrogen was made soon afterwards, with the first simultaneous confinement of $\overline{\mathrm{p}}$ and e^+ in the same trap [45], the first e^+ cooling of $\overline{\mathrm{p}}$ in a nested Penning trap [46], and robust accumulation of larger numbers of $\overline{\mathrm{p}}$ [47].

Observation of cold $\overline{\mathrm{H}}$ atoms was first reported in 2002, by both the ATRAP [3] and ATHENA [5] collaborations. Several years followed in which ATRAP investigated the character of these atoms, including measurements of their field ionization spectrum [4] and velocity [48]. In addition, an alternative method to produce cold $\overline{\mathrm{H}}$ involving a double charge-exchange process [49] was developed [50] and successfully realized [51].

Focus then shifted towards achievement of the next significant milestone: the trapping of cold $\overline{\mathrm{H}}$. ATRAP employed a quadrupole Ioffe trap [52], after calculating that charged particles in a combined Penning-Ioffe quadrupole trap could still remain stably confined despite the loss of cylindrical symmetry [53]. However, others claimed that in the presence of the quadrupole Ioffe field, radial transport in charged particle plasmas would inhibit $\overline{\mathrm{H}}$ production (and hence trapping) [54, 55]. ATRAP nonetheless demonstrated in 2007 that $\overline{\mathrm{p}}$ and e^+ could indeed be confined in a combined Penning-Ioffe trap for at least 5 minutes (long enough to create $\overline{\mathrm{H}}$) [56]. One year later, ATRAP completed the task by producing $\overline{\mathrm{H}}$ in a combined Penning-Ioffe trap for the first time, a crucial step towards $\overline{\mathrm{H}}$ trapping [57].

Trapping cold $\overline{\mathrm{H}}$ atoms, the next large milestone in $\overline{\mathrm{H}}$ research, was achieved in

2010 and 2011 by the ALPHA [58] and ATRAP [59] collaborations. ALPHA initially reported 0.1 $\overline{\mathrm{H}}$ atoms per trial on average, trapped for 172 ms. This result was later improved upon, giving 1 $\overline{\mathrm{H}}$ atom per trial (on average), trapped for up to 1000 s [60]. By using many more $\overline{\mathrm{p}}$ and e^+ for $\overline{\mathrm{H}}$ formation, ATRAP trapped 5 $\overline{\mathrm{H}}$ atoms per trial (on average) for 15 - 1000 s. The final milestone - precision tests of CPT and gravitational studies using trapped $\overline{\mathrm{H}}$ - will require larger numbers of trapped atoms to be feasible. However, given that a factor of 10 more $\overline{\mathrm{p}}$ are already available for $\overline{\mathrm{H}}$ experiments and that the ELENA upgrade to the AD promises many more [61], scaling up the number of trapped $\overline{\mathrm{H}}$ appears viable.

1.3 Overview of this work

The focus of this thesis is the characterization and control of the number, geometry, and temperature of $\overline{\mathrm{p}}$ and e^+ plasmas that enabled the creation and observation of trapped $\overline{\mathrm{H}}$. Serious efforts to better understand the behavior of these plasmas started in early 2009, after the first observation of $\overline{\mathrm{H}}$ created in a Penning-Ioffe trap. Though I was closely involved with a number of other enterprises undertaken by the ATRAP collaboration, I report in detail here only on those projects which I directly piloted. Previous theses may be referenced for more thorough explanations of $\overline{\mathrm{H}}$ formation methods [62], charged particle stability and $\overline{\mathrm{H}}$ production in a Penning-Ioffe trap [63, 64], improved plasma diagnostics and the design of a new Ioffe trap [65], and improved laser-controlled charge-exchange production of $\overline{\mathrm{H}}$ [66].

Chapter 2 introduces the apparatus in which all of the measurements presented in this thesis were taken. Many pieces of this apparatus had already been designed and

constructed when I joined the ATRAP collaboration, so I assisted with the mechanical assembly, electrical wiring, and initial testing. In addition, a few others in the collaboration and I were responsible for standard maintenance as well as the design and installation of upgrades and improvements.

Chapter 3 discusses the relevant theory of non-neutral plasmas in Penning and Ioffe traps, laying the groundwork for later discussions of plasma manipulations within the apparatus. Chapter 4 details many of the standard methods used in all current experiments, including $\overline{\mathrm{p}}$ and e^+ capture, cooling, and accumulation, particle transfer, and $\overline{\mathrm{H}}$ formation. Although many of these techniques were developed before my time at ATRAP, new contributions include an improved particle transfer routine and the accumulation of a factor of 20 more $\overline{\mathrm{p}}$.

Chapter 5 reports the observation of centrifugal separation of $\overline{\mathrm{p}}$ from the e^- that cool them. This was the first observation of centrifugal separation in any system that cannot be laser cooled or optically imaged. Furthermore, this served as an excellent indication of the improved characterization and control of our plasma geometries.

Chapter 6 demonstrates the improved control and characterization of the temperature of our $\overline{\mathrm{p}}$ plasmas. Measurement of the loss rate of $\overline{\mathrm{p}}$ over a barrier as the barrier height is reduced gives a direct measure of the $\overline{\mathrm{p}}$ temperature, when combined with corrections from a particle-in-cell simulation. New applications of electron cooling allow for a demonstrated $\overline{\mathrm{p}}$ temperature of 31 K, while new applications of adiabatic cooling reduce the $\overline{\mathrm{p}}$ temperature to 3.5 K or below.

Chapters 7-9 describe our observation of 105 ± 21 trapped $\overline{\mathrm{H}}$ atoms in 20 trials. In addition to the general experimental procedure, concerns regarding mirror-trapped $\overline{\mathrm{p}}$

are addressed and a detailed analysis of the detector system and candidate events is performed. Arguments that the trapped $\overline{\mathrm{H}}$ is in its ground state are presented as well as a crude limit on the gravitational acceleration of antimatter.

Chapter 10 recounts the design and construction of the electrodes to be used in an improved Penning-Ioffe trap. This new apparatus for $\overline{\mathrm{H}}$ trapping has now been assembled at CERN and is expected to be commissioned this year. Featuring a Ioffe trap with both octupole and quadrupole coils, significantly larger trap depths, and a turn-off time quick enough to resolve a single trapped $\overline{\mathrm{H}}$, this apparatus should secure the way towards increased numbers of trapped $\overline{\mathrm{H}}$ for precision measurements. Chapter 11 concludes with a summary and optimistic outlook for future $\overline{\mathrm{H}}$ studies.

Chapter 2

Apparatus

The synthesis and trapping of $\overline{\mathrm{H}}$ requires a large number of components in a multi-faceted apparatus working in concert with one another. The apparatus presented here, BTRAP, is the second iteration of a design that incorporates a Penning trap for $\overline{\mathrm{p}}$ and e^+ confinement as well as a quadrupole Ioffe trap for magnetic confinement of $\overline{\mathrm{H}}$. Like previous designs, BTRAP is a cryogenic apparatus, which allows for colder particle temperatures and a vacuum of better than 5×10^{-17} Torr [67].

The world's only source of cold $\overline{\mathrm{p}}$ is located at CERN. High energy protons are created in CERN's Proton Synchrotron and are made to collide with a dense iridium target, forming $\overline{\mathrm{p}}$ by the reaction $\mathrm{p} + \mathrm{p} \rightarrow \mathrm{p} + \mathrm{p} + \mathrm{p} + \overline{\mathrm{p}}$. These $\overline{\mathrm{p}}$ are then collected and cooled in CERN's Antiproton Decelerator (AD) from an incoming kinetic energy of 2.7 GeV down to a final energy of 5.3 MeV [68]. Approximately every 100 s, the AD delivers a 200 ns pulse of 3×10^7 $\overline{\mathrm{p}}$ to one of five experimental zones connected to the beamline.

Given this source constraint for $\overline{\mathrm{p}}$, BTRAP has been assembled and installed

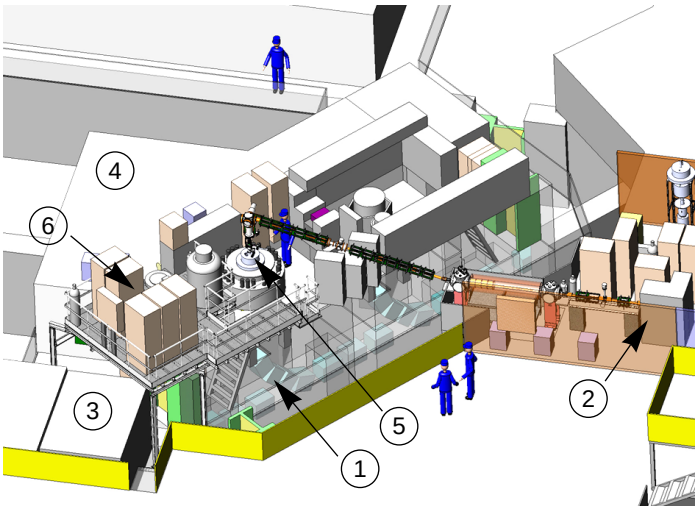

Figure 2.1: View of the experimental area within the AD hall, with numbers indicating the (1) AD beamline magnets, (2) e^+ source, (3) experiment control room, (4) laser cabin, (5) BTRAP apparatus, and (6) platform for equipment racks and dewars.

inside the AD hall. As shown in Figure 2.1, the apparatus sits atop the $\overline{p}$ beamline (1), allowing $\overline{p}$ to enter from below, while e^+ are emitted by a ^{22}Na source (2), steered along a magnetic guide, and enter the apparatus from above. Voltage supplies and other sensitive electronics are housed in the experimental control room (3), which acts as a Faraday cage to minimize pickup of rf noise. The lasers necessary for forming $\overline{H}$ via double charge-exchange are located in a second Faraday cage (4), as will be the lasers necessary for $\overline{H}$ cooling and spectroscopy.

Located at the heart of the experimental zone, the BTRAP apparatus (5) is comprised of multiple sub-assemblies. The executive functions of charged and neutral particle trapping are performed by the Penning and Ioffe traps (respectively), while crucial supporting roles are played by the liquid helium dewar, "insert dewar," field-boosting solenoid, X-Y translation stage, 1 K pot, and scintillating detectors. These components, shown in Fig. 2.2, will now be described in greater detail.

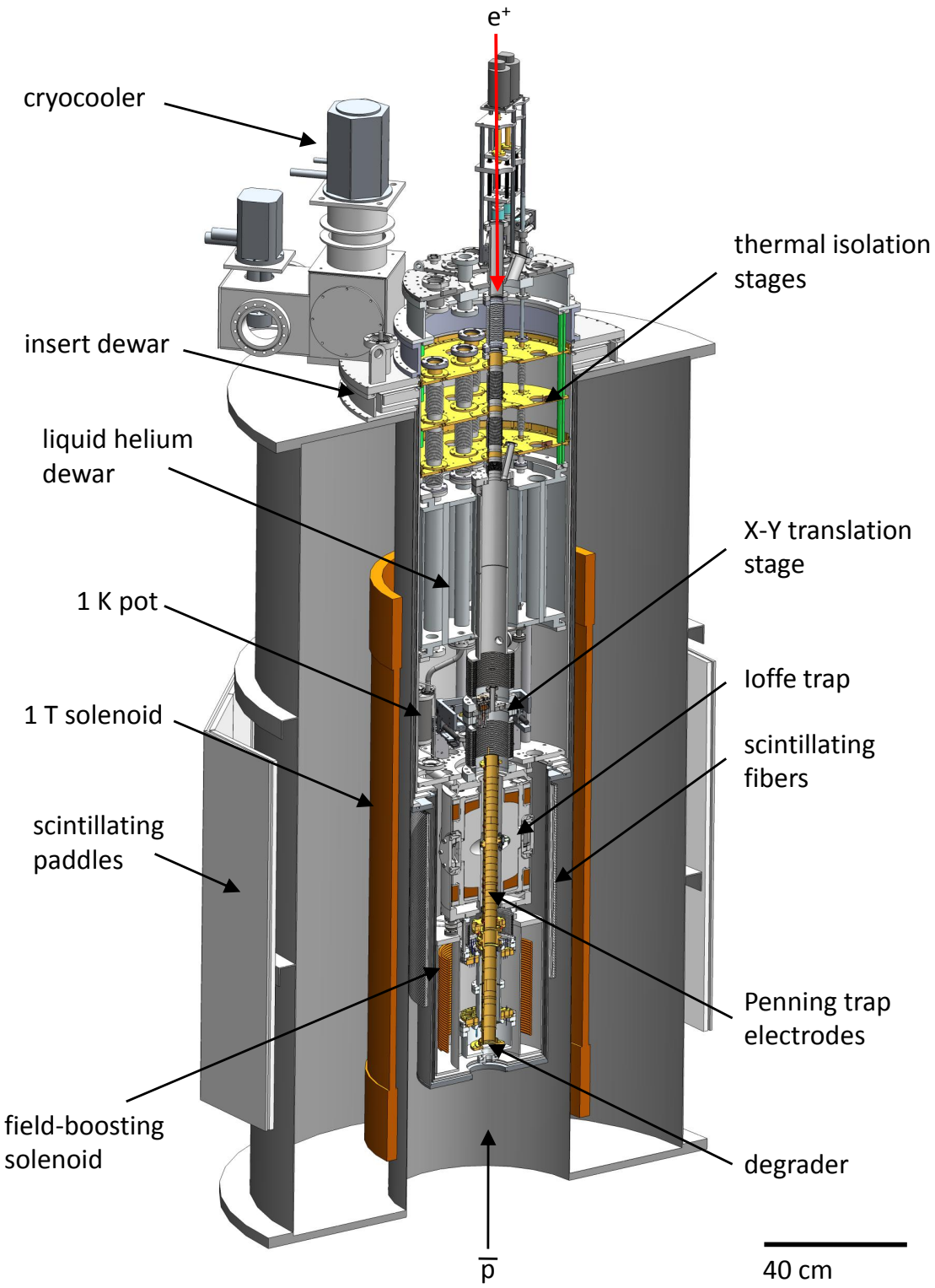

Figure 2.2: Section view of the full Penning-Ioffe trap apparatus, insert dewar, 1T solenoid, and scintillating detectors. Bursts of $\overline{\text{p}}$ arrive from the AD at the bottom of the Penning trap, while e^+ enter through the top.

2.1 Penning Trap

2.1.1 Theory

A Penning trap confines charged particles using a combination of static magnetic and electric fields [69], with the motion governed by the Lorentz force law

$$\vec{F} = q(\vec{E} + \vec{v} \times \vec{B}). \tag{2.1}$$

Classically, a charged particle in a magnetic field executes a cyclotron motion around a field line at frequency $\omega_c = q|\vec{B}|/m$. This confines the particle radially, though it is free to move along the direction of the magnetic field. Trapping along the third dimension may then be accomplished via the addition of a confining electric field. Historical implementations of Penning traps [70] have employed a uniform axial magnetic field $\vec{B} = B_0\hat{z}$ and an electric quadrupole potential $\phi(\rho, z) = \frac{V_0}{2d^2}\left(z^2 - \frac{\rho^2}{2}\right)$, where $d^2 = \frac{1}{2}(z_0^2 + \rho_0^2/2)$ is a geometrical factor describing a trap with distances z_0 and ρ_0 to the electrode walls. Substituting this configuration of fields into Eqn. 2.1, the equations of motion may then be written

$$m\ddot{x} = \frac{qV_0}{2d^2}x + qv_yB_0 \tag{2.2}$$

$$m\ddot{y} = \frac{qV_0}{2d^2}y - qv_xB_0 \tag{2.3}$$

$$m\ddot{z} = -\frac{qV_0}{d^2}z \tag{2.4}$$

The axial motion $z(t)$ is a simple harmonic oscillation at frequency

$$\omega_z = \sqrt{\frac{qV_0}{md^2}} \tag{2.5}$$

The radial equations may be solved by substituting $u = x + iy$ and the expressions for ω_c and ω_z above, giving

$$\ddot{u} + i\omega_c\dot{u} - \frac{1}{2}\omega_z^2 u = 0 \tag{2.6}$$

This differential equation has a general solution of form $u = e^{-i\omega_\pm t}$, where

$$\omega_\pm = \frac{1}{2}\left(\omega_c \pm \sqrt{\omega_c^2 - 2\omega_z^2}\right) \tag{2.7}$$

For a charged particle to undergo stable, periodic motion, the oscillation frequencies $\omega_\pm$ must be real, which requires $\omega_c \geq \sqrt{2}\omega_z$. The physical origin of this constraint can be traced back to the structure of the electric quadrupole potential, which is confining along $\hat{z}$ and repulsive along $\hat{\rho}$ (as must be the case to satisfy Laplace's equation). If the electric field (parameterized by ω_z) grows too large compared to the magnetic field (parameterized by ω_c), the magnetic radial confinement will become undone, and particle trajectories will no longer be bound.

Given the typical magnetic fields and potentials applied in a Penning trap, this requirement is easily satisfied since $\omega_c \gg \omega_z$. In this limit,

$$\omega_+ \approx \omega_c - \frac{\omega_z^2}{2\omega_c} \tag{2.8}$$

is identified as the "trap modified" cyclotron frequency, which is slightly reduced from ω_c on account of the repulsive radial electric field. Likewise,

$$\omega_- \approx \frac{\omega_z^2}{2\omega_c} \tag{2.9}$$

is the magnetron frequency ω_m, which may be understood as a force-free drift with velocity $\vec{v} = \vec{E} \times \vec{B}/|\vec{B}|^2$. These three separable motions, with frequency hierarchy $\omega_c \gg \omega_z \gg \omega_m$, are depicted schematically in Fig. 2.3.

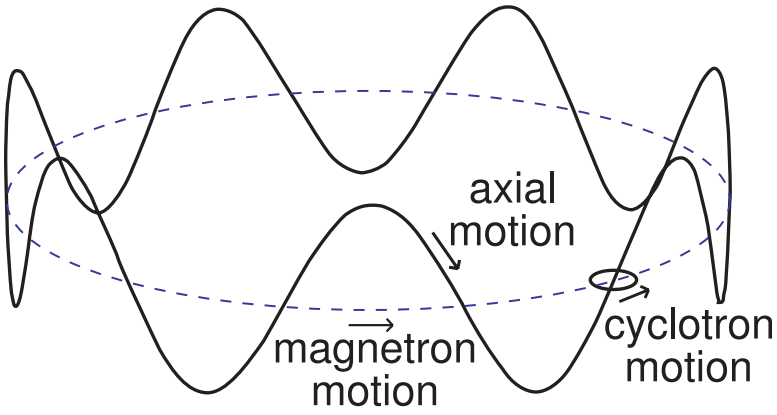

Figure 2.3: A single particle in a Penning trap exhibits three distinct motions at different frequencies.

2.1.2 Cylindrical Penning Traps

The equipotentials of an ideal quadrupole electric field are hyperbolas; placing conducting surfaces along these equipotentials (and biasing them appropriately) would allow for creation of the quadrupole field. Although such traps have had a long and successful history in making precision measurements [22], they carry several disadvantages for $\overline{\mathrm{H}}$ experiments. First, this geometry restricts particle access to the trap, which would make it difficult or impossible to load the $\overline{\mathrm{p}}$ and e^+ necessary for $\overline{\mathrm{H}}$ formation. Second, since the classic Penning trap can only confine particles of a single sign of charge, trapping $\overline{\mathrm{p}}$ and e^+ simultaneously would not be possible. Additionally, machining hyperbolic electrodes can be costly and difficult.

To surmount these problems, Penning traps were developed in which the electric potential is generated by cylindrical electrodes [71, 72] with open endcaps [73]. Cylindrical electrodes are substantially easier to machine and may be stacked on top of each other and biased independently to create independent voltage wells for confining oppositely charged particles. Deviations from the ideal quadrupole potential

can be made small when multi-well potentials are applied, while open endcaps permit unhindered access to the trap for $\overline{\mathrm{p}}$ and e^+ loading.

The electrostatic potential within a stack of cylindrical electrodes is slightly more complicated than that of an ideal quadrupole. However, finding an exact solution is critical for understanding the potential well structures on- and off-axis during particle manipulation and $\overline{\mathrm{H}}$ formation, minimizing the energy gained by particles during their transfer along the electrode stack, and calculating the geometry of plasmas confined within the Penning trap. Analytic and numeric methods have both been employed to calculate the potential for this geometry, depending on the desired level of accuracy and application.

To find an analytic solution, we begin by writing the general form of the potential in cylindrical coordinates as [74]

$$\Phi(\rho, \phi, z) = R(\rho)Q(\phi)Z(z) \tag{2.10}$$

Substitution of Eqn. 2.10 into Laplace's equation (in cylindrical coordinates) yields the separable differential equation

$$\frac{1}{R}\left[\frac{\partial^2 R}{\partial \rho^2} + \frac{1}{\rho}\frac{\partial R}{\partial \rho}\right] + \frac{1}{\rho^2}\frac{1}{Q}\frac{\partial^2 Q}{\partial \phi^2} + \frac{1}{Z}\frac{\partial^2 Z}{\partial z^2} = 0 \tag{2.11}$$

If Eqn. 2.11 is to hold for any arbitrary value of ρ, ϕ, and z, then each of the three terms in Eqn. 2.11 must be separately constant. If we choose the constants for the last two terms as

$$\frac{1}{\rho^2}\frac{1}{Q}\frac{\partial^2 Q}{\partial \phi^2} = -\frac{\nu^2}{\rho^2} \tag{2.12}$$

$$\frac{1}{Z}\frac{\partial^2 Z}{\partial z^2} = -k^2 \tag{2.13}$$

then this constrains the first term to be

$$\frac{1}{R}\left[\frac{\partial^2 R}{\partial \rho^2} + \frac{1}{\rho}\frac{\partial R}{\partial \rho}\right] = \left(k^2 + \frac{\nu^2}{\rho^2}\right) \tag{2.14}$$

The solutions to Eqns. 2.12 and 2.13 are simply given by

$$Q(\phi) = C\cos(\nu\phi) + D\sin(\nu\phi) \tag{2.15}$$

$$Z(z) = A\cos(kz) + B\sin(kz) \tag{2.16}$$

Using the substitution $x = k\rho$, Eqn. 2.14 may be written

$$\frac{\partial^2 R}{\partial x^2} + \frac{1}{x}\frac{\partial R}{\partial x} - \left(1 + \frac{\nu^2}{x^2}\right) R = 0 \tag{2.17}$$

which is Bessel's equation, solved by the modified Bessel functions $I_\nu(x)$ and $K_\nu(x)$.

Starting with these general solutions, we now impose the boundary conditions of a single cylindrical electrode with radius ρ_0 and axial half-length z_0 biased at potential V_0. We require the potential to be finite at $\rho = z = 0$, posses reflection symmetry about the $z = 0$ plane, and fall to 0 as $z \to \infty$. Though it is a slight approximation, we impose a ground plane at $z = L$, with $L \gg z_0$, to facilitate calculations.

First, we note that due to cylindrical symmetry, there can be no ϕ-dependence in the potential. Thus, $\nu = 0$ and $Q(\phi) = 1$. Next, the condition that the potential be finite at $\rho = 0$, along with the condition $\nu = 0$, eliminates all contributing Bessel functions in the radial solution except $I_0(k\rho)$. For Eqn. 2.16, reflection symmetry demands $B = 0$, while the ground plane at $z = L$ requires that k may only take the particular values

$$k_n = \frac{(n + \frac{1}{2})\pi}{L} \qquad (n = 0, 1, 2, 3, \ldots) \tag{2.18}$$

Combining these results, the full potential may now be written

$$\Phi(\rho, \phi, z) = \sum_{n=0}^{\infty} I_0(k_n \rho) \left[A_n \cos(k_n z) \right] \tag{2.19}$$

We may calculate the A_n terms by imposing the final boundary condition that $\Phi(\rho, \phi, z) = V_0$ at $\rho = \rho_0$ from $-z_0 \leq z \leq z_0$ (and 0 everywhere else when $\rho = \rho_0$). This eliminates the ρ dependence in Eqn. 2.19 and allows us to treat Φ as a Fourier expansion with coefficients $I_0(k_n \rho_0) A_n$. Multiplying both sides by $\cos(k_m z)$ and integrating,

$$A_n = \frac{2}{I_0(k_n \rho_0) L} \int_0^{z_0} V_0 \cos(k_n z) dz \tag{2.20}$$

$$= \frac{2V_0}{L k_n} \frac{\sin(k_n z_0)}{I_0(k_n \rho_0)} \tag{2.21}$$

Substitution of Eqn. 2.21 back into Eqn. 2.19 gives an analytic form for the potential due to a single electrode within the trap. For any arbitrary configuration of voltages applied to multiple electrodes, the total potential may simply be found by superposition of the single-electrode potentials.

It is often useful to know by how much the cylindrical potential differs from the ideal quadrupole, or conversely, how to generate a nearly ideal quadrupole by simultaneously applying different voltages to multiple electrodes. If the general potential is expanded in terms of Legendre polynomials in spherical coordinates, we may write

$$\Phi(r, \theta) = \frac{V_0}{2} \sum_{\substack{j=0 \\ \text{even}}}^{\infty} C_j \left(\frac{r}{d} \right)^j P_j(\cos\theta) \tag{2.22}$$

where we have again used reflection symmetry to eliminate the odd terms in the expansion. The constants C_j are a measure of the size of the harmonic (z^2) and

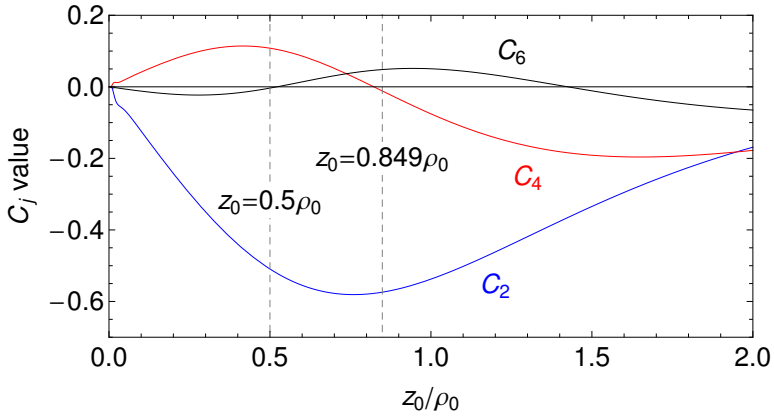

Figure 2.4: C_2, C_4, and C_6 coefficients for a cylindrical electrode as a function of electrode length. Two common values of z_0/ρ_0 for electrodes in BTRAP are indicated.

anharmonic $(z^4, z^6, \ldots)$ terms in the expansion, while $d = \sqrt{\frac{1}{2}(z_0^2 + \rho_0^2/2)}$ is the geometric factor defined earlier. By equating these two expressions for the potential, Eqns. 2.19 and 2.22, and setting $\rho = 0$, we can solve for the constants C_j

$$C_j = \frac{2}{V_0}\frac{(-1)^{j/2}}{j!}\sum_{n=0}^{\infty} A_n (k_n d)^j \tag{2.23}$$

For an ideal quadrupole, the anharmonic coefficients $C_{j>2} = 0$. For a cylindrical electrode, however, non-zero coefficients $C_{j>2}$ are unavoidable. As shown in Fig. 2.4, these higher-order coefficients vary as a function of the electrode length. One common choice of electrode length in BTRAP, $z_0 = 0.849\rho_0$, minimizes the first anharmonic correction to the potential ($\propto C_4 z^4$). Another common length, $z_0 = 0.5\rho_0$, minimizes the z^6 term while keeping C_4 small.

To cancel out both C_4 and C_6 simultaneously and create a more ideal quadrupole, we can make use of nearby electrodes to shape the potential. Compared with the single-electrode case, two new tunable parameters are necessary to ensure a sufficient number of degrees of freedom to eliminate C_4 and C_6. One possibility is to set the half-

length of the nearest-neighbor electrodes to $z_1 = 2.52z_0$ while biasing with a potential $V_1 = 0.881V_0$ (where z_0 and V_0 are the half-length and applied potential for the central electrode). Measurements performed in such traps have been demonstrated to meet or exceed the precision of those in traps with hyperbolic electrodes [75]. If nearby electrodes are all of the same length, an alternative is to apply voltages $V_1 = 0.931V_0$ and $V_2 = 0.706V_0$ to the nearest-neighbor and next-nearest-neighbor electrodes (respectively). Even higher order C_j terms may be eliminated by involving more electrodes, though in practice, imperfections in the electrode lengths and applied voltages will always cause slight deviations from the ideal quadrupole. A comparison of the electrostatic potentials for various electrode configurations is shown in Fig. 2.5.

Unfortunately, a difficulty arises when using this analytic solution far off-axis. Eqn. 2.19 contains an infinite sum of terms, which must be cut off at some order to enable calculation. However, as ρ increases, $I_0(k_n\rho)$ increases sharply, and higher-order terms in the expansion have an increasingly large effect. To circumvent these issues, the potential within the trap may instead be determined by a numerical relaxation calculation [76, 77].

Numerical relaxation is a scheme to iteratively solve Laplace's equation on a grid of discrete points. Consider a 2D grid in the xy-plane with points labeled by indices $\{i, j\}$, point spacings h, and the potential at each point given by $\phi_{i,j}$. The first derivatives in the x and y directions may be written

$$\frac{\partial\phi}{\partial x} = \frac{\phi_{i,j} - \phi_{i-1,j}}{h} \qquad \frac{\partial\phi}{\partial y} = \frac{\phi_{i,j} - \phi_{i,j-1}}{h} \tag{2.24}$$

Similarly, the second derivatives are given by

$$\frac{\partial^2\phi}{\partial x^2} = \frac{\phi_{i-1,j} + \phi_{i+1,j} - 2\phi_{i,j}}{h^2} \qquad \frac{\partial^2\phi}{\partial y^2} = \frac{\phi_{i,j-1} + \phi_{i,j+1} - 2\phi_{i,j}}{h^2} \tag{2.25}$$

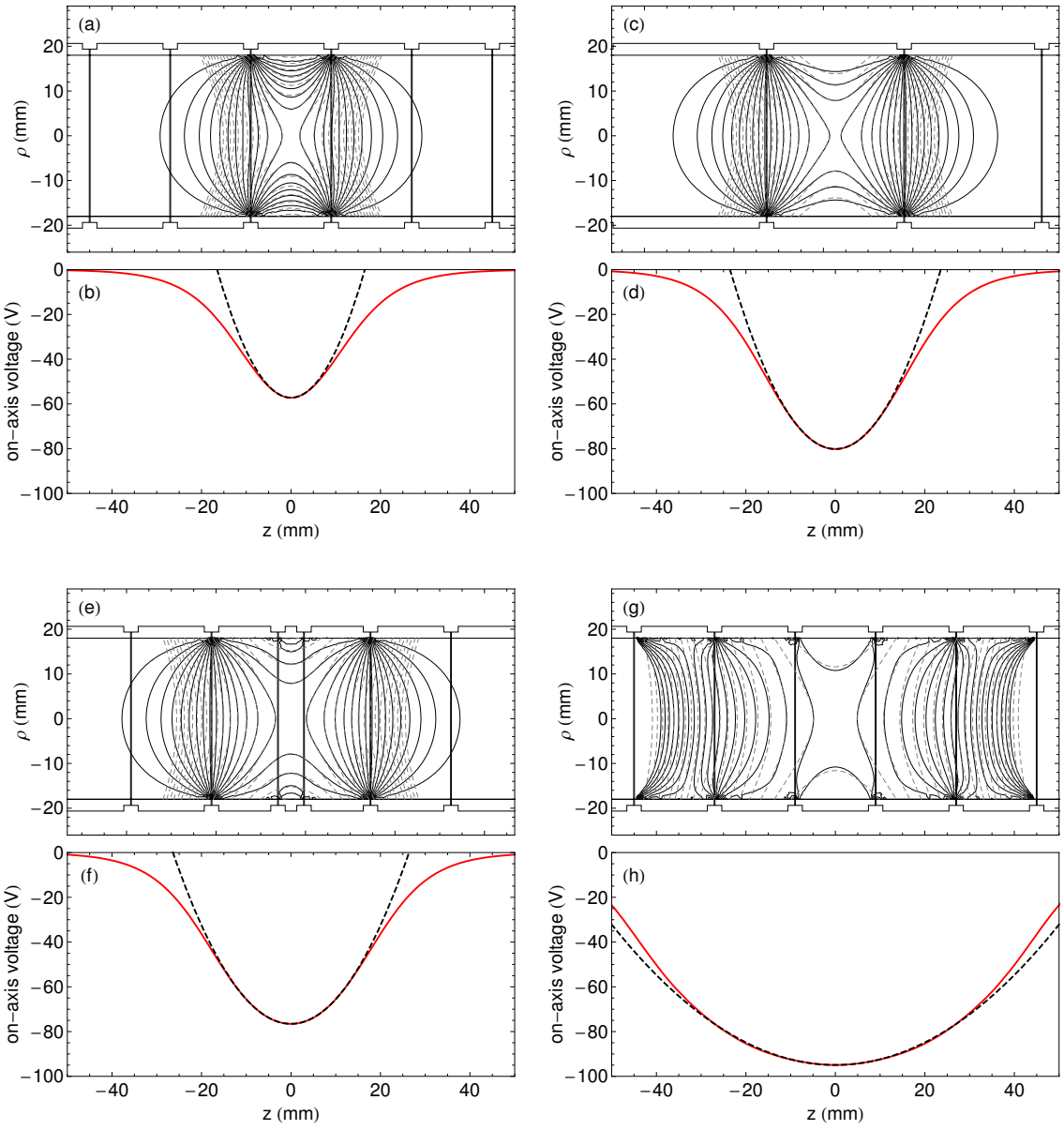

Figure 2.5: Comparison of the real potential within the cylindrical trap (solid lines) to the ideal quadrupole potential (dashed lines). All central electrodes are biased to -100 V. Equipotentials and the on-axis potential are shown for a single electrode with $z_0 = 0.5\rho_0$ (a)-(b), a single electrode with $z_0 = 0.849\rho_0$ (c)-(d), a 3-electrode harmonic well with $z_1 = 2.52z_0$ and $V_1 = 0.881V_0$ (e)-(f), and a 5-electrode harmonic well with $V_1 = 0.931V_0$ and $V_2 = 0.706V_0$ (g)-(h).

The potential at any gridpoint $\phi_{i,j}$ may now be found by setting $\nabla^2\phi = 0$

$$\phi_{i,j} = \frac{1}{4}(\phi_{i-1,j} + \phi_{i+1,j} + \phi_{i,j-1} + \phi_{i,j+1}) \tag{2.26}$$

which is the elegant result that the potential at gridpoint $\{i, j\}$ is the average of the potentials at the 4 neighboring gridpoints. To iteratively solve for the potential $\phi_{i,j}$ anywhere, one starts with a trial solution for ϕ with points on the edge of the grid satisfying the external boundary conditions. For every timestep, the potential at point $\phi_{i,j}$ is calculated using Eqn. 2.26. Over time, the fixed boundary conditions "diffuse" throughout the grid, until after many iterations, a stable solution is reached.

In cylindrical coordinates, the solution is more complicated than Eqn. 2.26, but is solvable in the same way. Calculating the first and second derivatives in the ρz plane and substituting into Laplace's equation in cylindrical coordinates, we find

$$\phi_{i,j} = \frac{1}{4}\left[\phi_{i-1,j} + \phi_{i+1,j} + \phi_{i,j-1} + \phi_{i,j+1} + \frac{h}{2\rho}(\phi_{i,j+1} - \phi_{i,j-1})\right] \tag{2.27}$$

where now the grid spacing h and the radial coordinate ρ appear in the expression for $\phi_{i,j}$. On account of the $1/\rho$ term, Eqn. 2.27 is unsolvable on the axis. Recognizing that the behavior of the Laplacian as $\rho \to 0$ is

$$\lim_{\rho\to 0}\left[\frac{1}{\rho}\frac{\partial}{\partial\rho}\left(\rho\frac{\partial\phi}{\partial\rho}\right) + \frac{\partial^2\phi}{\partial z^2}\right] = 2\frac{\partial^2\phi}{\partial\rho^2} + \frac{\partial^2\phi}{\partial z^2} \tag{2.28}$$

the solution on-axis is given by

$$\phi_{i,0} = \frac{1}{6}(\phi_{i-1,0} + \phi_{i+1,0} + 4\phi_{i,1}) \tag{2.29}$$

Using Eqns. 2.27 and 2.29, $\phi_{i,j}$ has been calculated everywhere within the BTRAP electrode stack, allowing for an accurate determination of the potential both on- and off-axis.

2.1.3 Synchrotron cooling

On account of its cyclotron, axial, and magnetron motions, a charged particle in a Penning trap is constantly accelerating and radiating away synchrotron energy. Here we consider the energy lost by a particle due to its cyclotron motion, which dominates over the other loss rates since $\omega_c \gg \omega_z \gg \omega_m$. Classically, the power radiated by an accelerating charge is given by the Larmor formula

$$\frac{dE}{dt} = -\frac{q^2}{6\pi\epsilon_0 c^3}|\ddot{\vec{r}}|^2 \tag{2.30}$$

A particle undergoing cyclotron motion feels a Lorentz force

$$F = m\ddot{\vec{r}} = q\dot{\vec{r}} \times \vec{B} \tag{2.31}$$

Using that $\vec{B} = B_0\hat{z}$ and $\dot{\vec{r}} = v_\phi\hat{\phi}$,

$$|\ddot{\vec{r}}|^2 = \left(\frac{qB_0}{m}\right)^2 v_\phi^2 \tag{2.32}$$

Since the energy of the cyclotron motion is $E = mv_\phi^2/2$, we may rewrite the right-hand side of Eqn. 2.30 in terms of E

$$\frac{dE}{dt} = -\frac{E}{\tau_s} \tag{2.33}$$

where τ_s is the synchrotron damping time

$$\tau_s = \frac{3\pi\epsilon_0 m^3 c^3}{q^4 B_0^2} \tag{2.34}$$

The solution to Eqn. 2.33 is a simple exponential decay, $E(t) = E_0 e^{-t/\tau_s}$, with time constant τ_s. On account of the m^3 dependence of τ_s, the synchrotron cooling time varies widely between different types of particles. For instance, a $\overline{\text{p}}$ in a typical magnetic field of $B_0 = 3.7$ T gives $\tau_s \approx 37$ years, while an electron in the same field has a damping time of only $\tau_s \approx 0.19$ seconds.

2.1.4 BTRAP Penning Trap

In the BTRAP Penning trap, the magnetic field necessary for radially confining charged particles is produced by a superconducting 1 T solenoid, as shown in Fig. 2.2. This magnet features a 50.8 cm inner bore into which the BTRAP apparatus is inserted and provides a field homogeneity of 1.5×10^{-4} within a 50 cm long $\times$ 5 cm diameter cylinder at the center of the windings. To reduce the cryogen boiloff rate, a liquid nitrogen shield surrounds the 550 L liquid helium space, the solenoid is operated in persistent mode, and the helium pressure in the magnet is actively regulated. Since this magnet can be operated up to a maximum field of 3 T, quench-free operation at 1 T throughout an entire 10-month run is possible, provided proper maintenance of cryogen levels.

A stack of cylindrical electrodes that are independently controlled provides axial confinement within the Penning trap, as seen in Figs. 2.2 and 2.6. These electrodes all have a radius of 18 mm and typical lengths of 30.56 mm in the lower part of the stack ($z_0/\rho_0 = 0.849$) and 18 mm in the upper stack ($z_0/\rho_0 = 0.5$). At two locations, a symmetric set of three electrodes satisfying $z_1/z_0 = 2.52$ and $V_1/V_0 = 0.881$ form a nearly ideal quadrupole potential, as shown in Fig. 2.5 (e)-(f). Elsewhere, a nearly ideal quadrupole can be formed by applying the appropriate potentials to five neighboring electrodes of the same length, as in Fig. 2.5 (g)-(h).

To ensure cylindrical symmetry within the trap, every electrode has been precision machined to a tolerance of 0.0002 inches. To further improve the finish, the inside surfaces have been hand-polished to a smoothness of 1 μm. The electrodes are fabricated from a cylinder of oxygen-free copper (OFHC) to minimize the internal

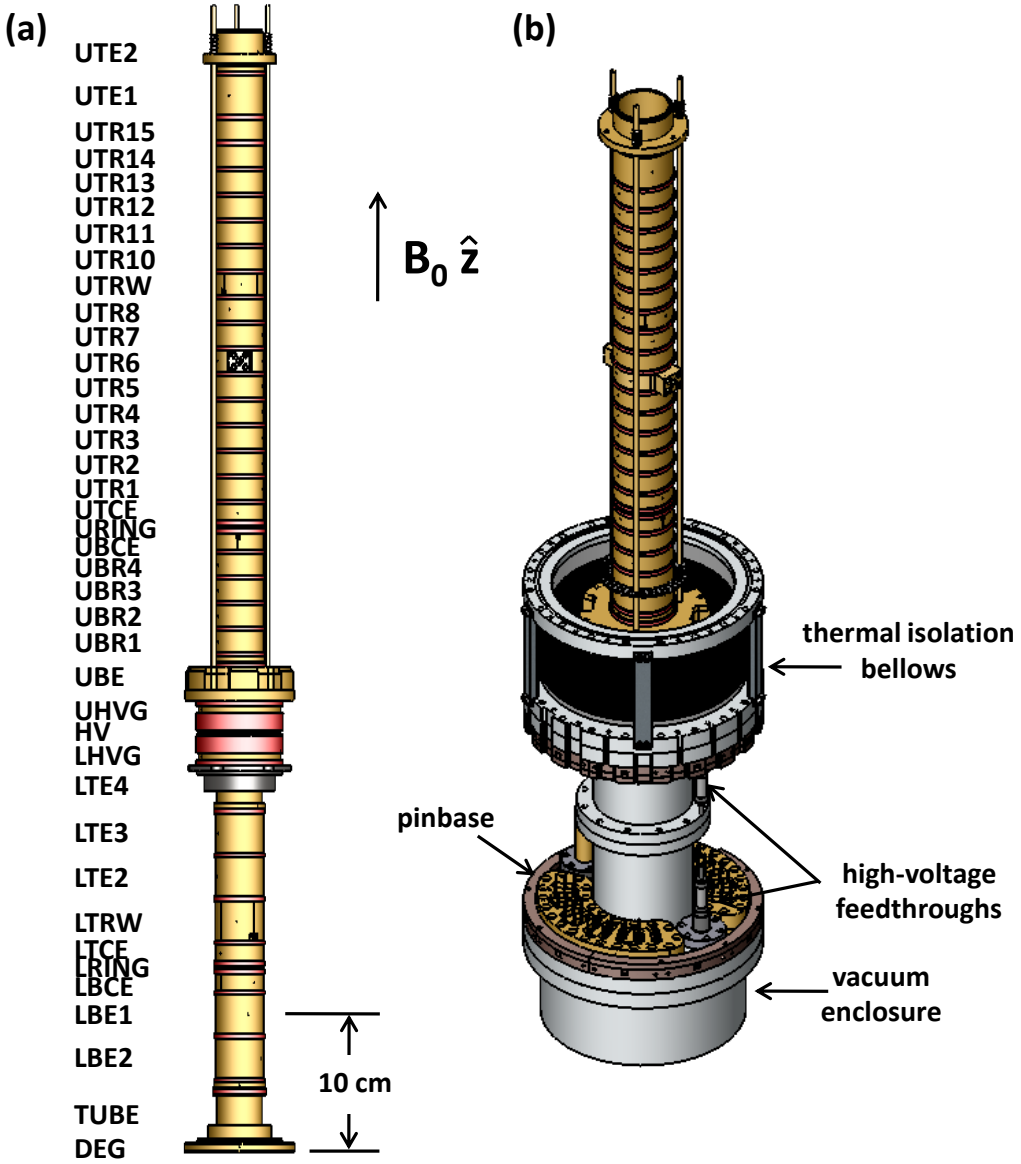

Figure 2.6: Electrodes providing the axial confining potential in the BTRAP Penning trap. The uniform magnetic field $B_0\hat{z}$ is directed along the trap axis. (a) Side view of the 39 independently controlled electrodes with names indicated. (b) Vacuum enclosure surrounding the electrode stack. Voltages from external supplies pass through vacuum feedthrough pins mounted on pinbases before connecting to the electrodes.

stresses in the material during machining and the electrical resistance at cryogenic temperatures respectively. Leads are brazed into the electrode body in a 800° C hydrogen oven, followed immediately by gold-plating of the electrode surfaces to prevent oxidation. These electrodes are mounted within a vacuum enclosure made entirely from non-ferrous materials, to prevent distortions of the homogeneous 1 T magnetic field.

All electrodes in the trap may be biased up to 1 kV, and up to 5 kV may be applied to the HV and DEG electrodes for $\overline{\mathrm{p}}$ catching. Voltages for each electrode are generated in a dedicated custom-built low-noise supply, pass through room-temperature RC and LC filters with 200 ms and 20 μs time constants (respectively), travel down to the cryogenic environment along 0.003 inch diameter constantan wire, are 1 ms RC filtered at cryogenic temperatures, and connect to the electrodes via vacuum feedthrough pins. Voltage ramps and a 50 Ω termination to ground may be also applied to any electrode through the DC line, and separate capacitively-coupled micro-coax or twisted pair lines allow for application of pulses or rf drives to any electrode.

The entire electrode stack is held at temperatures of 4.2 K or less, with a recent upgrade that further cools the electrodes to 1.2 K described in Sec. 2.6. Cold temperatures allow the walls to cryopump away any background gas and vastly decrease the pressure inside the apparatus, which is necessary for obtaining long trapping lifetimes for antimatter particles. In addition, trapped particles will only synchrotron cool until they reach thermal equilibrium with the blackbody radiation from their surroundings; colder electrode walls thus permit colder particle temperatures. To reach 4.2 K, a liquid helium dewar sits in the middle of the BTRAP apparatus (see Fig. 2.2)

and conduction cools all sub-assemblies below it. To reduce the liquid helium boiloff rate, three thermal isolation stages covered with aluminized mylar superinsulation minimize the radiative heat load from the top of the experiment while retractable high-current leads, stainless-steel micro-coax, thin constantan trap wiring, and a G10 (fiberglass) support structure minimize the conductive heat load. To reduce the radiative heat load from the $\sim$2 m long side, a pulse-tube cooled "insert dewar" is nested between the 4 K BTRAP apparatus and the 300 K bore of the 1 T magnet (see Fig. 2.2). With these measures in place, the 60 L capacity of the helium dewar is sufficient to keep the apparatus at 4.2 K for over 24 hours.

2.2 Ioffe Trap

2.2.1 Theory

A Ioffe trap confines neutral atoms using a static configuration of magnetic fields that create a magnetic minimum in three dimensions. Paramagnetic atoms, whose energy in a magnetic field changes as $-\vec{\mu}\cdot\vec{B}$, can be trapped in this magnetic minimum if they occupy low-field seeking states, for which the internal energy increases as $|\vec{B}|$ increases. Following their proposal [52], Ioffe traps have been employed in a wide variety of systems for confinement and spectroscopy of neutral atoms [28, 78, 79].

In the ground state levels of H (and $\overline{\mathrm{H}}$), the electron-nuclear spin-spin interaction introduces a term $\mathcal{A}\vec{I}\cdot\vec{S}$ into the Hamiltonian, where $\mathcal{A}$ is given by Eqn. 1.4 [80]. In the presence of a magnetic field, a Zeeman term $-\vec{\mu}\cdot\vec{B}$ is also added to the

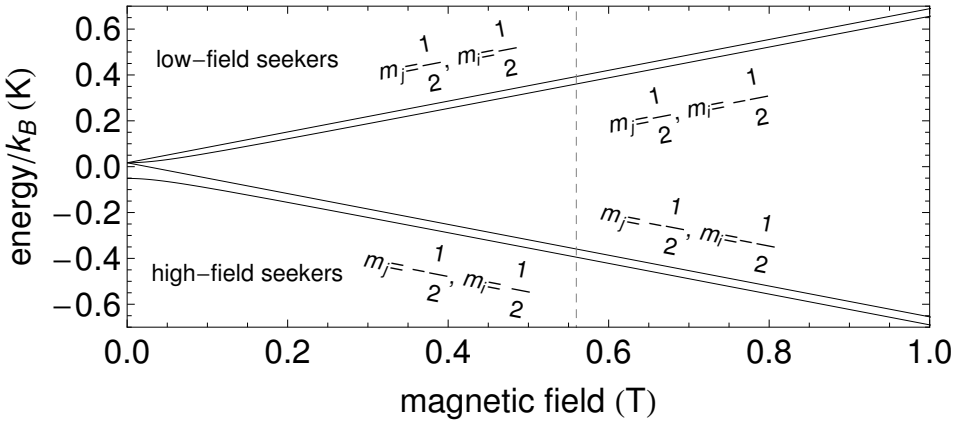

Figure 2.7: Ground state energy levels of H in a magnetic field, expressed in temperature units. Low-field seeking states are those for which the energy increases in an increasing magnetic field. The dashed line indicates the strength of the BTRAP Ioffe trap magnetic field.

Hamiltonian. For the ground state of H, we take

$$\vec{\mu} = \vec{\mu_s} = -\frac{|q|}{2m_e} g_e \vec{S} \tag{2.35}$$

since the orbital contribution to the magnetic moment vanishes ($\ell = 0$) and the nuclear contribution to the magnetic moment is smaller than the electron contribution by a factor m_e/m_p. Working in the basis $|m_j, m_i\rangle$, where m_j and m_i are the projections of the electron and nuclear spins along $\hat{z}$ respectively, the effect of these new terms is to introduce an energy shift of the four basis states $\left|m_j = \pm\frac{1}{2}, m_i = \pm\frac{1}{2}\right\rangle$. In the strong field limit ($|\vec{B}| \gtrsim 0.1$ T), this shift is given by

$$\Delta E = \mathcal{A}\hbar^2 m_j m_i + \frac{|q|\hbar}{2m_e}|\vec{B}| g_e m_j \tag{2.36}$$

which grows linearly with $|\vec{B}|$ at a rate of 0.67 K/T (in temperature units). The full energy level diagram for the weak-, intermediate-, and strong-field regimes is shown in Fig. 2.7.

Only particles in low-field seeking states may be trapped since only a magnetic minimum can be created in free space using static fields [81]. Low-field seekers have a magnetic moment anti-parallel to the direction of the magnetic field, giving $\vec{\mu}\cdot\vec{B} < 0$. Since the magnetic moment and spin are anti-parallel for an electron, the low-field seeking states in H have $m_j = 1/2$. Note that $\vec{\mu}$ and $\vec{S}$ are co-aligned for a positron, so the low-field seeking states in $\overline{\mathrm{H}}$ are those for which $m_j = -1/2$; the spin is anti-aligned with the magnetic field direction.

A schematic of the Ioffe trap geometry is shown in Fig. 2.8. In its simplest realization, a Ioffe trap may be created from six current-carrying bars: four straight bars with alternating directions of current flow to form a radial quadrupole and two "pinch coils" (i.e. loops) to form an axial well. Higher-order Ioffe traps are also possible, for which the number of straight bars is increased, and the alternating current flow pattern is retained. On account of the axial field generated by the pinch coils, $|\vec{B}| > 0$ at the magnetic minimum, and therefore atom loss due to Majorana spin-flip transitions is avoided [82].

The exact form of the radial Ioffe field for a multipole of order ℓ may be calculated by [83]

$$\vec{B}(\rho,\phi) = B_r \left(\frac{\rho}{\rho_0}\right)^{\ell-1} \left(\cos(\ell\phi)\hat{\rho} - \sin(\ell\phi)\hat{\phi}\right) \tag{2.37}$$

where the overall scale is set by the strength of the radial field B_r at $\rho = \rho_0$. The magnitude of the radial field is given by

$$|\vec{B}(\rho,\phi)| = \left[B_r^2 \left(\frac{\rho}{\rho_0}\right)^{2(\ell-1)} \left(\cos(\ell\phi)^2 - 2\cos(\ell\phi)\sin(\ell\phi)\hat{\rho}\cdot\hat{\phi} + \sin(\ell\phi)^2\right)\right]^{1/2} \tag{2.38}$$

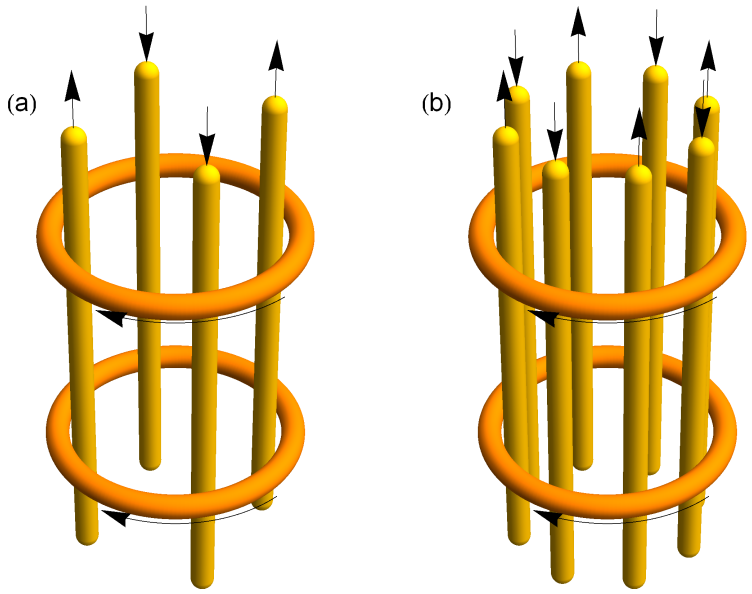

Figure 2.8: Simplified schematics of a quadrupole (a) and octupole (b) Ioffe trap. The direction of current flow through each of the current bars is indicated.

and since $\hat{\rho} \cdot \hat{\phi} = 0$,

$$|\vec{B}(\rho, \phi)| = B_r \left(\frac{\rho}{\rho_0} \right)^{\ell - 1} \tag{2.39}$$

which indicates that the magnitude of the radial field is ϕ-independent. For a quadrupole - the type of Ioffe trap used in BTRAP - the multipole order $\ell = 2$, so the radial field grows linearly with ρ.

The depth of a Ioffe trap may be defined as $|\mu|\Delta B$, where the ΔB is the difference between the minimum $|\vec{B}|$ along the boundary of the trap volume and the minimum $|\vec{B}|$ anywhere in the trap. In the presence of only the radial field, $\Delta B = B_r$. However, the addition of the field $B_z = B_p(z) + B_0$ must also be considered, where $B_p(z)$ is the pinch coil field and B_0 is a uniform axial background field. Note that B_0 is not created by the Ioffe coils, but is present in the BTRAP geometry due to the external

1 T solenoid.

The full strength of the magnetic field everywhere in the trap is now given by

$$|\vec{B}(r,\phi,z)| = \sqrt{|\vec{B}(r,\phi)|^2 + (B_p(z) + B_0)^2} \tag{2.40}$$

The axial confining field from the pinch coils can always be made large enough so that the minimum $|\vec{B}|$ on the trap boundary will lie at $\rho = \rho_0$ and $z = 0$ (by symmetry). Using this, we calculate

$$\Delta B = \sqrt{B_r^2 + (B_p(0) + B_0)^2} - (B_p(0) + B_0) \tag{2.41}$$

Compared to the radial-field only case, the trap depth has now been *reduced* due to the presence of the axial fields. Eqn. 2.41 prescribes two optimizations that will maximize the trap depth. First, the strength of the pinch coil field should only be increased until the radial and axial changes in $|\vec{B}|$ are equal. Further increases in the size of B_p will decrease ΔB in the radial direction. Second, the external background field B_0 should be made as small as possible without affecting the stability of the Penning trap. It is for this reason that B_0 is set to 1 T, even though the external solenoid permits a magnetic field as large as 3 T. As shown in Fig. 2.9, operating the background field at 3 T would nearly halve the Ioffe trap depth.

2.2.2 BTRAP Ioffe Trap

In the BTRAP quadrupole Ioffe trap, four current-carrying "racetrack" coils and two pinch coils create a magnetic minimum that can trap low-field seeking $\overline{\mathrm{H}}$. These coils are made from superconducting multistrand NbTi wire wound on titanium forms to produce the desired Ioffe geometry. The trap was designed at Harvard and con-

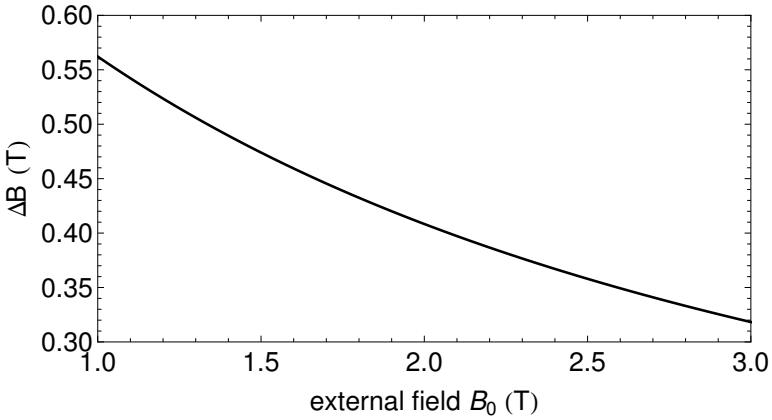

Figure 2.9: The Ioffe trap depth, proportional to ΔB, decreases with increasing external background field strength. The values for B_r and $B_p(0)$ match those for the BTRAP Ioffe trap.

structed in a cooperative effort between ATRAP members at the Forschungszentrum Jülich and ACCEL Instruments GmbH. The trap structure is fabricated from entirely non-magnetic materials to prevent distortions in the Ioffe or axial background fields. Tightly-fitting, precision machined titanium and aluminum pieces counteract the large forces from the magnet coils, while an all-titanium enclosure surrounds the windings and provides a volume in which liquid helium can accumulate to keep the coils cold. The BTRAP Ioffe trap surrounds the upper part of the electrode stack (see Fig. 2.2) and is shown in more detail in Fig. 2.10.

Four elliptical sideports pass through the magnet body. Small holes in an electrode vertically aligned with the sideports permit access to the center of the Penning trap from outside the experiment vacuum space. Two of these ports are in use on BTRAP to create and detect Rydberg cesium, the progenitor of $\overline{\mathrm{H}}$ produced via double-charge exchange. The two remaining ports are currently unused, though will become important for introducing Lyman α light for laser cooling of $\overline{\mathrm{H}}$ and 243 nm

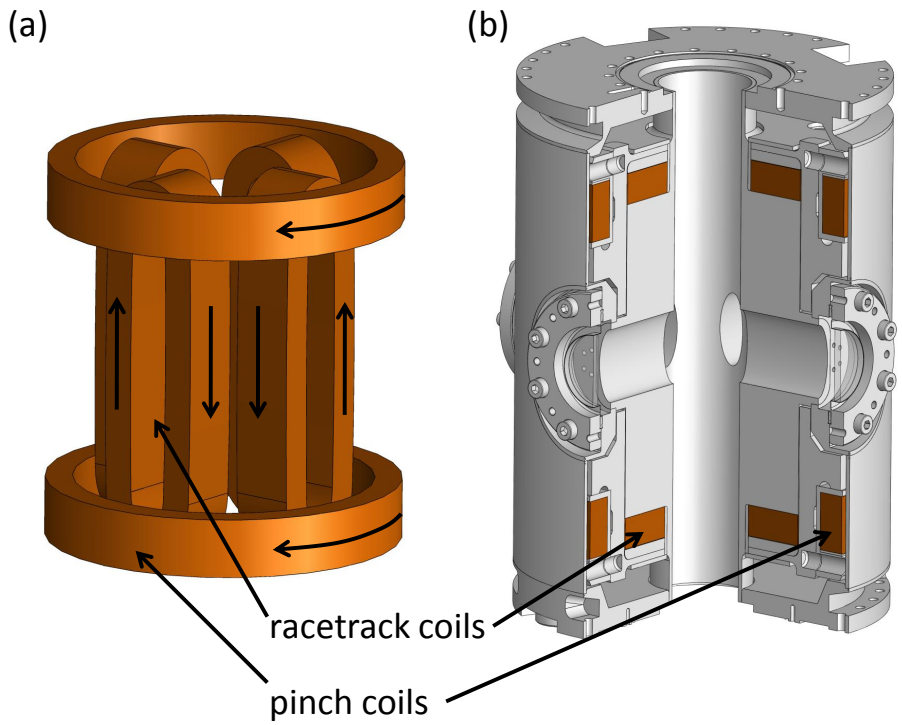

Figure 2.10: Drawing of the BTRAP Ioffe trap, showing the racetrack and pinch coils with the direction of current flow indicated (a) and the full magnet assembly (b). Four elliptical side ports enable access to the electrode stack within (not shown).

UV light for two-photon $1S - 2S$ spectroscopy. For this purpose, custom windows made from MgF_2 have been installed to seal the vacuum space while allowing for high transmission of UV and VUV laser light.

Currents of 69 A and 80 A are passed through the racetrack and pinch coils to produce a 0.56 T difference in magnetic field between the electrode walls and trap center, corresponding to a 375 mK trap depth for ground state $\overline{\mathrm{H}}$. The strength of the radial field grows linearly with ρ (as shown in Eqn. 2.39) with a gradient of 0.093 T/mm, giving $B_r = 1.7$ T at the electrode wall. The axial field due to the pinch coils reaches a maximum of 1.71 T, falling to 1.15 T at the center of the trap. The

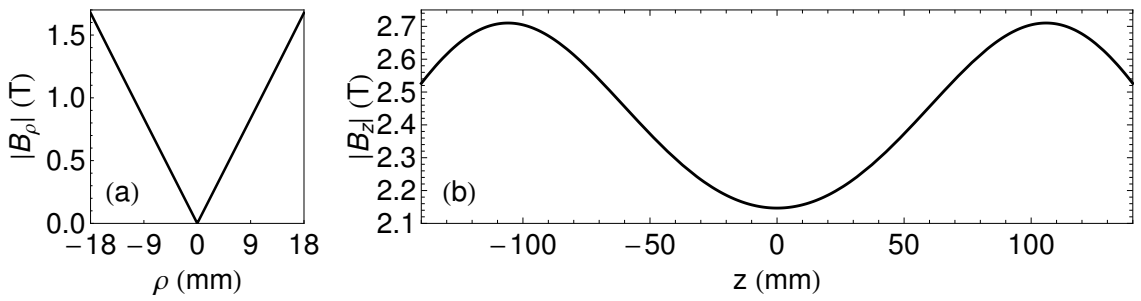

Figure 2.11: Magnitude of the radial (a) and axial (b) magnetic fields in the Ioffe trap, with the 1 T axial background field included.

magnitude of the radial and axial fields, including the 1 T background bias field, are plotted in Fig. 2.11.

Since the coils of the Ioffe trap are superconducting, they are prone to quenches which may rapidly heat and damage the windings. To protect against this, diodes are installed across each coil that allow the current to bypass the superconductor in the event of a quench. These diodes activate at a differential voltage of ≈ 5 V, limiting the maximum quench resistance in the quadrupole coils (for instance) to $R_q = 5$ V/69 A = 70 mΩ. Estimates of quench propagation [84] indicate that the diodes should activate within 4 ms of the quench, limiting the energy deposited to ≈ 30 J.

Passive quench protection has a drawback, however. Since the diodes will activate if more than 5 V is applied across the magnet leads, the magnet ramping rate is limited to $dI/dt = V/L = 1.5$ A/s for $L = 3.3$ H. Thus, de-energizing the magnet from full field would take nearly 1 minute. If a faster turn-off time is needed (as is the case for searches of trapped $\overline{\mathrm{H}}$), the Ioffe trap may be purposefully quenched to de-energize the magnet in ≈ 1 s. Two different methods to quench the Ioffe trap on demand have been employed. In the first, the currents in the racetrack and pinch coils may

be increased until a quench is triggered by motion of the windings in reaction to the increased magnetic forces or by exceeding the critical current. The second method is more gentle, with a quench induced by applying 14 W to a small resistive heater mounted only 4 mm away from one of the racetrack coils. Following quench events, which are often violent processes, the Ioffe trap may require up to 24 hours of recovery time before full field can be achieved again.

2.3 Penning-Ioffe Trap

The superposition of a Penning and Ioffe trap creates an environment in which charged and neutral particles may simultaneously be confined. Penning-Ioffe traps are crucial for capturing neutral $\overline{\mathrm{H}}$ formed during the interaction of charged $\overline{\mathrm{p}}$ and e^+. However, a natural competition arises between the uniform background field necessary for radial confinement in a Penning trap and the non-uniform radial field necessary for confinement in a Ioffe trap. Due to the loss of cylindrical symmetry, charged-particle confinement can no longer be guaranteed.

2.3.1 Charged Particle Trajectories

To determine whether a single charged particle will remain trapped in the Penning-Ioffe configuration, the particle trajectories may be analyzed as in Ref. [53]. As before, we begin by solving for the equations of motion using the Lorentz Force law. Now, the uniform axial magnetic field $\vec{B} = B_0\hat{z}$ has an additional field due to the superimposed

Ioffe trap, giving

$$\vec{B} = \frac{B_r}{\rho_0}(x\hat{x} - y\hat{y}) + B_z\hat{z} \tag{2.42}$$

where the first term in Eqn. 2.42 is simply Eqn. 2.37 rewritten in rectangular coordinates, and the second term $B_z\hat{z} = B_p(0)\hat{z} + B_0\hat{z}$ are the pinch and background axial fields, which we take to be constant near the center of the trap. If we assume an electric quadrupole potential, the presence of the Ioffe field introduces new terms into the Penning trap equations of motion (Eqns. 2.2-2.4)

$$m\ddot{x} = \frac{qV_0}{2d^2}x + qv_yB_z + q\frac{B_r}{\rho_0}yv_z \tag{2.43}$$

$$m\ddot{y} = \frac{qV_0}{2d^2}y - qv_xB_0 + q\frac{B_r}{\rho_0}xv_z \tag{2.44}$$

$$m\ddot{z} = -\frac{qV_0}{d^2}z - q\frac{B_r}{\rho_0}(yv_x + xv_y) \tag{2.45}$$

As before, charged particles execute cyclotron, axial, and magnetron motions and satisfy the hierarchy $\omega_c \gg \omega_z \gg \omega_m$, though each motion is altered by the new fields. The cyclotron motion is no longer perpendicular to $\hat{z}$ everywhere, but instead to the direction of the local magnetic field. On account of the radial field gradient, the cyclotron frequency now depends on position

$$\omega_c \approx \frac{q}{m}\sqrt{B_r^2\left(\frac{\rho}{\rho_0}\right)^2 + B_z^2} \tag{2.46}$$

Similarly, the axial motion is no longer along $\hat{z}$, but rather follows the trajectory of the local magnetic field line. In general, field lines in the Ioffe trap curve into the "twisted bow-tie" shape shown in Fig. 2.12a. Field lines diverge maximally in the $xz-$ and $yz-$planes, defined to be co-aligned with the Ioffe current bars. For instance, in the xz plane, the change in the x position of a field line given a fixed change in z

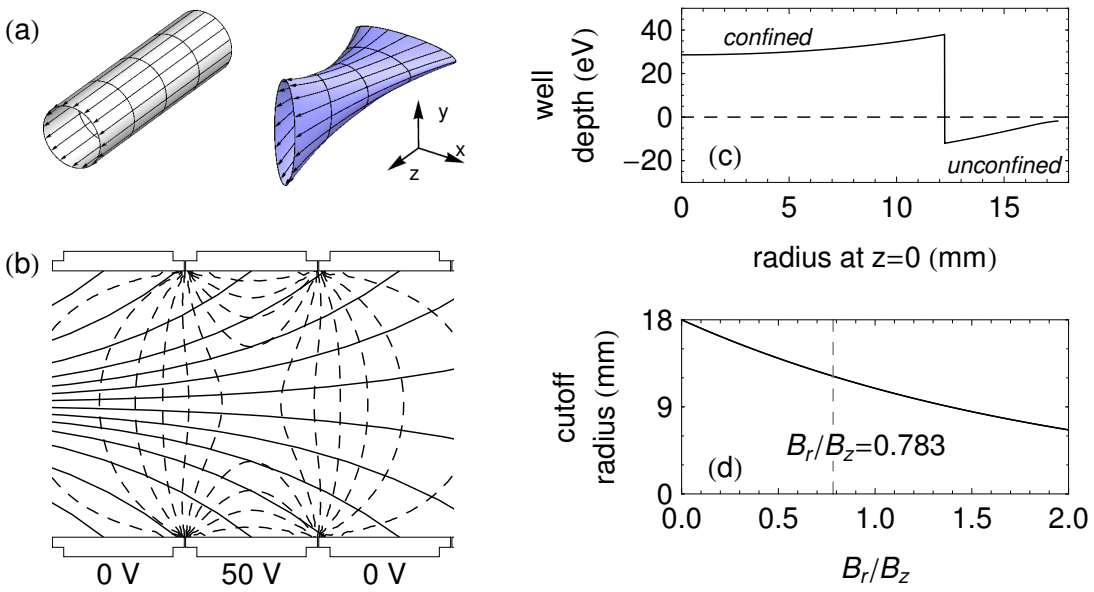

Figure 2.12: (a) The straight, cylindrically-symmetric field lines of a Penning trap (left) are transformed into a "twisted bow-tie" configuration in a quadrupole Penning-Ioffe trap (right). (b) Superposition of Penning-Ioffe magnetic field lines (solid) and electric field equipotentials (dashed) within the trap volume. (c) The well depth along field lines at different radii becomes negative at $\rho = 12$ mm, indicating that particles on field lines at larger radii cannot be confined . (d) The cutoff radius decreases as the strength of the radial field increases. The BTRAP value for B_r/B_z is indicated.

position is equal to the ratio of radial to axial field strengths at that position

$$\frac{dx}{dz} = \frac{B_r}{B_z}\frac{x}{\rho_0} \tag{2.47}$$

which is readily solved to give $x(z) = x_0 \exp\left[B_r z/(B_z \rho_0)\right]$. Fig. 2.12b shows several of these field lines at various radii. One striking difference here compared to the bare Penning trap is that field lines now diverge into the electrode walls; $\overline{\mathrm{p}}$ or e^+ executing axial motion along these field lines will be ballistically lost from the trap upon striking the electrodes. Since the radial component of the Ioffe field is small near the center of the trap, only particles at large radii move along field lines which intersect the walls of the trap. The well depth along the magnetic field lines is plotted as a

function of radius in Fig. 2.12c. When 50 V is applied to a radius-length electrode, the well depth becomes sharply negative at ρ =12 mm, indicating that particles starting at $\rho = 12$ mm or larger will annihilate on the walls before completing one axial bounce. As may be expected, the cutoff radius at which particles are first lost from the Penning-Ioffe trap decreases as the strength of the radial field is increased, as shown in Fig. 2.12d.

Particles in a Penning-Ioffe trap also undergo a force-free $\vec{E} \times \vec{B}$ magnetron drift, though this motion is no longer constrained to the xy-plane. To find the magnetron trajectory, we require

$$\vec{F} = q(\vec{E} + \vec{v} \times \vec{B}) = 0 \tag{2.48}$$

Dotting all sides of Eqn. 2.48 into $\vec{B}$, and recognizing that $(\vec{v} \times \vec{B}) \cdot \vec{B} = 0$, we find

$$q\vec{E} \cdot \vec{B} = 0 \tag{2.49}$$

Substituting the ideal quadrupole electric field for $\vec{E}$ and using the full magnetic field in the Penning-Ioffe trap from Eqn. 2.42, Eqn. 2.49 may be solved for z to give the force-free sheet

$$z = \frac{B_r}{B_z} \frac{x^2 - y^2}{2\rho_0} \tag{2.50}$$

Magnetron orbits thus follow the line defined by the intersection of a specific electrostatic equipotential and the surface defined by Eqn. 2.50.

Adiabatic invariants [85] may be identified for each of the three Penning-Ioffe motions, provided that the magnetic field changes slowly along the particle trajectory (a condition easily satisfied within the trap). For the cyclotron motion, the magnetic moment $|\vec{M}| \approx mv_c^2/(2|\vec{B}|)$, with v_c the local cyclotron velocity, is an adiabatic

invariant. As $\vec{B}$ changes, the cyclotron velocity (and radius) change to keep $|\vec{M}|$ fixed, while the direction of $\vec{M}$ remains aligned with the direction of $\vec{B}$. Similarly, the quantity $J \approx E_z/\omega_z$ is an adiabatic invariant for the axial motion; the axial energy and frequency change in proportion with one another. Finally, the magnetic flux enclosed by a cyclotron orbit Φ is a conserved quantity, implying that as the quadrupole field is ramped up, the magnetron orbits become tighter. So long as processes which may break these adiabatic invariants are avoided (e.g. resonances which couple axial and magnetron motion), the three motions of charged particles in a Penning-Ioffe trap are stable for exponentially long times.

2.3.2 Non-neutral Plasma Confinement

Though the above analysis predicts stable confinement for a single particle in a Penning-Ioffe trap, debate has ensued over the stability of plasmas in Penning-Ioffe traps. Early experiments in Penning-Ioffe traps with much longer electrodes (i.e. Malmberg Traps) [54] found a difficult-to-avoid resonance condition for radial loss of particles from the plasma given by $\omega_r/\omega_z = n/4$, with ω_r the plasma rotation frequency, ω_z the axial bounce frequency, and $n = (1, 2, 3, \ldots)$. Other studies suggested that in quadrupole Penning-Ioffe traps, diffusive losses in plasmas [86] and ballistic transport [55] would make accumulation of $\overline{\mathrm{p}}$ and e^+ "impossible."

It remained unclear, however, if these pessimistic predictions would directly apply to experiments performed at ATRAP. For instance, $\omega_r/\omega_z \ll 1/4$ for typical ATRAP parameters, indicating that the strong resonance conditions found in [54] could be avoided. Experiments demonstrating diffusive losses were performed in only a 0.4 T

magnetic field on plasmas whose temperature, density, and length were markedly different from plasmas at ATRAP. Though ballistic loss is unavoidable, it is much more severe in the long Malmberg-type electrodes considered in Ref. [55].

To investigate the stability of plasmas in Penning-Ioffe traps, ATRAP performed an experiment with $\overline{\mathrm{p}}$ and e^- (in lieu of e^+) [56]. Particles were loaded into a Penning trap, and the Ioffe field was then turned on and held for 300 seconds. After turning the Ioffe field off, the surviving fraction of $\overline{\mathrm{p}}$ and e^- was counted. The results were quite encouraging: 90% of 9×10^4 $\overline{\mathrm{p}}$ survived when the BTRAP ratio of radial to axial magnetic fields was applied for 300 s. In a more extreme test, 2.5×10^5 $\overline{\mathrm{p}}$ were subjected to a ratio of radial to axial field strengths over twice as large as in typical experiments, with 70% remaining after 300 s. A faster loss rate for e^- was observed in this larger gradient as well, yet approximately 50% still remained after 300 s. For both species, enough particles persisted in the Penning-Ioffe trap for long enough times to enable production of $\overline{\mathrm{H}}$ in principle. A summary of these results is shown in Fig. 2.13.

2.3.3 Antihydrogen Production

Though confinement of $\overline{\mathrm{p}}$ and e^- in a Penning-Ioffe trap was an important first step, $\overline{\mathrm{H}}$ production within a Penning-Ioffe trap remained to be demonstrated. Additional difficulties were expected, since the longer distance traversed by the $\overline{\mathrm{p}}$ during $\overline{\mathrm{H}}$ formation could potentially lead to larger ballistic loss. Furthermore, the Ioffe field causes significant distortions in the shapes of the $\overline{\mathrm{p}}$ and e^+ plasmas, and it was unknown if these distortions would inhibit the $\overline{\mathrm{H}}$ formation process. Nonetheless,

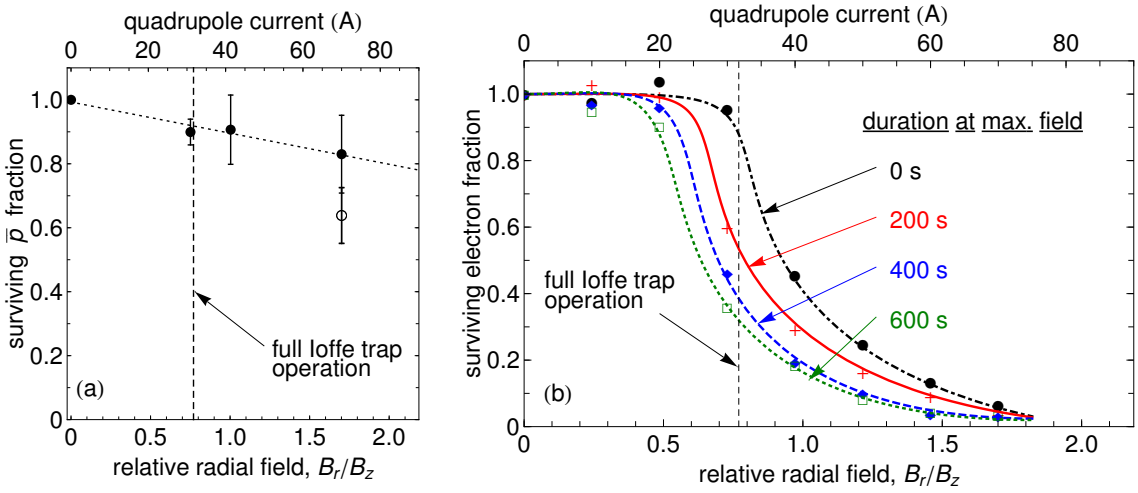

Figure 2.13: (a) The fraction of $\overline{\mathrm{p}}$ surviving after 300 s stays high even for large values of radial to axial magnetic field ratio. Trials with 9×10^4 $\overline{\mathrm{p}}$ (filled circles) and 2.5×10^5 $\overline{\mathrm{p}}$ (open circles) have been performed. (b) When the ratio of radial to axial field strengths is equal to the full-field value of 0.783, the fraction of e^- surviving is $\approx 50\%$ after 300 s and is nearly 40% after 10 minutes.

ATRAP demonstrated the first $\overline{\mathrm{H}}$ production in a Penning-Ioffe trap [57] using many similar techniques as when $\overline{\mathrm{H}}$ was first produced in 2002.

To begin, 2×10^5 $\overline{\mathrm{p}}$ and 6×10^7 e^+ were loaded into the quadrupole Penning-Ioffe trap. The confining potential for e^+ was then gently reduced to allow $\overline{\mathrm{p}}$ and e^+ to mix to form $\overline{\mathrm{H}}$. Weakly-bound $\overline{\mathrm{H}}$ was then field-ionized and counted as a measure of successful $\overline{\mathrm{H}}$ production. Surprisingly, a slight enhancement in the number of produced $\overline{\mathrm{H}}$ was observed with the Ioffe field on, possibly on account of the change in plasma geometry effected by the pinch coils (see Fig. 2.14). This demonstration proved that quadrupole Penning-Ioffe traps held promise for future $\overline{\mathrm{H}}$ production and trapping experiments.

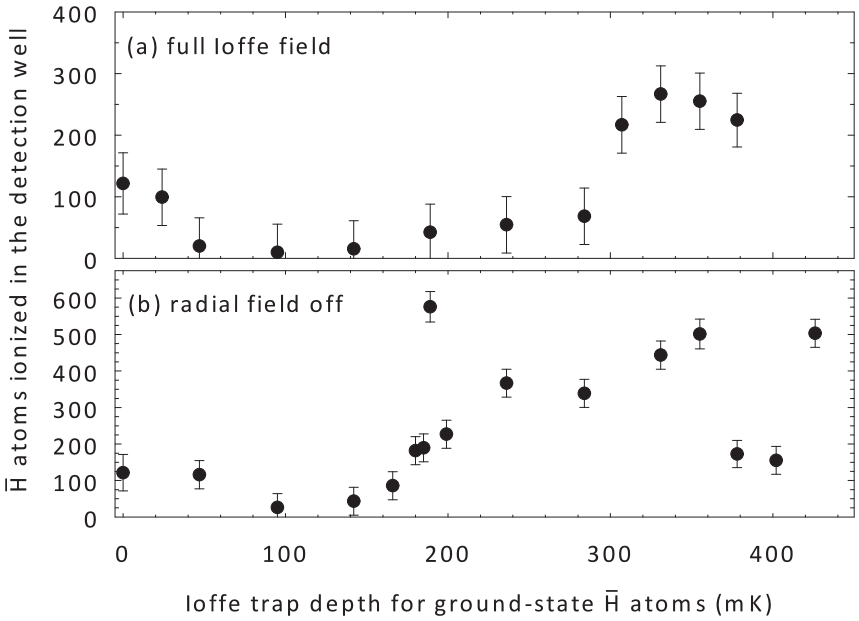

Figure 2.14: The production of $\overline{\mathrm{H}}$ is demonstrated both in the full Penning-Ioffe field (a) and with only the Penning and Ioffe pinch coil fields active (b). From Ref. [57].

2.4 Field-Boosting Solenoid

We have observed in our trap that $\overline{\mathrm{p}}$ are more efficiently captured from the AD when the strength of the Penning trap magnetic field $B_0\hat{z}$ is large. When high-energy $\overline{\mathrm{p}}$ enter the trap after ejection from the AD, their cyclotron radius $r_c = \sqrt{2mE_c}/(qB_0)$ may be large compared to the radius of the electrodes. Increasing B_0 will decrease the cyclotron radius and allow for improved $\overline{\mathrm{p}}$ catching, but will also lead to a decrease in Ioffe trap depth (as shown in Eqn. 2.41 and Fig. 2.9).

For this reason, a compact, field-boosting solenoid has been installed around the $\overline{\mathrm{p}}$ catching region of the Penning trap, as shown in Fig. 2.2. When operated at a current of 55 A, this field-boosting solenoid raises the local axial magnetic field from 1 T to 3.7 T (larger than the 3 T that would be possible with the large external solenoid).

The inductance of this compact solenoid is 28 H (compared with 247 H for the large solenoid), permitting the field to be ramped up or down within 6 minutes (compared with 1 hour). Its inner diameter of 18.8 cm is large enough to accommodate the Penning trap electrodes, vacuum enclosures, and trap wiring, while its outer diameter of 33 cm is just small enough to fit within the insert dewar.

The field-boosting solenoid was designed by members of the ATRAP collaboration and fabricated by Cryomagnetics, Inc. Like the Ioffe trap, it is constructed from entirely non-magnetic materials to prevent any aberrations in the axial field. The superconducting windings are made from twisted, multi-filament NbTi wire embedded in a copper matrix for mechanical and thermal stability, while diodes spanning the coil provide passive quench protection.

Measurements of $\overline{\mathrm{p}}$ loading with and without the field-boosting solenoid will be presented in Chap. 4.

2.5 X-Y Translation Stage

A movable, two-axis translation stage sits above the Penning and Ioffe traps. The stage allows for various windows and holes to be moved onto the center access of the trap, permitting a large amount of flexibility in accessing the deeply isolated electrode stack. The X-Y stage has been designed and constructed by the Harvard members of the ATRAP collaboration, with many revisions and improvements spanning many years. A drawing of the stage is shown in Fig. 2.15 with important features indicated.

A 1.5 mm diameter, 20 mm long hole typically remains on-axis to allow e^+ to enter the trap from above. The diameter is well-matched to the incoming size of the e^+

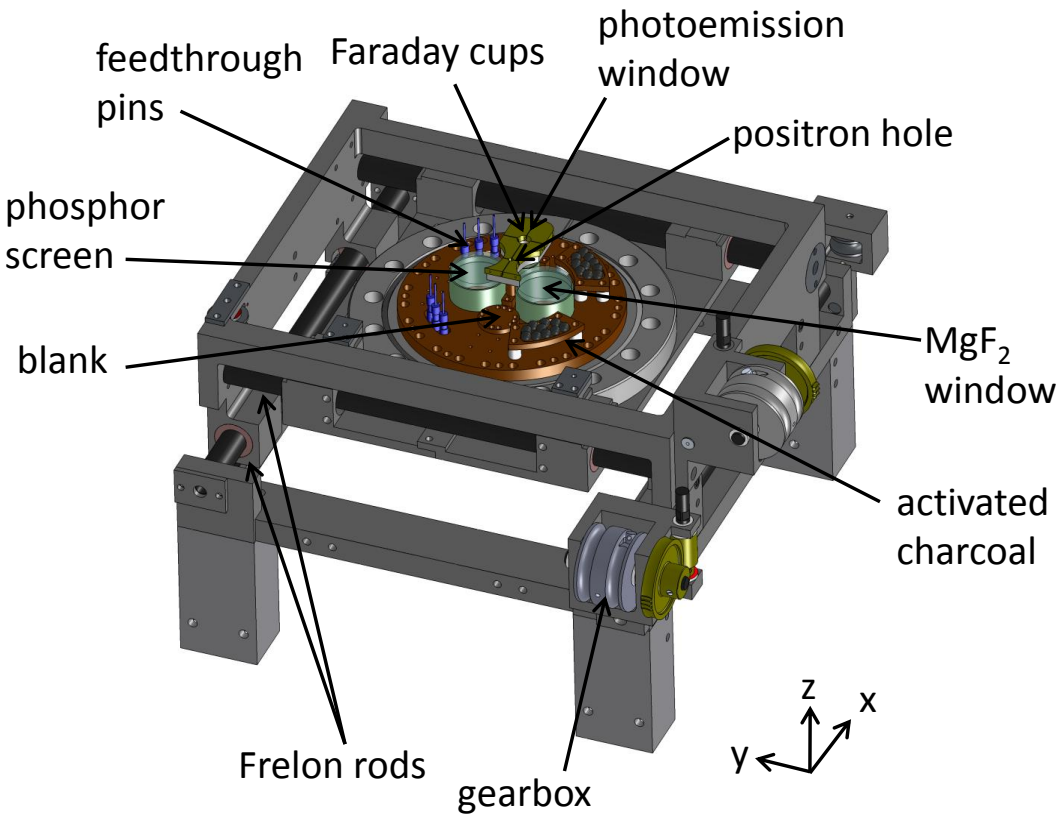

Figure 2.15: Drawing of the movable translation stage and window plate insert. Two bellows above and below (not shown) move in concert with stage to maintain the experiment vacuum space.

plasma, allowing for near-lossless passage into the electrode stack. In principle, this hole couples the 5×10^{-17} Torr experiment vacuum space with an ordinary UHV space, though in practice no detrimental effects on antimatter lifetimes have been observed. Nonetheless, activated charcoal surrounds this hole to assist in cryopumping away any background gas entering the trap volume.

Four other windows may be moved onto the central axis when e^+ are not being loaded. A photoemission window acts as an electron source when irradiated with a UV laser, and a phosphor screen has been installed with the hopes of directly imaging

the radial extent of $\overline{\mathrm{p}}$ and e^+ plasmas. UV lasers for spectroscopy and laser cooling may be introduced through a dedicated MgF_2 window as well as an additional port currently blanked off.

Achieving smooth, repeatable motion at cryogenic temperatures in high magnetic fields is a challenging endeavor. To translate the stage, gearboxes connected to copper cables pull separately on carriages mounted orthogonally to one another. These carriages slide along low-friction Frelon rods while the position is monitored by both resistance sensors and a set of LEDs and photodiodes. Two fiberglass drive shafts connect to the two gearboxes, allowing the stage to be controlled from outside the vacuum space either by hand or by drive motors. A pair of 130 μm wall-thickness edge-welded bellows above and below the X-Y stage keep the trap vacuum intact as the stage moves back and forth.

2.6 1 K Pot

As discussed in section 2.1.3, charged particles in Penning traps radiate away their energy until they come into thermal equilibrium with their surrounding environment. Lowering the electrode temperature from 4.2 K can thus be expected to yield colder particles, which are desirable for producing large numbers of $\overline{\mathrm{H}}$ cold enough to be trapped in a 0.375 K well. To this end, ATRAP has recently designed and implemented a pumped helium-4 system to cool the Penning trap electrodes to 1.2 K [87].

A small 1 K pot, shown in Fig. 2.2 and in detail in Fig. 2.16, is mounted below the main experiment liquid helium dewar. The pressure in the pot is reduced by pumping with an external scroll pump (Edwards XDS-35), reducing the temperature

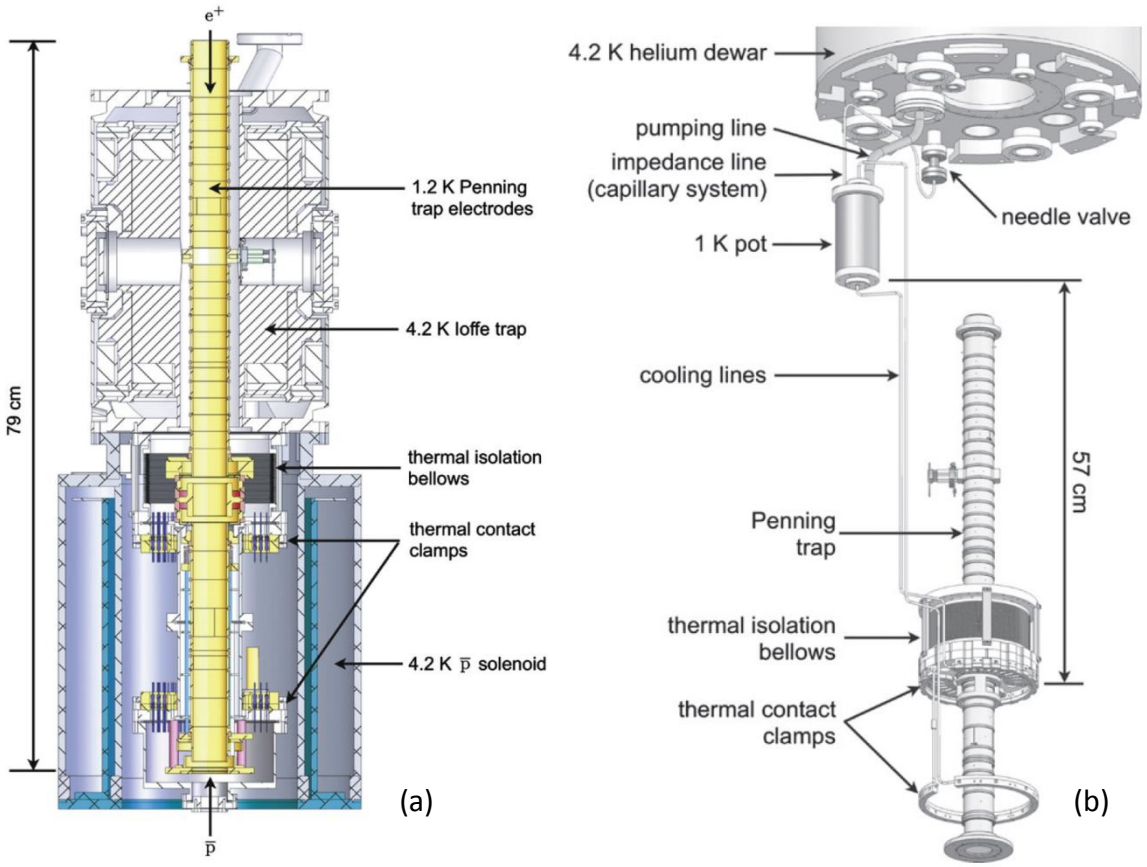

Figure 2.16: (a) The electrode stack is almost entirely surrounded by magnets cooled to 4.2 K, making access difficult. (b) Important features of the 1 K pot system. Cooling lines couple the pot to the electrode stack through thermal clamps. Figure adapted from [87].

of the liquid helium within to 1.2 K. The 4.2 K helium dewar and the 1 K pot are coupled with a thin-walled titanium impedance line. Four capillaries with a 60 μm diameter are epoxied inside of the impedance line, allowing only a small flow rate of helium and maintaining a pressure differential between the main dewar and the pot. Fine-tuning of the impedance and helium flow rate is achieved by turning a needle valve.

Cooling the electrode stack posed a significant geometrical challenge, since access to the electrodes is nearly completely obscured by the surrounding Ioffe trap and field-

boosting solenoid (see Fig. 2.16a). To couple the electrodes with the 1 K pot, copper tubes carry 1.2 K liquid helium along the side of the Ioffe trap and through the gap between the Ioffe trap and field-boosting solenoid before mating with thermal contact clamps on the electrode stack enclosure. To isolate the trap vacuum enclosure from the 4.2 K Ioffe trap from which it is suspended, thin-walled titanium edge-welded bellows are inserted to create a large thermal resistance between the two assemblies. With the 1 K pot system in place, maintenance free operation for as long as four months has been achieved.

2.7 Scintillating Detectors

As shown in Fig. 2.2, and in detail in Fig. 2.17, scintillating fibers and paddles surround the BTRAP apparatus to detect signatures of $\overline{\mathrm{p}}$ annihilations. Annihilation signals may be used to destructively count the number of $\overline{\mathrm{p}}$ loaded for an experimental trial, or determine the loss of $\overline{\mathrm{p}}$ during particle manipulations. Real-time monitoring of the detector signals enables fast optimization of $\overline{\mathrm{p}}$ steering and accumulation and provides indispensable information during $\overline{\mathrm{p}}$ and $\overline{\mathrm{H}}$ experiments. In addition, the scintillating fibers are sensitive to e^+ annihilations, though at a much reduced efficiency than for $\overline{\mathrm{p}}$.

When $\overline{\mathrm{p}}$ are released from the trap and strike a nearby wall, the annihilation gives rise to charged pions with energies up to a few hundred MeV. These pions are free to pass through the apparatus and strike the scintillating fibers and paddles. Just outside the Ioffe trap (on a 19.4 cm radius) sit four layers of 3.8 mm BICRON BCF-12 fibers (2 straight and 2 helical), with a peak emission wavelength of 435 nm. The two

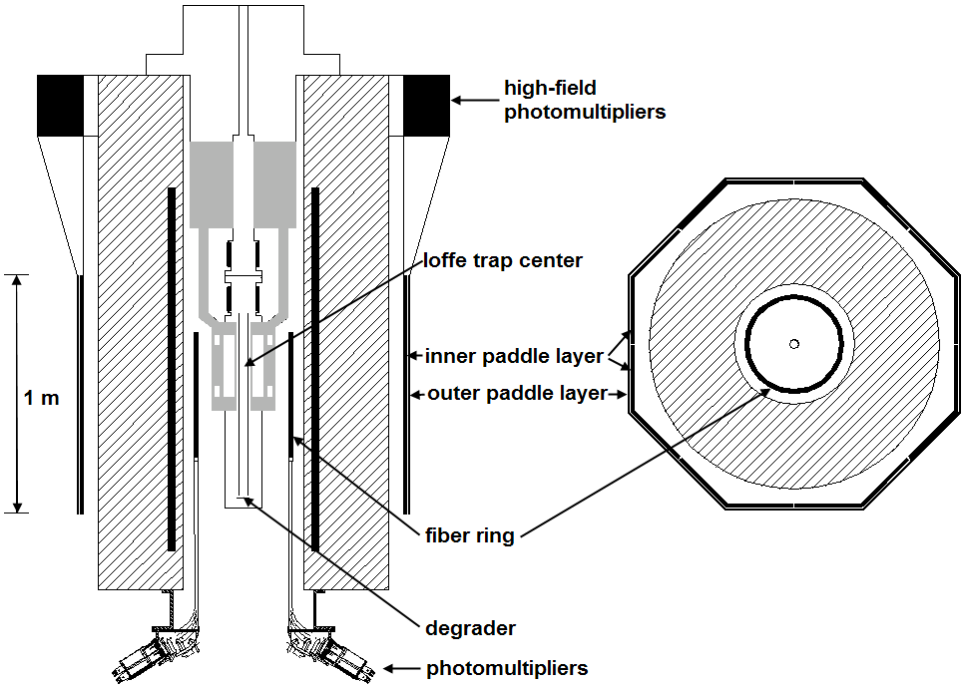

Figure 2.17: Schematic of the scintillating detectors surrounding the BTRAP apparatus.

straight layers consist of 448 total fibers, with the layers displaced from one another to prevent any gaps through which high-energy particles could pass undetected. Two similarly displaced helical layers surround the straight layers, with 336 fibers wound in a spiral, and each fiber subtending approximately 155° of arc. The total required length per fiber is about 784 mm, much shorter than the attenuation length of 2.7 m.

Just outside the dewar for the 1 T superconducting solenoid (on a 66 cm radius) sit a double layer of 24 BICRON BC404 scintillating paddles. The outer layer is comprised of 8 paddles arranged in an octagonal configuration around the experiment, while the inner layer is formed from 16 half-sized paddles located 7 mm in front of each outer paddle. All paddles are 1 m in height. Because the solid angle subtended by the inner and outer paddle layers is nearly identical, a high-energy particle that

passes through a half-sized inner paddle will also pass through the corresponding outer paddle with near unit probability. Accordingly, the two paddle layers are operated in coincidence with a 40 ns time window to suppress electronic noise signals.

To determine the scintillator efficiencies for detection of a single minimum ionizing particle (MIP), such as a $\overline{\text{p}}$ annihilation pion, we make use of the high-energy cosmic rays that perpetually bombard our experiment. After collecting several hours worth of cosmic ray data, events are selected for which signals in diametrically opposed fibers or paddles are observed. Such events allow reconstruction of a straight-line trajectory consistent with a cosmic ray passing through the detector system. Scintillator efficiencies are measured by observing the likelihood that intermediary fibers and paddles along each straight-line path are triggered. Using this method, we find a 95% detection efficiency of MIPs for the paddles and a 94.5% efficiency for the fibers.

The MIP efficiencies, detector geometry, and a Monte Carlo simulation of $\overline{\text{p}}$ annihilations are necessary for determining the $\overline{\text{p}}$ detection efficiency. Since the MIP efficiencies are measured to be very high, the limiting factor in our detection of $\overline{\text{p}}$ annihilations is the limited solid angle subtended by our fibers ($\sim 0.8 \times 4\pi$ steradian) and paddles ($\sim 0.6 \times 4\pi$ steradian). The Monte Carlo simulation, based on the GEANT4 tool-kit [88], determines the number and energy distribution of MIPs produced in $\overline{\text{p}}$-Au annihilations (appropriate for gold-plated electrodes), as well as the fraction of produced MIPs that traverse the scintillating detectors.

Combining these factors, we find a 68% efficiency for detecting $\overline{\text{p}}$ annihilations with the paddles and an 87% efficiency for detection with the fibers, with the relative efficiency of the fibers to paddles agreeing with experiment to within 10%. Coinci-

dences between at least one set of paddles and two fibers are used to further suppress background signals. Although this choice of trigger pattern reduces the $\overline{\mathrm{p}}$ detection efficiency to 54%, it also reduces the background rate from several hundred Hz to 41 Hz, markedly improving the signal to noise ratio for small numbers of $\overline{\mathrm{p}}$ annihilations.

Chapter 3

Non-neutral Plasmas in a Penning Trap

In the previous chapter, the Penning trap geometry and single-particle dynamics were introduced. However, the experiments described in this thesis for the production and trapping of cold $\overline{\mathrm{H}}$ use many more than one particle, requiring a new understanding of the dynamics within the Penning trap. The behavior is well-described by the theory of non-neutral plasmas [89]: "non-neutral", since the particles manipulated in our Penning trap are charged, and "plasmas" since the Debye length $\lambda_D = \sqrt{\epsilon_0 k_B T/nq^2} \approx 10 - 100$ μm is small compared with the several-mm dimensions of our cold particle clouds with density $n \approx 10^{12} - 10^{14}$ m^{-3}.

Since the Debye length - the characteristic length over which electric fields within the plasma are screened - is small relative to the cloud size, several new effects must be considered for plasmas compared with a single particle. First, the particles in a plasma behave collectively due to their Coulomb interactions; the N particles act like

N coupled oscillators, exhibiting N normal modes which may be excited or detected. Second, the presence of a high density of like-charges creates a self-potential (or "space-charge" potential) that can no longer be neglected. For a plasma to remain stably trapped, the sum of the Penning trap external potential and plasma self-potential must be confining. For a spherical plasma of 10^8 e^- or e^+ with a density of $n = 5 \times 10^{13}$ m^{-3}, the self-potential can be nearly 30 V, requiring at least this size external potential for stable trapping. Because the plasma rearranges itself to screen out external electric fields, the total potential (external plus space-charge) within the plasma remains constant throughout the bulk, and falls to 0 within several Debye lengths at the outer boundary.

In this chapter, we explore the properties of plasmas in Penning traps, which are crucial for understanding and undertaking cold $\overline{H}$ experiments. We begin with a general formalism describing non-neutral plasmas in cylindrically symmetric geometries, before restricting ourselves to plasmas in ideal Penning traps. Next, we describe the particle-in-cell code used to calculate plasma shapes in non-ideal Penning traps, which plays a significant role in determining the very cold $\overline{p}$ temperatures presented in Chapter 6. We discuss the dynamics of trapped plasmas and their relevant timescales and collision rates, concluding with methods to measure and control the plasma geometry.

3.1 Plasmas in a Cylindrical Trap

To investigate the behavior of non-neutral plasmas in a Penning trap, we begin with the less restrictive case of a plasma in a cylindrically symmetric trap, as shown

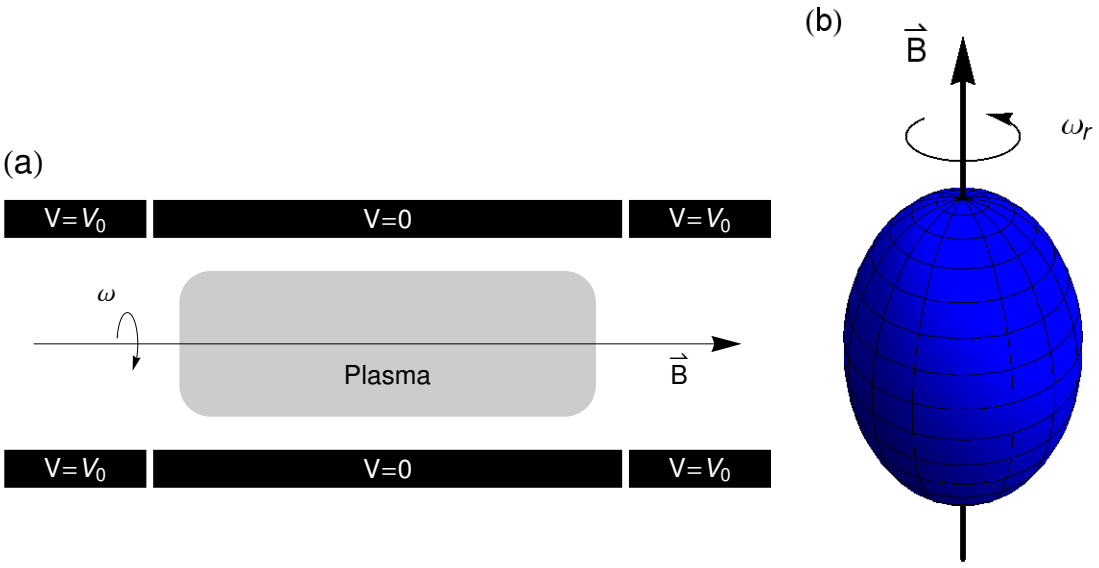

Figure 3.1: (a) Schematic of a plasma in a cylindrically symmetric geometry. (b) Spheroidal plasma arising in an ideal Penning trap.

in Fig. 3.1a. A magnetic field $\vec{B} = B_0\hat{z}$ points along the axis of the trap, while electric potentials confine the plasma axially. For such a configuration, the motion of particles is governed by the Hamiltonian [90]

$$H = \sum_{j=1}^{N} \frac{mv_j^2}{2} + q\phi(\vec{r}_j) \tag{3.1}$$

where the sum is over each particle in the plasma, and the potential $\phi(\vec{r})$ is the sum of the trap potential $\phi_T(\vec{r})$ and the plasma self-potential $\phi_P(\vec{r})$. In general, we must also account for the presence of image charges on the conducting boundary, though this effect is small in plasmas for which the outermost extent is far from the electrode walls.

We may rewrite Eqn. 3.1 as

$$H = \sum_{j=1}^{N} \left[\frac{p_{\rho_j}^2}{2m} + \frac{\left(p_{\theta_j} - \frac{q}{2} B_0 \rho_j^2\right)^2}{2m\rho_j^2} + \frac{p_{z_j}^2}{2m} \right] + q\left[\phi_T(\vec{r}_j) + \phi_P(\vec{r}_j)\right] \tag{3.2}$$

where we have substituted the canonical momenta [91]

$$p_\rho = m v_\rho \qquad p_\theta = m\omega\rho^2 + \frac{q}{2} B_0 \rho^2 \qquad p_z = m v_z \tag{3.3}$$

The symmetry properties of this Hamiltonian now allow us to determine the constants of the motion [92]. First, since there is no time-dependence in the Hamiltonian, the total particle energy E is conserved. Second, the cylindrical symmetry of the trap implies that $\phi(\vec{r}) = \phi(\rho, z)$. Hence, the Hamiltonian is rotationally invariant, and the total canonical angular momentum is conserved

$$\sum_{j=1}^{N} m\omega_j \rho_j^2 + \frac{q}{2} B_0 \rho_j^2 = \text{const.} \tag{3.4}$$

In practice, the first term in Eqn. 3.4 is several orders of magnitude smaller than the second term (for typical values of B_0), so we may approximate

$$\sum_{j=1}^{N} p_{\theta_j} \approx \sum_{j=1}^{N} \frac{q}{2} B_0 \rho_j^2 = \frac{q}{2} B_0 N \langle \rho^2 \rangle \tag{3.5}$$

which indicates that the mean square radius of a plasma is a conserved quantity.

Eqn. 3.5 represents a confinement theorem for cylindrically-symmetric plasmas. Consider the typical case for $\overline{\text{H}}$ experiments where a plasma with $\sqrt{\langle \rho^2 \rangle} = 3.8$ mm is trapped within an 18 mm radius electrode. For a single particle to escape from 3.8 mm to 18 mm, 23 particles must move from 3.8 mm to the central axis. At an absolute minimum, 96% of particles in the plasma will thus remain confined, independent of the starting conditions and dynamics. In practice, lossless confinement of plasmas

for several hours is possible, even though small holes, slits, and misalignments in the trap electrodes slightly break the cylindrical symmetry of the trap.

If the correlations within the plasma are small, the thermal equilibrium states of the plasma may be characterized by a Boltzmann distribution. Particle correlations may be quantified by the parameter $\Gamma = q^2/(4\pi\epsilon_0 a k_B T)$, where a is the inter-particle spacing defined by $(4/3)\pi a^3 n_0 = 1$. Correlations are small for $\Gamma \ll 1$; for typical plasmas in $\overline{\mathrm{H}}$ experiments, Γ may range between 0.01 and 0.1. Since the total energy and canonical angular momentum are conserved, the Boltzmann distribution may be written [93, 94]

$$f(\vec{r},\vec{v}) = \frac{N \exp\left[-\frac{1}{k_B T}(h + \omega_r p_\theta)\right]}{\int d^3\vec{r} d^3\vec{v} \exp\left[-\frac{1}{k_B T}(h + \omega_r p_\theta)\right]} \tag{3.6}$$

where ω_r is a rotation frequency and h and p_θ are the single particle Hamiltonian and canonical angular momentum:

$$h = \frac{mv^2}{2} + q\phi(\vec{r}) \qquad\qquad p_\theta = m\omega\rho^2 + \frac{q}{2}B_0\rho^2 \tag{3.7}$$

Substituting Eqns. 3.7 back into Eqn. 3.6 and carrying out the $d^3\vec{v}$ integral, the distribution $f(\vec{r},\vec{v})$ is simplified to

$$f(\vec{r},\vec{v}) = n(\rho,z)\left(\frac{m}{2\pi k_B T}\right)^{3/2} \exp\left[-\frac{m}{2k_B T}\left(\vec{v} + \omega_r\rho\hat{\theta}\right)^2\right] \tag{3.8}$$

where the density $n(\rho,z)$ is given by

$$n(\rho,z) = N\frac{\exp\left\{-\frac{1}{k_B T}\left[q\phi(\rho,z) + \frac{1}{2}m\omega_r(\omega_c - \omega_r)\rho^2\right]\right\}}{\int d^3\vec{r} \exp\left\{-\frac{1}{k_B T}\left[q\phi(\rho,z) + \frac{1}{2}m\omega_r(\omega_c - \omega_r)\rho^2\right]\right\}} \tag{3.9}$$

$$= n_0 \exp\left[-\frac{q\phi(\rho,z) + \frac{1}{2}m\omega_r(\omega_c - \omega_r)\rho^2}{k_B T}\right] \tag{3.10}$$

and $\omega_c = qB_0/m$ is the cyclotron frequency. Eqn. 3.8 may be thought of as a standard Boltzmann distribution, viewed in a frame rotating with angular frequency ω_r. In the

lab frame, this describes a plasma in thermal equilibrium that undergoes a shear-free rotation (at ω_r). This rotation frequency is akin to the magnetron $\vec{E} \times \vec{B}$ drift of a single particle, except now the $\vec{E}$ field includes contributions from both the applied potential and the plasma self-potential.

Since in the $T \to 0$ limit the plasma density (Eqn. 3.10) must remain finite, this requires

$$q\phi(\rho, z) + \frac{1}{2} m\omega_r(\omega_c - \omega_r)\rho^2 = 0 \tag{3.11}$$

which leads to a constant density inside the plasma: $n(\rho, z) = n_0$. Additionally, if Poisson's equation is to be satisfied,

$$\nabla^2\phi(\rho, z) = -\frac{qn_0}{\epsilon_0} \exp\left[-\frac{q\phi(\rho, z) + \frac{1}{2}m\omega_r(\omega_c - \omega_r)\rho^2}{k_B T}\right] \tag{3.12}$$

In the zero temperature limit, Eqn. 3.11 may be solved for $\phi(\rho, z)$ and substituted into the left hand side of Eqn. 3.12 to yield

$$n_0 = \frac{2\epsilon_0 m\omega_r(\omega_c - \omega_r)}{q^2} \tag{3.13}$$

which allows us to directly calculate the rotation frequency for our cold plasmas when only the density and magnetic field strength is known. The approximation $\omega_r \ll \omega_c$ is often employed since ω_r is smaller than ω_c by $5 - 6$ orders of magnitude for typical ATRAP parameters.

In addition to permitting calculation, Eqn. 3.13 suggests a physical coupling between the density and rotation frequency. Increasing ω_r, for instance, will effect a near-linear increase in the central density n_0. As will be described further in Sec. 3.6, controlling the plasma's rotation frequency is the primary method by which we manipulate the plasma geometry for $\overline{\mathrm{H}}$ experiments.

3.2 Plasmas in Penning Traps

3.2.1 Ideal Quadrupole Traps

So far, our description applies to any plasma in a cylindrically symmetric geometry. However, we can further specify characteristics of the plasma if the external electric and magnetic fields are known. Of particular interest for $\overline{\mathrm{H}}$ experiments is the behavior of plasmas in an ideal Penning trap.

As shown in Chapter 2, an ideal Penning trap contains a magnetic field $\vec{B} = B_0\hat{z}$ and an electric potential

$$\phi_T(\rho, z) = \frac{m\omega_z^2}{2q}\left(z^2 - \frac{1}{2}\rho^2\right) \tag{3.14}$$

Analogously to the single-particle case, three independent motions may be identified for particles within a plasma. As before, individual particles execute a cyclotron motion around magnetic field lines, with the cyclotron frequency dependent upon B_0. As shown in Eqn. 3.13, particles also undergo a shear-free rotation at frequency ω_r that depends upon the central density n_0. Additionally, for a plasma in an ideal quadrupole potential, the center-of-mass (COM) normal mode frequency ω_z is equivalent to the single-particle axial frequency ω_z. Thus, specification of the Penning trap fields $\vec{B}$ and $\vec{E}$ completely determine ω_c and ω_z.

Recalling that the total potential $\phi(\rho, z)$ is the sum of the trap and plasma potentials $\phi_T(\rho, z)$ and $\phi_P(\rho, z)$, we may use the known form of ϕ_T (Eqn. 3.14) and Eqn. 3.11 to find

$$\phi_P(\rho, z) = -\frac{m\omega_z^2}{2q}\left[\left(\frac{\omega_r(\omega_c - \omega_r)}{\omega_z^2} - \frac{1}{2}\right)\rho^2 + z^2\right] \tag{3.15}$$

It is often useful to introduce the plasma frequency ω_p, defined by

$$\omega_p^2 \equiv \frac{q^2 n_0}{\epsilon_0 m} = 2\omega_r(\omega_c - \omega_r) \tag{3.16}$$

which allows us to simplify Eqn. 3.15

$$\phi_P(\rho, z) = -\frac{m\omega_z^2}{2q}\left[\frac{1}{2}\left(\frac{\omega_p^2}{\omega_z^2} - 1\right)\rho^2 + z^2\right] \tag{3.17}$$

The plasma self-potential takes the quadratic form $a\rho^2 + bz^2$, which can only be generated by a spheroidal distribution of charges [95, 96]. Hence, a plasma in a Penning trap takes the shape of a spheroid, as shown in Fig. 3.1b.

For a cylindrically symmetric spheroidal plasma, the number of particles may be expressed in terms of the central density n_0

$$N = \frac{4}{3}\pi\rho_p^2 z_p n_0 = \frac{4}{3}\pi\rho_p^3 \alpha n_0 \tag{3.18}$$

where z_p and ρ_p are the plasma axial half-length and radius, respectively. The ratio of these two quantities, $\alpha \equiv z_p/\rho_p$, defines the plasma aspect ratio. For $\alpha > 1$, the plasma takes on a cigar-like shape, while a pancake-like shape results from $\alpha < 1$.

By comparing the potential due to a spheroid with uniform density n_0 with Eqn. 3.17, a relation between ω_z and ω_p may be extracted [97]

$$\frac{\omega_z^2}{\omega_p^2} = \frac{Q_1^0\left(\frac{\alpha}{\sqrt{\alpha^2-1}}\right)}{\alpha^2 - 1} \tag{3.19}$$

where Q_1^0 is the associated Legendre function of the second kind,

$$Q_1^0(z) = \frac{z}{2}\ln\left(\frac{z+1}{z-1}\right) - 1 \tag{3.20}$$

Eqn. 3.19 directly relates the density n_0 (through the plasma frequency) to the geometry (through the aspect ratio). The right hand side is a continuous and monotonically

decreasing function of α except at $\alpha = 1$, for which the right hand side of Eqn. 3.19 approaches 1/3.

Although many plasma parameters have been introduced ($n_0, \omega_r, \omega_p, N, \rho_p, z_p, \alpha$), there are many interrelations through Eqns. 3.13, 3.16, 3.18, and 3.19. Knowledge of the trap fields and as few as two of these plasma parameters is sufficient to completely specify the entire set. For instance, knowledge of the plasma frequency ω_p determines n_0 and ω_r through Eqn. 3.16. Combined with a known number of particles N, Eqns. 3.18 and 3.19 may be simultaneously solved to give ρ_p and z_p, from which the aspect ratio α may be determined. This method underlies the experimental measurement technique used to characterize plasma geometries, as will be described further in Sec. 3.5.2.

3.2.2 Non-Ideal Penning Traps

A plasma within a cylindrical Penning trap is necessarily subject to a non-ideal quadrupole potential. In general, as shown in Chapter 2, higher-order coefficients in the potential expansion are present, leading to anharmonicities. Even if voltages on nearby electrodes are manipulated to cancel out these coefficients, the cancellation only applies on-axis; it is impossible to create an ideal quadrupole everywhere off-axis. As a result, the geometry for a real plasma in a non-ideal quadrupole will deviate from a spheroid, with larger deviations concomitant with larger plasma radii.

Since the plasma shape and self-potential can no longer be calculated analytically, a numerical particle-in-cell calculation is used to solve for the plasma equilibrium. This code, *EQUILSOR*, iteratively solves Poisson's equation (Eqn. 3.12) until a

specified convergence limit is reached [98]. Relaxation methods, similar to those presented in Chapter 2, are used to find a self-consistent solution for ϕ on a grid, while the addition of Newton's method efficiently handles the non-linearity in ϕ that appears in Poisson's equation.

The computation makes use of the fact that Eqn. 3.12 may be written [99]

$$\nabla^2\phi(\rho,z) = -\frac{qn_0}{\epsilon_0}\exp\left[-\frac{q}{k_BT}\left(\phi(\rho,z)-\phi(0,0)\right)-\beta\rho^2\right] \tag{3.21}$$

where β is a constant to be determined. The central density n_0 is specified at the start of the computation and remains fixed. The plasma radius ρ_p may also be held constant as the code iterates by readjusting β after each step via

$$\beta = -\frac{q}{k_BT\rho_p^2}\left(\phi(\rho_p,0)-\phi(0,0)\right)+\frac{\ln 2}{\rho_p^2} \tag{3.22}$$

In practice, *EQUILSOR* is supplied a particle number N and a plasma radius ρ_p. Thus as code executes and the plasma shape approaches equilibrium, the density is adjusted every 100 steps to ensure that N is conserved, while β is set by Eqn. 3.22 to keep ρ_p fixed. Output results from a single *EQUILSOR* run are presented in Fig. 3.2, for a 6.5 mm radius plasma of 4×10^7 e^- confined in a 100 V well.

3.3 Plasma Dynamics

The N coupled particles in a plasma exhibit N collective modes of oscillation. In the preceding section, we have already introduced one such mode: the center-of-mass (COM) oscillation at frequency ω_z. However, $N-1$ additional modes may be present, with frequencies that depend upon the plasma density and geometry.

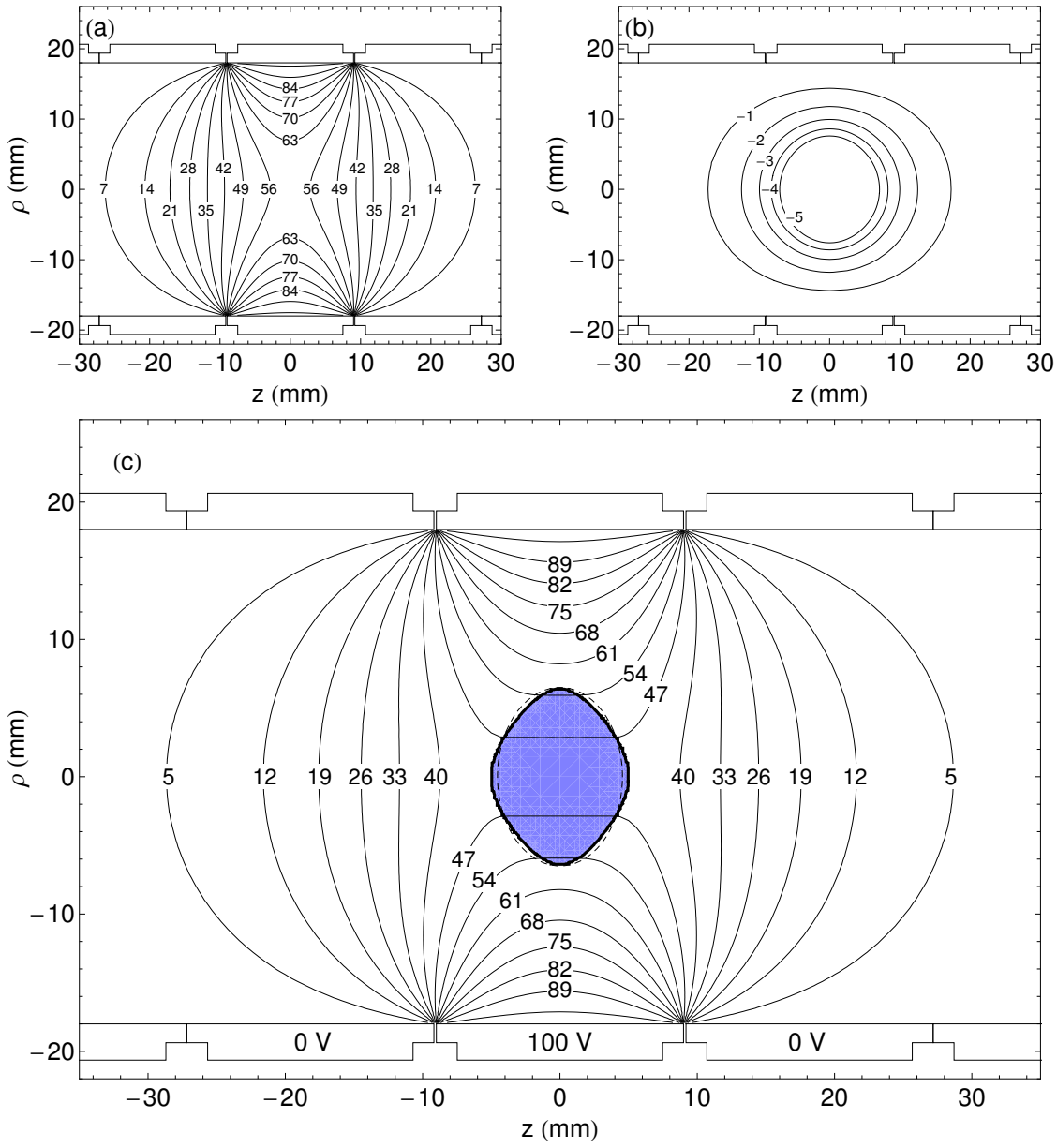

Figure 3.2: Results from an *EQUILSOR* calculation for a plasma with 4×10^7 e^- and a 6.5 mm radius. The central electrode is biased at 100 V, and all others are held at ground. (a) Equipotential contours for ϕ_T, the empty-well potential within the trap. (b) Equipotential contours for ϕ_P, the plasma self-potential. (c) The sum of ϕ_T and ϕ_P gives the total potential ϕ, with contours shown. The calculated equilibrium plasma shape is superimposed, and small deviations from the ideal spheroidal shape (dashed) are evident.

The normal modes within the plasma may be classified by the integers (ℓ, m), with $\ell > 0$ and $|m| < \ell$. Cylindrically symmetric modes have $m = 0$; $m \neq 0$ modes are suppressed in the cylindrically-symmetric Penning trap configuration. The COM mode is labeled by $(1, 0)$, while the quadrupole mode (in which the aspect ratio oscillates in time) has $(\ell, m) = (2, 0)$. For all (ℓ, m), the normal mode frequencies must be less than the plasma frequency ω_p.

The mode frequencies for spheroidal plasmas in ideal Penning traps have been calculated analytically by Dubin in the $T \to 0$ limit [100]. The mode frequency ω_ℓ is related to the plasma frequency ω_p and the aspect ratio α through the equation

$$1 - \frac{\omega_p^2}{\omega_\ell^2} = \frac{k_2}{k_1} \frac{P_\ell(k_1) Q_\ell'(k_2)}{P_\ell'(k_1) Q_\ell(k_2)} \tag{3.23}$$

where P_ℓ and Q_ℓ are the Legendre functions of the first and second kinds (respectively), P_ℓ' and Q_ℓ' are their derivatives, and k_1 and k_2 are defined by

$$k_1 = \frac{\alpha}{\sqrt{\alpha^2 - 1 + \omega_p^2/\omega_\ell^2}} \qquad\qquad k_2 = \frac{\alpha}{\sqrt{\alpha^2 - 1}} \tag{3.24}$$

The solutions for ω_ℓ of Eqn. 3.23 may be expressed in terms of α only, since ω_p is known in terms of ω_z and α from Eqn. 3.19. Fig. 3.3 shows the calculated frequencies for various low-order modes, normalized to ω_z.

Dubin has also proposed an approximate analytic treatment of the quadrupole mode, $\ell = 2$, at finite temperature [97]. The quadrupole frequency ω_2 is predicted to shift from the zero-temperature frequency ω_2^0 according to [101]

$$(\omega_2)^2 = (\omega_2^0)^2 + 5 \left[3 - \frac{\alpha^2}{2} \frac{\omega_p^2}{(\omega_2^0)^2} \frac{\partial^2 A_3}{\partial \alpha^2} \right] \frac{k_B T}{m z_p^2} \tag{3.25}$$

where $A_3 = 2Q_1(k_2)/(\alpha^2 - 1)$. Changes in the plasma temperature ΔT should thus manifest themselves as changes in the measured quadrupole frequency $\Delta\omega_2$. However,

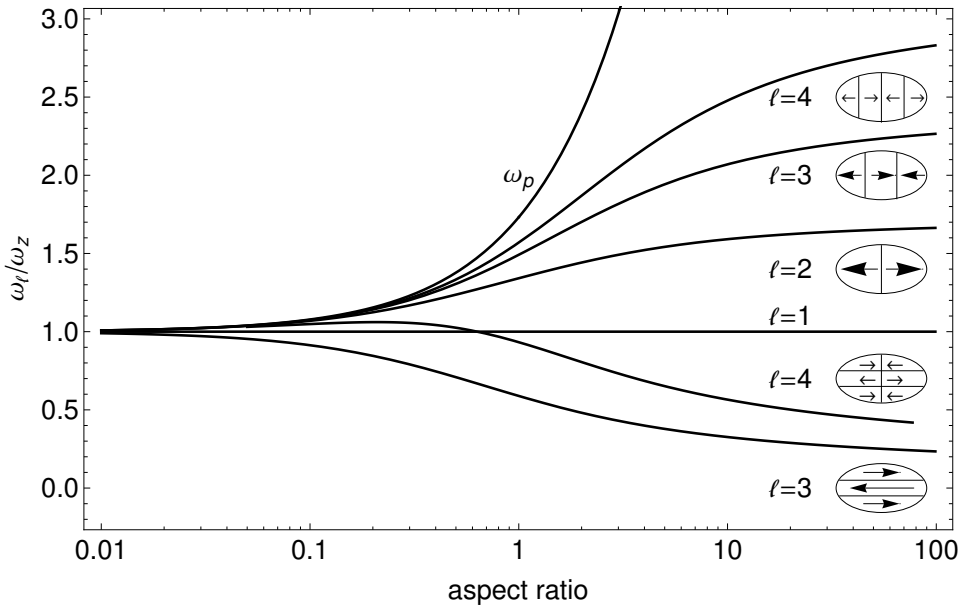

Figure 3.3: Plasma mode frequencies as a function of aspect ratio α, normalized to the COM frequency ω_z. Only the lowest order $(\ell, 0)$ modes are shown, along with their characteristic motions. All frequencies are lower than the plasma frequency ω_p, independent of aspect ratio. Adapted from Ref. [101].

it is important to point out that measurements of ω_2 can only be used to determine shifts in the plasma temperature, not the absolute value.

Since the analytic expressions describing plasma dynamics were derived for $T = 0$ spheroidal plasmas, numerical simulations are again necessary to determine the mode frequencies for finite-temperature plasmas in non-ideal Penning traps. The *RATTLE* code, which builds upon the equilibrium density distribution found by *EQUILSOR*, can calculate arbitrary $(\ell, 0)$ mode frequencies in a finite-length, cylindrically symmetric plasma [102]. *RATTLE* begins by displacing the plasma slightly away from its calculated equilibrium, and propagating the forces forward in time. As the plasma moves under the influence of the applied trap fields, *RATTLE* tracks the values of $\langle z \rangle, \langle z^2 \rangle, \langle z^3 \rangle, \ldots$ for the cloud. Taking the Fourier transform of each set of $\langle z^\ell \rangle$ values

yields the $\ell = 1, \ell = 2, \ell = 3, \ldots$ mode frequencies, with an accuracy proportional to the simulation time. Finite-temperature effects are also taken into account, and have been shown to agree well with experimental data [101].

3.4 Collision Rates

For a plasma to be in global thermal equilibrium, collisions between particles must redistribute energy throughout the plasma volume. When designing experiments, it is thus important to know the relevant collisional timescales as well as the rates at which the axial and cyclotron motions equilibrate. We concentrate here on single-species plasmas, with discussion of multi-species plasma collision rates reserved for Chapter 4.

Classically, the collision rate of particles within a plasma is given by

$$\nu_c = n_0 \sigma v \tag{3.26}$$

where n_0 is the density, σ is the collision cross-section, and v is the average particle velocity. For non-neutral plasmas, collisions are mediated by the infinitely long-range Coulomb interaction. Unlike hard-sphere scattering, Coulomb collisions tend to only slightly perturb the particle trajectory, so a proper treatment must account for the cumulative effects of many small-angle deflections. Collisions may be indexed by an impact parameter b, with the classical distance of closest approach b_{min} given by

$$b_{min} = \frac{1}{4\pi\epsilon_0} \frac{q^2}{k_B T} \tag{3.27}$$

which is found by equating the Coulomb and thermal energies.

Since the Coulomb potential $V \sim 1/r$, a description of all possible collisions requires integrating over the potential from $b = 0$ to $b = \infty$. However, both limits diverge for a $1/r$ integral, requiring a choice of lower and upper cutoffs for the integration range. The lower range is typically set to $b = b_{min}$ as defined in Eqn. 3.27, while the upper limit is chosen to be the Debye length $b = \lambda_D$, since the fields from charges more than a Debye length away will be effectively screened out. Integrating over the restricted range of impact parameters yields the Coulomb logarithm,

$$\ln \Lambda \equiv \ln \left(\frac{\lambda_D}{b_{min}} \right) \tag{3.28}$$

The Coulomb logarithm is a slowly-varying function of the plasma density and temperature, and typically falls within a range of $\ln \Lambda \approx 5 - 15$; setting $\ln \Lambda = 10$ is a reasonable and often-used approximation [103].

In a classic treatment, Spitzer treats the effect of multiple glancing collisions on a particle as a diffusion of its momentum, deriving a collision rate [104]

$$\nu_c = n_0 \left[\frac{8\sqrt{\pi}}{3\sqrt{2}} \frac{q^4 \ln \Lambda}{(4\pi\epsilon_0)^2 (k_B T)^2} \right] v \tag{3.29}$$

$$= \frac{8\sqrt{\pi}}{3\sqrt{2}} \frac{n_0 q^4 \ln \Lambda}{(4\pi\epsilon_0)^2 \sqrt{m} (k_B T)^{3/2}} \tag{3.30}$$

where we have used $v = \sqrt{k_B T/m}$ in the second line. It may be surprising at first that Eqn. 3.30 predicts an increase in the collision rate at colder temperatures. However, the distance of closest approach b_{min} increases as the thermal energy becomes smaller, decreasing the mean free path between collisions in a fixed density plasma.

Eqn. 3.30 was derived for $B = 0$, but new considerations arise for a plasma in the strong magnetic field of a Penning trap. If a particle's thermal cyclotron radius $r_c = \sqrt{m k_B T}/qB$ becomes small compared to the distance of closest approach b_{min},

exchange of axial and cyclotron energy is inhibited as particles are pinned to their field lines. In this strongly-magnetized regime, it may then be possible for the two motions to maintain two different temperatures, $T_\parallel$ and $T_\perp$, with global thermal equilibrium reached at an isotropization rate $\nu_I < \nu_c$.

In weakly magnetized plasmas, for which the magnetization parameter $\kappa \equiv b_{min}/r_c < 1$, the isotropization rate between $T_\parallel$ and $T_\perp$ was calculated to be only a factor of 3.5 smaller than the zero-field collision rate ν_c [105]. Later work modified this prediction somewhat, substituting the distance of closest approach b_{min} in the Coulomb logarithm for the cyclotron radius r_c [106]. In both cases, the approximations break down as the magnetization parameter $\kappa \to 1$.

In the strongly magnetized regime ($\kappa > 1$), identification of a nearly-conserved adiabatic invariant allowed calculation of an axial-cyclotron isotropization rate [107]

$$\nu_I = n_0 \left[4\sqrt{2}b_{min}^2\right] vI(\bar{\kappa}) \tag{3.31}$$

where $\bar{\kappa} \equiv \sqrt{2}\kappa$, and $I(\bar{\kappa})$ is a suppression factor defined by

$$I(\bar{\kappa}) \simeq (0.67)\int_0^\infty dx \frac{e^{-x^2/2}}{x} e^{-(3.14)\bar{\kappa}/x^3} \tag{3.32}$$

which reduces in the $\kappa \gg 1$ limit to

$$I(\bar{\kappa}) = (0.47)\bar{\kappa}^{-1/5} e^{-(2.04)\bar{\kappa}^{2/5}} \tag{3.33}$$

Substitution of Eqn. 3.33 back into Eqn. 3.31 thus gives the equipartition rate in the very strongly magnetized ($\kappa \gg 1$) regime.

A later numerical treatment calculates the isotropization rate in the intermediate regime ($\kappa \approx 1$), improves upon the $\kappa \gg 1$ result, and shows good agreement with the

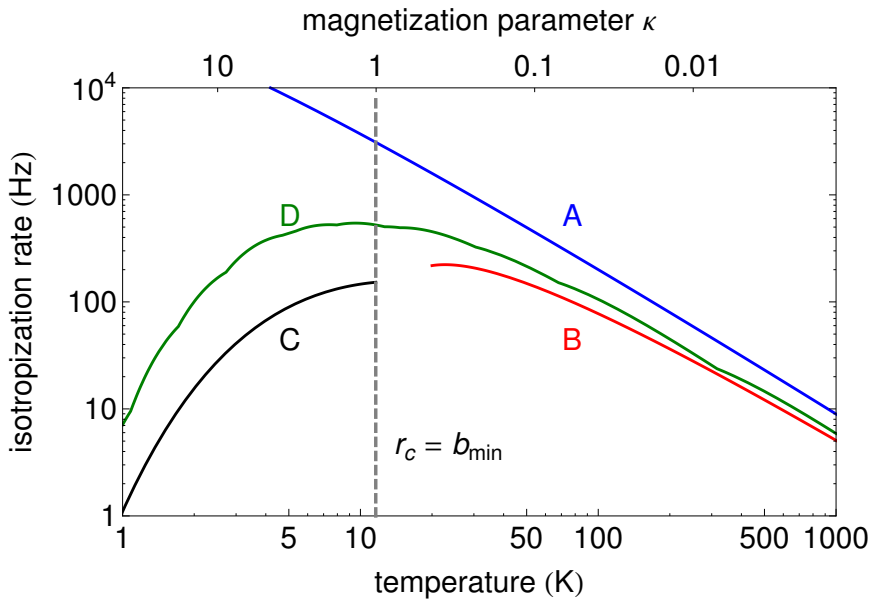

Figure 3.4: Predicted axial-cyclotron energy isotropization rate for a $\overline{\mathrm{p}}$ plasma with central density $n_0 = 1 \times 10^6$ cm^{-3}. The four curves are based on calculations performed in Refs. [105] (A, blue), [106] (B, red), [107] (C, black), and [108] (D, green).

$\kappa < 1$ rates discussed above [108]. This analysis, along with the previous analyses in the weakly- and strongly- magnetized limits, are plotted together in Fig. 3.4 for a typical $\overline{\mathrm{p}}$ plasma of density 1×10^6 cm^{-3}. As will be shown in Chapter 6, our equilibrated $\overline{\mathrm{p}}$ temperatures are measured to be between 3.5 - 30 K, giving an intermediate magnetization ($\kappa \approx 1$) with an isotropization rate of several hundred Hz. (Lepton isotropization rates tend to be nearly 2 orders of magnitude larger on account of the higher densities). At these low temperatures, the $\overline{\mathrm{p}}$ rate ν_I is almost an order of magnitude lower than the zero-field collision rate ν_c. However, nearly all manipulations performed on $\overline{\mathrm{p}}$ plasmas throughout the course of experiments occur on timescales much longer than the few milliseconds needed to ensure global thermal equilibrium.

3.5 Plasma Characterization

To engineer repeatable and systematic $\overline{\mathrm{H}}$ experiments, it is crucial to completely characterize the constituent $\overline{\mathrm{p}}$ and e^+ plasmas. Various plasmas may be uniquely indexed by their number and radius, since these parameters are sufficient to determine all other plasma properties (e.g. aspect ratio, density, etc.). Experimentally, measurement of the particle number N, as well as the COM and quadrupole mode frequencies ω_z and ω_2, singularly characterizes a plasma. First, the ratio ω_2/ω_z may be used to determine the aspect ratio α (see Fig. 3.3). Knowledge of α, together with ω_z and Eqn. 3.19, determines ω_p (and hence n_0 and ω_r by Eqn. 3.16). Finally, N, α, and n_0 may be substituted into Eqn. 3.18 to find ρ_p. Here we present the methods by which N, ω_z, and ω_2 are measured, so that our plasmas may be fully specified.

3.5.1 Number

Charge-counting and annihilation detection methods determine the number of particles in our lepton (e^- or e^+) and $\overline{\mathrm{p}}$ plasmas, respectively. For leptons, the sizable number of particles (typically $10^7 - 10^8$) makes them directly amenable to destructive charge counting, while counting via annihilation detection is impossible for e^- and low-efficiency (0.5%) for e^+. Conversely, the relatively few charges in our $\overline{\mathrm{p}}$ plasmas (typically 10^6) are difficult to charge-count directly, but their annihilation detection efficiency may be as high as 75%. Both particle counting methods are destructive, so we must rely upon the reproducibility of particle loading to ensure an accurate determination of N. The error on such measurements is at the $5 - 10\%$ level.

Charge counting of lepton plasmas proceeds by pulsing the particles onto a Fara-

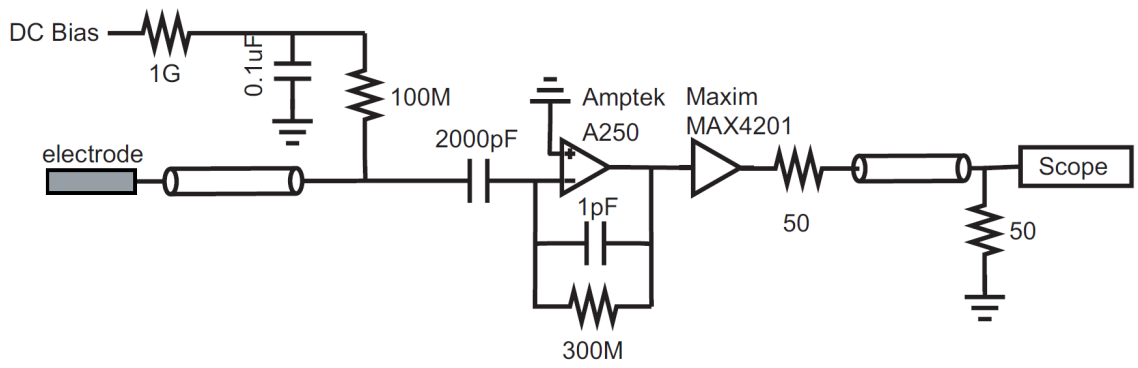

Figure 3.5: Charges collected on a Faraday cup electrode are converted to a voltage signal in a charge-sensitive preamplifier and read out by a scope.

day cup, then measuring the charge deposited with a charge-sensitive preamplifier (see Fig. 3.5). The input charge Q is connected to the negative terminal of an Apmtek A250 operational amplifier, the positive terminal is grounded, and a 1 pF capacitance C_f is placed in the feedback loop. Since the input terminals remain at equal voltage, the voltage at the output terminal is simply the voltage drop across the capacitor, $V = -Q/C_f$. An additional 300 MΩ resistor placed in the feedback loop allows the charge to drain away in $RC = 300$ μs, resetting the device.

In practice, we cannot ignore other capacitances in the system (e.g. the blocking capacitor at the input to the preamplifier or the coax capacitance). The net result is an effective capacitance, C_{eff}, which may be measured by applying calibrated charges and observing the voltage response. Once C_{eff} has been determined, the voltage signal seen on the scope due to N charges is given by

$$V = -\frac{Nq}{2C_{\text{eff}}} \tag{3.34}$$

where the factor of 2 in the denominator accounts for the input termination of the scope.

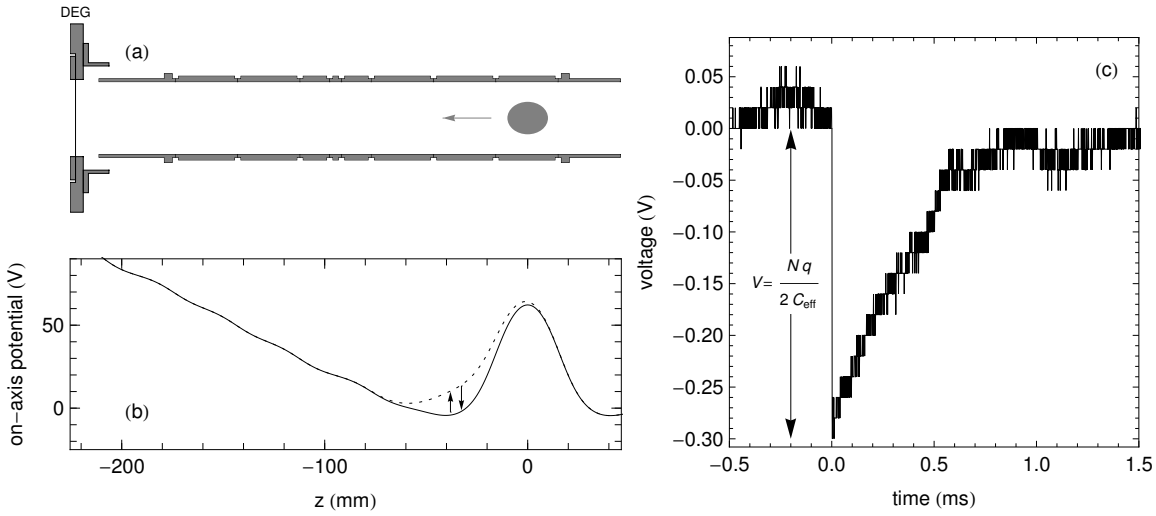

Figure 3.6: (a) A lepton plasma is pulsed towards the degrader electrode (DEG), to which the charge-sensitive preamplifier is connected. (b) Voltage structure during plasma confinement (solid) and during the 75 ns pulse (dashed). Any particles with energies between the pre- and post-pulse barrier heights will escape towards DEG. (c) The peak height of the observed voltage signal during the pulse is proportional to the number of escaping particles N, and falls away with a 300 μs time constant.

The charge-sensitive preamplifier is connected to a metal plate at the bottom of the electrode stack, labeled DEG in Fig. 3.6. To begin the pulsed charge counting procedure, the plasma is confined in an electrostatic well, and a ramped potential is applied towards DEG, which is biased to prevent emission of any secondary e^-. A 75 ns pulse reduces the barrier height between the confining well and the ramped potential, allowing any particles within that energy band to escape and strike DEG. The measured voltage signal induced on DEG then allows reconstruction of the number of particles N that escaped during the pulse. Anywhere from 1×10^5 to 5×10^7 particles may be counted in a single pulse before noise and saturation issues (respectively) negatively impact the measurement.

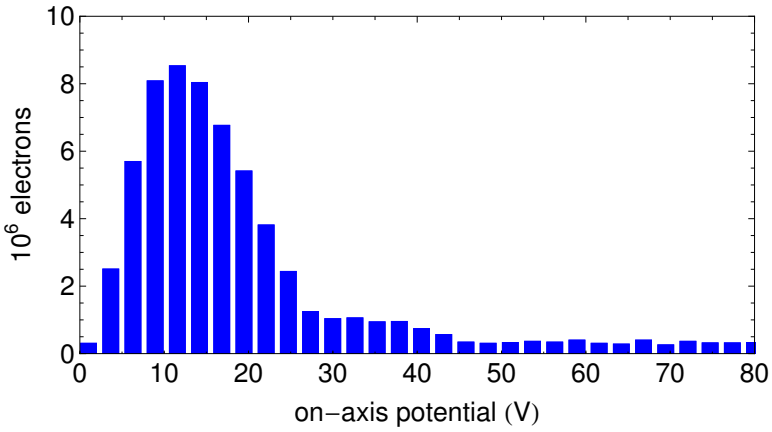

Figure 3.7: The number of e^- escaping the trap as the confining potential is reduced in 2.5 V increments gives information about the energy distribution and the total number confined.

To measure particle numbers larger than 5×10^7, as well as gain information about their energy distribution, the above procedure may be repeated several times for progressively smaller confining wells. The 2×10^8 e^- shown in Fig. 3.7 are initially trapped in an 80 eV deep well. Every 1 s, the well depth is pulsed downwards by 2.5 V until the well is inverted. The number of e^- accelerated towards DEG is counted at each step, the sum of which gives the total number of trapped e^-. Additionally, the distribution of released particles gives a measure of the space-charge potential of the plasma.

Annihilation counting of the $\overline{p}$ plasma number proceeds in a similar manner. The depth of the $\overline{p}$ plasma confining well is smoothly reduced, allowing $\overline{p}$ to escape towards DEG and annihilate. High-energy pions produced in the annihilation are then detected by scintillating paddles and fibers, as described in Chapter 2. Observation of the number and timing of annihilation counts during the voltage ramp allows the $\overline{p}$ number and energy distribution to be reconstructed.

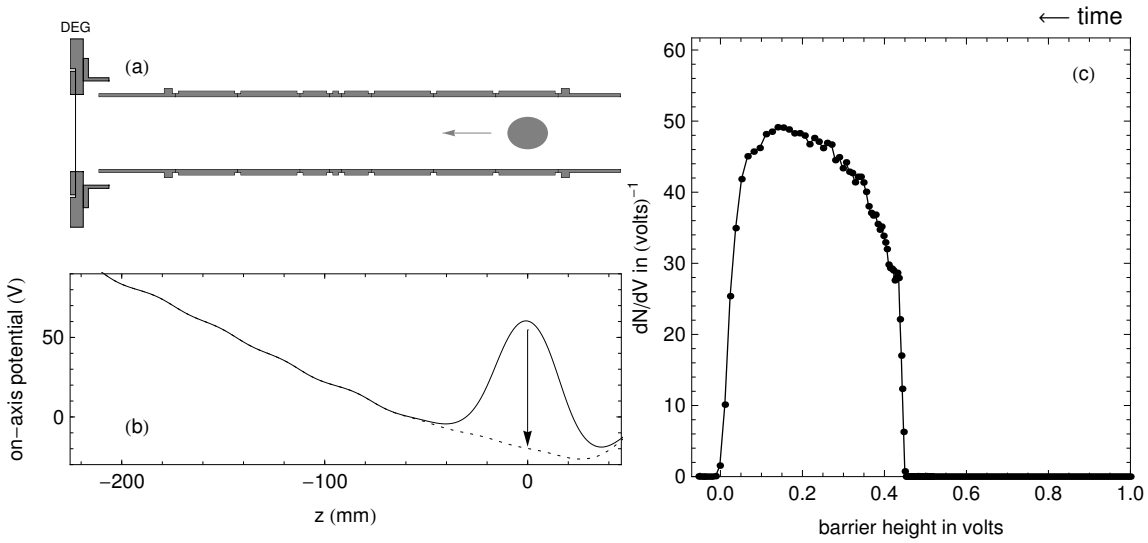

Figure 3.8: (a) A $\overline{\text{p}}$ plasma is ramped towards the degrader electrode (DEG), where it annihilates. (b) Voltage structure at the beginning (solid) and end (dashed) of the voltage ramp. Any escaping $\overline{\text{p}}$ are accelerated towards DEG. (c) The number of $\overline{\text{p}}$ escaping as their confining well barrier height changes, dN/dV, is plotted as a function of barrier height. None of the 1×10^6 $\overline{\text{p}}$ in this example were lost until the barrier height was only 0.45 V.

Fig. 3.8 shows the principle of the measurement, as well as an example with 1×10^6 $\overline{\text{p}}$. To begin the measurement, a hardware trigger initiates a linear voltage ramp in the confining electrode potential from V_i to V_f in a time t_r. The same hardware trigger additionally instructs a multi-channel scaler (MCS) to begin acquiring the number of annihilation counts in each of 125,000 time bins, with a bin width equal to $t_r/125{,}000$. A high-speed analog-to-digital converter (HSADC) compares the timebases of the voltage ramp and the MCS, allowing the number of counts as a function of voltage to be extracted.

As we will see in Chapter 6, the energy distribution of $\overline{\text{p}}$ escaping over a barrier may be used to determine the temperature of the $\overline{\text{p}}$ plasma. For now, we content ourselves with the ability to use this distribution to measure the $\overline{\text{p}}$ number. A simple sum

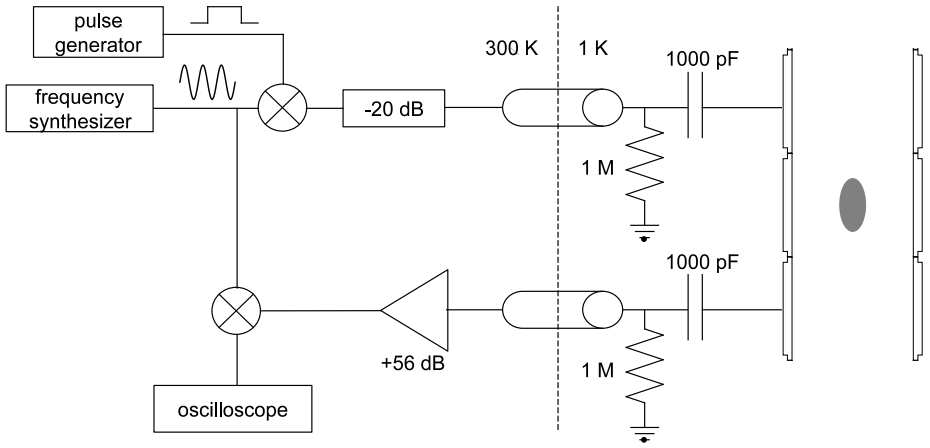

Figure 3.9: Schematic of the plasma mode excitation and detection setup.

of all annihilation counts observed by the MCS, divided by the detection efficiency, gives the desired result - functionally equivalent to integrating the area underneath the curve in Fig. 3.8c.

3.5.2 Mode Frequencies

In addition to the particle number, measurement of the plasma COM and quadrupole mode frequencies are necessary to completely characterize the geometry. Plasma modes have long been studied in myriad systems [109, 110, 111, 112] and have become an important diagnostic tool in $\overline{\mathrm{H}}$ experiments [113, 114]. Unlike the methods for measuring particle number presented above, measurements of plasma mode frequencies are non-destructive.

Plasma modes are measured using the "pulsed-ringdown" technique. To excite the mode oscillation, the output from a frequency synthesizer (Programmed Test Source PTS250) is applied to the electrode above the plasma, as shown in Fig. 3.9.

Drive frequencies from 10 to 100 MHz may be sent to the trap and are gated to 1 μs using an rf switch (Mini-circuits ZYSWA-2-50DR), giving an excitation bandwidth of 160 kHz. Attenuators ensure that the drive signal amplitude reaching the trap (typically -20 dBm) does not alter the oscillation frequency.

When the plasma motion is excited, it induces current oscillations on nearby electrodes. We wait 3 μs after the application of the drive frequency before observing the induced oscillations on the electrode below the plasma. The signal is broadband amplified at room temperature, heterodyned with the drive frequency, and recorded on a scope. The ringdown spectrum is then fast Fourier transformed to determine the mode frequency. Oscillations are visible for typically 100 μs before damping away, giving a $\approx$ 10 kHz resonance width. The peak frequency may be determined to 0.5-1 kHz (with the uncertainty set by trial-to-trial fluctuations), and averaging of repeated measurements gives a result at the several-hundred Hz accuracy level. Uncertainties in the Lorentzian fits to the fast Fourier transform spectrum contribute to the error at the sub-100 Hz scale.

Fig. 3.10 shows a measurement example for a plasma with 10^8 e^- confined in an 80 eV well in a 3.7 T magnetic field. The COM and quadrupole frequencies are measured to be $\omega_z/2\pi = 35.6980 \pm 0.0005$ MHz and $\omega_2/2\pi = 51.326 \pm 0.001$ MHz, corresponding to an aspect ratio $\alpha = 1.937 \pm 0.001$ (by Fig. 3.3). Substituting ω_z and α back into Eqn. 3.19, we find $\omega_p/2\pi = 84.22 \pm 0.03$ MHz, $n_0 = (8.797 \pm 0.003) \times 10^7$ cm^{-3}, and $\omega_r/2\pi = 34.24 \pm 0.03$ kHz. Using the measured particle number $N = (96 \pm 2) \times 10^6$ for this plasma, we find by Eqn. 3.18 that $\rho_p = 5.12 \pm 0.04$ mm and $z_p = 9.92 \pm 0.08$ mm (using $\alpha \equiv z_p/\rho_p$). All plasma parameters have now been

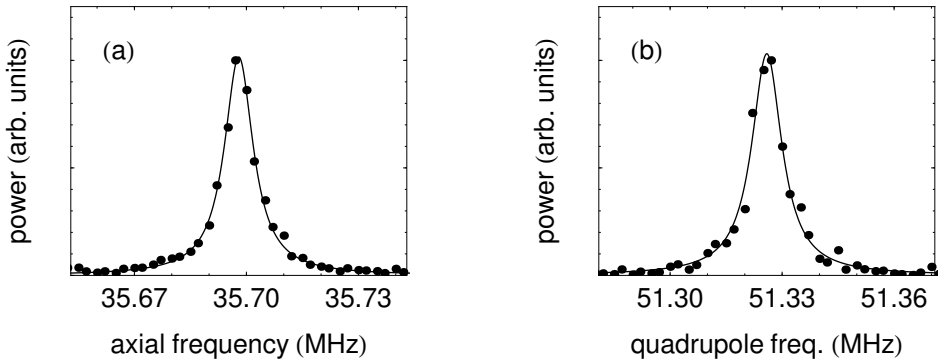

Figure 3.10: Resonances reveal the COM axial oscillation frequency ω_z (a) and the quadrupole frequency ω_2 (b) for a plasma of 10^8 e^- in an 80 eV potential well.

completely specified, starting with only a measurement of N, ω_z, and ω_2. We find this method to be fast and robust, enabling full characterization in less than 2 minutes.

3.6 Plasma Control

The reproducibility of plasma geometries loaded into Penning traps may vary on a daily basis. Small changes in $\overline{p}$ or e^+ beam position, for instance, may lead to plasmas with significantly altered angular momenta and radii. Furthermore, the plasma geometry itself serves as a tunable variable for optimizing $\overline{H}$ formation. It is therefore highly desirable to control the plasma geometry to effect repeatable and systematic experiments. Cylindrically symmetric trap fields and an asymmetric "rotating wall" may be used to manipulate and tune the pertinent plasma parameters.

3.6.1 Cylindrically Symmetric Fields

The cylindrically symmetric electric and magnetic fields in a Penning trap may be used to change a plasma's shape. Since these fields are cylindrically symmetric, no torques are applied to the plasma, so the canonical angular momentum is conserved. As shown in Eqn. 3.5, this implies that either the mean square radius of the plasma $\langle \rho_p^2 \rangle$ is conserved (for constant magnetic field), or that $B_0 \langle \rho_p^2 \rangle$ is conserved in a changing magnetic field.

Fig. 3.11a shows that when the magnetic field is held constant and the electric confining potential V_0 is increased, the plasma length decreases in response. Mathematically, Eqns. 3.18 and 3.19 may be rearranged for fixed ρ_p to derive

$$\frac{Q_1^0\left(\frac{\alpha}{\sqrt{\alpha^2-1}}\right)}{\alpha\left(\alpha^2-1\right)} = \text{const.} \times V_0 \tag{3.35}$$

where we have used that $\omega_z \propto \sqrt{V_0}$. Since the left-hand side of Eqn. 3.35 is a monotonically decreasing function of z_p, the plasma length shortens when the well-depth deepens. Physically, this may be understood as a plasma axially compressing as a result of the higher concavity applied potential when V_0 is increased.

Complimentarily, changes in the applied magnetic field B_0 at fixed V_0 alter the plasma radius $\sim 1/\sqrt{B_0}$. Fig. 3.11b shows this effect for 10^8 e^- in an 80 eV deep well, though the principle is widely applied to any non-neutral plasma in a cylindrically symmetric trap. This result has profound effects for $\overline{\text{p}}$ captured at 3.7 T in the field-boosting solenoid described in Chapter 2. As the magnetic field is reduced from 3.7 T to 1 T to avoid impacting the Ioffe trap well depth, the $\overline{\text{p}}$ plasma will radially expand by a factor of $\sqrt{3.7} = 1.9$. Hence, if the cloud starts at 3.7 T with a radius larger

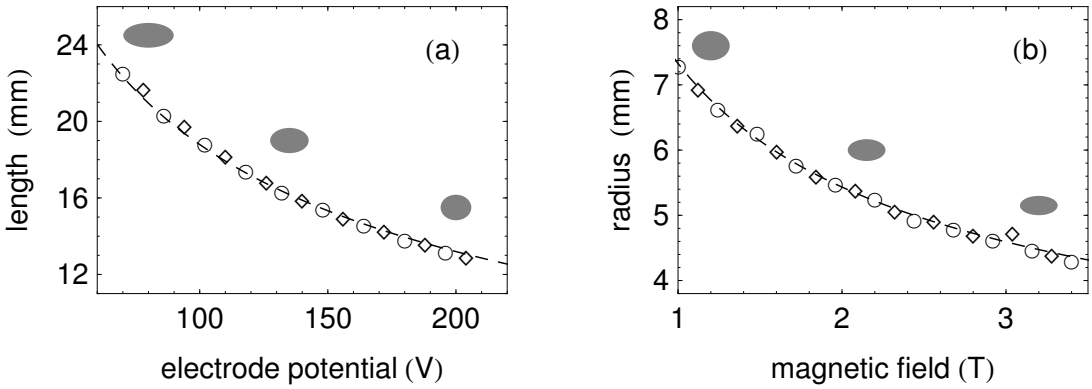

Figure 3.11: The length and radius of a 10^8 e^- plasma are determined by measurements of ω_z and ω_2. (a) As the confining electrode potential is increased, the plasma length decreases significantly. (b) As the Penning trap magnetic field is increased, the plasma radius decreases as $\sqrt{B_0}$ according to Eqn. 3.5. Circles (diamonds) indicate mode frequency measurements taken as the trap fields are increased (decreased), and the dashed lines indicate the predicted behavior.

than about 9 mm, many $\overline{\mathrm{p}}$ will be lost by annihilations with the trap walls at 18 mm while B_0 is reduced to 1 T. Even if the final $\overline{\mathrm{p}}$ radius remains just inside the trap walls, the radially extended plasma may prove difficult to control on account of field imperfections, inhomogeneities, and anharmonicities.

3.6.2 Rotating Wall

When cylindrically symmetric trap fields are used to change the plasma geometry, the plasma's canonical angular momentum is conserved. This can be a *disadvantage*, since the new geometry is ephemeral; when the trap fields are returned to their initial values, the plasma shape returns as well. A new method that changes the plasma's angular momentum would effect a more permanent shift in plasma geometry. Such a

method has general applications to trapped plasmas, which slowly lose angular momentum and expand due to collisions with background gas and small drag forces due to cylindrical trap asymmetries. Specific applications to ATRAP would also include preparing $\overline{\mathrm{p}}$ and e^+ plasmas to increase their spatial overlap during $\overline{\mathrm{H}}$ formation, opposing the expansion of plasmas held in short, anharmonic wells, and preparing $\overline{\mathrm{p}}$ at a small enough radius to prevent the significant losses otherwise observed when the 3.7 T field is reduced to 1 T.

Early studies altered the angular momentum of trapped $^9\mathrm{Be}^+$ plasmas by using off-resonant laser beams to apply a torque [95, 110]. Further work developed the "rotating wall" technique which used an asymmetric, rotating potential to change the plasma rotation frequency [115]. Since no optical transitions are accessible for fundamental particles, ATRAP experiments rely exclusively upon rotating wall methods.

The rotating wall as implemented at ATRAP uses an electrode split into four quadrants. Voltages of the form $V = V_0 \cos(\omega_{RW} t - \pi j/2)$, for $j = \{0, 1, 2, 3\}$, are applied to each of the quadrants (respectively), as shown in Fig. 3.12. These drives create an asymmetric dipole potential that rotates about the center axis with frequency ω_{RW}, exerting a torque on the trapped plasma. Higher-order rotating wall potentials may also be engineered by using 6 or 8 azimuthal electrode segments and applying oscillating potentials with phases incremented by $2\pi/N_{seg}$.

Initial rotating wall demonstrations chose a drive frequency ω_{RW} resonant with plasma modes indexed by $(\ell, m \neq 0)$ [116, 117, 118]. A rotating dipole potential, for which $m = \pm 1$ (depending upon the rotation direction), was found to excite the $m = \pm 1$ Trivelpiece-Gould (TG) modes within the plasma [119]. These excited,

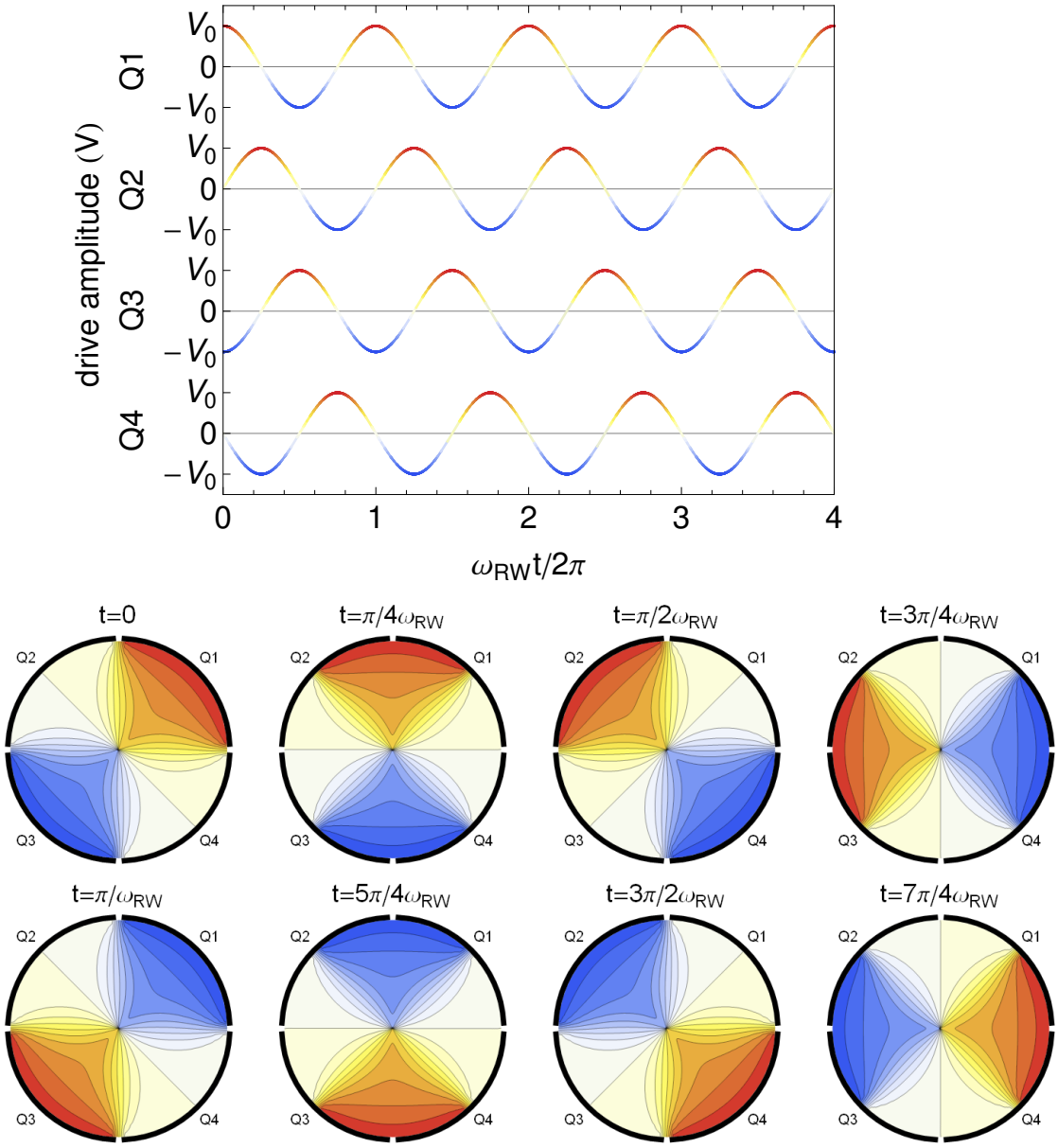

Figure 3.12: (Top) The drive amplitudes applied to the four rotating wall electrode quadrants $Q1-Q4$ oscillate between amplitudes V_0 and $-V_0$. Each quadrant is offset in phase by $\pi/2$ from its neighbors. (Bottom) The potential in the $z = 0$ plane as a function of time shows the rotating wall for which this electrode is named.

non-zero angular momentum modes equilibrated with the rest of the plasma through collisions, thereby sharing the angular momentum imparted by the rotating wall. If the frequency of the excited mode $\omega_{TG} > \omega_r$, the plasma rotation frequency and density will both increase, and the plasma radius will decrease. However, limitations in the maximum achievable compression were observed on account of drag forces on the plasma that increase at higher densities [120] as well as heating-induced shifts in the plasma mode frequencies due to the rotating wall drive [117].

Recent rotating wall demonstrations have successfully increased the plasma rotation frequency to $\omega_r \approx \omega_{RW}$, without tuning to TG modes, by applying a strong drive to high aspect ratio plasmas [121, 122]. In this "strong-drive" regime, good compression was achieved over a broad range of frequencies ω_{RW}, with the final density only weakly dependent upon the drive amplitude (above some threshold). However, the mechanism by which the torque-balanced final state is achieved is not yet well understood [123].

Lingering theoretical uncertainties notwithstanding, ATRAP has implemented two 4-split rotating wall electrodes to control plasma geometries in the $\overline{\mathrm{p}}$ and e^+ catching regions of the Penning trap. A custom-built multichannel synthesizer supplies the phase-offset oscillating voltages to the four rotating wall quadrants, with a drive amplitude of up to 9 V peak-to-peak and a frequency between 100 kHz and 10 MHz. The drive is carried to the rotating wall electrode along twisted pair lines, avoiding the 50 Ω termination and the ≈ 0.8 W heat load that would be present if coaxial lines were used.

During the application of the rotating wall drive, the plasma is transferred into

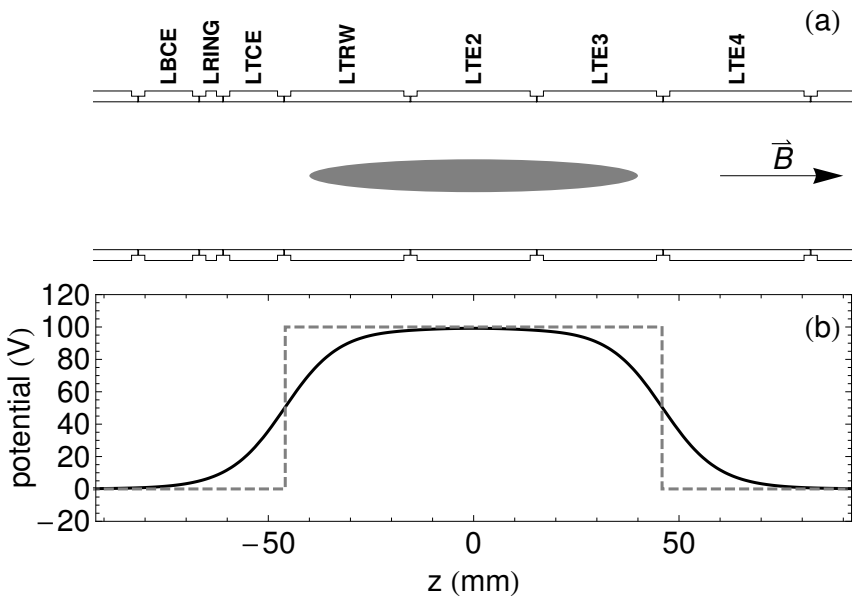

Figure 3.13: (a) The plasma spans 3 electrodes, with the rotating wall electrode LTRW at one end, during the application of the drive. (b) DC potential structure on-axis (solid) and at the wall (dashed) during the rotating wall drive.

the potential structure shown in Fig. 3.13. Through extensive explorations of the drive parameter space, we found that a 3-electrode long well maximized the achievable radial compression while avoiding particle losses. These long, flat wells closely mirror the Malmberg-style potentials of the original rotating wall experiments [115]. ATRAP has also realized good plasma compression when using a multi-well harmonic potential structure.

Fig. 3.14 shows the results of applying rotating wall drives at different frequencies for varying lengths of time. For these studies, a 9 V peak-to-peak rotating wall drive was turned on, and a 1.2×10^8 e^- plasma was transferred into a 4-, 3-, or 2-electrode long potential well. At the conclusion of the drive, the plasma was transferred back to a single electrode well and allowed to cool for 60 s before its COM and quadrupole

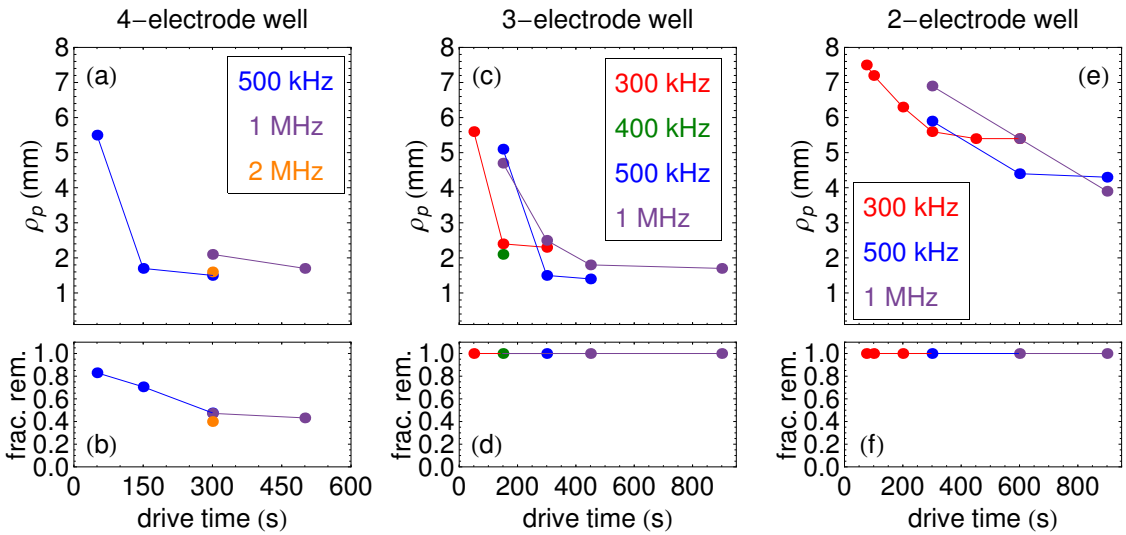

Figure 3.14: The effect of the rotating wall drive time on the plasma radius and number is shown for 4-electrode (a-b), 3-electrode (c-d), and 2-electrode (e-f) wells. Losses were observed in 4-electrode wells, while 2-electrode wells were not successful in achieving maximal compression.

modes were measured and its particle number counted.

Maximal, loss-free compression to $\rho_p \approx 2$ mm was observed in 3-electrode wells when a 500 kHz drive was applied for 300 s. Applying the drive for longer periods of time or at higher frequencies was found to have little effect; presumably the plasma's torque-balanced state is reached at $\rho_p = 2$ mm within our trap. The insensitivity of the plasma radius to the drive frequency indicates that we are not quite in the "strong-drive" regime, although the observed compression over a broad range of frequencies suggests that we are not addressing individual plasma resonances either. Our parameters may perhaps be in an intermediate regime, with the frequency drive conceivably addressing a multitude of TG plasma modes broadened significantly by heating.

In this chapter, we have investigated the relevant properties of plasmas confined in

a Penning trap. We have seen how the plasma number and geometry may be measured and controlled, which is critical for performing repeatable and well-parameterized studies. With a thorough understanding of the relevant plasma physics and the apparatus as presented in Chapter 2, we are now in a position to discuss the standard methods and techniques common to all $\overline{\mathrm{H}}$ experiments at ATRAP.

Chapter 4

Standard Methods

The techniques used at ATRAP to accumulate antimatter particles and transfer them into position for $\overline{\mathrm{H}}$ production have been refined and standardized over the course of the past two decades. Compared with our very first experiments in which 41 $\overline{\mathrm{p}}$ were captured in-flight from a high-energy beam [40], ATRAP now has the ability to amass 10^7 $\overline{\mathrm{p}}$ for $\overline{\mathrm{H}}$ production. Similarly, our initial demonstration of 3.5×10^4 trapped e^+ [124] has since blossomed to the current world record of 4×10^9.

In this chapter, we review the standard methods used to load $\overline{\mathrm{p}}$ (and the e^- that cool them) and e^+, and we detail improvements in the past two years that allow over an order of magnitude more particles of each species to be collected within our Penning trap. A new adiabatic manipulation of electrode potentials smoothly transfers $\overline{\mathrm{p}}$ and e^+ from their initial positions to the center of the Ioffe trap, significantly decreasing the particle losses heating observed with previous transfer methods. Finally, we give an overview of the $\overline{\mathrm{H}}$ formation process via three-body recombination, the mechanism that has produced the vast majority of cold $\overline{\mathrm{H}}$ to date.

4.1 Antiproton Capture

At CERN's Antiproton Decelerator (AD), a beam of 5.3 MeV $\overline{\mathrm{p}}$ is guided along a magnetic beamline that ends ≈ 1 m away from the bottom of the BTRAP apparatus. Using dipole and quadrupole magnets surrounding the beamline, these $\overline{\mathrm{p}}$ are steered and focused to ensure that they are ejected along the center axis of the Penning trap. Since their incoming energy is still large compared with laboratory voltages, $\overline{\mathrm{p}}$ are slowed in a beryllium metal foil and an energy-tuning gas cell to less than 5 keV. Application of kilovolt-scale potentials and strong magnetic fields are shown to boost the $\overline{\mathrm{p}}$ capture efficiency.

4.1.1 Beam Steering

To serve as a steering diagnostic, a segmented silicon detector is placed a few cm above the point at which $\overline{\mathrm{p}}$ are ejected from the CERN beamline. The silicon detector is mounted on a rotatable feedthrough to allow the $\overline{\mathrm{p}}$ to either impinge on the detector during steering or pass unimpeded during loading. Currents in the CERN beamline steering magnets are adjusted to maximize the current induced on the 7 mm diameter central segment of the silicon detector during $\overline{\mathrm{p}}$ ejection. Since $\overline{\mathrm{p}}$ must still travel ≈ 1 m before entering the Penning trap, the silicon detector is used only for rough beam alignment.

Fine-tuning of of the $\overline{\mathrm{p}}$ beam position is achieved by using a Parallel Plate Avalanche Counter (PPAC) [42, 125] mounted just underneath the entrance to the Penning trap. As shown in Fig. 4.1, the PPAC consists of two sets of anode-cathode electrode pairs oriented perpendicularly to the beam path and to each other. Each

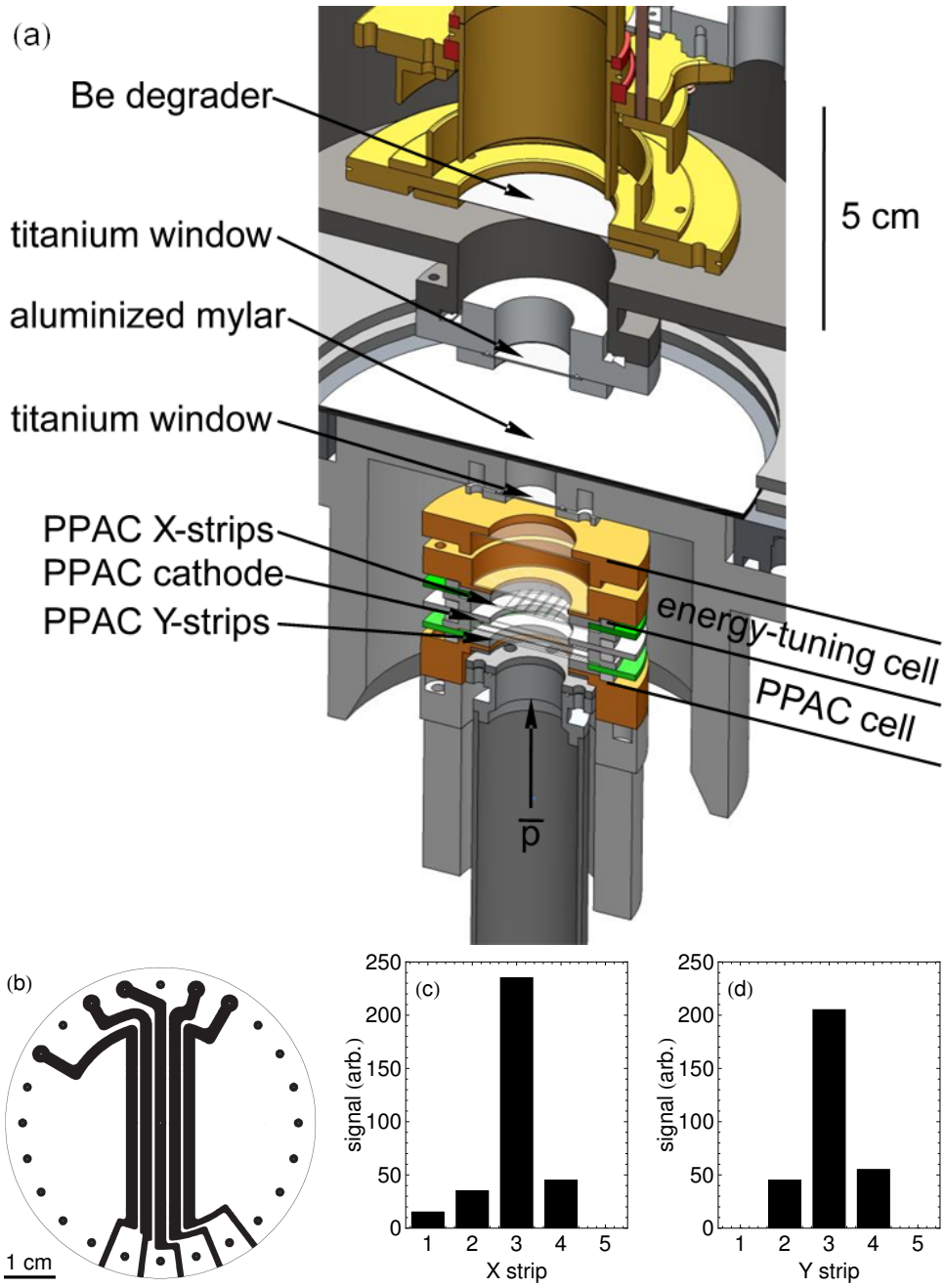

Figure 4.1: (a) After being ejected from the AD beamline, $\overline{\text{p}}$ traverse the PPAC and energy tuning cells before passing through a Be degrader and entering the Penning trap. (b) Each PPAC anode is comprised of five aluminum strips evaporated on a mylar substrate. (c)-(d) Optimal beam steering has been achieved when the signal is well-centered.

anode is comprised of five independent aluminum strip electrodes, 2 mm wide with a 0.5 mm spacing, evaporated onto a mylar substrate.

The PPAC is filled with 1 atm of argon gas, some of which is ionized as high-energy $\overline{\text{p}}$ pass through the cell. Voltages of 150 V are applied to the X- and Y-strips of the PPAC to attract the liberated electrons. The device operates in linear (not avalanche) mode, so that number of charges collected on each strip is proportional to the number of $\overline{\text{p}}$ passing through the strip's cross-sectional area. The generated voltage signal from each strip is read out by an oscilloscope, integrated, and displayed as in Fig. 4.1c-d. For a well-steered beam, the signals observed in the central channels of the Silicon detector and PPAC are maximized and fall off symmetrically.

4.1.2 Antiproton Slowing

To reduce the $\overline{\text{p}}$ energy from 5.3 MeV to several keV, the ejected $\overline{\text{p}}$ beam is made to pass through a gas-filled energy tuning cell, two 10 μm titanium foil windows, six layers of 6.4 μm aluminized mylar foil, and a 100 μm beryllium degrader. Collisions with matter cause the $\overline{\text{p}}$ to lose energy, and approximately 1 in 200 emerge with energies at 5 keV or less. Optimizations of the foil thicknesses and energy-tuning gas mixture are necessary to reduce the $\overline{\text{p}}$ energies enough so they may be trapped, but not so much that they may annihilate upon the matter nuclei.

Most of the $\overline{\text{p}}$ energy loss occurs when they pass through a Be degrader. The thickness of the degrader was chosen to be roughly half the range of 5.3 MeV protons in Be, as calculated by the Stopping and Range of Ions in Matter (SRIM) tables [126]. (The stopping range of $\overline{\text{p}}$ deviates from the proton value by a few percent on account

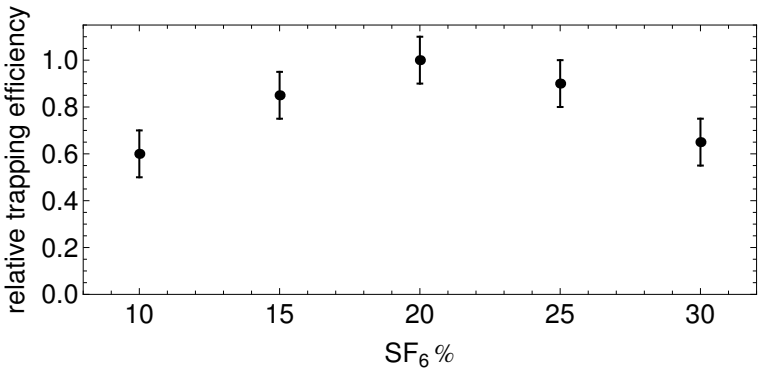

Figure 4.2: The number of trappable $\overline{p}$ is maximized when a 20% SF_6-80% He mixture (by number) occupies the energy tuning cell.

of the Barkas effect [42, 127]). The titanium windows and aluminized mylar foils that provide vacuum containment and cryogenic insulation (respectively) are chosen to be as thin as possible, but still precipitate a notable reduction in $\overline{p}$ energy.

To provide in-situ optimization of the trappable $\overline{p}$ fraction, an energy-tuning cell sits between the PPAC and the degrader. A mixture of SF_6 and He gases is maintained at 1 atm within the cell, with larger fractions of SF_6 leading to a larger $\overline{p}$ energy loss. The full tuning range - the difference between 0% and 100% SF_6 - corresponds to $\approx$ 0.5 MeV in energy. For $\overline{p}$ loading, the gas mixture is set to 20% SF_6-80% He (by number), determined by optimizing the number of captured $\overline{p}$ as the percentage of SF_6 was scanned (see Fig. 4.2). By coincidence, the $\overline{p}$ energy loss through this mixture is nearly identical to the loss through 100% N_2, which has sometimes been used as a substitute.

4.1.3 Antiproton Trapping

After passing through the PPAC, energy tuning cell, and the degrader, $\overline{p}$ enter the Penning trap, where potentials as large as -5 kV may be applied to the HV and

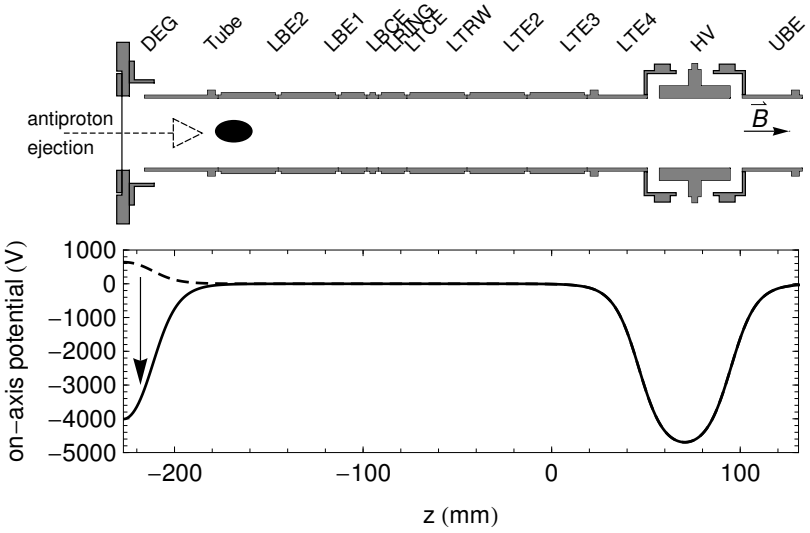

Figure 4.3: Lower electrode stack and on-axis potentials for $\overline{\mathrm{p}}$ catching. The voltage applied to the degrader is initially positive to allow $\overline{\mathrm{p}}$ to enter (dashed) and is quickly switched negative after the AD ejection (solid).

degrader (DEG) electrodes for confinement. As shown in Fig. 4.3, before a $\overline{\mathrm{p}}$ shot is received from the AD, the degrader is held at a positive voltage (typically 600 V). This allows $\overline{\mathrm{p}}$ to pass into the lower electrode stack unimpeded, while suppressing emission of secondary electrons from the degrader that may interfere with $\overline{\mathrm{p}}$ accumulation. A custom-built high-voltage switch applies -5 kV to the degrader after the $\overline{\mathrm{p}}$ enter the trap, making a complete axial confining well [128].

The timing of the pulse that triggers the high-voltage switch must be precisely controlled. If the high-voltage is applied too early relative to the AD ejection, low-energy $\overline{\mathrm{p}}$ will reflect off the -5 kV barrier on DEG and fail to enter the trapping region. Conversely, if the switch fires too late, $\overline{\mathrm{p}}$ will reflect off the -5 kV barrier on HV and escape before the complete well has been formed. Fig. 4.4 shows the effect of varying the switch delay time on the $\overline{\mathrm{p}}$ capture efficiency. The $\approx$ 200 ns leading edge indicates the duration of the entering $\overline{\mathrm{p}}$ pulse, while the long tail shows that the

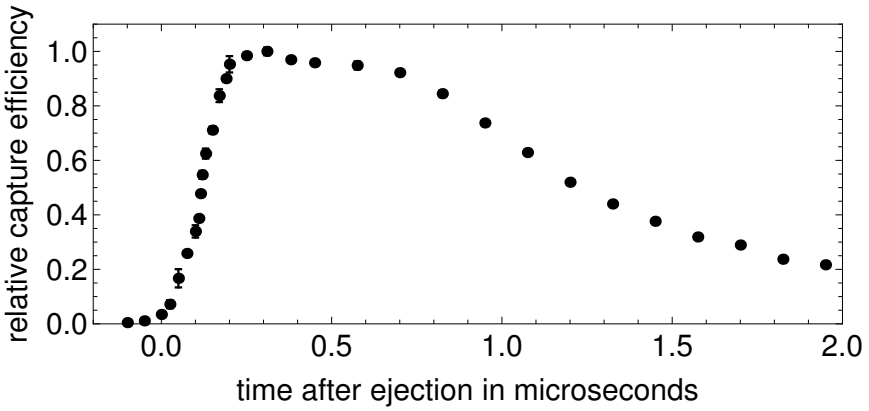

Figure 4.4: Relative $\overline{\text{p}}$ capture efficiency as a function of high-voltage switch delay time.

$\overline{\text{p}}$ energy distribution has been significantly broadened after traversing the degrader. The ≈ 0.7 μs plateau corresponds to the round-trip time for 5 keV $\overline{\text{p}}$ to travel from the degrader to the HV electrode and back. Setting the timing delay to 300 ns after ejection optimizes the capture efficiency.

4.1.4 Field-Boosting Solenoid

After passing through the degrader, $\overline{\text{p}}$ emerge typically with several keV of cyclotron energy E_c. If the $\overline{\text{p}}$ cyclotron diameter, defined by

$$d_c = 2r_c = 2\frac{\sqrt{2m_pE_c}}{qB_0} \tag{4.1}$$

grows large compared with the electrode radius $\rho_0 = 18$ mm, $\overline{\text{p}}$ will be lost upon annihilating with the walls of the trap. As can be seen in Eqn. 4.1 and Fig. 4.5, increasing the background magnetic field leads to a proportional decrease in cyclotron diameter.

As introduced in Sec. 2.4, a field-boosting solenoid surrounds the $\overline{\text{p}}$ catching region of the Penning trap. When fully energized, the solenoid increases the local

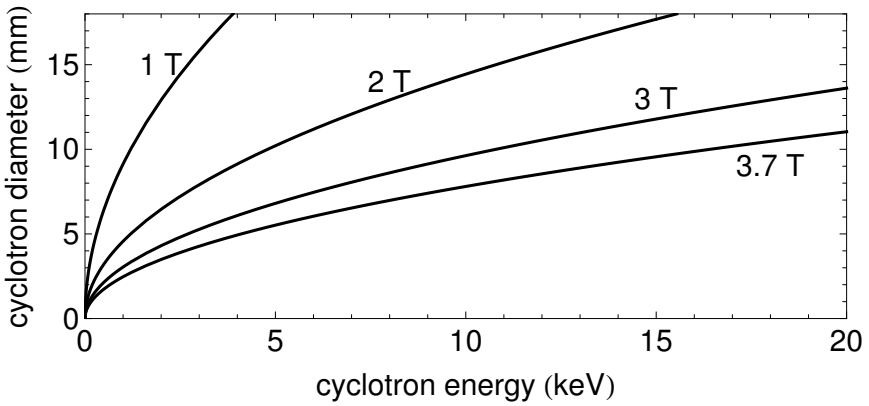

Figure 4.5: For large cyclotron energies, the cyclotron diameter becomes comparable to the trap radius $\rho_0 = 18$ mm. For any given cyclotron energy, increasing the magnetic field decreases the cyclotron diameter.

magnetic field from 1 T to 3.7 T, decreasing the cyclotron radius by the same factor and leading to many more trapped $\overline{\mathrm{p}}$. Fig. 4.6 demonstrates the improved capture efficiency for $\overline{\mathrm{p}}$ at larger magnetic fields. As the total magnetic field is ramped from 1 T to 3.7 T, the number of $\overline{\mathrm{p}}$ retained per AD ejection rises from 3×10^4 to 1.6×10^5 - over a factor of 5 improvement. However, further increases in the magnetic field are not predicted to yield significantly better loading rates, since large cyclotron radii are no longer a limiting factor.

As a general principle, more $\overline{\mathrm{p}}$ per AD ejection may be captured when larger high voltages are applied to the DEG and HV electrodes. However, as demonstrated in Fig. 4.7, the incremental gains depend strongly upon the applied magnetic field. At 1 T, the capture efficiency is limited by the large cyclotron radius, and only small improvements may be realized by increasing the applied catching voltage. At 3.7 T, however, further increases in the catching voltage should yield an even greater number of $\overline{\mathrm{p}}$ loaded per AD cycle.

In Chapter 3, annihilation detection was presented as a means to determine the

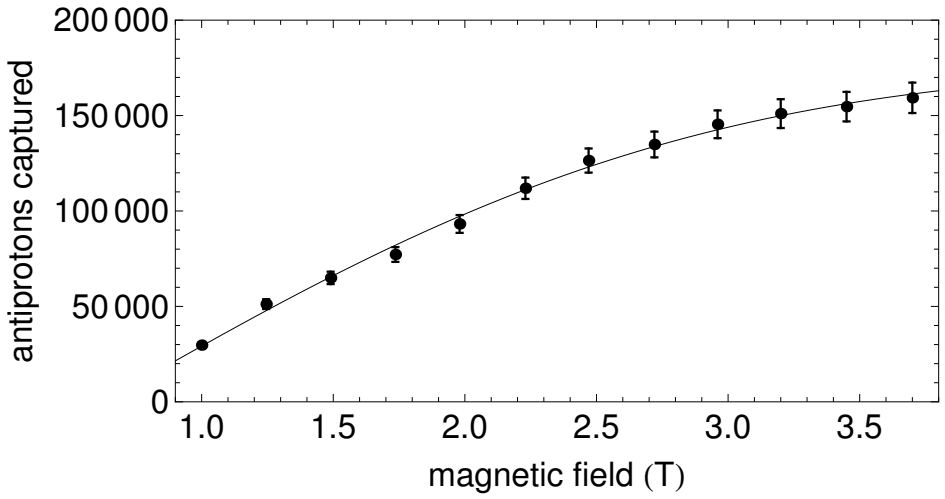

Figure 4.6: The number of captured $\overline{\mathrm{p}}$ per AD ejection increases with the applied background magnetic field.

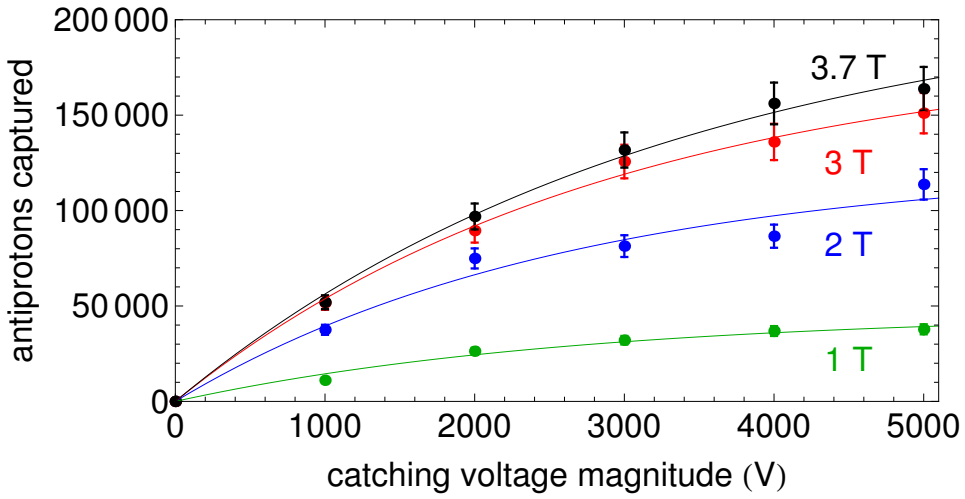

Figure 4.7: The number of $\overline{\mathrm{p}}$ captured per AD ejection increases with increasing catching voltage. For small magnetic fields, the capture efficiency is limited by the large cyclotron radius.

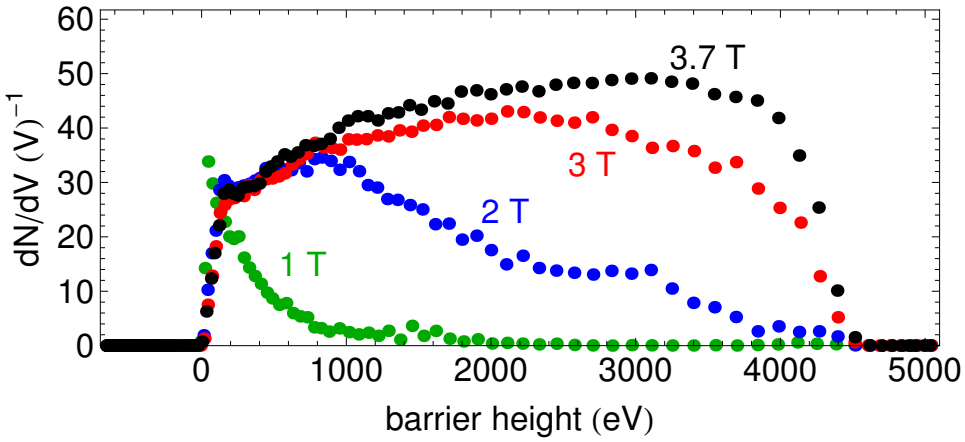

Figure 4.8: The loss rate of captured $\overline{\text{p}}$ while the voltage barrier is decreased reveals their energy distribution. Larger magnetic fields permit capture of larger numbers of high-energy $\overline{\text{p}}$.

trapped $\overline{\text{p}}$ number and energy distribution. First, the $\overline{\text{p}}$ are held in the lower Penning trap for 60 s and allowed to equilibrate. To count and measure the distribution of our captured $\overline{\text{p}}$, the degrader voltage is switched from -5 kV to $+600$ V with an RC time constant of ≈ 20 ms. As the barrier height of the confining well is reduced, $\overline{\text{p}}$ are free to escape and annihilate upon striking the degrader.

With the trapping high-voltage set to -5 kV, the energy distribution of the captured $\overline{\text{p}}$ was probed for varying strengths of magnetic field. Fig. 4.8 shows that as B_0 is increased, both higher energy and larger numbers of $\overline{\text{p}}$ are collected. Note that even though -5 kV is applied, the on-axis potential is slightly smaller on account of the finite electrode lengths. At 3.7 T, the sharp falloff in the loss rate at large axial energies (compared with the exponential falloff at 1 T) provides further evidence that increasing the trapping voltage could substantially improve the $\overline{\text{p}}$ catching efficiency.

One striking feature of Fig. 4.8 is the very small fraction of $\overline{\text{p}}$ that have cooled to 100 V or less, which is the scale of voltages applied in the trap after particle accu-

mulation. After capture, $\overline{\mathrm{p}}$ can theoretically cool by emitting synchrotron radiation, though in Sec. 2.1.3 this mechanism was shown to have a time constant of ≈ 37 years. We therefore require a new process which quickly reduces the $\overline{\mathrm{p}}$ energy to make them usable for $\overline{\mathrm{H}}$ experiments.

4.2 Electron Loading

Since the synchrotron cooling time constant is $\propto m^3$, e^- in a 3.7 T magnetic field radiate their energy away in less than 1 s. Additionally, e^- have the same sign of charge as $\overline{\mathrm{p}}$, so both species may be confined simultaneously in the same voltage well. Hence, e^- make an excellent candidate for collision-cooling of $\overline{\mathrm{p}}$ [43].

Before capturing $\overline{\mathrm{p}}$ from the AD, photoelectrons [129] are liberated from the Be degrader by intense UV laser pulses and are trapped in an 80 eV confining well in the lower electrode stack [130]. The UV light is generated in a KrF gas excimer laser (GAM Lasers EX-5) which outputs 20 mJ, 10 ns pulses at a repetition rate of 1 Hz and a wavelength of 248 nm. The energy per photon of $hc/\lambda = 5.0$ eV, which is larger than the 3.6 eV work function of oxidized Be [131], allows for robust loading of 10^8 e^- in less than 30 s.

Fig. 4.9 shows the path taken by the UV laser beam as it enters BTRAP and strikes the degrader. Since high-transmission fibers carrying 248 nm laser pulses are not readily available, the beam is guided through the apparatus using anti-reflection coated UV-grade fused-silica mirrors. The laser output is reflected off of two mirrors (not shown) to fall upon two angled mirrors that guide the beam into the vacuum apparatus. A 45° mirror is mounted at the end of a movable translation stage to

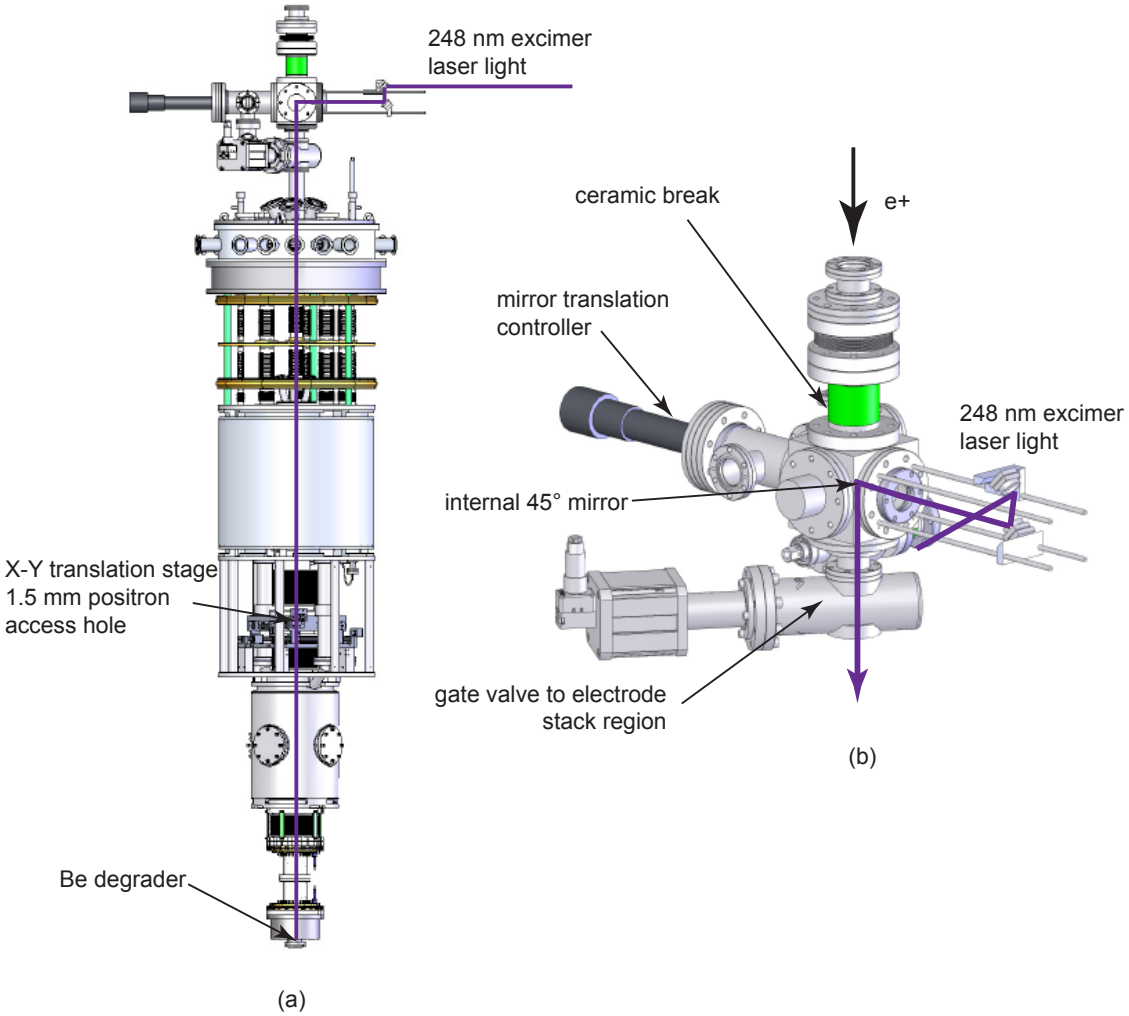

Figure 4.9: A 248 nm UV laser liberates e^- from a Be degrader. (a) The laser beam enters the apparatus through the central axis from above, passes through the 1.5 mm hole in the X-Y translation stage, and strikes the degrader at the bottom. (b) Detail view showing the two external alignment mirrors and the position of an internal, 45° mirror mounted on a translation stage.

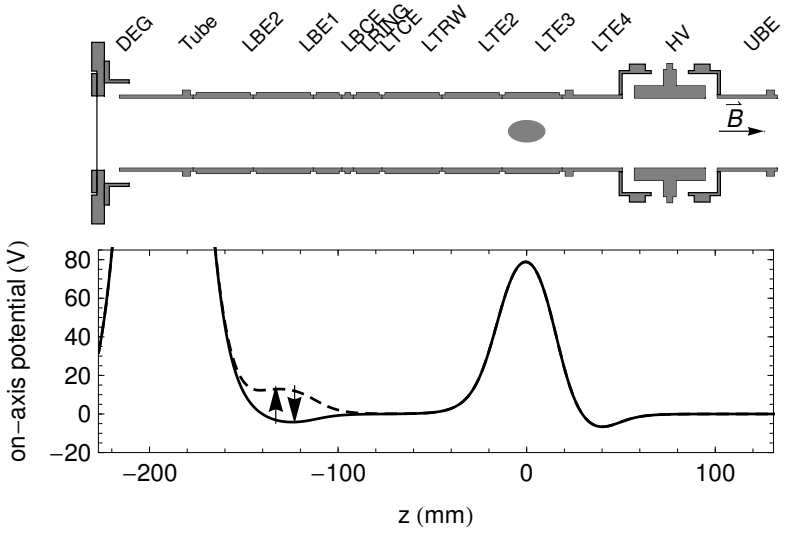

Figure 4.10: 1.8 μs after the excimer laser strikes the degrader to produce e^-, the voltage on electrode LBE1 (solid) is temporarily pulsed upwards (dashed) to allow the e^- to enter the confining well. Synchrotron cooling causes the e^- to collect within electrode LTE3.

reflect the UV light down the central axis of the trap. Because e^+ are also loaded down the central axis, the motorized translation stage moves the 45° mirror out of the way during e^+ loading. The UV beam passes through the 1.5 mm e^+ aperture in the X-Y translation stage (see Sec. 2.5) before continuing towards the degrader. Alignment is aided by monitoring the currents induced by the laser in four gold-plated copper Faraday cups (work function 4.2 eV) surrounding the e^+ access hole.

To capture e^- ejected from the degrader, the potentials shown in Fig. 4.10 are applied to the electrodes in the lower stack. Analogously to the $\overline{p}$ loading procedure, a several-electrode long potential well is formed between electrodes LBE1 and LTE4. The "front-door" to this well on electrode LBE1 is pulsed open 1.8 μs after the excimer laser fires to allow e^- to enter, then is returned to its original value 600 ns later to trap the e^- within. A large positive voltage is applied to TUBE to accelerate e^- away

from the degrader. As the e^- synchrotron cool, they fall deeper into the confining well on LTE3 until the trap forces and e^- plasma Coulomb repulsion forces are balanced.

To load the 10^8 e^- typically used for cooling $\overline{p}$, multiple laser shots are required. To reduce the amount of kinetic energy the e^- must radiate away, the confining voltage on LTE3 is initially set to only 1 V. The voltage applied to LTE3 is then increased by 1 V for every subsequent laser shot, to ensure that the well depth is always larger than the e^- plasma self-potential. Approximately 10-20 pulses are required to capture the desired 10^8 e^- (depending upon the alignment quality and excimer laser power), after which the voltage on LTE3 is set to 100 V to strongly confine the e^- in anticipation of $\overline{p}$ loading.

4.3 Antiproton Accumulation

The accumulation of large numbers of $\overline{p}$ is a multi-stage process. First, the correct number and geometry of cooling e^- must be pre-loaded before $\overline{p}$ shots from the AD are received. The $\overline{p}$ captured from individual ejections are "stacked" [47] until the target number of $\overline{p}$ is reached. The multi-species $\overline{p}$ – e^- plasma is transferred to a 3-electrode long rotating wall potential (Fig. 3.13) to reduce the plasma radius, followed by fast voltage pulses which eject nearly all of the e^-. After allowing the $\overline{p}$ and few remaining e^- to equilibrate, the field-boosting solenoid is ramped down, reducing the magnetic field from 3.7 T to 1 T. The $\overline{p}$ are then ready for $\overline{H}$ experiments, with the total process of accumulating 10^6 $\overline{p}$ taking approximately 1 h. Utilization of the field-boosting solenoid and rotating wall techniques enable up to 10^7 $\overline{p}$ to be loaded into the trap, compared with the previous best value of 7×10^5 $\overline{p}$ [63].

4.3.1 Electrons

Using the methods outlined in Sec. 4.2, a plasma of 10^8 e^- with a 6 mm radius is pre-loaded into a 100 V well before $\overline{p}$ are captured. Both the number and geometry of the e^- plasma were chosen to allow for both fast cooling of incoming $\overline{p}$ as well as good spatial overlap between the e^- and $\overline{p}$ clouds. While small (up to $\sim 20\%$) deviations from these parameters may be tolerated, significant departures have been observed to have adverse effects on the $\overline{p}$ loading and cooling efficiencies.

The rate at which e^- can cool $\overline{p}$ depends directly upon the ratio of the e^- and $\overline{p}$ numbers N_e and $N_{\overline{p}}$. The change in temperature of each species may be modeled by Newton's Law of Cooling [132]

$$\frac{d}{dt}T_{\overline{p}} = -\nu_c \left(T_{\overline{p}} - T_e\right) \tag{4.2}$$

$$\frac{d}{dt}T_e = \frac{N_{\overline{p}}}{N_e}\nu_c \left(T_{\overline{p}} - T_e\right) - \frac{1}{\tau_s}\left(T_e - T_w\right) \tag{4.3}$$

where T_e and $T_{\overline{p}}$ are the e^- and $\overline{p}$ temperatures, T_w is the temperature of the electrode wall (1.2 K), and τ_s is the synchrotron cooling time constant (see Eqn. 2.34). The collision rate ν_c that appears in Eqns. 4.2-4.3 is slightly modified from Eqn. 3.30 on account of multiple species with different masses. The zero-magnetic field result is given by [104]

$$\nu_c = \frac{8\sqrt{2\pi}}{3}\frac{1}{(4\pi\epsilon_0)^2}\frac{\sqrt{m_{\overline{p}}m_e}n_0 q^4 \ln\Lambda}{(m_e k_B T_{\overline{p}} + m_{\overline{p}} k_B T_e)^{3/2}} \tag{4.4}$$

with a correction of order $I(\bar{\kappa})$ (Eqn. 3.32) applied in strong magnetic fields. However, for high-energy $\overline{p}$, the zero-field rate Eqn. 4.4 is a good approximation since the cyclotron radius $r_c \gg b_{min}$, the distance of closest approach.

The coupled differential equations 4.2-4.3 may be solved for different values of

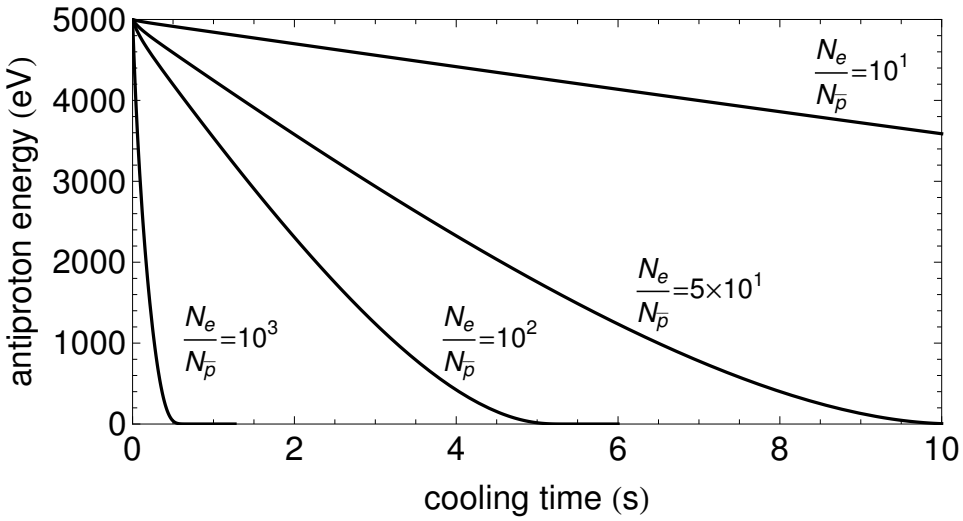

Figure 4.11: The e^- cooling of $\overline{p}$ proceeds at different rates based on the ratio of the e^- to $\overline{p}$ number, $N_e/N_{\overline{p}}$. Results are shown here for a 6 mm radius plasma with $N_{\overline{p}} = 10^6$ and $N_e = \{1 \times 10^7, 5 \times 10^7, 1 \times 10^8, \text{and } 1 \times 10^9\}$.

$N_e/N_{\overline{p}}$ to determine the timescale over which e^- cool $\overline{p}$. Fig. 4.11 shows the results for a 6 mm plasma with 10^6 $\overline{p}$ starting with an initial energy of 5 keV and cooling to equilibrium with 1.2 K e^-. As expected, the cooling rate is increased for larger values of $N_e/N_{\overline{p}}$. Our choice of loading 10^8 e^- for typical experiments ($N_e/N_{\overline{p}} = 10^2$) strikes a balance between reasonably fast cooling and reasonably short e^- loading times. Additionally, setting $N_e = 10^8$ allows even larger numbers of $\overline{p}$ to be cooled in a time shorter than the ≈ 100 s AD cycle.

Initially, the e^- cloud is loaded with a radius of between 6 and 9 mm. A rotating wall drive is applied to reduce the radius to 6 mm, maximizing the overlap between the cooling e^- and the incoming $\overline{p}$ shot. If the e^- radius is too small, $\overline{p}$ at larger radii will remain uncooled and will escape from the trap when the -5 kV catching potential is turned off. Oppositely, setting the e^- radius too large reduces the density and cooling rate (Eqn. 4.4) and leads to a larger radius $\overline{p}$ plasma that is difficult to

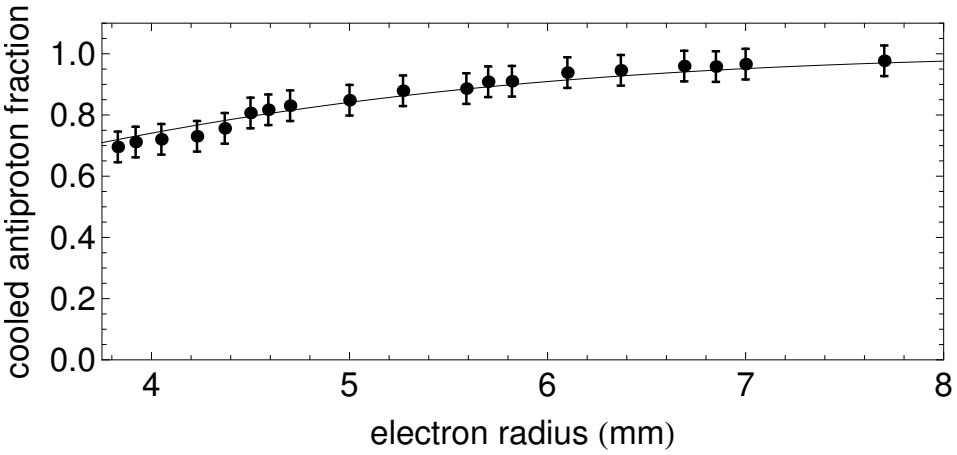

Figure 4.12: The fraction of $\overline{\mathrm{p}}$ cooled by e^- decreases at smaller e^- radii.

retain as the field-boosting solenoid is turned off. The target e^- radius is thus the smallest one that cools a large majority of incoming $\overline{\mathrm{p}}$.

Fig. 4.12 shows the effect of varying the starting e^- radius on the fraction of $\overline{\mathrm{p}}$ cooled. Choosing $\rho_e = 6$ mm cools 90% of the $\overline{\mathrm{p}}$ while avoiding the large plasma radii that prove troublesome when the field-boosting solenoid is de-energized. If the $\overline{\mathrm{p}}$ beam profile is assumed to be Gaussian, the data in Fig. 4.12 may be fit to an error-function to predict an initial $\overline{\mathrm{p}}$ radius (FWHM/2) of 3.5 mm. This radius is notably larger than the 1.5 mm radius measured at the PPAC (see Fig. 4.1) since the $\overline{\mathrm{p}}$ beam emittance is increased by traversing the energy tuning cell and degrader.

4.3.2 Antiproton Stacking

With the cooling e^- pre-loaded, multiple $\overline{\mathrm{p}}$ shots may be accumulated ("stacked") until the desired $N_{\overline{\mathrm{p}}}$ is attained. The potential structure, shown in Fig. 4.13, is identical to the structure in Fig. 4.3 except for the 80 eV well on electrode LTE3 populated with e^-. After a shot of $\overline{\mathrm{p}}$ is received from the AD, $\overline{\mathrm{p}}$ and e^- are allowed

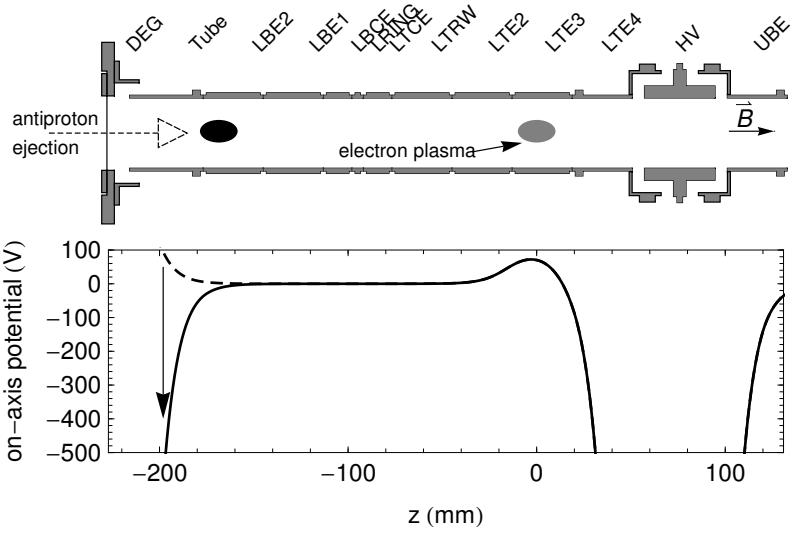

Figure 4.13: Pre-loaded e^- are placed on electrode LTE3 in preparation for $\overline{p}$ stacking. Capture of $\overline{p}$ proceeds as described in Sec. 4.1, after which the $\overline{p}$ cool into the well on LTE3 through collisions with e^-.

to thermalize for 60 s before the voltage on DEG is switched positive to prepare for the next shot. Through collisions with e^-, the $\overline{p}$ fall into the well on LTE3 and thus remain confined when the -5 kV potential is turned off.

Approximately 10% of the $\overline{p}$ per shot are not cooled by the e^- in 60 s and escape the trap when the voltage on DEG is switched positive. Fig. 4.14 demonstrates the stark difference that cooling e^- can make. In addition to a vastly smaller number of escaping $\overline{p}$, the distribution has been shifted to lower energy; an even smaller fraction of $\overline{p}$ would leave if the cooling time (set ultimately by the $\approx$ 100 s AD cycle) was longer.

Between 1.6×10^5 and 2×10^5 $\overline{p}$ may be captured and cooled per shot, depending on the performance of the AD. Typically, 6 stacked shots are required to attain the 10^6 $\overline{p}$ used for $\overline{H}$ experiments, taking $\approx$ 11 m of accumulation time. Stacking of up to 10^7 $\overline{p}$ has been achieved in 90 m when the AD is operating optimally. Though still

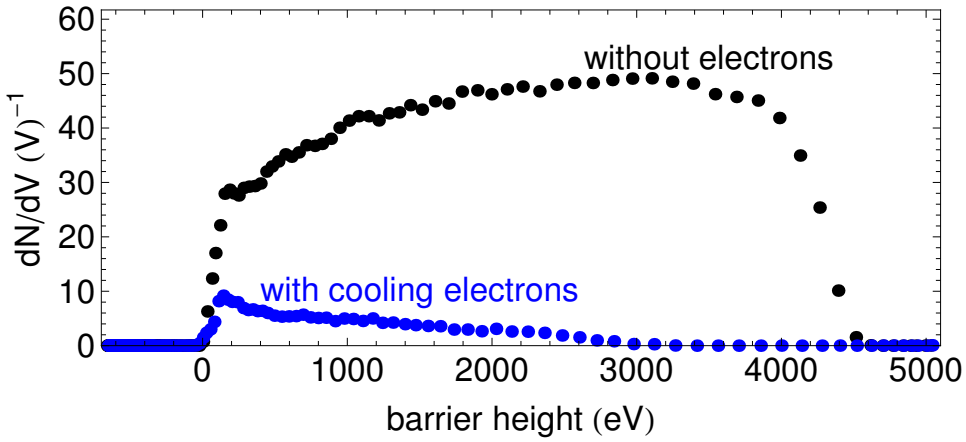

Figure 4.14: The number of $\overline{\mathrm{p}}$ escaping the trap after 60 s is dramatically reduced when cooling e^- are present.

larger numbers of $\overline{\mathrm{p}}$ may be stacked, we have so far been unable to avoid significant losses when the magnetic field is reduced from 3.7 T to 1 T.

4.3.3 Rotating Wall

When 10^6 or more $\overline{\mathrm{p}}$ are stacked, the plasma radius grows large enough that annihilation losses on the electrode walls are observed when the local magnetic field is reduced from 3.7 T to 1 T. To counter this effect, the multi-species $\overline{\mathrm{p}}$ – e^- plasma is transferred to a 3-electrode long well and exposed to a rotating wall drive. A 1 MHz drive at 9 V peak-to-peak is applied for 783 s to slowly compress the plasma to a final radius of 2 mm. We have found that slow compression rates are necessary; fast compression may lead to a spatial decoupling of the e^- and $\overline{\mathrm{p}}$, an effect seen in other mixed-species plasmas [133]. When the drive has completed, the 3-electrode long well is un-made, and the plasma is returned to an 80 eV well on LTE3 to cool for 30 s. We observe no losses during this procedure for our typical 10^6 $\overline{\mathrm{p}}$ plasmas.

Losses during the rotating wall drive begin to appear when $N_{\overline{\mathrm{p}}} \approx 3 \times 10^6$, though

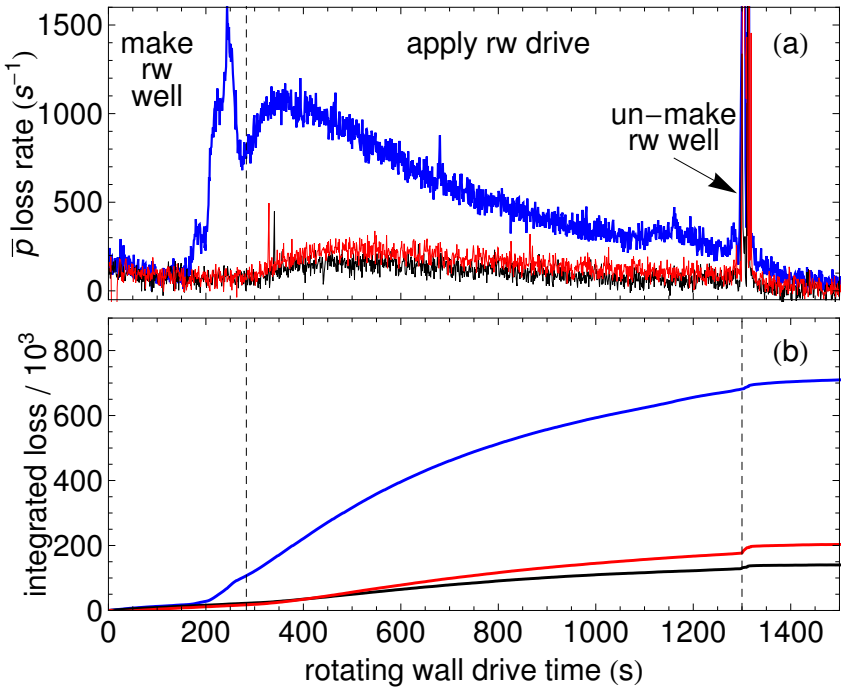

Figure 4.15: (a) The $\overline{\text{p}}$ loss rate per second during application of the rotating wall drive for 6.8×10^6 (black), 8.3×10^6 (red), and 1.05×10^7 (blue) $\overline{\text{p}}$. Losses increase as $\overline{\text{p}}$ are brought into the 3-electrode long well and slowly subside until the $\overline{\text{p}}$ are returned to a single-electrode well. (b) Integrated total $\overline{\text{p}}$ loss during the drive, for curves shown in (a).

they may be forestalled by changing the parameters of the drive. We have observed that by driving for longer times at smaller peak-to-peak voltages, $\overline{\text{p}}$ losses can be reduced. Maintaining an equilibrium between the $\overline{\text{p}}$ cooling and heating rates during the drive may enable such stability. For instance, increasing $N_{\overline{\text{p}}}$ by a factor of 2 decreases the electron cooling rate by roughly the same factor; reducing the drive amplitude by a factor $\sqrt{2}$ would lead to comparably less heating.

Fig. 4.15 shows the losses during the rotating wall drive for three large $\overline{\text{p}}$ plasmas that were subjected to a 1 MHz, 5 V peak-to-peak drive for 1283 s. Most of the losses occur as the plasmas initially enter the 3-electrode long well. For the 6.8×10^6 $\overline{\text{p}}$

plasma, the total loss of $\approx 1.5 \times 10^5$ compares favorably to the 1.1×10^6 lost when driven at 9 V peak-to-peak for 783 s. Likewise, the integrated loss for the 1.05×10^7 $\overline{\mathrm{p}}$ plasma may be further reduced from the $\approx 7 \times 10^5$ shown in Fig. 4.15 to $\approx 3 \times 10^5$ by driving at 3 V peak-to-peak for 1783 s.

4.3.4 Electron Pulse-out

After the compressed $\overline{\mathrm{p}}$ – e^- plasma is returned to a single electrode well, the e^- are ejected using a series of fast pulses. The axial bounce times for e^- and $\overline{\mathrm{p}}$ in their 80 eV potential well on electrode LTE3 are 28 ns and 1.2 μs, respectively; pulsing the well voltage to zero and restoring it within 75 ns allows the e^- to escape, but not the more massive $\overline{\mathrm{p}}$. The potential structure is identical to the one shown in Fig. 3.6, and the escaping electrons are pulse-counted using the same techniques that were introduced in Sec. 3.5.1.

Typically 3 or 4 pulses are used to eject all but 6×10^3 or 9×10^2 electrons, respectively. These numbers are too small to be directly measured by charge-counting methods, but are instead determined from a measurement of $\overline{\mathrm{p}}$ heating rates, as described in Chapter 6. The $\overline{\mathrm{p}}$ temperature may be elevated to several thousands of Kelvin by the pulse-out process, so a wait time of 10 minutes is introduced to allow the few remaining electrons to cool the now $\overline{\mathrm{p}}$-dominated plasma.

4.3.5 Magnetic Field Reduction

As the final step in $\overline{\mathrm{p}}$ accumulation, the field-boosting solenoid is de-energized to reduce the magnetic field in the lower stack from 3.7 T to 1 T. The initially

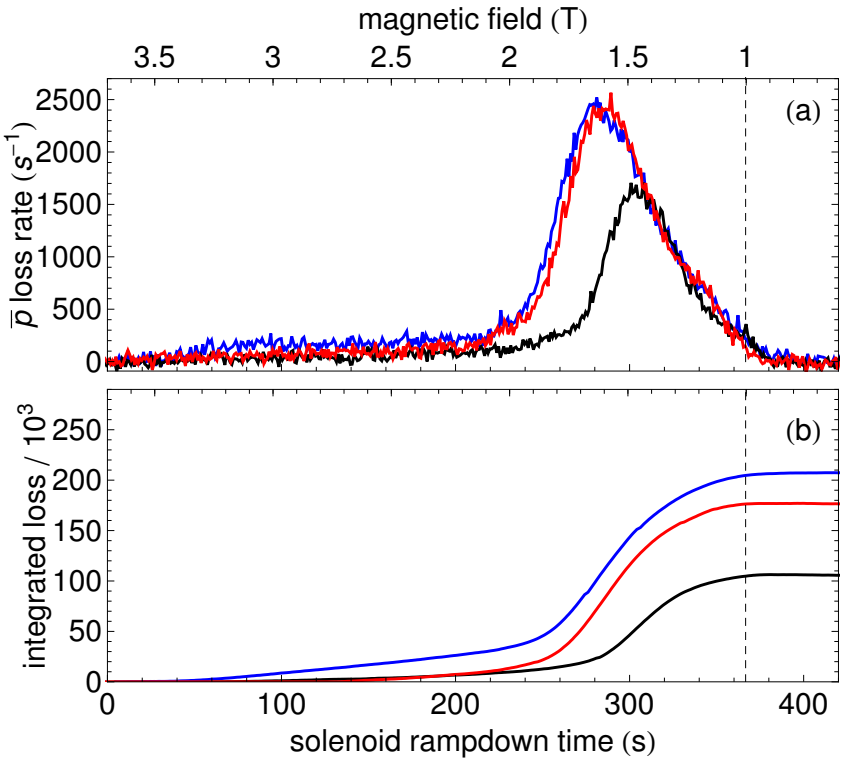

Figure 4.16: (a) The $\overline{\mathrm{p}}$ loss rate per second during the reduction of the magnetic field from 3.7 T to 1 T in 366 s is shown for 6.8×10^6 (black), 8.3×10^6 (red), and 1.05×10^7 (blue) $\overline{\mathrm{p}}$. (b) Integrated total $\overline{\mathrm{p}}$ loss during the solenoid rampdown, for curves shown in (a).

≈ 2 mm radius $\overline{\mathrm{p}}$ plasma expands by a factor of $\sqrt{3.7}$ to conserve its canonical angular momentum, reaching a final radius of ≈ 4 mm. For our typical plasmas with $N_{\overline{\mathrm{p}}} = 10^6$, no losses are observed during the reduction of the magnetic field.

When large $N_{\overline{\mathrm{p}}}$ plasmas are loaded, some losses are observed during the magnetic field rampdown (see Fig. 4.16), though the losses are smaller than those observed during the rotating wall drive. This result is surprising, given that the $\overline{\mathrm{p}}$ plasma radius should remain well within the electrode wall. Additionally, the $\overline{\mathrm{p}}$ loss rate begins to slow even while the magnetic field continues to decrease. One possible explanation is a decoupling of the $\overline{\mathrm{p}}$ and e^- clouds during the rotating wall drive.

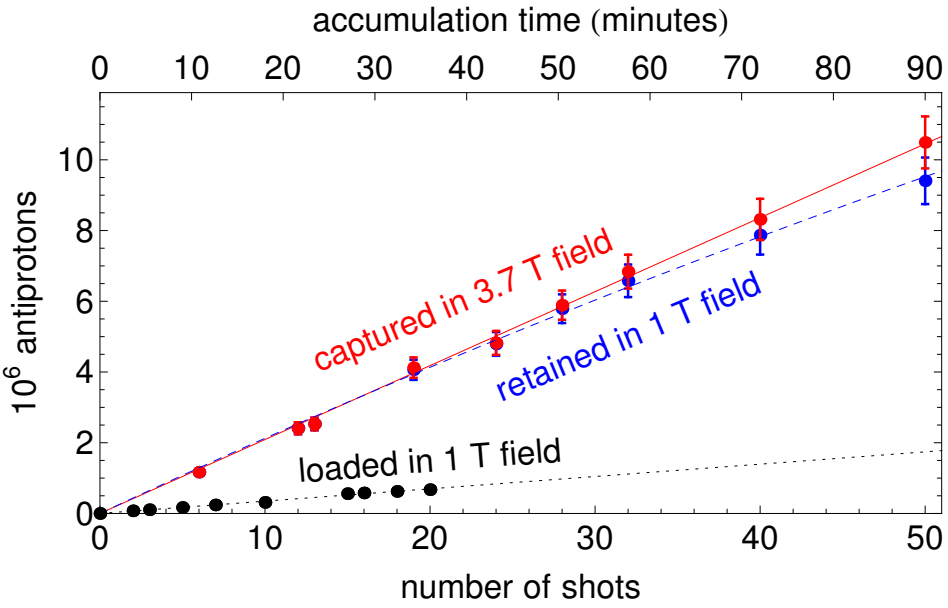

Figure 4.17: The number of accumulated $\overline{\mathrm{p}}$ grows linearly with the number of shots received from the AD (red), and nearly all are retained after reducing the magnetic field to 1 T (blue). For comparison, the best loading achieved before the field-boosting solenoid was implemented is shown on the same scale (black).

A small percentage of $\overline{\mathrm{p}}$ may remain orphaned at large radii and annihilate on the walls when the magnetic field is reduced. Still slower rotating wall drives may thus be required to ensure global thermal equilibrium throughout the entire process for very large $\overline{\mathrm{p}}$ plasmas.

4.3.6 Accumulation Results

A summary of the accumulated $\overline{\mathrm{p}}$ number is shown in Fig. 4.17. The field-boosting solenoid and rotating-wall techniques have facilitated the linear stacking of up to 10^7 $\overline{\mathrm{p}}$ at a rate of 2×10^5 per shot, or 1.2×10^5 per minute. Nearly all of these $\overline{\mathrm{p}}$ are retained in a 1 T field and ready for $\overline{\mathrm{H}}$ experiments after their radius is compressed

and cooling e^- pulsed out. The attainment of 10^7 $\overline{p}$ represents a factor of 14 increase from the 7×10^5 $\overline{p}$ that were formerly accumulated at 1 T without the field-boosting solenoid. It is anticipated that when the newly-approved ELENA cooling ring is added to the AD, the number of $\overline{p}$ trapped per ejection will further improve by 1-2 orders of magnitude, significantly decreasing the accumulation time displayed at the top of Fig. 4.17 [61].

4.4 Positron Accumulation

A radioactive ^{22}Na source supplies the e^+ used for $\overline{H}$ experiments at ATRAP. High-energy e^+ emitted in a reverse-β decay process pass through a solid neon moderator [134], reducing their energy to $\approx$ 15 eV. These e^+ are magnetically guided into a room-temperature Penning trap filled with 10^{-3} to 10^{-6} torr of N_2 buffer gas [135]. Through collisions, the e^+ cool into regions of the trap with progressively deeper potential wells and lower buffer gas pressures. Radial confinement is provided by a 0.14 T axial magnetic field while a rotating wall electrode prevents the e^+ radius from growing too large. The accumulation rate of 8×10^5 s^{-1} for the 20 mCi source is over three orders of magnitude larger than the rates observed with earlier accumulation methods used at ATRAP [136].

Ideally, the buffer-gas accumulator would be aligned coaxially with the Penning-Ioffe trap to expedite transfer of e^+ for $\overline{H}$ experiments. However, the limited vertical space above BTRAP due to an overhead bridge crane in the AD makes such alignment impossible. Instead, the accumulator is mounted horizontally in the closest available location, 8 m away from the 1 T solenoid. As shown in Fig. 4.18, a long transfer line

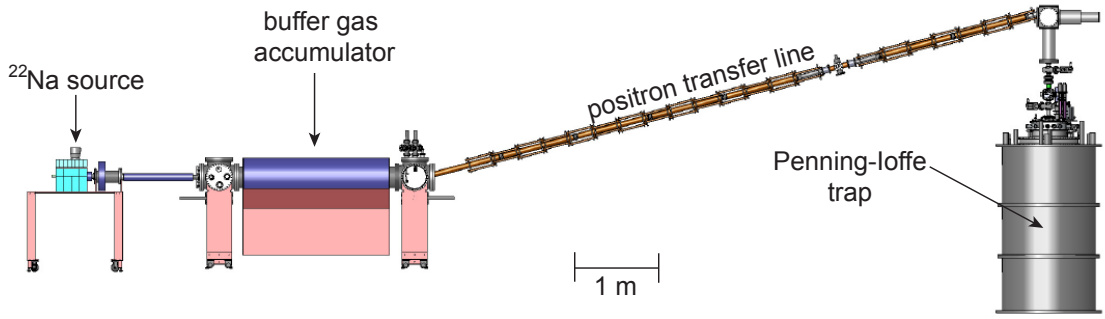

Figure 4.18: e^+ from a radioactive ^{22}Na source are captured in a buffer-gas accumulator and transferred along a magnetic guide to the Penning-Ioffe trap three times per AD cycle.

with 15° and 105° bends and nearly 100 independently-controlled steering magnets connects the accumulator with the Penning-Ioffe trap [137]. Segmented Faraday cups may be moved into the beam path along the magnetic guide to serve as a steering diagnostic.

Three times per AD cycle, a pulse of e^+ is transferred from the accumulator, through the 1.5 mm aperture in the X-Y translation stage, and into the cryogenic Penning trap from above with nearly unit efficiency. To prepare for e^+ catching in the Penning trap, e^- are pre-loaded into the potential structure shown in Fig. 4.19. A long catching well is formed by applying a positive bias to electrodes UTE2 and UBR4, and two deeply confining wells flank the electrode on which e^- are held. Coincident with the arrival of a e^+ pulse, the voltage on electrode UTE2 is temporarily pulsed downwards to allow e^+ to enter, then quickly restored to its initial value.

We observe the incoming kinetic energy of the e^+ pulse to be between 60-70 eV. Upon entering the upper electrode stack, e^+ are made to climb a 58 eV potential hill, which significantly reduces their energy. Collisions with 1.5×10^8 pre-loaded cooling e^- allow the e^+ to fall into deep confining wells on electrodes UTR7 and UTRW,

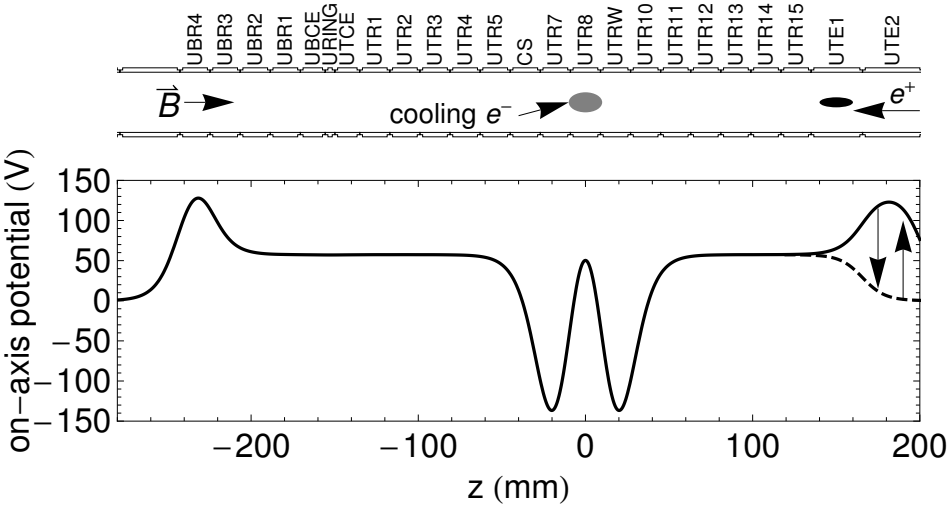

Figure 4.19: A blocking potential on electrode UTE2 is quickly pulsed downwards (dashed) to allow e^+ to enter the upper electrode stack, then restored (solid) to trap the e^+ within. The e^+ cool into potential wells on electrodes UTR7 and UTRW through collisions with pre-loaded e^-.

with annihilations between the two species unlikely due to the relatively large e^+ velocity and the long-range nature of the Coulomb interaction. After e^+ loading has completed, the e^- may be smoothly ejected by decreasing the voltage on electrode UTR8.

Previously, up to 2×10^8 e^+ could be linearly stacked at ATRAP before sizable losses were observed [63]. This may be expected, since the e^+ plasma experiences radial growth with each subsequent shot until it annihilates on the electrode walls. Additionally, Ref. [66] reports a radial growth rate of 0.01 mm/s for a comparable e^- plasma as consequence of confinement in anharmonic trapping potentials.

Implementation of rotating wall techniques counteracts the radial growth observed during e^+ loading, allowing for the accumulation of up to 4×10^9 e^+. After every 50 shots have been transferred, the e^+ are moved to a 5-radius-length electrode long

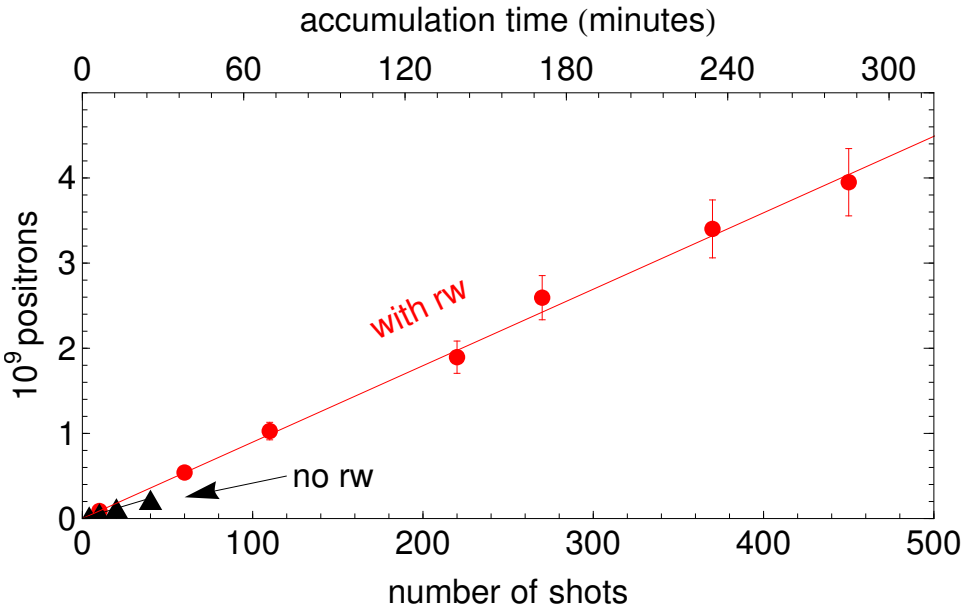

Figure 4.20: With rotating wall techniques implemented, the accumulated number of e^+ grows linearly with the number of shots up to 4×10^9 (red circles). The previous best e^+ loading data is shown for comparison (black triangles).

flat well and subjected to a 5 MHz, 9 V peak-to-peak rotating wall drive to reduce their radius to 3 mm. As shown in Fig. 4.20, repetition of this procedure extends the linear stacking regime by a factor of 20 compared to previous results. The number of e^+ now available for $\overline{H}$ formation is sufficiently large that no current or currently planned experiment could make use of them all.

4.5 Particle Transfer

After $\overline{p}$ and e^+ have been loaded, they need to be brought together and allowed to mix to form $\overline{H}$. Since both particle species are accumulated away from the center of the Ioffe trap where $\overline{H}$ is made, each plasma must be moved along the electrode stack to the interaction region of the trap. Ideally, the particle transfer would be lossless,

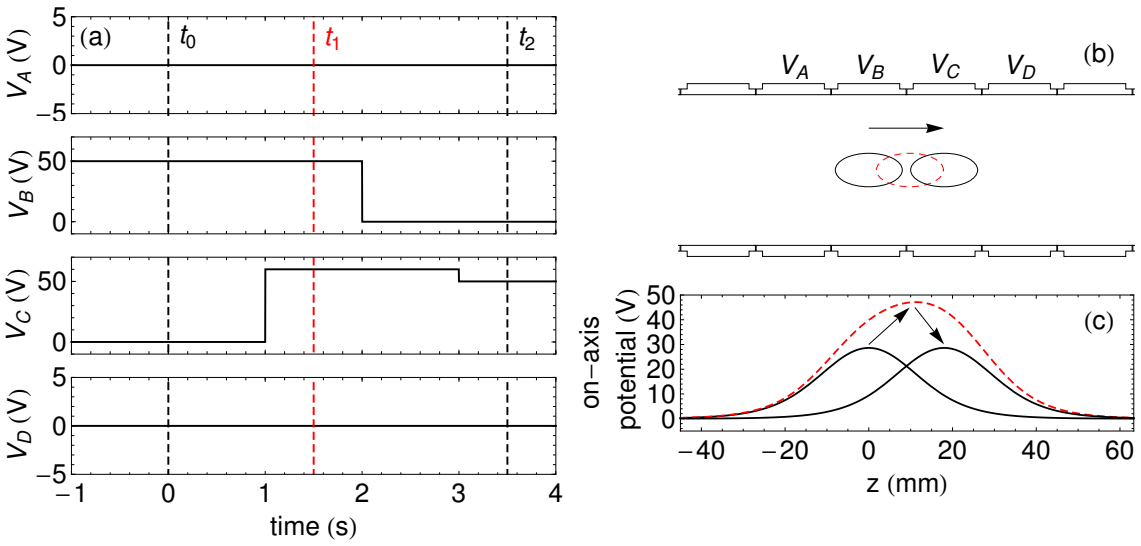

Figure 4.21: The original particle transfer routine. (a) The voltages V_A, V_B, V_C, and V_D applied to four neighboring electrodes are shown as a function of time. Only the voltages on the start (B) and end (C) electrodes are manipulated. (b) The plasma position in the electrode stack, and (c) the on-axis potential are shown at the times t_0, t_1, and t_2 during the move.

preserve the plasma geometry, and limit motion-induced heating.

The original particle transfer technique, shown in Fig. 4.21, manipulated the voltages on two electrodes to move particles from one to the other. Each change in voltage is applied over 1 ms, adiabatic with respect to the 1 μs (or less) axial bounce time for $\overline{\mathrm{p}}$ (or e^+). Though this method was the workhorse of particle transfer for nearly a decade, the sudden changes in the concavity and depth of the voltage well at intermediate stages were observed to cause particle losses during the shuttling of large ($N_{\overline{\mathrm{p}}} > 2 \times 10^5$) $\overline{\mathrm{p}}$ plasmas throughout the trap. For a typical $\overline{\mathrm{p}}$ plasma with $N_{\overline{\mathrm{p}}} = 10^6$, between $30 - 40\%$ did not survive a move from the lower electrode stack to the center of the Ioffe trap. Additionally, the temperature of the surviving fraction was measured to be several thousands of Kelvin, highly elevated from an

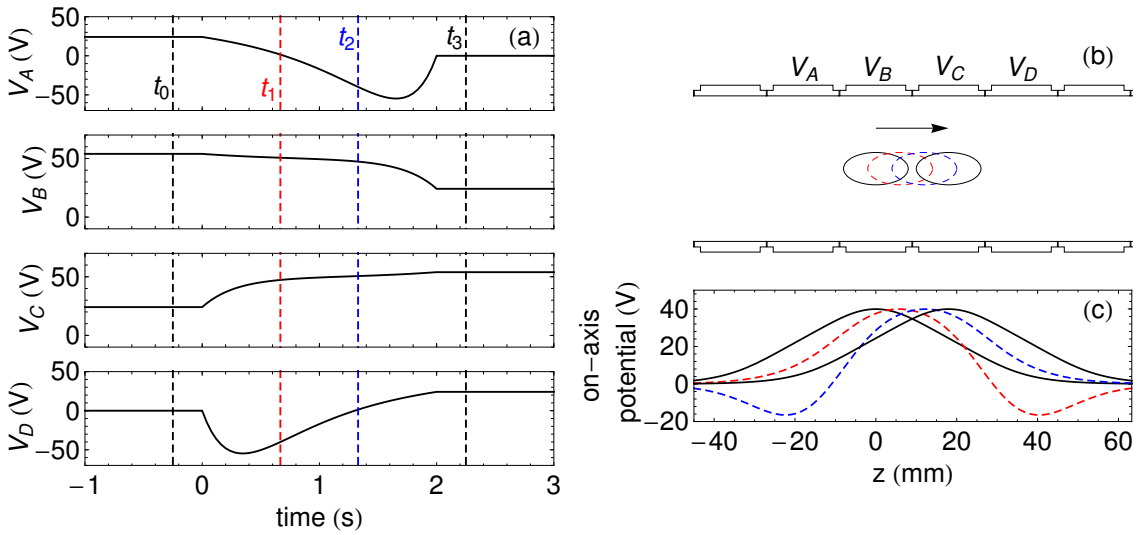

Figure 4.22: The improved particle transfer routine. (a) The voltages V_A, V_B, V_C, and V_D applied to four neighboring electrodes are shown as a function of time. All four electrode voltages are manipulated during the transfer. (b) The plasma position in the electrode stack, and (c) the on-axis potential are shown at the times t_0, t_1, t_2, and t_3 during the move.

initial temperature of ≈ 30 K.

For these reasons, an improved transfer method was developed to forfend particle losses and limit transfer-induced heating. This new method, inspired by ion-shuttling routines developed for planar Paul traps [138, 139], manipulates voltages so as to maintain the shape of the confining well during the transfer. In our implementation, independent voltages applied to four neighboring electrodes provide the four degrees of freedom necessary to keep the potential well offset and concavity constant, while keeping the linear and cubic terms equal to zero.

The voltages applied to the four electrodes as a function of time, in addition to the plasma positions and well shapes during the transfer, are shown in Fig. 4.22. A series of 50 steps, 40 ms each, smoothly translate the central position of the voltage well from one electrode to another. To solve for the voltages applied to each of the

four nearby electrodes at each step, we make use of the potential expansion derived in Chapter 2 (Eqn. 2.19). On-axis, the potential at any step may be written

$$\Phi(z) = V_A\phi_A(z) + V_B\phi_B(z) + V_C\phi_C(z) + V_D\phi_D(z) \tag{4.5}$$

where the V_i are the voltages applied to each of the electrodes. The individual electrode potentials $\phi_i(z)$ are given by

$$\phi_i(z) = \sum_{n=0}^{\infty} \frac{2}{k_n L} \frac{\sin(k_n z_i)}{I_0(k_n \rho_0)} \cos\left[k_n(z - z_c^i)\right] \tag{4.6}$$

where z_i and z_c^i are the axial half-length and center position of the i^{th} electrode, respectively, and $k_n = (n + 1/2)\pi/L$ as before.

To good approximation, the shape of the well will be maintained throughout the transfer if the voltage offset V_0 and the harmonic coefficient C_2 remain fixed, and the asymmetric linear C_1 and cubic C_3 coefficients are held at zero. Since the on-axis potential (Eqn. 4.5) at each step may be Taylor-expanded

$$\Phi(z) = \Phi(0) + \Phi'(0)z + \Phi''(0)\frac{z^2}{2!} + \Phi'''(0)\frac{z^3}{3!} + \dots \tag{4.7}$$

we may readily compare the potential term-by-term to the desired form

$$\Phi(z) = V_0 + (0)z + C_2 z^2 + (0)z^3 + \dots \tag{4.8}$$

to write four equations and solve for the four unknowns V_A, V_B, V_C, and V_D.

Implementation of the improved routine successfully transfers our $N_{\overline{\text{p}}} = 10^6$ $\overline{\text{p}}$ plasmas throughout the trap with no losses. For the first time, plasmas with $N_{\overline{\text{p}}} = 5 \times 10^6$ may be moved and manipulated, with losses of only $\approx 2\%$ observed. Additionally, the measured $\overline{\text{p}}$ temperature after the transfer to the upper electrode stack was measured

to be only 200 K (rather than thousands of Kelvin as with the previous method). After allowing a short time for the few embedded e^- within the $\overline{p}$ plasma to reduce the temperature to $\approx$ 30 K, a stable, sizable $\overline{p}$ plasma is ready to participate in $\overline{H}$ formation.

4.6 Antihydrogen Production

4.6.1 Antihydrogen Formation Processes

Following the initial creation of cold $\overline{H}$ atoms [3, 4, 5], nearly 10 years of refinements and improvements have made the production of $\overline{H}$ routine. To synthesize $\overline{H}$, an initially free $\overline{p}$ and e^+ must bind together, and a third body must carry away the excess energy and momentum. Here we discuss proposals in which the role of the third body is played by a photon (radiative recombination) [140], an e^- stripped from Rydberg positronium (charge exchange) [49], and a second nearby e^+ (three-body recombination) [141].

Radiative recombination proceeds by the reaction

$$\overline{p} + e^+ \rightarrow \overline{H}(n) + \gamma \tag{4.9}$$

where $\overline{H}$ (n) refers to an atom formed in a state with principal quantum number n, and the photon γ is needed to conserve energy and momentum. Similarly to Eqn. 3.26, the radiative recombination rate per $\overline{p}$ may be written

$$\nu_{rr} = n_e \sigma_{rr} v_e \tag{4.10}$$

where n_e and v_e are the e^+ density and velocity, respectively. The total recombination

cross section σ_{rr} is defined by

$$\sigma_{rr} = \sum_{n=1}^{\infty} \sigma_{rr}^{(n)} \tag{4.11}$$

with $\sigma_{rr}^{(n)}$ the cross section for recombination into a particular n state [140],

$$\sigma_{rr}^{(n)} = \left(8.38 \times 10^{-12}\right) \frac{1}{T^2} \frac{1}{n^3} \int_0^{\infty} \frac{\exp\left[-\frac{157890}{Tn^2}u\right]}{1+u} du \text{ cm}^2 \tag{4.12}$$

and T the e^+ temperature in Kelvin.

During $\overline{\text{H}}$ formation in the quadrupole Ioffe trap, the total recombination rate per $\overline{\text{p}}$ would be $\nu_{rr} = 6 \times 10^{-4}$ s^{-1} for typical e^+ densities and temperatures of 1×10^7 cm^{-3} and 4 K (respectively), with the low n states populated preferentially. Though finite, the radiative recombination rate has proven too small to be observed directly for $\overline{\text{H}}$. Any atoms formed through radiative recombination apparently disappear when compared with the large $\overline{\text{H}}$ signal caused by simultaneously-occuring three-body recombination [142]. Though a method to enhance the radiative recombination rate via stimulated emission has been proposed [143], experiments have not yielded observable $\overline{\text{H}}$ production with this technique [144].

Double charge-exchange production of $\overline{\text{H}}$ proceeds by the reaction

$$\text{Cs} + h\nu \rightarrow \text{Cs}^* \tag{4.13}$$

$$\text{Cs}^* + \text{e}^+ \rightarrow \text{Ps}^* + \text{Cs}^+ \tag{4.14}$$

$$\text{Ps}^* + \overline{\text{p}} \rightarrow \overline{\text{H}} + \text{e}^- \tag{4.15}$$

Efforts to produce $\overline{\text{H}}$ with this method realized initial success in 2004 [51], followed by a factor of 200 improvement in the number created in 2010 [66]. After cesium atoms emitted from an oven are excited to Rydberg states by application of 852 nm and 511 nm laser light, they pass through and charge-exchange with a e^+ plasma.

The positronium production cross section is proportional to the principal quantum number n_{Cs}^4, motivating the Rydberg excitation of Cs. A second charge-exchange between Rydberg positronium and a $\overline{\mathrm{p}}$ plasma (with a cross section $\propto n_{\mathrm{Ps}}^4$) forms Rydberg $\overline{\mathrm{H}}$ with a binding energy similar to that of the original Cs* atom. The total $\overline{\mathrm{H}}$ production cross section for double charge-exchange has been calculated in zero magnetic field [49], with recent simulations predicting only a small magnetic-field dependence [145].

Experimentally, the production rate per $\overline{\mathrm{p}}$ in the BTRAP apparatus was measured to be 6×10^{-7} s^{-1} when 5×10^6 $\overline{\mathrm{p}}$ and 3×10^8 e$^+$ were used. In total, 3600 atoms were detected during 20 minutes of Rydberg Cs excitation and $\overline{\mathrm{H}}$ formation. Though this observation represents a sizable increase compared with previous results, further improvements will be required for the charge-exchange method to yield similar production numbers as three-body recombination.

The third body in three-body recombination (TBR) is a second e$^+$ in the vicinity of the recombining $\overline{\mathrm{p}}$ and e$^+$, with $\overline{\mathrm{H}}$ formation described by the process

$$\overline{\mathrm{p}} + \mathrm{e}^+ + \mathrm{e}^+ \rightarrow \overline{\mathrm{H}} + \mathrm{e}^+ \tag{4.16}$$

The recombination rate per $\overline{\mathrm{p}}$ is given by

$$\nu_{tbr} = (n_e \sigma_{tbr} v_e) \left(\frac{4}{3} \pi b_{min}^3 n_e \right) \tag{4.17}$$

where $b_{min} = q^2/(4\pi\epsilon_0 k_B T)$ is the minimum distance of closest approach first introduced in Eqn. 3.27. Eqn. 4.17 may be understood as the classical collision rate of a $\overline{\mathrm{p}}$ within a e$^+$ plasma multiplied by the probability that a second e$^+$ is nearby. Since $\sigma_{tbr} \propto b_{min}^2$, we may write

$$\nu_{tbr} = C n_e^2 b_{min}^5 v_e \tag{4.18}$$

where C is a constant. Since $b_{min} \propto T^{-1}$ and $v_e \propto T^{1/2}$, Eqn. 4.18 scales as $n_e^2 T^{-9/2}$.

The value of the constant C appearing in Eqn. 4.18 has been calculated for several different values of magnetic field. In the zero-field limit, C was found to be of order unity [146, 147], while a different calculation found $C \approx 0.07$ as $|\vec{B}| \to \infty$ [148]. More recently, C has been calculated in an intermediate regime, giving $C \approx 0.11$ for 4 K e^+ in a 3 T magnetic field.

On account of the $T^{-9/2}$ dependence, the TBR rate dominates over all other $\overline{\mathrm{H}}$ formation mechanisms at low temperature. Taking $C = 0.11$ and using typical e^+ densities and temperatures of 1×10^7 cm^{-3} and 4 K (respectively), the calculated production rate per $\overline{\mathrm{p}}$, $\nu_{tbr} = 1.1 \times 10^2$ s^{-1}, dwarfs the radiative recombination rate by over 5 orders of magnitude. Starting with the initial creation of cold $\overline{\mathrm{H}}$ atoms in 2002, TBR has overwhelmingly produced more $\overline{\mathrm{H}}$ than any other method.

4.6.2 Antiproton-Positron Mixing

Because $\overline{\mathrm{p}}$ and e^+ carry opposite charges, they cannot be confined together in the same potential well. Instead, a nested well potential structure [141] holds the two species in close proximity to each other until some external manipulation forces the $\overline{\mathrm{p}}$ and e^+ to interact. Typically, $\overline{\mathrm{p}}$ are made to pass through a high-density e^+ plasma located at the center of the nested well to benefit from the n_e^2 scaling of the TBR rate. $\overline{\mathrm{H}}$ atoms are then formed with a temperature dominated by the temperature of the recombining $\overline{\mathrm{p}}$, since $m_{\overline{\mathrm{p}}} \gg m_e$. Three variations of this technique, represented graphically in Fig. 4.23, have successfully produced large numbers of $\overline{\mathrm{H}}$ atoms.

In the simplest scheme (Fig. 4.23b), $\overline{\mathrm{p}}$ are pulsed into the nested well with an en-

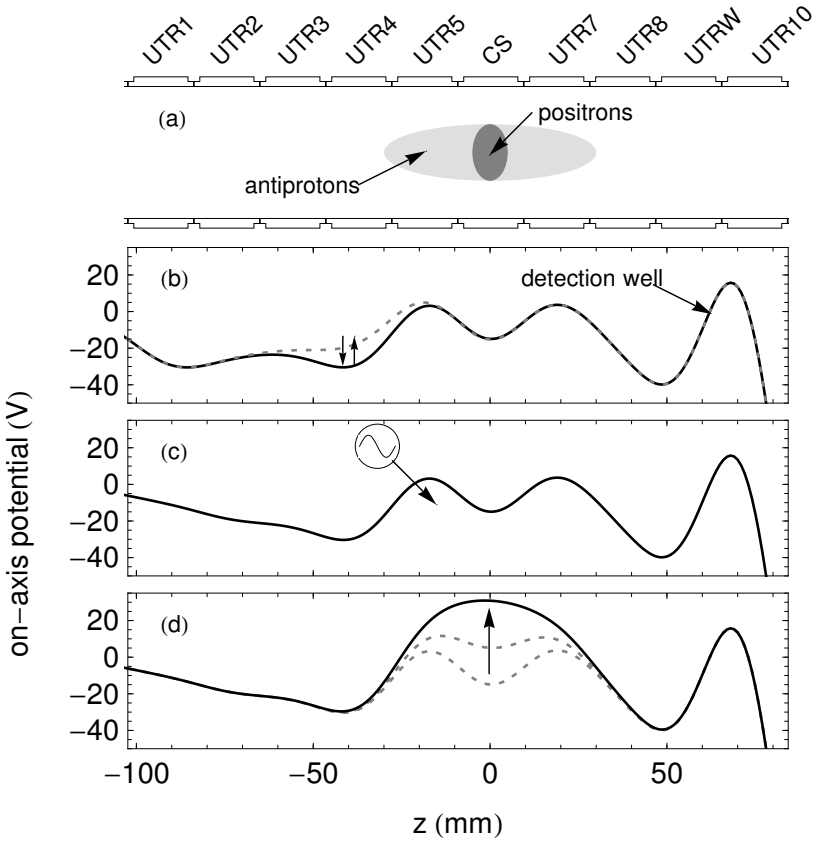

Figure 4.23: Trap potentials utilized for three different methods to form $\overline{\mathrm{H}}$ in a nested well via TBR. (a) e^+ are located at the center of the nested well, and $\overline{p}$ are made to pass through the e^+ plasma. (b) $\overline{p}$ initially confined on electrode UTR3 enter the nested well when a blocking potential is quickly pulsed down (dashed) and restored (solid) and interact with e^+ until cooling into the sides of the nested well. (c) $\overline{p}$ initially confined on electrode UTR5 are excited by an rf drive until their thermal energy takes them into the e^+ plasma. (d) The original nested well structure (dashed) is inverted (solid), allowing $\overline{p}$ to mix with e^+ when they have just enough energy to pass the central barrier.

ergy significantly above the central nested well barrier. After multiple passes through the e^+ cloud, a $\overline{p}$ may either form $\overline{H}$ by TBR or be collisionally-cooled by the e^+ [46] into one of the side wells on electrodes UTR5 and UTR7. Though $\overline{H}$ atoms are produced prolifically by this method, they are formed with very high temperatures due to the several-eV incoming $\overline{p}$ energies.

Fig. 4.23c shows a variation of the nested well technique in which the $\overline{p}$ energies are excited by an rf drive, allowing them to climb the central barrier and interact with the e^+. Drives in which the rf frequency is fixed [4], chirped downwards [149], or broadened by noise [62] have all yielded copious numbers of $\overline{H}$ atoms. Since the drive parameters can be precisely tuned, the $\overline{p}$ can be made to enter the e^+ plasma with only small amounts of kinetic energy, forming much colder $\overline{H}$ atoms compared to the pulse-in scheme described above.

The final often-used procedure to form $\overline{H}$ is to reduce the depth of the e^+ well, as in Fig. 4.23d. As the central barrier height is reduced, collisions between $\overline{p}$ in the side wells (UTR5 and UTR7) allow some $\overline{p}$ to gain energy and interact with the e^+. Completely inverting the e^+ potential ensures that all $\overline{p}$ have the opportunity to cross the center of the nested well. As with the rf drive method, $\overline{p}$ can be made to mix with e^+ at low energies to form cold $\overline{H}$ atoms.

4.6.3 Detection of Antihydrogen

For each of the three mixing methods described above, detection of $\overline{H}$ atoms is accomplished via field ionization [3]. As shown in Fig. 4.23, $\overline{H}$ atoms traveling in the $+\hat{z}$ direction encounter a strong electric field. An $\overline{H}$ atom will be ionized if

its principal quantum number $n \gtrsim 40$, (common for atoms formed through TBR), and the constituent $\overline{\mathrm{p}}$ will be recaptured in the detection well. The number of $\overline{\mathrm{p}}$ collected in the detection well may then be annihilation counted to gauge the number of $\overline{\mathrm{H}}$ produced. Note that bare $\overline{\mathrm{p}}$ cannot travel from the nested well region to the detection well on account of the large blocking potential on electrodes UTR8 and UTRW.

One deficiency of field-ionization detection is its insensitivity to cold, trappable $\overline{\mathrm{H}}$ atoms. Cold atoms are likely to have comparable axial and radial kinetic energies, and are thus unlikely to reach the detection well before annihilating upon the trap electrodes. An experiment to measure the velocity of $\overline{\mathrm{H}}$ atoms reaching the detection well confirmed this effect, finding an $\overline{\mathrm{H}}$ velocity ≈ 20 times larger than the average thermal speed of the $\overline{\mathrm{p}}$ within the nested well [48]. Unfortunately, no method for detecting the coldest atoms has been proposed or implemented, apart from looking for signals of trapped $\overline{\mathrm{H}}$.

4.6.4 Trappable Antihydrogen

Trapping even a small fraction of the $\overline{\mathrm{H}}$ produced within a minimum-$|\vec{B}|$ Ioffe trap is a formidable challenge. Trappable $\overline{\mathrm{H}}$ atoms must have an energy (in temperature units) lower than the 375 mK Ioffe trap depth if they are to remain confined. We shall see in Chapter 6 that the lowest recorded $\overline{\mathrm{p}}$ temperature in our trap is 3.5 K; if $\overline{\mathrm{H}}$ atoms are formed with a thermal distribution at this temperature, only 2.5% will have $T < 375$ mK. As the $\overline{\mathrm{H}}$ temperature increases, the trappable fraction decreases even further as $T^{-3/2}$. The situation is nevertheless not entirely bleak, on account of

the larger magnetic moments and magnetic trap depths for high-n Rydberg $\overline{\mathrm{H}}$. This effect, coupled with an identified decay-induced cooling mechanism [150], leads to the prediction that nearly 25% of $\overline{\mathrm{H}}$ starting with $n \approx 40$ and $T = 10$ K will remain confined in their ground state in a 400 mK Ioffe trap, assuming they are formed with zero radial velocity and the correct spin state.

Both the axial and radial velocities must be considered when determining the $\overline{\mathrm{H}}$ temperature. During the TBR process, a $\overline{\mathrm{p}}$ must enter a rotating e^+ plasma, and it acquires a larger rotational velocity as a result of the higher e^+ density. If the $\overline{\mathrm{p}}$ rotational velocity exceeds 80 m/s, any $\overline{\mathrm{H}}$ formed will have a temperature greater than 375 mK and may only be trapped if subsequent collisions with nearby e^+ reduce the $\overline{\mathrm{H}}$ energy. For a typical e^+ plasma of density 1×10^7 cm^{-3}, we may use Eqn. 3.13 to find that only $\overline{\mathrm{p}}$ with $\rho < 1.8$ mm can form $\overline{\mathrm{H}}$ with a rotational velocity of less than 80 m/s. Since the radius of the $\overline{\mathrm{p}}$ plasma is ≈ 4 mm, much of the $\overline{\mathrm{H}}$ formed will be untrappable unless collisions can carry away the excess energy.

Finally, a requirement for confining $\overline{\mathrm{H}}$ in a minimum-$|\vec{B}|$ trap is that the atoms be low-field seekers. Naïvely, one may expect that 50% of $\overline{\mathrm{H}}$ atoms should occupy low-field seeking states. Yet, in the strong magnetic field of the Penning-Ioffe trap, significantly fewer than 50% of $\overline{\mathrm{H}}$ formed are trappable. Before recombination, the magnetic moments of the $\overline{\mathrm{p}}$ and e^+ preferentially point along the magnetic field direction, and the two particles maintain this orientation when forming very weakly-bound $\overline{\mathrm{H}}$. However, as described in Sec. 2.2.1, the e^+ magnetic moment must be anti-aligned with the magnetic field to create a low-field seeking $\overline{\mathrm{H}}$ atom. Consequently, the majority of $\overline{\mathrm{H}}$ formed in a Penning-Ioffe trap are high-field seekers.

Simulations of TBR in a 1 T magnetic field have predicted that $16 - 31\%$ of $\overline{\mathrm{H}}$ will be produced in low-field seeking states [145, 151]. The low-field seeking fraction was shown in Ref. [151] to depend upon the binding energy of the $\overline{\mathrm{H}}$, with more deeply bound states increasingly likely to be low-field seekers. Additionally, low-field seeking $\overline{\mathrm{H}}$ atoms must not undergo a spin flip if they are to remain trapped during their radiative decay to the ground state. However, atoms tend to be driven to large-m circular Rydberg states during the cascade [152], indicating that only those $\overline{\mathrm{H}}$ for which $m \approx 0$ are highly susceptible to ejection from the trap during decay.

Surmounting these difficulties to create trappable $\overline{\mathrm{H}}$ requires careful control of the $\overline{\mathrm{p}}$ and e^+ plasma number, geometry, and temperature. In this chapter, we have already seen the methods by which up to 10^7 $\overline{\mathrm{p}}$ and 4×10^9 e^+ may be accumulated. In the following two chapters, we report two additional observations towards this end: centrifugal separation between $\overline{\mathrm{p}}$ and e^-, indicating the necessary control and characterization of our plasma geometries, and adiabatic cooling of $\overline{\mathrm{p}}$ to 3.5 K, demonstrating full command over our plasma temperatures.

Chapter 5

Centrifugal Separation of Antiprotons and Electrons

Centrifugal separation has been applied in a wide range of contexts, from extracting nuclei and mitochondria from cells to uranium enrichment. Particles with mass m within a fluid rotated at angular frequency ω_r experience a centrifugal force $F = m\omega_r^2\rho$, with ρ the radial distance from the rotation axis. In a multi-component fluid, heavier particles will diffuse to larger radii, since the centrifugal force increases for larger masses.

Similarly, the particles in a rotating, multi-species plasma may also centrifugally separate [153]. Centrifugal separation has been observed in several experiments using plasmas that can be laser cooled (to enhance the separation effect) and optically imaged (to detect the distributions of the different species). The original demonstration used Hg^+ ions confined in a Penning trap and sympathetically cooled by Be^+ [154]. Later experiments successfully measured complete separation in two-component plas-

mas of Be^+– Mg^+ [155] and Be^+– Cd^+ ions [156]. Additionally, separation has been observed in Be^+– e^+ plasmas [157], for which the mass of the two species differs by a factor of $\approx 10^4$.

In this chapter, we describe the first observation of centrifugal separation in a $\overline{p}$ – e^- plasma [158]. Despite the fact that neither $\overline{p}$ nor e^- can be laser cooled, the plasma densities and temperatures may be controlled well enough to allow the separation to occur. Even though neither $\overline{p}$ nor e^- can be optically imaged, we detect the separation using two complimentary methods - reduction of either the confining electric or magnetic field within the Penning trap. We begin with an introduction to the theory detailing the relevant temperature and length scales and the equilibrium density distribution. We then discuss the experimental setup, procedure, and results for our two independent observation techniques. Our demonstration serves as an example of the newfound control and characterization of the plasma geometry recently afforded to us by the rotating wall, trap fields, and plasma mode measurements.

5.1 Temperature and Length Scales for Centrifugal Separation

As introduced in the previous chapter, the collisional e^- cooling of $\overline{p}$ is the only method to cool $\overline{p}$ to cryogenic temperatures [43]. It has enabled the trapping of a single $\overline{p}$ (for the best measurement of the p-$\overline{p}$ mass ratio [23]) and up to 10^7 $\overline{p}$ for $\overline{H}$ experiments, and it makes the production of slow $\overline{p}$ beams possible [159]. Knowledge of the $\overline{p}$ and e^+ distributions within the two-component plasma is crucial

for understanding the distribution and temperature of the $\overline{\mathrm{p}}$ after the e^- are ejected (Sec. 4.3.4) and may inform a new method to produce a controlled mixture of $\overline{\mathrm{p}}$ and e^-.

Though the $\overline{\mathrm{p}}$ – e^- system is used in a variety of circumstances, centrifugal separation had not been observed until ATRAP's recent demonstration. We find clear signatures of separation when using the typical plasma parameters ($N_e = 10^8$, $n_e \approx 10^8$ cm^{-3}, $N_{\overline{\mathrm{p}}} = 10^6$) and magnetic fields (3.7 T down to 1 T) implemented during the e^- cooling of $\overline{\mathrm{p}}$. The first e^- cooling studies [43, 132] would not have been sensitive to separation on account of much smaller electron numbers and densities, combined with a larger magnetic field. Another group with N_e and n_e similar to the ATRAP values initially failed to see centrifugal separation of $\overline{\mathrm{p}}$ and e^- [133], though a recent report shows evidence of the effect in their experiments as well [160].

As the $\overline{\mathrm{p}}$ – e^- plasma rotates, there arises a centrifugal energy difference ΔE proportional to the difference in $\overline{\mathrm{p}}$ and e^- masses

$$\Delta E = \frac{1}{2}(m_{\overline{\mathrm{p}}} - m_e)\omega_r^2 \rho^2 \tag{5.1}$$

where ρ is the plasma radius. At high temperatures, the $\overline{\mathrm{p}}$ may have a thermal energy large compared to ΔE, in which case centrifugal separation is a weak effect. At low temperatures, however, the centrifugal energy barrier causes the separation to become more pronounced. Equating the centrifugal and thermal energies and approximating $m_{\overline{\mathrm{p}}} \gg m_e$ allows us to determine a characteristic separation temperature

$$T_{\mathrm{sep}} = \frac{m_{\overline{\mathrm{p}}} q^2}{8\epsilon_0^2 k_B}\left(\frac{n_0 \rho}{B_0}\right)^2 \tag{5.2}$$

where we have used Eqn. 3.13 along with the good approximation $\omega_c \gg \omega_r$ to write $\omega_r \approx q n_0/(2\epsilon_0 B_0)$. It is important to note that while T_{sep} parameterizes the separation

temperature, there is no sharp phase transition; the strength of the effect increases steadily as T is decreased through $T_{\rm sep}$.

For the plasmas in this study with radial extent from 4 to 8 mm and $B_0 = 3.7$ T, $T_{\rm sep}$ ranges from 50 to 100 K. Observation of centrifugal separation thus suggests that the plasma temperature within the 1.2 K electrode stack is below $T_{\rm sep}$, consistent with both intuition and the directly measured $\overline{\rm p}$ temperatures presented in Chapter 6. For the typical parameters in early e^- cooling studies (e.g. Ref. [43]), $T_{\rm sep}$ is calculated to be approximately 1 K [132], so it is not surprising that separation was not observed in their 4.2 K apparatus.

By comparing the centrifugal and thermal energies, we may similarly extract a class of scale lengths $\ell_{\overline{\rm p}e}(\rho)$ to describe the separation [153]

$$\frac{1}{\ell_{\overline{\rm p}e}(\rho)} = \frac{d}{d\rho}\left[\frac{1}{2}\left(m_{\overline{\rm p}} - m_e\right)\frac{\omega_r^2\rho^2}{k_B T}\right] \tag{5.3}$$

Centrifugal separation becomes salient when the scale length is smaller than the plasma radius, $\ell_{\overline{\rm p}e}(\rho_p) < \rho_p$. For our typical parameters, the scale length $\ell_{\overline{\rm p}e}(\rho_p)$ is less than 1 mm, which again predicts that separation should be observable in our 4-8 mm radius plasmas. Complete separation, in which the two species are separated by a radial gap, requires $\ell_{\overline{\rm p}e}(\rho_p)$ to be less than the Debye length. This condition is not satisfied for our plasmas, for which $\lambda_D \approx 10 - 100$ μm.

5.2 Density Distribution for Multi-Species Plasmas

We wish to gain an understanding of the equilibrium distribution of the two-component plasma as a function of temperature. The simple case of a multi-species

plasma occupying an infinitely long column has been treated analytically [153, 161], but no exact treatment of spheroidal geometries exists. Numerical methods also exhibit difficulties, with convergence failures caused by the large mass difference between $\overline{\mathrm{p}}$ and e^- [162]. Consequently, we make use of the approximation that the two-component plasma is dominated by a single species (the e^-), with only a trace admixture of the second (the $\overline{\mathrm{p}}$). This approximation is justified by the $100:1$ ratio of N_e to $N_{\overline{\mathrm{p}}}$ as well as measurements which show that the e^- geometry is unchanged (to within our measurement uncertainty) when the 10^6 $\overline{\mathrm{p}}$ are added.

We start by rewriting the density for a single-component e^- plasma (Eqn. 3.10) in the form

$$n_e(\rho,z) = n_0 \exp\left[-\frac{q\phi_e(\rho,z) + \frac{1}{2}m_e\omega_r(\omega_c^{(e)} - \omega_r)\rho^2}{k_B T}\right] \tag{5.4}$$

where $\phi_e(\rho,z)$ is the total potential due to the applied fields and the self-potential of the e^- plasma, and $\omega_c^{(e)}$ is the e^- cyclotron frequency. If we approximate that the $\overline{\mathrm{p}}$ act as only a small perturbation to the total potential $\phi_e(\rho,z)$, we may similarly write for the $\overline{\mathrm{p}}$ density

$$n_{\overline{\mathrm{p}}}(\rho,z) = n_0^{(\overline{\mathrm{p}})} \exp\left[-\frac{q\phi_e(\rho,z) + \frac{1}{2}m_{\overline{\mathrm{p}}}\omega_r(\omega_c^{(\overline{\mathrm{p}})} - \omega_r)\rho^2}{k_B T}\right] \tag{5.5}$$

where $n_0^{(\overline{\mathrm{p}})}$ is the $\overline{\mathrm{p}}$ central density and $\omega_c^{(\overline{\mathrm{p}})}$ is the $\overline{\mathrm{p}}$ cyclotron frequency. Though the central $\overline{\mathrm{p}}$ density may not be known initially, it may be calculated by integrating the exponential in Eqn. 5.5 over all space and choosing $n_0^{(\overline{\mathrm{p}})}$ to yield the correct $N_{\overline{\mathrm{p}}}$.

For each species i, the cyclotron frequency $\omega_c^i = qB_0/m_i$ may be substituted into Eqns. 5.4-5.5 to give

$$n_i(\rho,z) = n_0^i \exp\left[-\frac{q\phi_e(\rho,z) + \frac{1}{2}qB_0\omega_r\rho^2 - \frac{1}{2}m_i\omega_r^2\rho^2}{k_B T}\right] \tag{5.6}$$

Three terms are present in the numerator of the exponential in Eqn. 5.6: the electric potential, the potential induced by rotation through the magnetic field B_0, and the centrifugal potential. For the two species, Eqn. 5.6 differs only in the central density and the centrifugal term, allowing us to succinctly write $n_{\overline{\mathrm{p}}}$ in terms of n_e

$$n_{\overline{\mathrm{p}}}(\rho, z) = \frac{n_0^{(\overline{\mathrm{p}})}}{n_0} n_e(\rho, z) e^{\Delta E/(k_B T)} \tag{5.7}$$

where we have substituted the centrifugal energy barrier ΔE from Eqn. 5.1.

The behavior of the $\overline{\mathrm{p}}$ density distribution (Eqn. 5.7) may now be analyzed in the high- and low-temperature limits. When $k_B T \gg \Delta E$, the exponential in Eqn. 5.7 evaluates to ≈ 1. Thus, the $\overline{\mathrm{p}}$ distribution matches the e^- distribution (up to a normalization constant), and the two species are well-mixed within the plasma. For $k_B T \ll \Delta E$, the exponential in Eqn. 5.7 can no longer be ignored, and increases $\propto \exp(\rho^2)$. The $\overline{\mathrm{p}}$ density would then grow without bound if the exponential were not multiplied with the e^- density $n_e(\rho, z)$, which is roughly constant throughout the plasma and falls to zero within a few Debye lengths of the edge. The net result is a $\overline{\mathrm{p}}$ density that is exponentially small throughout the bulk of the plasma and sharply peaked at the outer boundary.

The e^- and $\overline{\mathrm{p}}$ density distributions at four different temperatures are shown in Fig. 5.1 for a typical $N_e = 10^8$, $N_{\overline{\mathrm{p}}} = 10^6$ plasma. In all cases, the e^- density drops quickly to zero at the plasma edge (6 mm radius), with an edge width governed by the Debye length ($\propto \sqrt{T}$). The $\overline{\mathrm{p}}$ density profile undergoes a smooth but dramatic change as the temperature is reduced through $T_{\mathrm{sep}} \approx 60$ K, strongly skewing to large radii for $T < T_{\mathrm{sep}}$. The high- and low-temperature distributions qualitatively described above are borne out in the $T = 1000$ K and $T = 4$ K curves of Fig. 5.1, for which T_{sep} is a

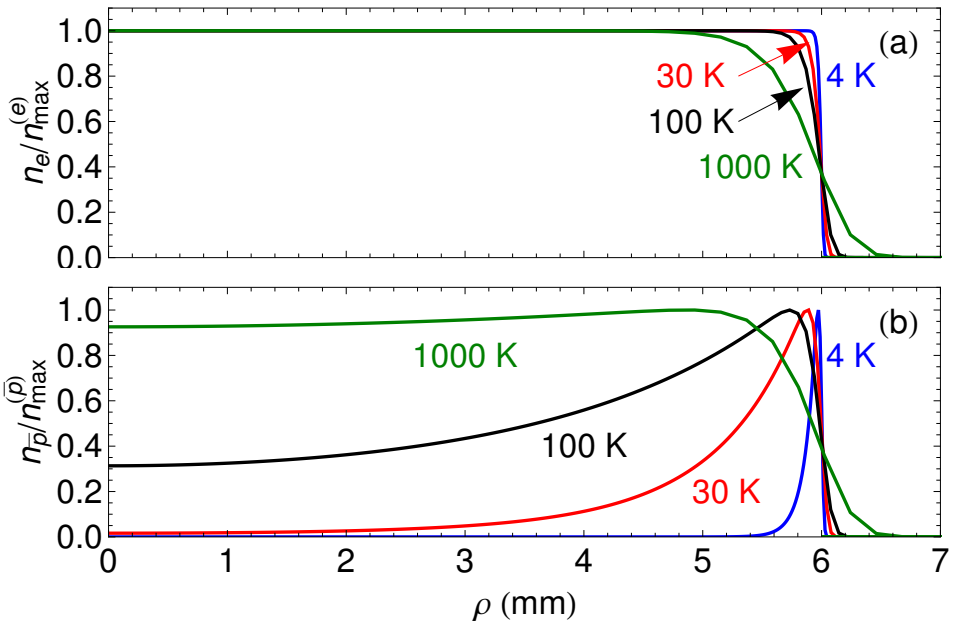

Figure 5.1: Normalized radial density for e^- and $\bar{p}$ in a multi-species plasma at various temperatures. (a) The e^- density is roughly constant until falling to 0 within a few Debye lengths, with a sharper edge at colder temperatures. (b) The $\bar{p}$ density profile roughly matches the e^- profile for $T = 1000$ K, but becomes strongly peaked at large radii as the temperature is decreased.

factor of ≈ 15 smaller and larger, respectively.

5.3 Demonstration by Axial Potential Reduction

Two independent methods demonstrate the centrifugal separation of $\bar{p}$ and e^-. In the first, we systematically remove a well-controlled fraction of the cooling e^- from the $\bar{p}$ – e^- plasma by reducing the axial confining potential. We observe a clear separation between the radially-centered e^-, which escape the trap first, and the radially-extended $\bar{p}$, which escape just before the well is inverted.

This method exploits the fact that the confining potential in an axially-symmetric Penning trap is smallest on-axis and increases with radius. Fig. 5.2 shows the plasma

geometries and potentials when 10^8 e^- and 10^6 $\overline{p}$ are held in a confining well on electrode LTE3. As the applied voltage is reduced, particles leak out preferentially from the axis; off-axis loss is exponentially suppressed due to the larger barrier heights. If the voltage well containing a centrifugally-separated, multi-species plasma is lowered, the lighter, radially-centered particles will be the first to escape.

To begin the demonstration, $N_e = 10^8$ e^- are loaded into an 80 eV well on electrode LTE3 using the methods described in Sec. 4.2. The on-axis potential is very nearly harmonic ($z_0 = 0.849\rho_0$, see Figs. 2.4 and 5.2a), so the confined e^- plasma is a spheroid to good approximation. The e^- are initially loaded at a radius between $6 - 9$ mm, with charge counting of the e^- number (Sec. 3.5.1) and a non-destructive measurement of the COM and quadrupole modes (Sec. 3.5.2) used to determine the e^- plasma geometry. A rotating wall drive (Sec. 3.6.2) compresses the plasma to 5 mm, giving a final density of 9×10^7 cm^{-3} and rotation frequency $\omega_r/(2\pi) = 34$ kHz.

With the e^- pre-loaded, 10^6 $\overline{p}$ are accumulated in 9 shots from the AD. Two minutes are allowed for equilibration between the e^- and $\overline{p}$, long enough for both collisional cooling (Sec. 4.3.1) and outward radial transport of $\overline{p}$ within the two-component plasma [99]. As will be shown in Chapter 6, the $\overline{p}$ – e^- plasma reaches an equilibrium temperature well below the calculated $T_{\rm sep} \approx 75$ K.

The voltage applied to electrode LTE3 may be reduced either non-adiabatically or adiabatically, and we have investigated both possibilities. Fig. 5.3 shows the result of reducing the axial potential in a series of non-adiabatic, 2 V steps separated by 1 s time delays. Particles ejected from the well are accelerated towards the degrader, where they are either charge-counted (for e^-) or annihilation-counted (for $\overline{p}$). The

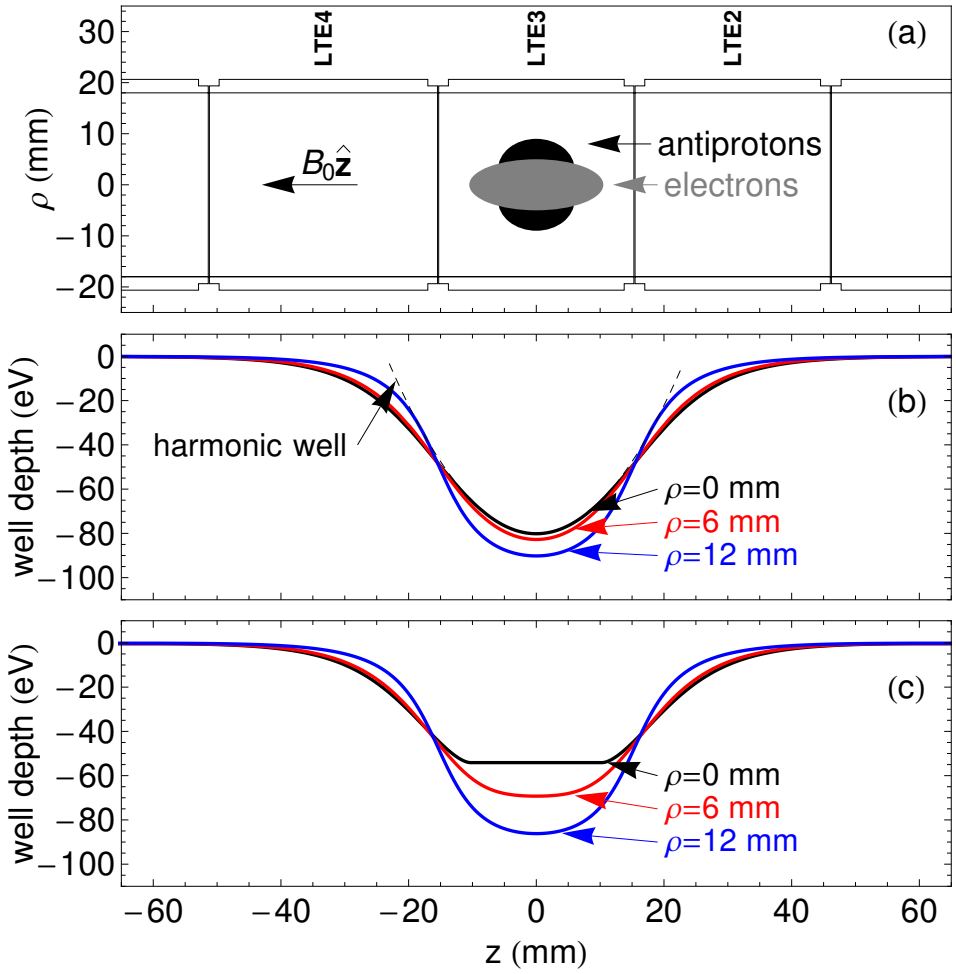

Figure 5.2: Plasma geometry and potential wells during the demonstration of centrifugal separation. (a) A $\rho = 5$ mm spheroidal e^- plasma is held within the axially symmetric trap electrodes. The centrifugally separated $\overline{p}$ have the indicated maximum radius, but their distribution along the $\hat{z}$ axis is unknown. (b) 100 V applied to electrode LTE3 creates a nearly-harmonic 80 eV well on-axis and deeper wells off-axis. (c) The distinction between shallower well depths on-axis and deeper well depths off-axis is accentuated when the total potential (including the e^- space charge) is considered. The $\rho = 0$ mm total potential is significantly flattened by the presence of the e^- plasma.

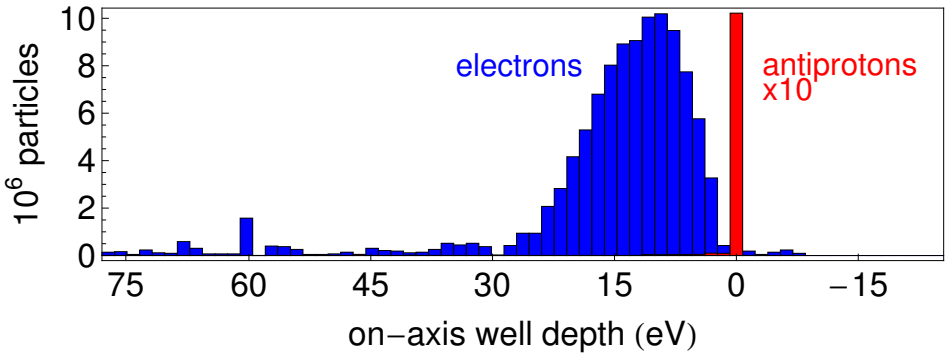

Figure 5.3: The number of $\overline{\mathrm{p}}$ and e^- escaping the trap each time the potential is reduced by non-adiabatic, 2 V steps. The majority of $\overline{\mathrm{p}}$ are ejected in the final step.

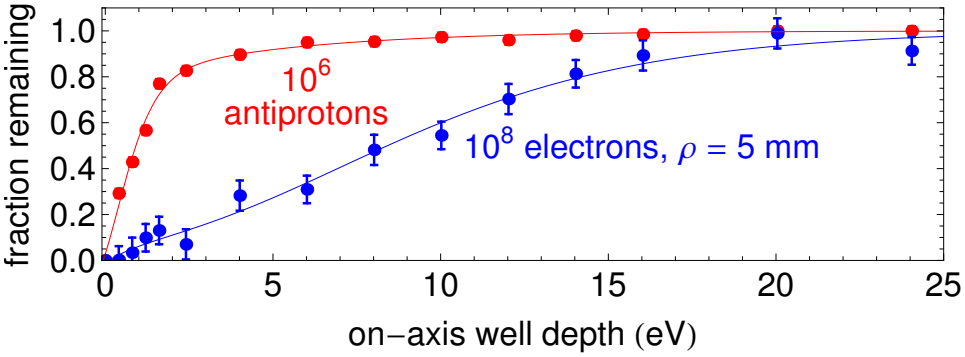

Figure 5.4: The fractions of $\overline{\mathrm{p}}$ and e^- remaining after the well depth is ramped adiabatically to the indicated value (with curves to guide the eye). The initial e^- plasma has a 5 mm radius in an 80 eV well.

e^- are first observed to escape when the on-axis well depth becomes shallower than $\approx$ 25 eV, while $\overline{\mathrm{p}}$ are not ejected until the well is nearly inverted. As expected, the centrifugally separated $\overline{\mathrm{p}}$ leave the trap after the e^-, since they are located in more deeply confining off-axis potential wells.

The e^- are similarly observed to escape first when the well depth is reduced adiabatically, as shown in Fig. 5.4. With the $\overline{\mathrm{p}}$ – e^- plasma initially in an 80 eV well, the on-axis well depth was smoothly ramped downwards to the various values

indicated in Fig. 5.4. When the desired value was reached, the remaining fraction of $\overline{\mathrm{p}}$ and e^- was measured using our usual charge- and annihilation-counting techniques. As before, most of the e^- have escaped from the trap before any substantial $\overline{\mathrm{p}}$ loss is seen, indicating a centrifugally separated plasma. The results were not observed to change when the time over which the ramp occurred was varied from 0.1 s to 10 s. Additionally, Fig. 5.4 suggests that it should be possible to produce a controlled mixture of $\overline{\mathrm{p}}$ and e^- by gently lowering the well depth to eject the desired number of e^-, then restoring the well to its initial value.

5.4 Demonstration by Magnetic Field Reduction

Confirmation of centrifugal separation comes when we implement a second measurement method sensitive to the radial distribution of the two-component plasma. In Sec. 5.3, the confining electric field was reduced, and the particles closest to the axis were the first to escape from the trap. In a complimentary technique, we reduce the radially confining magnetic field, causing the particles furthest from the axis to be lost first as they collide with the electrode walls.

For a spheroid with N particles and an outer radius ρ, the sum of the canonical angular momenta gives

$$\sum_{j=1}^{N} p_{\theta_j} \approx \sum_{j=1}^{N} \frac{q}{2} B_0 \rho_j^2 = \frac{1}{5} N q B_0 \rho^2 \tag{5.8}$$

Conservation of canonical angular momentum thus demands that the quantity $B_0\rho^2$ remains fixed. For a plasma prepared at radius ρ_i in a magnetic field B_0, its outer

radius ρ at magnetic field B changes according to

$$\rho = \rho_i \left(\frac{B_0}{B} \right)^{1/2} \tag{5.9}$$

Excellent agreement is found between the predictions of Eqn. 5.9 and measurements made within our trap (see Fig. 3.11).

With a plasma prepared at radius ρ_i in a $B_0 = 3.7$ T magnetic field, the field-boosting solenoid is ramped down to change $|\vec{B}|$ from 3.7 T to 1 T. If the outer radius of the plasma expands to $\rho = 18$ mm, the outermost particles will be removed through annihilations or collisions with the electrode walls. Knowledge of the magnetic field strength B at which the first particles are lost, the radius at which they are lost ($\rho = 18$ mm), and the initial field ($B_0 = 3.7$ T) allows for a determination of the initial plasma radius ρ_i by Eqn. 5.9.

To begin the measurement, $N_e = 10^8$ e^- are loaded into an 80 eV well on electrode LTE3. A rotating wall is used to compress their radius to between 4.8 and 7.8 mm, giving a final density of between 1.3×10^8 cm^{-3} and 4.7×10^7 cm^{-3} and rotation frequency between 52 and 18 kHz. As before, 10^6 $\overline{p}$ are captured and allowed to equilibrate with the e^- for 120 s before the field-boosting solenoid is de-energized.

Centrifugal separation is observed when most of the $\overline{p}$ and virtually none of the e^- are lost as the magnetic field is decreased to 1 T. Fig. 5.5 shows an example measurement that allows determination of an initial $\overline{p}$ radius ρ_i. The $\overline{p}$ annihilation rate counted by scintillating detectors is monitored as the magnetic field is reduced from its initial value. At $t \approx 220$ s in Fig. 5.5, corresponding to $B = 2.1$ T, a sudden increase in $\overline{p}$ loss indicates that the plasma has expanded into the electrode wall. Using Eqn. 5.9, we deduce that the starting $\overline{p}$ radius at $B_0 = 3.7$ T was 13.5 mm.

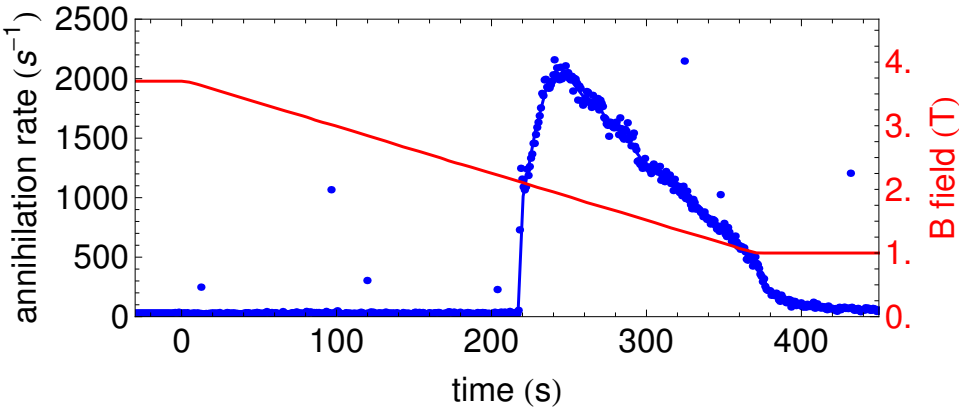

Figure 5.5: The $\overline{\mathrm{p}}$ annihilation count rate per second (blue) is monitored as the magnetic field is decreased from 3.7 T to 1 T (red). The sudden jump in the number of annihilations indicates that the $\overline{\mathrm{p}}$ plasma has expanded into the electrode wall at $\rho = 18$ mm.

Many such measurements of the initial $\overline{\mathrm{p}}$ radius were made as the e^- radius was varied from 4.8 to 7.8 mm. As shown in Fig. 5.6, the $\overline{\mathrm{p}}$ radius (determined by the method in Fig. 5.5) was found in all cases to be larger than the e^- radius (determined by plasma mode measurements). The deduced $\overline{\mathrm{p}}$ radial extent decreases when the e^- radius is more tightly compressed, suggesting that the two species are not decoupled from each other. Though the field-boosting solenoid inductance limits the magnetic field ramp rate to 7×10^{-3} T/s, the results shown do not change if the ramp is slowed by a factor of 2.

It is not surprising that e^- are not lost during this procedure. The largest e^- plasma studied has an initial radius of 7.8 mm, which expands to just over 15 mm (well short of the 18 mm electrode radius) as the magnetic field is reduced to 1 T. Similarly, no $\overline{\mathrm{p}}$ annihilations are observed for the smallest tested values of e^- radius, indicating an outer $\overline{\mathrm{p}}$ radius $\rho_i < 18/\sqrt{3.7} = 9.4$ mm.

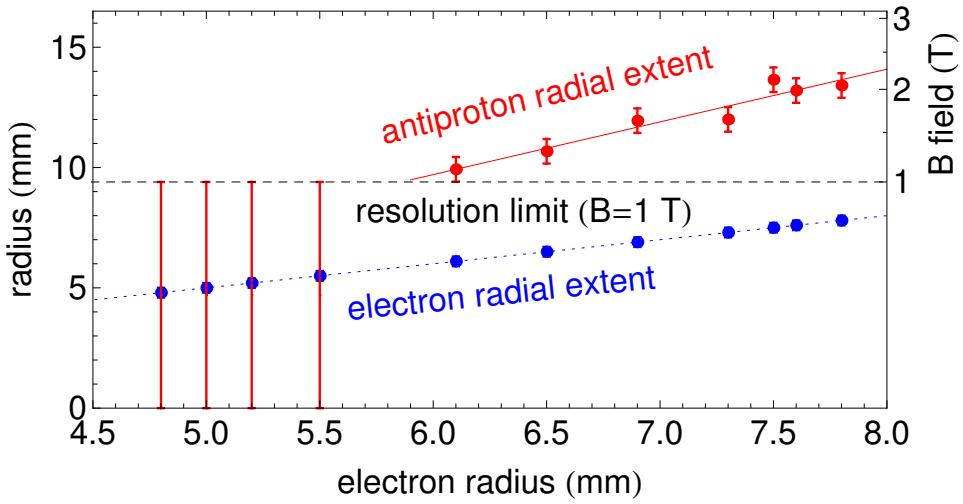

Figure 5.6: The outer $\overline{\mathrm{p}}$ plasma radius (red) at 3.7 T as a function of the e^- plasma radius, deduced by ramping B from 3.7 T to 1 T and observing the value at which $\overline{\mathrm{p}}$ annihilations begin. No annihilations were observed for the four measurements on the left, indicating a $\overline{\mathrm{p}}$ plasma radius smaller than 9.4 mm. The e^- plasma radius (blue) is included for comparison.

5.5 Summary and Discussion

Centrifugal separation of $\overline{\mathrm{p}}$ and e^- has been observed with two complimentary methods. This effect is crucial for understanding the $\overline{\mathrm{p}}$ plasma geometry and temperature before and after the e^- are pulsed out. In addition, our demonstration exhibits enhanced control over our plasma geometries and suggests a new method to prepare a carefully-controlled fraction of $\overline{\mathrm{p}}$ and e^- within a multi-species plasma.

The $\overline{\mathrm{p}}$ distribution after e^- ejection is important since the radii of the $\overline{\mathrm{p}}$ and e^+ plasmas should be well-matched to ensure efficient $\overline{\mathrm{H}}$ production. At high temperatures, when centrifugal separation is only a weak effect, the uniform mixture of $\overline{\mathrm{p}}$ throughout the two-component plasma leads to a constant radius before and after the e^- are pulsed out. For a centrifugally separated plasma, however, $\overline{\mathrm{p}}$ rearrange them-

selves through collisions to fill the vacant core left when the e^- are ejected. Since the mean square radius must remain fixed, the outer radius grows to $\rho = \sqrt{\frac{5}{4}(\rho_1^2 + \rho_2^2)}$, where ρ_1 and ρ_2 are the inner and outer radii of the $\overline{p}$ ring before e^- ejection.

The $\overline{p}$ temperature after e^- ejection is important since cold $\overline{p}$ are a requirement for synthesizing cold, trappable $\overline{H}$. The pulsed e^- removal should be more efficient in a centrifugally separated plasma since the e^- will avoid collisions with $\overline{p}$ and escape along the axis unimpeded. Fewer pulses, and hence less motional acceleration of $\overline{p}$, should be needed to eject the e^-.

The multi-species plasma temperature must be less than ≈ 50 K for centrifugal separation to be observed. After the e^- are pulsed out, however, the $\overline{p}$ temperature is measured to be several thousands of Kelvin. With the techniques necessary to prepare and measure a wide range of plasma geometries now demonstrated, we turn our attention towards reducing the temperature of our $\overline{p}$ plasmas from this several thousand Kelvin value to 3.5 K - the coldest value ever recorded.

Chapter 6

Embedded Electron and Adiabatic Cooling of Antiprotons

Cold $\overline{\mathrm{p}}$ are a crucial ingredient for creating $\overline{\mathrm{H}}$ cold enough to be confined in the sub-Kelvin Ioffe trap depths currently available. With no intrinsic cooling mechanism, $\overline{\mathrm{p}}$ can easily be heated to several hundreds or thousands of Kelvin by eV-scale manipulations of trap voltages and remain at these elevated temperatures indefinitely. Cooling $\overline{\mathrm{p}}$ back down to Kelvin-scale temperatures is thus a primary challenge and requirement for producing trappable $\overline{\mathrm{H}}$.

This chapter presents a two-step method to cool up to 3×10^6 $\overline{\mathrm{p}}$ to 3.5 K [163] - a factor of 10^3 more cold $\overline{\mathrm{p}}$ at a temperature 3 times lower than previously reported [164]. First, a small number of e^- embedded within the $\overline{\mathrm{p}}$ plasma collisionally cool the $\overline{\mathrm{p}}$ to 31 K. Next, the $\overline{\mathrm{p}}$ are cooled by adiabatic expansion when the confining electric potential is lowered and the plasma grows in volume. Temperatures as low as 3.5 K have been directly measured, with some $\overline{\mathrm{p}}$ perhaps as cold as 0.4 K.

In contrast to evaporative cooling methods [164], embedded e^- and adiabatic cooling are lossless processes. This is a significant advantage for rare particles such as $\overline{p}$, given the effort and accumulation time needed to collect up to 10^7 $\overline{p}$ for $\overline{H}$ experiments. If one is willing to tolerate large $\overline{p}$ losses, then temperatures colder than 3.5 K may be achieved by first performing embedded e^- cooling, followed by adiabatic cooling, then evaporative cooling.

We begin by describing the procedure through which the $\overline{p}$ plasma temperature is determined. Next, we demonstrate the effectiveness of embedded e^- cooling, wherein far fewer than the usual 10^8 e^- are used to cool large numbers of $\overline{p}$. Finally, we discuss the adiabatic cooling method, results, and implications for $\overline{H}$ experiments.

6.1 Plasma Temperature Measurements

In order for the efficacy of various cooling techniques to be evaluated, it is critical to have an accurate and robust method for determining the temperature of the $\overline{p}$ plasma. The initial observed rate of $\overline{p}$ escaping from a well as the well depth is reduced, together with a correction due to the finite plasma self-potential, allows for an accurate measurement of the $\overline{p}$ temperature down to 3.5 K. The method may in principle be applied to the measurement of e^+ temperatures, subject to some model-dependent limitations.

6.1.1 Measurement Procedure

We directly probe the temperature distribution of the $\overline{p}$ plasma by counting the number of $\overline{p}$ that escape over a potential barrier of known height. This technique has

been used in the past to measure temperatures of $\approx 10^4$ K in high aspect-ratio e^- plasmas [165]. We extend the method to the low-temperature, $\alpha \approx 1$ regime, with escaping $\overline{p}$ detected via their annihilation signals with 75% efficiency.

Implicit in our analysis is that the axial $\overline{p}$ energy E_z may be described by a Maxwell-Boltzmann distribution of the form

$$f_E(E_z)dE_z = \sqrt{\frac{1}{\pi E_z k_B T}} \exp\left(-\frac{E_z}{k_B T}\right) dE_z \tag{6.1}$$

The assumption of thermal equilibrium is well-justified, since the $1 - 100$ ms $\overline{p}$-$\overline{p}$ collision time for the parameters used in these experiments (see Sec. 3.4) is short compared with the several minute-long equilibration time. Additionally, the axial-cyclotron isotropization time of $3 - 160$ ms ensures that the two motions are in thermal equilibrium with each other, and the $\overline{p}$ plasma may be described by a single temperature.

In the simplest variation of the measurement technique, a plasma at temperature T could be confined in a potential well of depth W, with W several times larger than $k_B T$. Particles within the plasma could then escape by evaporation, at a loss rate given by [166]

$$\frac{dN_{ev}}{dt} = -N\nu_{ev} = -\frac{3Nk_B T\nu_c}{\sqrt{2}W} \exp\left(-\frac{W}{k_B T}\right) \tag{6.2}$$

where N is the total particle number, ν_{ev} is the single-particle evaporation rate, and ν_c is the inter-particle collision rate (Eqn. 3.30). Comparing the loss rates at different fixed values of W would then allow the plasma temperature T to be extracted.

Several technical reasons complicate such a measurement. First, it is important that W be large enough so that the evaporation rate (Eqn. 6.2) is slow, but small enough so that a loss signal may be observed above background. Large particle losses

are synonymous with evaporative cooling and would systematically skew temperature measurements lower. Second, since the evaporation rate must be slow, the measurement process may take as long as several minutes. Finally, trial-to-trial variations in the number of particles loaded (and hence the plasma self-potential) make it impossible to know *a priori* how to set W only a few k_BT above the total potential. In practice, one must start with W conservatively deep, then decrease W in steps of order $k_BT \approx 3$ meV while looking for particle losses - a tedious, time-intensive process.

The difficulties encountered in the above method can be avoided by continuously ramping the well depth W downwards until all particles are ejected from the well. Only the first $\approx 0.1\%$ of particles to escape are analyzed, a fraction small enough to ensure that the bulk spatial and thermal distribution has not been significantly altered. The measurement may be performed in an arbitrarily short time, subject only to the constraint that the particle loss rate should not be so large as to saturate the scintillating detectors. The initial well depth W need not be precisely determined, since it may be initially set well above k_BT before it is ramped downwards, with no adverse effects on the measurement.

A schematic of the measurement process is shown in Fig. 6.1. The plasma is confined in a potential well on electrode LTE2. In the absence of any particles, the well-depth is parameterized by W_0, which is controlled by applying a voltage to LTE2. When $\overline{\mathrm{p}}$ are added to the well, the plasma space charge decreases the well depth to W. By ramping the applied voltage on LTE2 downwards, the well-depths W_0 and W decrease until all particles are ejected.

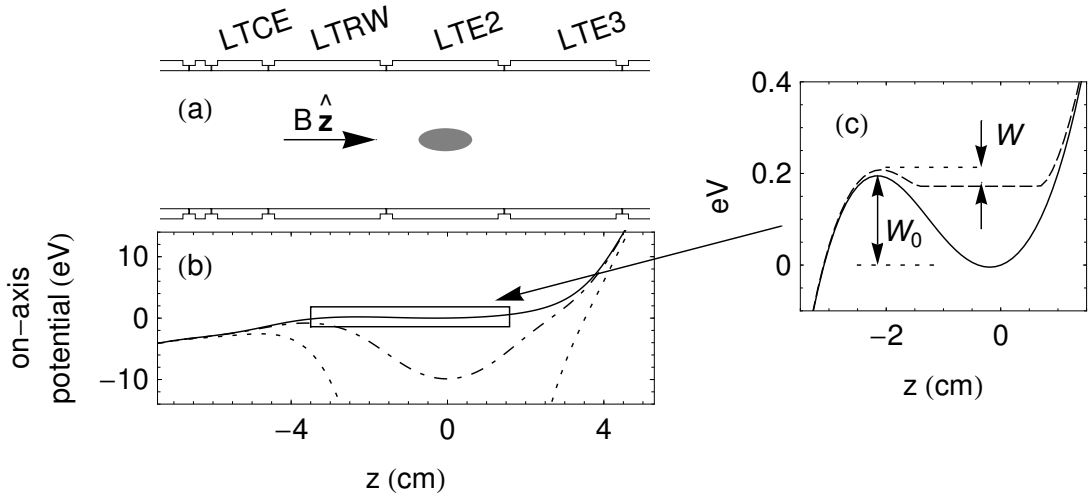

Figure 6.1: (a) Cross section of labeled trap electrodes with the location of the $\overline{\mathrm{p}}$ plasma. (b) On-axis potential energies for empty-well trap depths $W_0 = 0.2$ (solid), 9 (dash-dot), and 77 (dotted) eV. (c) Expanded view of the on-axis potential without (solid) and with (dashed) the space charge contribution from 5×10^5 $\overline{\mathrm{p}}$. The empty-trap well depth W_0 and the total well depth W are shown.

As the total trap depth W is reduced by a small amount dW, we can calculate the number of particles expected to escape by integrating over the Maxwell-Boltzmann distribution (Eqn. 6.1)

$$dN = N \int_W^{W+dW} \sqrt{\frac{1}{\pi E_z k_B T}} \exp\left(-\frac{E_z}{k_B T}\right) dE_z \tag{6.3}$$

$$= N \left[\mathrm{erf}\left(\sqrt{\frac{W+dW}{k_B T}}\right) - \mathrm{erf}\left(\sqrt{\frac{W}{k_B T}}\right)\right] \tag{6.4}$$

$$\approx N \left[\mathrm{erf}\left(\sqrt{\frac{W}{k_B T}}\left(1+\frac{dW}{2W}\right)\right) - \mathrm{erf}\left(\sqrt{\frac{W}{k_B T}}\right)\right] \tag{6.5}$$

where in the last line we have used the approximation $dW \ll W$. If we define $x \equiv \sqrt{W/(k_B T)}$, so that $dx = dW/(2\sqrt{W k_B T})$, we can substitute into Eqn. 6.5 to write

$$dN = N\left[\mathrm{erf}(x+dx) - \mathrm{erf}(x)\right] \tag{6.6}$$

Using that $\mathrm{erf}'(x) = 2e^{-x^2}/\sqrt{\pi}$, Eqn. 6.6 simplifies to

$$dN = \frac{2}{\sqrt{\pi}} N \exp\left(-x^2\right) dx \tag{6.7}$$

After converting back to the original variables, we find the number of particles lost due to an incremental change in well depth dW

$$\frac{dN}{dW} = \frac{N}{\sqrt{\pi W k_B T}} \exp\left(-\frac{W}{k_B T}\right) \tag{6.8}$$

Eqn. 6.8 predicts an exponential increase in the number of escaping particles as the well depth W is lowered. This result may have been guessed from the start, given that the high-energy tail of the Boltzmann distribution falls off exponentially, so the integral will also exhibit exponential behavior.

When performing a measurement, the temperature may be extracted by fitting a line to the logarithm of dN/dW

$$\ln\left(\frac{dN}{dW}\right) = -\frac{W}{k_B T} + \ln\left(\frac{N}{\sqrt{\pi k_B T}}\right) - \frac{1}{2}\ln W \tag{6.9}$$

where the second term in Eqn. 6.9 is a constant offset, and the third term is also taken to be constant since $\ln W$ varies by 5% or less over the measurement range. Hence when $\ln(dN/dW)$ is plotted vs. W, the slope of the fitted line is equal to $k_B T$.

It is assumed that the temperature distribution of the particles remains fixed throughout the measurement. However, this assumption would not be valid in the limit that the ramp time is long compared with the evaporation time $1/\nu_{ev}$, since particle loss would evaporatively cool the plasma. Calculating ν_{ev} according to Eqn. 6.2, we find an evaporation time $1/\nu_{ev} \gtrsim 1$ s. Since this is very long compared to the ≈ 10 ms typical measurement time, we can safely neglect evaporation effects in our analysis.

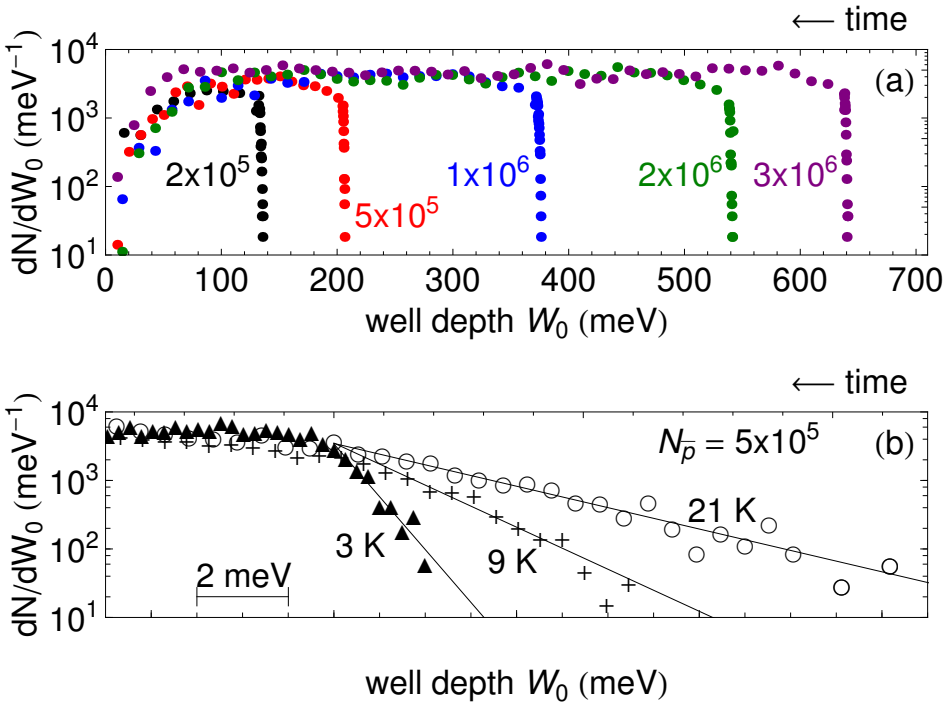

Figure 6.2: (a) Superposition of $\overline{\mathrm{p}}$ loss spectra for indicated $N_{\overline{\mathrm{p}}}$ as the empty-well trap depth W_0 is reduced linearly in time (i.e. right to left). Plasmas with larger $N_{\overline{\mathrm{p}}}$ have a larger space-charge potential, leading to earlier losses as the well depth is decreased. (b) Expanded view of the edge of three loss spectra, for $N_{\overline{\mathrm{p}}} = 5 \times 10^5$. The plasma temperature is determined from the exponential slope of the first thousand $\overline{\mathrm{p}}$ to escape as W_0 is reduced. The three curves are aligned so the slopes can be readily compared, and the indicated temperature includes the space-charge correction to be discussed in Sec. 6.1.3. Lines indicate the best fit to the edge, with a fit range that varies in these examples from 3 meV to 10 meV.

6.1.2 Antiproton Temperature Measurements

Typical results for $\overline{\mathrm{p}}$ temperature measurements are shown in Fig. 6.2. Plasmas with $N_{\overline{\mathrm{p}}}$ between 2×10^5 and 3×10^6 are accumulated in a 3.7 T magnetic field, collisionally cooled by 10^8 e^- (which are later ejected) [43], and compressed to a 2 mm radius using a rotating wall drive [115]. Temperature measurements begin by transferring the $\overline{\mathrm{p}}$ into the potential structure shown in Fig. 6.1. The empty-trap well

depth W_0 is then reduced linearly at 2.2 eV/s to eject the $\overline{\mathrm{p}}$ while the annihilation rate is recorded. The first $\approx 10^3$ $\overline{\mathrm{p}}$ escape the well in a time of order 10 ms (short compared with the evaporation time) and are used to determine the plasma temperature. We have found no change in the results when the ramping rate has been halved to 1.1 eV/s or doubled to 4.4 eV/s.

Fig. 6.2a shows data from five different trials over a range of $\overline{\mathrm{p}}$ number. In each case, a sharp edge indicates the onset of $\overline{\mathrm{p}}$ loss, with the edge position determined by the plasma self-potential. Small trial-to-trial variations in the number of $\overline{\mathrm{p}}$ and the plasma radius lead to an uncertainty in the edge position of about 10 meV, but do not change the slope of the edges.

Fig. 6.2b shows a more detailed view of the loss edge for three different $\overline{\mathrm{p}}$ plasmas with varying temperatures and $N_{\overline{\mathrm{p}}} = 5 \times 10^5$. The temperatures are determined by examining the slope of the loss rate and multiplying by an appropriate correction factor that depends on the space-charge potential of the plasma (to be discussed in Sec. 6.1.3). Uncertainties of $\sim 10\%$ are seen in individual trials due to small-number counting statistics, while we observe trial-to-trial fluctuations of $\sim 20\%$.

A primary difficulty in performing this measurement is that we only have direct control over the empty well trap depth W_0, and we only observe the loss rate dN/dW_0. A mapping is thus required to connect W_0 to W and dN/dW_0 to dN/dW so that the temperature may be extracted from Eqn. 6.9. Since this mapping will depend exclusively upon the radius, number, and temperature of the plasma within a non-ideal trap, the *EQUILSOR* particle-in-cell code introduced in Sec. 3.2.2 [98] is implemented to correct for the plasma space-charge effects.

6.1.3 Space Charge Correction

The plasma space charge plays an important role in shaping the total potential and must be considered when determining the $\overline{\mathrm{p}}$ temperature. The approximation $W_0 \approx W$, valid for deep potentials, may no longer be applied as $\overline{\mathrm{p}}$ are escaping ($W \to 0$), since the plasma self-potential of several hundred meV becomes comparable to the empty-trap well depth W_0. In addition, the space charge contribution is not constant as W_0 is decreased because the plasma lengthens as the confining potential is reduced.

Since the well structure is substantially anharmonic just before $\overline{\mathrm{p}}$ are ejected, we use *EQUILSOR* to solve for the trap depth W given a known plasma geometry and empty-well trap depth W_0. Multiple *EQUILSOR* calculations allow us to determine W as a function of W_0 and the plasma parameters, providing the means to convert $W_0 \leftrightarrow W$ and $dN/dW_0 \leftrightarrow dN/dW$. If space-charge is mistakenly neglected (i.e. $W = W_0$ assumed), the incorrectly deduced temperature would typically be 1.3 to 2 times larger than the correct value (the latter for the lowest temperatures).

The slope determined from a fit of the first thousand $\overline{\mathrm{p}}$ to escape (Fig. 6.2b) must be multiplied by a correction factor to account for the plasma space charge. We derive this factor by starting with Eqn. 6.9

$$\ln\left(\frac{dN}{dW}\right) = -\frac{W}{k_B T} + \text{const.} \tag{6.10}$$

Using the chain rule,

$$\ln\left(\frac{dN}{dW}\right) = \ln\left(\frac{dN}{dW_0}\frac{dW_0}{dW}\right) \tag{6.11}$$

$$= \ln\left(\frac{dN}{dW_0}\right) + \ln\left(\frac{dW_0}{dW}\right) \tag{6.12}$$

The second term in Eqn. 6.12 is found through simulation to exhibit only a weak dependence on W_0, and we regard it as constant. Explicitly writing W as a function of W_0, we then have

$$\ln\left(\frac{dN}{dW_0}\right) = -\frac{W(W_0)}{k_B T} + \text{const.} \tag{6.13}$$

We may now Taylor-expand $W(W_0)$ around the empty-well trap depth a, chosen to be within the fit range of the first 10^3 escaping $\overline{\text{p}}$. The precise choice of a is unimportant if we continue to treat dW_0/dW as constant. Taylor expanding,

$$W(W_0) \approx W(a) + \left.\frac{dW}{dW_0}\right|_a (W_0 - a) + \ldots \tag{6.14}$$

Substituting Eqn. 6.14 back into Eqn. 6.13 and collecting all constants, we find

$$\ln\left(\frac{dN}{dW_0}\right) = -\left.\frac{W_0}{k_B T}\frac{dW}{dW_0}\right|_a + \text{const.} \tag{6.15}$$

Hence, if a slope with magnitude m_0 is fitted to a plot of $\ln(dN/dW_0)$ vs. W_0 (as in Fig. 6.2b), the temperature may be extracted by solving

$$T = \left.\frac{1}{m_0 k_B}\frac{dW}{dW_0}\right|_a \tag{6.16}$$

Since the slope m_0 is determined by measurement and k_B is a known constant, one need only calculate the correction factor dW/dW_0 to find the plasma temperature. Fig. 6.3 shows the results of *EQUILSOR* calculations for over 50 different $\overline{\text{p}}$ plasmas with $N_{\overline{\text{p}}} = 5 \times 10^5$ and varied radii, temperatures, and confining potentials. To begin each simulation, a plasma with specified number, radius, and temperature is placed into a well with an empty-trap well depth W_0. *EQUILSOR* outputs the plasma density distribution and the total potential everywhere within the trap (see Fig. 6.3a), allowing determination of the total potential trap depth W.

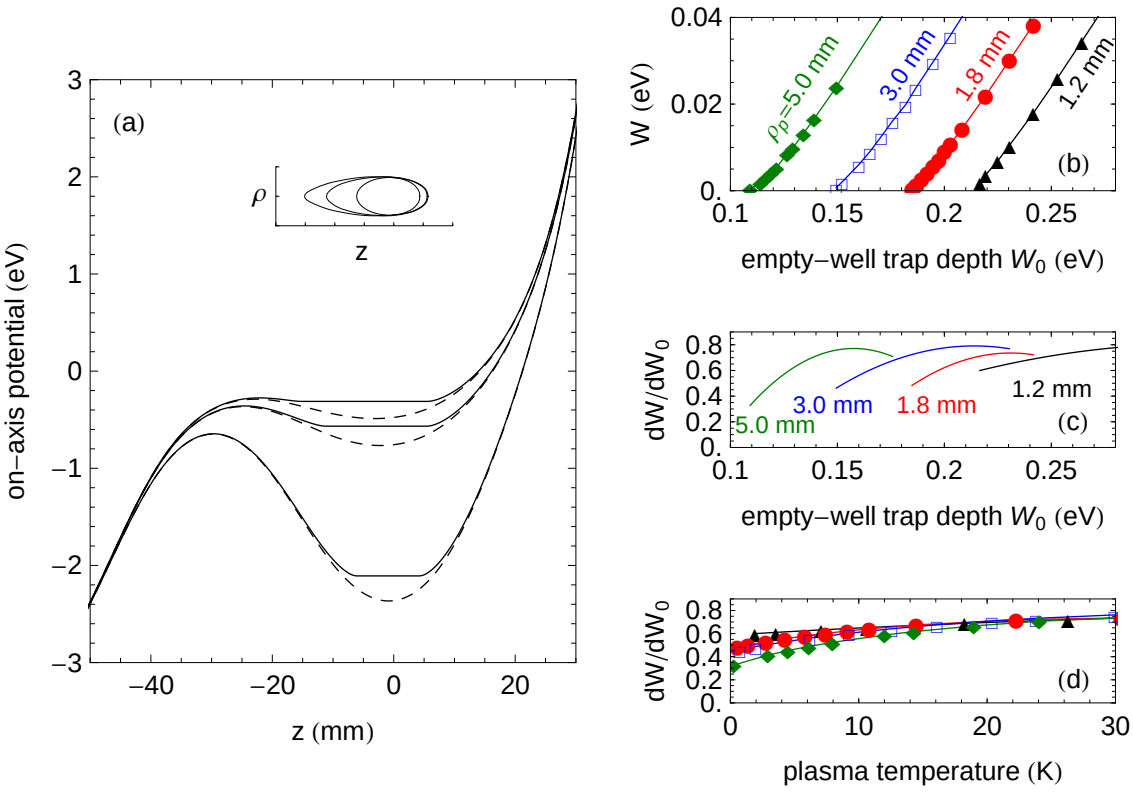

Figure 6.3: (a) Total on-axis potential (solid) and empty-well potential (dashed) at three times during the temperature measurement of a $\overline{\text{p}}$ plasma with $N_{\overline{\text{p}}} = 5 \times 10^5$ and $\rho_p = 3$ mm. The trap depth W is always less than the empty-well trap depth W_0. Inset: outer plasma boundary as the well depth is reduced. (b) *EQUILSOR* calculation of the total trap depth W as a function of W_0 and ρ_p, for $N_{\overline{\text{p}}} = 5 \times 10^5$ and $T = 1$ K. (c) The derivatives of the curves in part (b) give dW/dW_0 as a function of W_0. (d) The derivative dW/dW_0 only weakly depends on the plasma temperature.

When multiple calculations are performed with fixed plasma parameters and variable W_0, the functional dependence of the trap depth W on W_0 may be traced out, as in Fig. 6.3b. For plasmas with fixed $N_{\overline{\mathrm{p}}}$, the space charge contribution decreases as the radius increases since the density is lower. As a result, W strongly depends both on W_0 and the plasma radius ρ_p. Since we prepare our $\overline{\mathrm{p}}$ plasmas with a 2 mm radius, the 1.8 mm simulated points in Fig. 6.3b (red curve) most closely describe our data. In addition, Fig. 6.3b predicts that a 1.8 mm plasma will begin escaping when $W_0 \approx 0.2$ eV ($W \approx 0$), in agreement with our measurements for 5×10^5 $\overline{\mathrm{p}}$ presented in Fig. 6.2a.

By taking the derivative of the simulated curves in Fig. 6.3b, we find the correction factors dW/dW_0 necessary for determining the plasma temperature via Eqn. 6.16. As shown in Fig. 6.3c, these derivatives are all < 1, indicating that the correct temperature will be lower than the temperature deduced when space charge is neglected. The point a at which dW/dW_0 must be evaluated in Eqn. 6.16 still remains to be chosen. We choose a to be halfway between the endpoints of the fit range used to extract the temperature (see Fig. 6.2b). From Fig. 6.3c, the change in dW/dW_0 over a conservative 10 meV fit range is at most $\pm 5\%$ for a 1.8 mm radius plasma, demonstrating the insensitivity of the measurement to the choice of a and validating our earlier approximation.

We have also examined the dependence of dW/dW_0 on the plasma temperature, with the results shown in Fig. 6.3d. Only a weak dependence is observed, particularly at higher temperatures. However, in all cases we use the curves in Fig. 6.3d to iteratively determine the self-consistent set $\{dW/dW_0, T\}$.

6.1.4 Applications and Limitations

The techniques presented here robustly measure the temperature of a $\overline{\mathrm{p}}$ plasma with $\rho_p = 2$ mm and $N_{\overline{\mathrm{p}}}$ between 2×10^5 and 3×10^6. Uncertainties of between $10 - 20\%$ are typical, with roughly equal contributions from the error in the fitted slope m_0 and the space charge correction. It is possible to apply this technique more broadly to measure the temperature of even more variegated $\overline{\mathrm{p}}$ plasmas, though some limitations must be kept in mind.

The method should be well-suited to measuring the temperature of plasmas with $N_{\overline{\mathrm{p}}} > 3 \times 10^6$ and $\rho_p < 2$ mm. For plasmas with larger numbers of $\overline{\mathrm{p}}$, many more particles may be used to determine the slope of the loss edge while probing only $\approx 0.1\%$ of the distribution, leading to a reduction in the fit error. Similarly, since the correction factor dW/dW_0 is found to change less rapidly as a function of W_0 for smaller radius plasmas, a smaller error from the space charge correction would result. Temperature measurements of plasmas for which $N_{\overline{\mathrm{p}}} < 1 \times 10^5$ are found to suffer from large uncertainties, since only a few annihilation counts can be used to determine the slope of the loss edge.

An important experimental detail is the relation between the annihilation sampling rate and the rate at which the confining potential is decreased. As may be seen in Fig. 6.2b, the typical measurement range of 10 meV (3 meV for the coldest temperatures) is swept through in 4.5 ms (1.4 ms) when W_0 is reduced at 2.2 eV/s. It is thus a requirement that the $\overline{\mathrm{p}}$ annihilation sampling time be several times shorter than 1 ms to ensure a sufficient number of data points for fitting. As described in Sec. 3.5.1, the annihilation sampling time is set by the bin widths of a custom-built multi-channel

scaler (MCS). If the empty-well trap depth W_0 is ramped from W_0^i to W_0^f at 2.2 eV/s, each of the 125,000 bins will have a width of $(W_0^i - W_0^f)/(2.2 \times 125,000)$. If we demand at least 10 data points along the leading edge of the $\overline{\text{p}}$ loss, then the difference between the initial and final empty-well trap depth must be less than ≈ 40 eV.

This technique is not amenable to measuring the temperature of e^- plasmas since they do not make annihilation signals within our detectors. However, it may in principle be applied with two caveats to e^+ plasmas. First, the e^+ annihilation detection efficiency is only $\approx 0.5\%$ - vastly lower than the 75% $\overline{\text{p}}$ efficiency. Thus, over two orders of magnitude more e^+ are required to determine the fitted slope m_0 to the same level of accuracy. Given the demonstrated accumulation of up to 4×10^9 e^+ (Fig. 4.20), this condition can be easily satisfied within our apparatus. Second, the significantly larger e^+ plasmas are much more difficult to simulate using *EQUILSOR* on account of their much larger space charge. We have found convergence issues when solving for the equilibrium state of a plasma with $N_e = 10^8$ in the extremely shallow wells just before particles are ejected. Resultingly, we have no direct measure of lepton plasma temperatures. As we will see in Sec. 6.2, however, we may infer the e^- and e^+ temperatures by measuring the temperature of the $\overline{\text{p}}$ that they collisionally cool.

6.2 Embedded Electron Cooling

We have already shown in Sec. 4.3.1 that large numbers of e^- may be used to collisionally cool $\overline{\text{p}}$. However, large numbers of e^- contribute many eV of space charge to the total potential, demanding deep confining wells for particle trapping

and manipulation and markedly increasing the rotational frequency and velocity of the $\overline{\mathrm{p}}$. When large numbers of e^- remain within a two-component $\overline{\mathrm{p}}$ – e^- plasma, the $\overline{\mathrm{p}}$ centrifugally separate to larger radii [158], making them more susceptible to particle loss as the field-boosting solenoid is reduced or as the plasma is transferred through the electrode stack. The formation rate of $\overline{\mathrm{H}}$ can be inhibited by large numbers of e^-, since they can destroy weakly-bound $\overline{\mathrm{H}}$ atoms via replacement collisions with e^+ during the recombination process [148, 167]. It is clear that after large numbers of e^- have reduced the $\overline{\mathrm{p}}$ energies from the keV to eV scale, their presence becomes a hindrance.

However, it is highly desirable to retain some cooling mechanism for $\overline{\mathrm{p}}$. The e^- ejection process has been measured to elevate $\overline{\mathrm{p}}$ temperatures by several thousands of Kelvin, while the adiabatic routine to transfer particles through the electrode stack - though improved - may still impart several hundreds of Kelvin more. Without a cooling mechanism, $\overline{\mathrm{p}}$ would remain at these high temperatures and be unable to form cold, trappable $\overline{\mathrm{H}}$.

Consequently, we have investigated techniques to leave a small number (of order 10^3) of embedded e^- confined along with the $\overline{\mathrm{p}}$. The $\overline{\mathrm{p}}$ are cooled through collisions with e^- no less effectively, though much more slowly than before. To retain the few embedded e^-, we limit the number of pulses used to eject the majority of the 10^8 e^- which initially cool $\overline{\mathrm{p}}$ from 5 keV. Three or four pulses leave all of the $\overline{\mathrm{p}}$ in the trap, along with only $N_e = 6 \times 10^3$ or 9×10^2 e^-, respectively. After the e^- ejection raises the $\overline{\mathrm{p}}$ temperature by several orders of magnitude, the handful of remaining e^- are sufficient to recool the $\overline{\mathrm{p}}$ plasma to the steady-state temperature T_i, determined by

blackbody radiation from the trap electrodes and by electrical noise that drives the particles directly.

6.2.1 Cooling Efficiency

The rate at which e^- can cool $\overline{p}$ depends upon the ratio $N_{\overline{p}}/N_e$, as discussed in Sec. 4.3.1. For embedded e^- cooling, the typical limit (in which $N_e \gg N_{\overline{p}}$) is inverted, allowing the dynamics to be simplified. In the limit $N_{\overline{p}} \gg N_e$, the two-component plasma is described by a single temperature T if the collision rate is faster than the cooling rate, and the coupled rate equations 4.2-4.3 reduce to

$$\frac{dT}{dt} = -\frac{1}{\tau_s}\frac{N_e}{N_{\overline{p}}}(T - T_i) \equiv -\gamma_{\overline{p}}(T - T_i) \tag{6.17}$$

where τ_s is the e^- synchrotron cooling time defined in Eqn. 2.34 (0.19 s in a 3.7 T magnetic field) and $\gamma_{\overline{p}}$ is the defined embedded e^- cooling rate. For times much longer than $(\gamma_{\overline{p}})^{-1}$, both e^- and $\overline{p}$ share the steady-state temperature T_i.

The assumption that the collision rate ν_c is much faster than the cooling rate $\gamma_{\overline{p}}$ is well-justified. For $N_{\overline{p}} = 5 \times 10^5$ and $N_e = 6 \times 10^3$ or 9×10^2 e^-, the cooling rate is calculated to be $\gamma_{\overline{p}} = (17\text{ s})^{-1}$ or $(103\text{ s})^{-1}$, respectively. For comparison, a zero-field calculation (Eqn. 3.30) gives a collision rate ν_c a factor of 10^6 larger than $\gamma_{\overline{p}}$. Though the presence of the strong magnetic field is predicted to suppress the collision rate by a factor of $\approx 10^3$ (see. Ref. [108] and Fig. 3.4), ν_c remains larger than $\gamma_{\overline{p}}$ by at least 3 orders of magnitude.

The effect of embedded e^- cooling is demonstrated in Fig. 6.4. After most of the 10^8 e^- are ejected, the $\overline{p}$ plasma is left with a substantially higher temperature. Furthermore, this temperature can range from 10^3 K to, in one observed trial, over

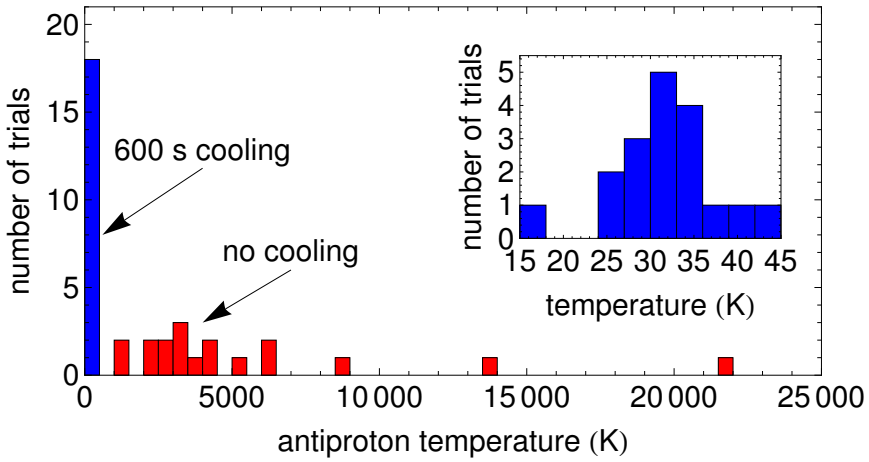

Figure 6.4: Distribution of $\overline{\mathrm{p}}$ temperatures measured directly after e^- ejection (red) and 600 s after e^- ejection (blue). The embedded e^- remaining after the pulse-out cool the $\overline{\mathrm{p}}$ to an equilibrium temperature centered around 31 K (inset).

2×10^4 K. Since the embedded e^- cooling rate can be as slow as $(103\ \mathrm{s})^{-1}$ when only 9×10^2 e^- remain, we allow 600 s of equilibration time for the $\overline{\mathrm{p}}$ to cool to a steady-state temperature T_i. We find that after 600 s, all $\overline{\mathrm{p}}$ plasmas that we have studied reach an equilibrium temperature centered around 31 K. Embedded e^- cooling effectively erases the temperature history of the $\overline{\mathrm{p}}$ plasma, always leaving it at 31 K given enough equilibration time.

The steady-state temperature of 31 K comes from a balance between cooling from e^- synchrotron radiation and heating from blackbody radiation and electrical noise. Identifying and reducing noise that heats the e^- (perhaps from radio or TV stations, or from the many electrical signals within the decelerator hall) should make T_i approach the 1.2 K electrode temperature. For example, we have recently found that the high-voltage switch used to catch $\overline{\mathrm{p}}$ during the AD ejection was coupling noise down to the HV electrode. Disconnecting the switch after $\overline{\mathrm{p}}$ accumulation yielded a reduction

in T_i from 31 K to 17 K. Many more such noise sources are likely to exist, and we are confident that a still-colder T_i may be realized if only these sources can be found and eliminated.

A final comment about the cooling efficiency of embedded e^- is that the cooling rate $\gamma_{\overline{p}} = N_e/(N_{\overline{p}}\tau_s)$ depends on the strength of the magnetic field as $\sim B_0^2$. Equilibration times in 1 T fields can thus become exceedingly long. When 9×10^2 embedded e^- are present, for instance, the $1/e$ cooling time is over 20 minutes; over an hour wait time would be necessary since multiple $e-$foldings are desired. Whenever possible, we seek to employ embedded e^- cooling only in elevated magnetic fields to profit from the increased cooling efficiency.

6.2.2 Embedded Electron Number

Throughout this section, we have been quoting the number of embedded e^- after three and four pulses as $N_e = 6 \times 10^3$ and 9×10^2, respectively. However, these few numbers of e^- are much too small to be directly charge-counted. Instead, we determine N_e by observing the rate at which $\overline{p}$ return to thermal equilibrium after they have been adiabatically cooled below the steady-state temperature T_i (described soon in Sec. 6.3).

Typically, the embedded e^- are used to cool heated $\overline{p}$. However, if $\overline{p}$ are reduced to a temperature lower than the steady-state e^- temperature T_i, the e^- heat $\overline{p}$ through collisions until equilibrium is reestablished. Eqn. 6.17 directly shows that cooling or heating with embedded e^- proceeds at the rate $\gamma_{\overline{p}} = N_e/(N_{\overline{p}}\tau_s)$. Since $N_{\overline{p}}$ is easily determined with annihilation counting techniques and τ_s is easily calculated,

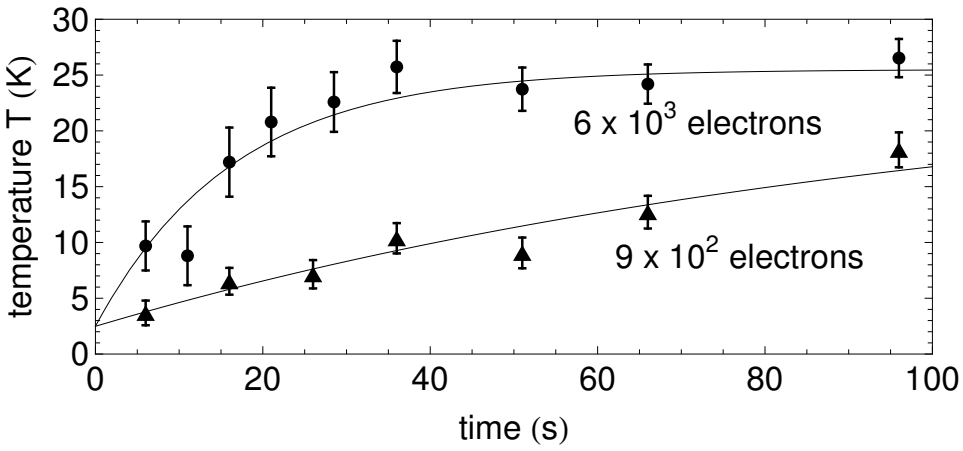

Figure 6.5: After 5×10^5 $\overline{\mathrm{p}}$ have been cooled below the steady-state temperature T_i, thermal equilibrium is slowly reestablished at a rate $\gamma_{\overline{\mathrm{p}}}$ that is proportional to N_e. The two curves show the result of taking three pulses to eject most of the 10^8 initial e^- (circles) and four pulses (triangles).

measurement of $\gamma_{\overline{\mathrm{p}}}$ provides a sensitive measure of the small number of embedded e^- N_e.

Fig. 6.5 shows the return to equilibrium after T is cooled below T_i when three (circles) and four (triangles) pulses are used to eject most of the 10^8 initial e^-. As expected, the rate $\gamma_{\overline{\mathrm{p}}}$ (determined by an exponential fit) is faster when fewer e^- have been pulsed out. Both curves in Fig. 6.5 rise to the same T_i, suggesting that e^- rather than $\overline{\mathrm{p}}$ are being heated to make $T_i > 1.2$ K. A consistent $\gamma_{\overline{\mathrm{p}}}$ can be similarly and independently determined from the T measured as embedded e^- reduce the temperature of hot $\overline{\mathrm{p}}$ to T_i.

The 31 K equilibrium temperature for $\overline{\mathrm{p}}$ cooled by embedded e^- is still large compared with the 0.4 K quadrupole Ioffe trap depth. However, embedded e^- cooling is only the first step in a process that reduces the $\overline{\mathrm{p}}$ temperature to 3.5 K or lower. We now turn our attention to the second stage: adiabatic cooling of $\overline{\mathrm{p}}$ that have been pre-cooled to 31 K by the embedded e^-.

6.3 Adiabatic Cooling

Adiabatic cooling provides a method to reduce $\overline{\mathrm{p}}$ temperatures by over an order of magnitude while suffering no particle losses. In a harmonic trap potential, adiabatic cooling takes place when the restoring force F and potential energy U that confine $\overline{\mathrm{p}}$ are reduced. The axial bounce frequency f for particles in such a potential parameterizes both the restoring force and well depth, since $\omega = 2\pi f$ determines $F = -m\omega^2 z$ and $U = m\omega^2 z^2/2$. As the initial axial oscillation frequency f_i is reduced to f_f, particles are cooled adiabatically from temperature T_i to T_f. The process is reversible, with adiabatic heating taking place when $f_f > f_i$. Depending on the particle density, we may treat adiabatic cooling either as a single-particle effect or an ideal gas effect. Here we consider both cases, discuss the relevant cooling timescales, and demonstrate the cooling of between 2×10^5 to 3×10^6 $\overline{\mathrm{p}}$ to the lowest temperatures directly measured, $T = 3.5 \pm 0.7$ K.

6.3.1 Single-Particle Picture

For a low-density cloud of non-interacting particles, adiabatic cooling is a single-particle effect. Adiabatic cooling of $\overline{\mathrm{p}}$ oscillators [132], implications for the energy analysis of the first trapped [40] and e^- cooled [43] $\overline{\mathrm{p}}$, and cooling of hot ions [168] has been considered within this framework. Classically, the ratio of a particle's energy E to its oscillation frequency f forms an adiabatic invariant $J = E/f$. Since J remains constant for adiabatic changes, decreasing the oscillation frequency from f_i to f_f is predicted to reduce the particle temperature from T_i to $T_f = (f_f/f_i)T_i$. If a coupled oscillatory motion contributes heat capacity but no additional cooling (e.g.

$\overline{\mathrm{p}}$ cyclotron motion), then the individual particle prediction is $T_f = (f_f/f_i)^{1/2}T_i$.

In the quantum picture, classical adiabatic invariants may be equated to a set of quantum numbers [169, 170]. The energies for a particle oscillating in a harmonic potential at frequency f are quantized, with $E_n = hf(n+1/2)$. As noted by Einstein at the first Solvay conference [171, 172], the quantum number n remains fixed for adiabatic changes. Hence, the classical adiabatic invariant that is quantized is precisely the $J = E/f$ from the classical picture. As before, $E_f = (f_f/f_i)E_i$ unless additional modes are coupled to the system.

6.3.2 Ideal Gas Picture

For our demonstration of adiabatic cooling, the density of $\overline{\mathrm{p}}$ is large enough so that it is a true plasma (i.e. the Debye length λ_D is smaller than the cloud size). We use the approximation of an uncorrelated, non-interacting plasma, justified since the kinetic energy of the $\overline{\mathrm{p}}$ is larger than the average Coulomb repulsion between neighboring $\overline{\mathrm{p}}$. In this limit, the $\overline{\mathrm{p}}$ within the bulk of the plasma may be treated as an ideal gas rotating at frequency ω_r (the plasma rotation frequency) [173, 174].

If an ideal gas is allowed to expand adiabatically, it will do work at the expense of its internal energy, and its temperature will decrease. Starting with the ideal gas law, first law of thermodynamics, and the condition that no heat be absorbed during an adiabatic process (i.e. $đQ = 0$), we derive the relation [175]

$$V^{2/d}T = \text{const.} \tag{6.18}$$

where V is the volume of the plasma, T is the temperature, and d is the number of degrees of freedom that share the $\overline{\mathrm{p}}$ energy. Here we assume the usual case of

$d = 3$. As the depth of the confining potential is reduced and the COM frequency f_i decreases to f_f, the plasma grows in length along the $\hat{z}$ axis (as shown in Fig. 3.11a). Since the plasma radius remains fixed during this manipulation, the plasma volume V increases from V_i to V_f, and the temperature decreases according to

$$T_f = (V_i/V_f)^{2/3} T_i \tag{6.19}$$

The relationship between the plasma volume and the axial bounce frequency f is neither analytic nor simple. For a fixed-radius plasma, the length (and volume) are defined implicitly as a function of the applied potential V_0 through Eqn. 3.35. Though in harmonic wells the relation $f \propto \sqrt{V_0}$ allows f to be written in terms of the plasma volume, substantial deviations are expected as the well depth is made shallow. Consequently, we integrate the equations of motion to find the bounce frequency f in a potential well characterized by V_0. Hence, f remains a parameter of the empty well rather than being defined as an oscillation frequency of a trapped plasma.

6.3.3 Cooling Timescales

In the single-particle picture, changes in the $\overline{\mathrm{p}}$ oscillation frequency f are adiabatic if $\dot{f}/f \ll f$ (i.e. f varies very little during an oscillation period). For the case of a dense $\overline{\mathrm{p}}$ plasma, the plasma has been changed adiabatically if its final temperature T_f is independent of the rate at which f is changed. Reversibility is a hallmark of adiabaticity, and changing f from $f_i \to f_f \to f_i$ should leave the plasma at its initial temperature T_i.

In general, the cooling process may be made arbitrarily long, provided the adiabatic condition is satisfied. However, its effectiveness can only be realized if it occurs

on a timescale faster than any other process that may change the $\overline{\mathrm{p}}$ temperature. In our specific case, this requires adiabatic cooling to be performed and observed more quickly than the embedded e^- can restore the plasma to temperature T_i. The $1/e$ equilibration time $(\gamma_{\overline{\mathrm{p}}})^{-1}$ is fastest when 6×10^3 e^- remain embedded amongst the $\overline{\mathrm{p}}$, with $(\gamma_{\overline{\mathrm{p}}})^{-1} = 17$ s. We therefore demand that adiabatic cooling take place over a time $t \ll 17$ s.

6.3.4 Demonstration of Adiabatic Cooling

In preparation for adiabatic cooling, up to 3×10^6 $\overline{\mathrm{p}}$ cooled by embedded e^- are confined in a potential with an on-axis empty-well trap depth W_0 between 0.4 and 800 eV, corresponding to f_i between 90 kHz and 3 MHz. To adiabatically cool, the total trap depth W is lowered from its initial value to a final value just large enough to keep $\overline{\mathrm{p}}$ from escaping. Decreasing W thereby reduces f_i to f_f and increases the plasma volume from V_i to V_f. The resulting $\overline{\mathrm{p}}$ temperature is then immediately measured by the method introduced in Sec. 6.1. Over the range of plasma temperatures in this demonstration, f_f (determined mostly by space charge) varies by $\pm 2\%$, so repeated measurements may be safely compared.

The adiabatic cooling and subsequent temperature measurements are completed in hundreds of ms, much shorter than $(\gamma_{\overline{\mathrm{p}}})^{-1} = 17$ s. Adiabaticity is checked by varying the cooling time by a factor of 5, with no differences observed. An additional test finds the same $\overline{\mathrm{p}}$ temperature before and after the well depth is reduced then restored to its initial value, confirming that the process is adiabatic and reversible.

The temperature of $\overline{\mathrm{p}}$ adiabatically cooled by different amounts is shown in Fig.

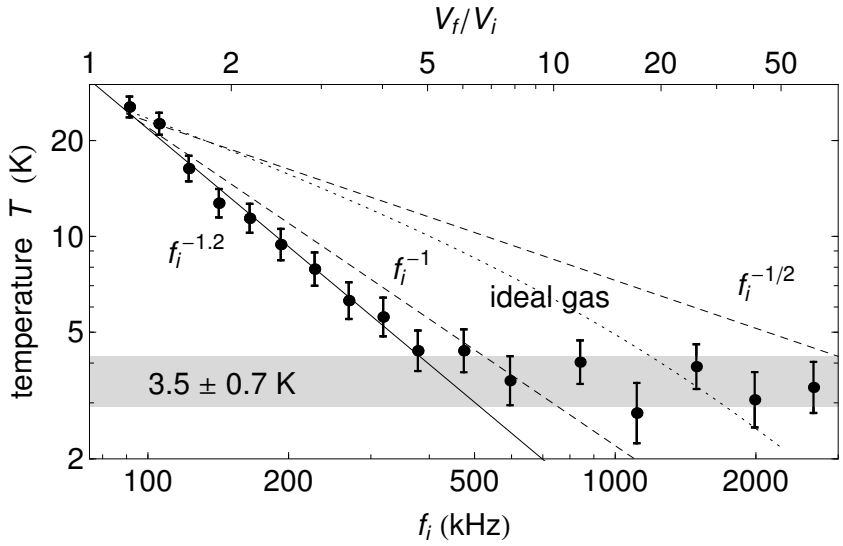

Figure 6.6: Measured and predicted temperatures for 5×10^5 $\overline{\mathrm{p}}$ after adiabatic cooling. The measured T fits a power law (solid curve) down to the lowest T measured (gray band). The factor by which the plasma volume is predicted to expand is shown on the top axis.

6.6. Plasmas with $N_{\overline{\mathrm{p}}} = 5 \times 10^5$ equilibrate with embedded e^- to $T_i = 31$ K in wells of varying f_i. The confining potential is then reduced, lowering f_i to f_f (at which point the $\overline{\mathrm{p}}$ escape) and effecting an increase in the plasma volume from V_i to V_f. More adiabatic cooling is both expected and observed for larger initial values of f_i.

Adiabatic cooling produces $\overline{\mathrm{p}}$ temperatures of 3.5 ± 0.7 K (the gray band in Fig. 6.6) for $f_i \gtrsim 500$ kHz, the lowest directly measured. For $f_i < 500$ kHz, the measured T is well-fit to a power law in f_i, with more effective cooling than predicted by either the single-particle oscillator models or the ideal gas model. The measurements are reproducible to within the uncertainties shown on the plot.

Deviations from the single-particle adiabatic cooling predictions may be expected since the $\overline{\mathrm{p}}$ plasma is comprised of 5×10^5 particles. It is more surprising that the ideal gas prediction, calculated using Eqn. 6.19 and plasma volumes output from

EQUILSOR, disagrees with the data. The prediction does not change noticeably when the plasma shapes are approximated as spheroids [176], the required geometry within an idealized quadrupole potential.

Two assumptions must be valid before treating the $\overline{\mathrm{p}}$ plasma as an ideal gas: the plasma must be uncorrelated, and the plasma size must be large compared to the Debye length λ_D. In Sec. 3.1, we introduced the correlation parameter $\Gamma = q^2/(4\pi\epsilon_0 a k_b T)$, with a the inter-particle spacing defined by $(4/3)\pi a^3 n_0 = 1$. Correlations are small if $\Gamma \ll 1$, indicating that the thermal energy $k_B T$ is much larger than the Coulomb repulsion energy $q^2/(4\pi\epsilon_0 a)$ between neighboring $\overline{\mathrm{p}}$. For $\overline{\mathrm{p}}$ in this demonstration, Γ may be as large as 0.1, indicating that the plasma is weakly correlated.

Initially, $\overline{\mathrm{p}}$ plasmas in this demonstration have a Debye length $\lambda_D = \sqrt{\epsilon_0 k_B T/nq^2}$ of approximately 100 μm. Though this is small compared with the $\overline{\mathrm{p}}$ plasma radius of 2 mm, approximately 13% of the plasma volume lies within one Debye length of the edge. The Debye length is increased markedly during adiabatic cooling, since the plasma volume expands and the density decreases. For instance, when $f_i = 500$ kHz, the density decreases by a factor of ≈ 6.5, increasing λ_D by a factor of ≈ 2.5. Since the plasma radius remains unchanged during the adiabatic expansion, the fraction of plasma volume that lies within one Debye length of the edge has increased to 30%. Edge effects that can no longer be ignored, as well as the effects of the changing Debye length during adiabatic cooling, have yet to be included in the theoretical description.

For $f_i \gtrsim 500$ kHz in Fig. 6.6, all measured temperatures are consistent with 3.5 ± 0.7 K, the value recorded from 18 repeated measurements at $f_i = 600$ kHz

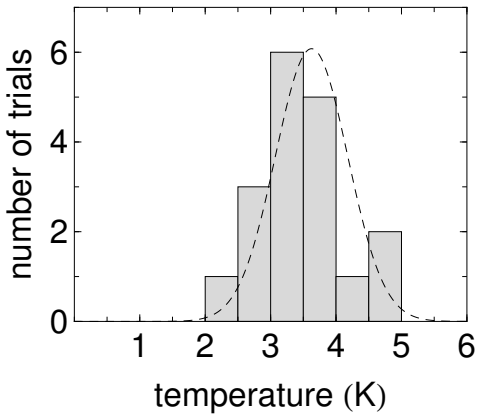

Figure 6.7: Repeated measurements with $N_{\overline{\mathrm{p}}} = 5 \times 10^5$ and $f_i = 600$ kHz show $T = 3.5 \pm 0.7$ K.

(see Fig. 6.7). It is not yet understood why lower temperatures are not observed. It seems likely that this temperature is a measurement limit for the apparatus and method, since varying f_i, $N_{\overline{\mathrm{p}}}$, and T_i all yield the same 3.5 K value after adiabatic cooling. The actual $\overline{\mathrm{p}}$ temperatures could then be as low as 0.4 K, if the $f_i^{-1.2}$ scaling persists to the largest f_i used. However, no physical mechanism that may cause such a measurement limit has yet been identified. It may also be possible that some technical noise keeps $\overline{\mathrm{p}}$ from reaching a lower T, though a potential source for such noise has not been found. Finally, it may be possible that a better theoretical understanding of adiabatic cooling in non-idealized plasmas will reveal a slope change in the cooling curve (Fig. 6.6) around $f_i \approx 500$ kHz.

6.4 Summary and Discussion

Adiabatic cooling has been shown to be an effective method for cooling far more $\overline{\mathrm{p}}$ to far lower temperatures than have been previously demonstrated. Adiabatic cooling

thus promises to be an important step in creating $\overline{\mathrm{H}}$ cold enough to be confined in a magnetic trap of depth less than 0.4 K. An important feature of adiabatic cooling for a rare species like $\overline{\mathrm{p}}$ is that particle loss is neither expected nor observed. Large numbers of cold $\overline{\mathrm{p}}$ are therefore available to participate in $\overline{\mathrm{H}}$ formation, a necessary (though not sufficient) step towards creating large numbers of trappable $\overline{\mathrm{H}}$ atoms.

Both $\overline{\mathrm{H}}$ formation methods (three-body recombination [141] and charge-exchange [49]) can profit from adiabatically cooled $\overline{\mathrm{p}}$. For three-body recombination, $\overline{\mathrm{p}}$ excitations in which the applied drive frequency is chirped downwards seek to increase the energy in the plasma COM mode, but not the plasma temperature [149]. When the $\overline{\mathrm{p}}$ are excited to interact with the e^+, they ideally would remain at their adiabatically cooled temperature and form $\overline{\mathrm{H}}$ sufficiently cold to trap. Furthermore, since the three-body recombination rate $\nu_{tbr} \propto T_e^{-9/2}$, adiabatically cooling the e^+ before mixing will improve the $\overline{\mathrm{H}}$ production rate.

Conversely, Rydberg charge-exchange relies upon highly-excited Ps atoms interacting with a stationary $\overline{\mathrm{p}}$ plasma. If $\overline{\mathrm{p}}$ are adiabatically cooled just before the charge-exchange is allowed to proceed, $\overline{\mathrm{H}}$ will be formed at the much-reduced $\overline{\mathrm{p}}$ temperature. For both three-body recombination and charge-exchange, the adiabatic cooling process is naturally compatible with producing $\overline{\mathrm{H}}$ that can be trapped since the $\overline{\mathrm{p}}$ angular velocities are low in the shallow well that remains after cooling is completed.

The $\overline{\mathrm{p}}$ are prepared for adiabatic cooling by embedded e^- cooling. This method, demonstrated to cool large $\overline{\mathrm{p}}$ plasmas with only a small number of e^-, is important in its own right. The embedded e^- remove heat imparted to the $\overline{\mathrm{p}}$ after pulsed e^- ejection and transfer through the electrode stack. The e^- additionally permit equilibration

to $T_i = 31$ K for arbitrary well depths and starting frequencies f_i, allowing for the adiabatic cooling demonstration shown in Fig. 6.6. Finally, determining the efficacy of embedded e^- and adiabatic cooling was enabled by an accurate and robust method to measure plasma temperatures.

Characterization and control of our plasma number, geometry, and temperature has been a central theme of this work. In the previous two chapters, the accumulation of up to 10^7 $\overline{p}$ and 4×10^9 e^+ and the observation of centrifugal separation between $\overline{p}$ and e^- have demonstrated significant progress towards the first two of these leitmotifs. In this chapter, we have seen how $\overline{p}$ temperatures as low as 3.5 K may be attained via adiabatic cooling and measured, thereby completing the specification and manipulation of all plasma parameters. In the next few chapters, we will apply these advances towards the simultaneous trapping of multiple $\overline{H}$ atoms.

Chapter 7

Trapped Antihydrogen: Searches and Formation Methods

The long-term goal [1] of performing precise spectroscopic and gravitational measurements on $\overline{\mathrm{H}}$ requires substantial numbers of trapped atoms in their ground state. Tests of CPT symmetry and Lorentz invariance using laser spectroscopy of $\overline{\mathrm{H}}$ may require upwards of 10^3 simultaneously trapped atoms [29]. Similarly, sensitive tests of antimatter gravity will likely demand that many atoms be laser cooled to probe for any small differences in the spatial density distributions of trapped H and $\overline{\mathrm{H}}$ [34, 36]. The following three chapters report steady progress towards this long-term goal, with 5 ± 1 $\overline{\mathrm{H}}$ atoms (on average) simultaneously trapped for 15 – 1000 s [59], long enough to ensure that the atoms reach their ground state. The $\overline{\mathrm{H}}$ energies are below 375 mK, the Ioffe trap depth for ground-state $\overline{\mathrm{H}}$ atoms (with the low energy expressed in temperature units). Though reproducibility challenges remain in making large numbers of cold $\overline{\mathrm{p}}$ and e^+ interact, we have observed substantially more simultaneously trapped

$\overline{\mathrm{H}}$ than previously reported.

Recently, the ALPHA collaboration has announced observations of $\overline{\mathrm{H}}$ confined for up to 2000 seconds using 1.5×10^4 $\overline{\mathrm{p}}$ and 10^6 e^+ [60]. They report 0.7 $\overline{\mathrm{H}}$ atoms per trial (on average) trapped from 15 – 1000 s, improving upon their initial average of 0.1 $\overline{\mathrm{H}}$ trapped for 172 ms [58]. Our demonstration of 5 $\overline{\mathrm{H}}$ atoms per trial, using 10^6 $\overline{\mathrm{p}}$ and 3×10^7 e^+, compares favorably and suggests that it may be possible to further scale up the number of simultaneously trapped $\overline{\mathrm{H}}$ using the 10^7 $\overline{\mathrm{p}}$ and many more e^+ currently available. Increases in the number of simultaneously trapped $\overline{\mathrm{H}}$ are critical if laser cooling of $\overline{\mathrm{H}}$ and spectroscopy at high levels of precision are to be achieved.

We begin this chapter with the general experimental method by which searches for trapped $\overline{\mathrm{H}}$ proceed. Next, we describe the protocol for quickly de-energizing the Ioffe trap to allow trapped $\overline{\mathrm{H}}$ atoms to escape and annihilate. Finally, we detail four different techniques used to excite $\overline{\mathrm{p}}$ into the e^+ plasma so that $\overline{\mathrm{H}}$ atoms may be created.

7.1 Searches for Trapped Antihydrogen

Searches for trapped $\overline{\mathrm{H}}$ began in earnest in 2007 after the first demonstration of $\overline{\mathrm{H}}$ production within a quadrupole Ioffe trap [57]. The general experimental procedure has remained similar ever since, though the trial-to-trial details have met with myriad modifications. In this section, we discuss the themes common to our recent trapped $\overline{\mathrm{H}}$ searches, reserving the variations for Sec. 7.2.

The typical trial begins with the accumulation of 10^6 $\overline{\mathrm{p}}$ and 9×10^7 e^+, with each plasma compressed to a 2 mm radius. The $\overline{\mathrm{p}}$ are transferred into the 1 T field near

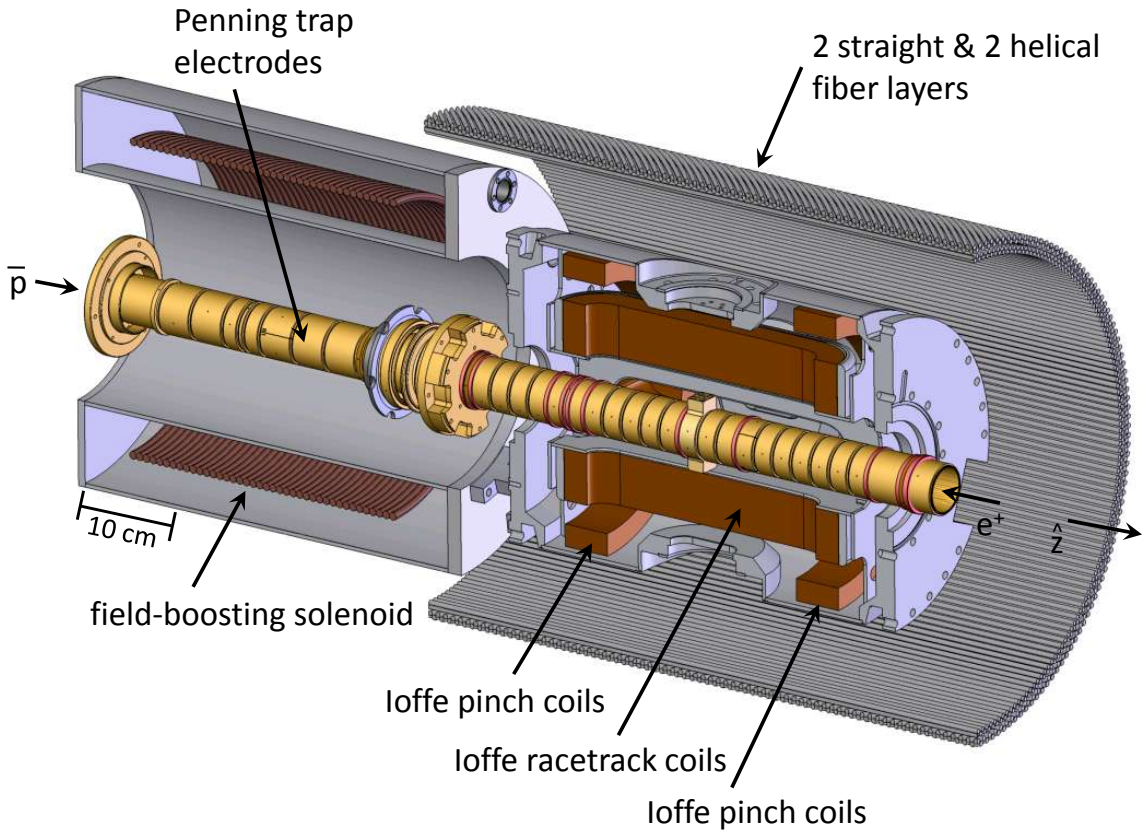

Figure 7.1: Cross-section view showing the critical subassemblies during trapped $\overline{\mathrm{H}}$ searches. Penning trap electrodes store $\overline{\mathrm{p}}$ and e^+ before and during $\overline{\mathrm{H}}$ formation, and the Ioffe trap coils are energized to store $\overline{\mathrm{H}}$ atoms. Voltages induced in the field-boosting solenoid coils provide quench timing information. Scintillating paddles (not shown) and fiber layers surrounding the Ioffe trap region detect $\overline{\mathrm{p}}$ annihilations. Much of the vacuum enclosure and cooling system is hidden for clarity. The trap axis $\hat{z}$ is vertical.

the center of the Ioffe trap (and expand in radius by roughly a factor of 2), while e^+ are transfered to a well adjacent to the $\overline{p}$. The Ioffe field is then energized, and $\overline{p}$ and e^+ are mixed to form $\overline{H}$ via three-body recombination. After all charged particles are cleared away, the Ioffe trap is quickly de-energized so that trapped $\overline{H}$ may escape and create detectable annihilation signals. Fig. 7.1 shows the directly relevant parts of the apparatus used during trapped $\overline{H}$ searches.

Each trial may take up to 2 hours. One hour is used to accumulate and cool $\overline{p}$, followed by 30 minutes of e^+ accumulation and cooling. The final 30 minutes is used to bring $\overline{p}$ and e^+ into position, ramp up the Ioffe field, form $\overline{H}$ atoms, and look for trapped $\overline{H}$. This process may be potentially shortened by ≈ 40 minutes by developing techniques to decrease the rotating wall compression time and by simultaneously accumulating $\overline{p}$ and e^+.

After their initial loading and cooling, $\overline{p}$ and e^+ are placed in the distorted nested well structure shown in Fig. 7.2a. Both species equilibrate to $T_i = 31$ K within wells that are artificially deepened to prepare for later adiabatic cooling [163]. Additionally, holding particles in deep wells is advantageous during the ramp up of the Ioffe field. Large confining potentials compress the axial extent of the plasma, thereby limiting the radial excursions and ballistic loss that would otherwise be experienced in the Penning-Ioffe trap (see Eqn. 2.47).

After moving the particles into position, currents of 69 A and 80 A are introduced into the racetrack and pinch coils of the Ioffe trap, respectively. This creates a 375 mK trap depth for a low-field seeking $\overline{H}$ atom in its ground state, with equipotential contours and the on-axis field strength shown in Fig. 7.2b-c. The current ramp rates

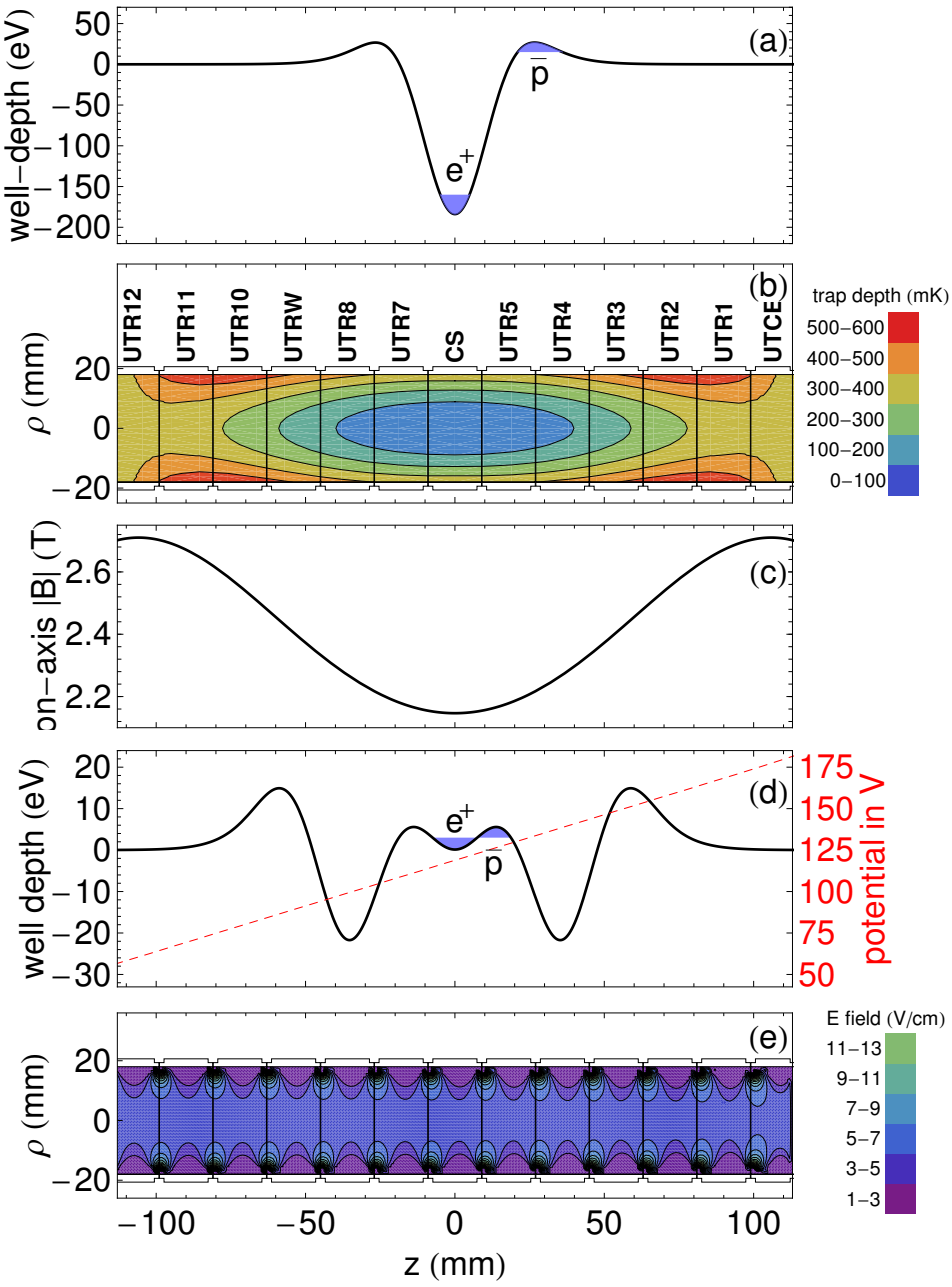

Figure 7.2: (a) Initial on-axis well structure for confining $\overline{\mathrm{p}}$ and e^+ before the Ioffe field is energized. (b) Trap electrode cross sections with equipotential energy contours for a low-field seeking, ground-state $\overline{\mathrm{H}}$ in our Ioffe trap. (c) The magnitude of the on-axis magnetic field rises from 2.15 T at the center of the trap to 2.71 T near the pinch coils. (d) Potentials along the center axis of the trap used to contain (solid) and remove (dashed) charged particles during and after $\overline{\mathrm{H}}$ formation. (e) Contours of the axial electric field used to clear $\overline{\mathrm{p}}$ and e^+ before trapped $\overline{\mathrm{H}}$ are detected.

of 0.1 A/s and 0.15 A/s for the racetrack and pinch coils (respectively) are empirically determined to minimize the total ramp time while avoiding a Ioffe trap quench. Such quenches may occur if the nearly 10^5 N forces acting on the racetrack coils are applied rapidly enough to mechanically shift the position of the windings. The pinch coils are purposefully ramped at a faster rate so that the radial compression due to the increasing axial field may offset ballistic loss due to the quadrupole field.

Nonetheless, e^+ radii are directly observed to increase as the Ioffe trap field is ramped up ($\overline{p}$ radii are unknown since they cannot be directly measured). For e^+, we find an initial expansion rate of ≈ 0.01 mm/s, accelerating to nearly double this value as the radius grows. Before the full Ioffe field of 375 mK is established, of order 10^7 e^+ cross the cutoff radius for the Penning-Ioffe trap and follow trajectories into the electrode walls. No $\overline{p}$ losses are observed during the magnetic field ramp up or while the full field is maintained.

After the Ioffe trap is fully energized but just before $\overline{p}$ and e^+ are mixed, both species are adiabatically cooled to 3.5 K (or lower) as the nested well structure (Fig. 7.2d) is established. Reductions in the e^+ well depth lead to axial expansion of the plasma, and large numbers of e^+ are lost immediately as they follow magnetic field lines into the electrode walls and annihilate. All of the 10^6 $\overline{p}$, but only 3×10^7 e^+, survive the ramp up of the Ioffe trap and transfer into the nested well potential structure (Fig. 7.2d).

Immediately after adiabatic cooling, $\overline{p}$ and e^+ are mixed by applying a frequency drive to excite $\overline{p}$ into the e^+. $\overline{H}$ atoms form by the three-body interaction of a $\overline{p}$ with two e^+. Ongoing searches for the most efficient cold $\overline{H}$ production method lead to

different techniques to drive $\overline{\mathrm{p}}$ through the e^+ plasma. In general, applied frequency drives aim to maintain resonance with the anharmonic $\overline{\mathrm{p}}$ center-of-mass frequency as the $\overline{\mathrm{p}}$ oscillation energy increases [4, 149]. We have explored two approaches in detail: one in which the drive frequency is broadened by noise and applied for up to 10 minutes, and another in which a coherent drive is chirped in frequency for a duration of 2 ms to 15 minutes. Further details about these individual approaches will be presented in Sec. 7.2.

The production and trapping of $\overline{\mathrm{H}}$ continues for the 2 ms to 15 minutes that the $\overline{\mathrm{p}}$ and e^+ interact in the various trials. Once mixing is complete, the $\overline{\mathrm{p}}$ and e^+ (but not the trapped $\overline{\mathrm{H}}$) are cleared away by axial electric fields of ± 5 V/cm (Fig. 7.2d-e). These fields are chosen to be much stronger than stray fields from patch potentials (maximally of order ≈ 100 mV/cm) that could otherwise trap a $\overline{\mathrm{p}}$, and are large enough to eject any $\overline{\mathrm{p}}$ that could be trapped directly by the Ioffe pinch coils (discussed further in Chapter 8). A 1 s delay is introduced between the end of mixing and the application of the clearing field to ensure that trapped $\overline{\mathrm{H}}$ atoms are sufficiently deeply bound so that they will not be ionized. Indeed, in Sec. 9.2.3 we argue that 1 s is more than sufficient to ensure that the $\overline{\mathrm{H}}$ atoms have already reached their ground state.

After all charged particles are swept away, the trapped $\overline{\mathrm{H}}$ are released by quenching the superconducting racetrack coils of the Ioffe trap and annihilate on the electrode walls. As described in Sec. 2.2.2, quenches allow for a much more rapid decrease in the Ioffe magnetic field (≈ 1 s) compared with even the fastest achievable ramp-down time (≈ 60 s). Quenches are induced by either applying 14 W to a small heater

mounted near one of the superconducting racetrack coils or by increasing the current in the Ioffe trap to exceeding the critical current. The time between the application of the clearing electric field and the quench ranges from 15 to 60 s, setting a lower limit on the time that any $\overline{\mathrm{H}}$ atom remains confined within the Ioffe trap. However, in many trials the $\overline{\mathrm{H}}$ storage time may be as long as the 1000 s between the commencement of $\overline{\mathrm{H}}$ production and the quench.

The quench process is shown in Fig. 7.3. As one of the Ioffe racetrack coils quenches, the magnetic trap becomes unconfining in the radial direction, allowing $\overline{\mathrm{H}}$ to escape (Fig. 7.3a). The rapid decrease in magnetic field induces a voltage across the windings of the field-boosting solenoid just underneath the Ioffe trap (see Fig. 7.1). This voltage is recorded on a scope and integrated so that the precise quench timing and trap depth over time may be determined (Fig. 7.3b-c). Within the first 1 s after the quench, the trap depth is sufficiently low that 93% of $\overline{\mathrm{H}}$ will have escaped, assuming a uniform distribution of $\overline{\mathrm{H}}$ energies. In this 1 s interval, the signal from escaping $\overline{\mathrm{H}}$ annihilating on the surrounding electrodes competes with the cosmic ray background (Fig. 7.3d).

A trapped $\overline{\mathrm{H}}$ signal is observed when a statistically significant number of detector counts above background is seen within the first second after the Ioffe trap quench. When ATRAP initially produced $\overline{\mathrm{H}}$ atoms within a Ioffe trap [57], no trapped $\overline{\mathrm{H}}$ signals were found. In an average of N trials, our detector could detect an average of $20/\sqrt{N}$ simultaneously trapped $\overline{\mathrm{H}}$ atoms per trial at a 3σ significance level. It was unclear whether we were trapping too few atoms to be observed or none at all [57].

Increases in the number of simultaneously trapped $\overline{\mathrm{H}}$, the number of trials N,

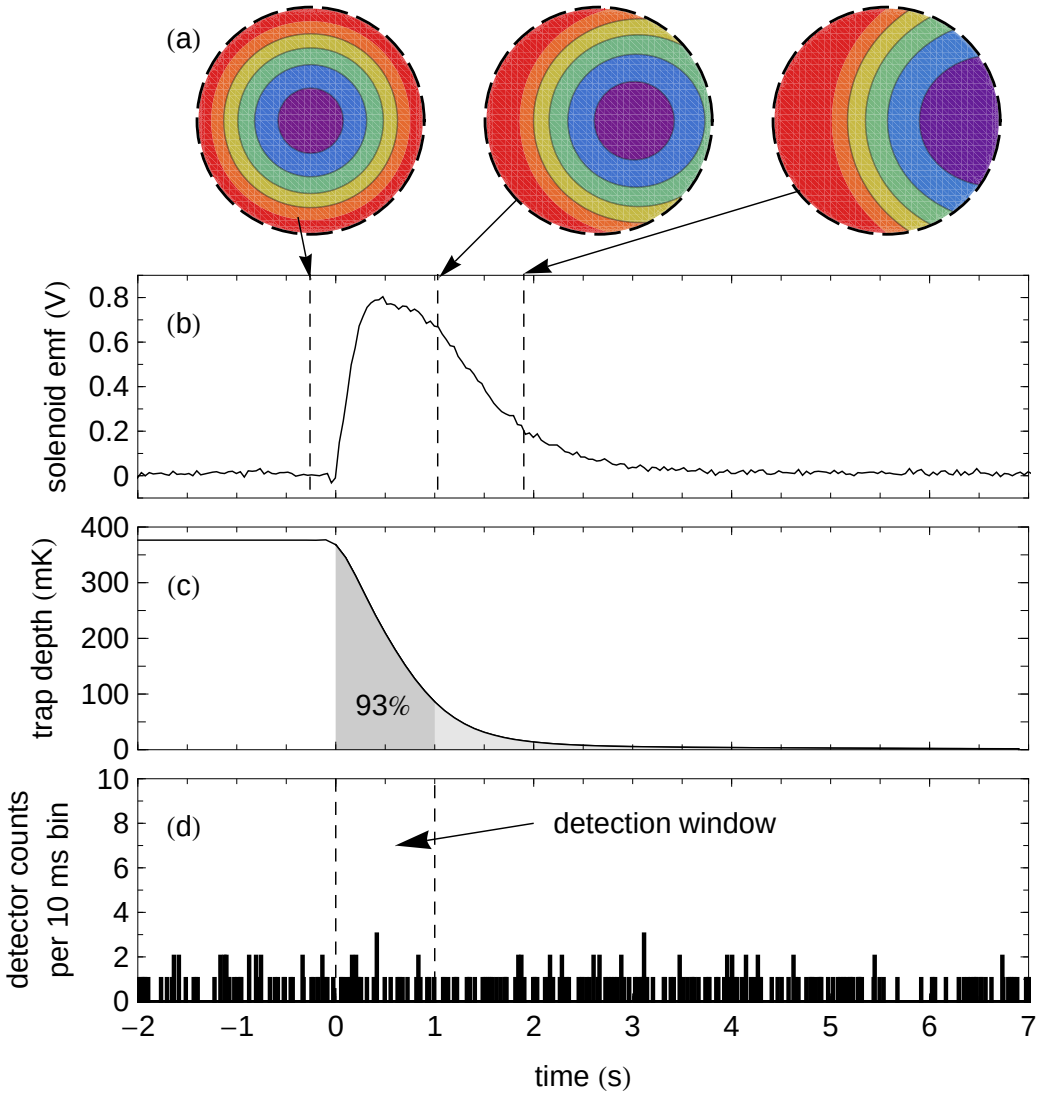

Figure 7.3: (a) Cross section of trap depth contours as one Ioffe racetrack coil is quenched. (b) The sudden change in magnetic field induces an electromotive force (emf) within the coils of the field-boosting solenoid, allowing (c) a reconstruction of the Ioffe trap depth for ground state $\overline{\mathrm{H}}$ as a function of time. Within 1 s, 93% of $\overline{\mathrm{H}}$ will escape is they fill the trap uniformly in energy. (d) We search for annihilation signals from trapped $\overline{\mathrm{H}}$ within the first second after the Ioffe trap quenches.

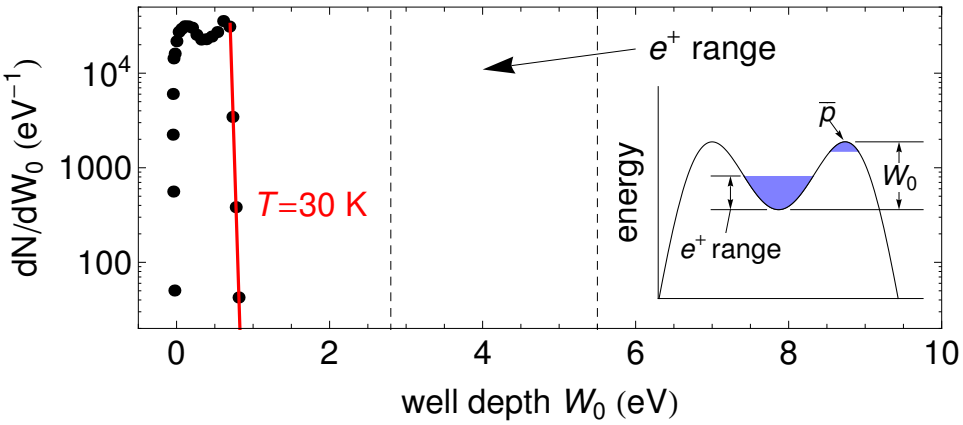

Figure 7.4: The $\overline{\mathrm{p}}$ distribution after loading into the nested well structure, but without adiabatic cooling. Embedded e^- cool the $\overline{\mathrm{p}}$ to an equilibrium temperature $T_i = 30$ K. The $\overline{\mathrm{p}}$ must gain energy before they can interact with the e^+, the energy range for which is plotted on the same scale for comparison. Inset: nested well structure showing the space charge potential range of the e^+.

and/or the detection efficiency were thus required. To improve the $\overline{\mathrm{H}}$ production and trapping rate, we greatly increased the number of $\overline{\mathrm{p}}$ and e^+ available for $\overline{\mathrm{H}}$ formation, developed techniques to optimize $\overline{\mathrm{p}}$ and e^+ plasma geometries, cooled the electrodes to 1.2 K [87], and markedly reduced the particle temperatures using embedded-electron and adiabatic cooling (as demonstrated in Chapters 4-6). Though the data rate is woefully slow, we have increased the number of trapped $\overline{\mathrm{H}}$ trials to 20 in 2011, from fewer than 10 in previous years. Finally, improvements in the detection efficiency now permit the observation of $12/\sqrt{N}$ atoms (on average) in N trials. In Sec. 9.1, we will discuss the recently implemented event detection and classification procedures that have led to such enhancement.

7.2 Experimental Trials

Before the $\overline{\mathrm{p}}$ and e^+ are mixed together, the $\overline{\mathrm{p}}$ plasma is in a state illustrated in Fig. 7.4. The $\overline{\mathrm{p}}$ have equilibrated with the few embedded e^- to a temperature of about 30 K (before adiabatic cooling). Since the $\overline{\mathrm{p}}$ and e^+ are confined in neighboring but separate wells, there necessarily exists an energy barrier between the two species that the $\overline{\mathrm{p}}$ must cross before $\overline{\mathrm{H}}$ formation can proceed.

As described above, the precise method by which $\overline{\mathrm{p}}$ are excited into the e^+ plasma is routinely varied. In all cases, the $\overline{\mathrm{p}}$ are exposed to an rf frequency drive supplied by a function generator (SRS DS345). For the 20 $\overline{\mathrm{H}}$ trapping trials performed in 2011, we employed exclusively drives comprised of white noise between 300 kHz and 1 MHz and drives in which the frequency was chirped downwards. After some trials in which the frequency was chirped, the e^+ well depth was swept downwards and inverted to allow all particles the opportunity to participate in $\overline{\mathrm{H}}$ formation. Further details about the various methods and drive parameters are discussed in the subsections below.

Because the $\overline{\mathrm{p}}$ are confined in an anharmonic well, their center-of-mass (COM) frequency varies as a function of their energy. To successfully excite $\overline{\mathrm{p}}$ to progressively higher energies, some frequency component of the applied drive must be in resonance with the $\overline{\mathrm{p}}$ COM oscillation. This condition is readily accomplished by noise drives, since there are Fourier components at all oscillation frequencies. Chirp drives satisfy the resonance condition by changing the applied frequency throughout the drive so as to match the changing $\overline{\mathrm{p}}$ resonant frequency. Historically, noise drives, chirped drives, and fixed-frequency drives [4, 62] have all been used to excite $\overline{\mathrm{p}}$ into the e^+ cloud to form $\overline{\mathrm{H}}$.

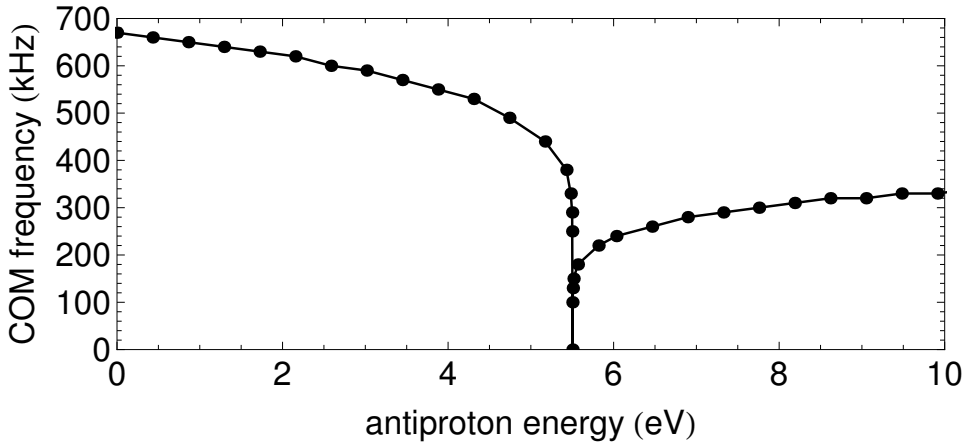

Figure 7.5: The $\overline{\mathrm{p}}$ COM frequency in the nested well varies as a function of the excitation energy. Points to the right of the sharp singularity indicate that the $\overline{\mathrm{p}}$ are energetic enough to cross the central nested well barrier.

The $\overline{\mathrm{p}}$ COM frequency as a function of excitation energy is shown in Fig. 7.5. For $\overline{\mathrm{p}}$ energies of less than about 5 eV, the decreasing concavity of the confining well leads to a decreasing resonant frequency. As the energy increases towards 5.5 eV, the COM frequency drops precipitously. The singularity at 5.5 eV is a real artifact of the nested well structure, since $\overline{\mathrm{p}}$ with *just* the right kinetic energy will reach a turning point at the center of the nested well and remain in an unstable equilibrium. As the energy is increased past the bifurcation point, the $\overline{\mathrm{p}}$ gain access to the second half of the nested well. The resonant frequency is roughly halved since the $\overline{\mathrm{p}}$ traverse roughly twice the distance in an oscillation period. Excitation drives attempt to increase the $\overline{\mathrm{p}}$ energy to just below the bifurcation point so that they may enter the e^+ plasma with as little axial energy as possible. Continuing to drive $\overline{\mathrm{p}}$ higher in energy (with $f \lesssim 300$ kHz) leads to hot $\overline{\mathrm{p}}$, which must be heavily cooled by e^+ before they may participate in cold $\overline{\mathrm{H}}$ formation.

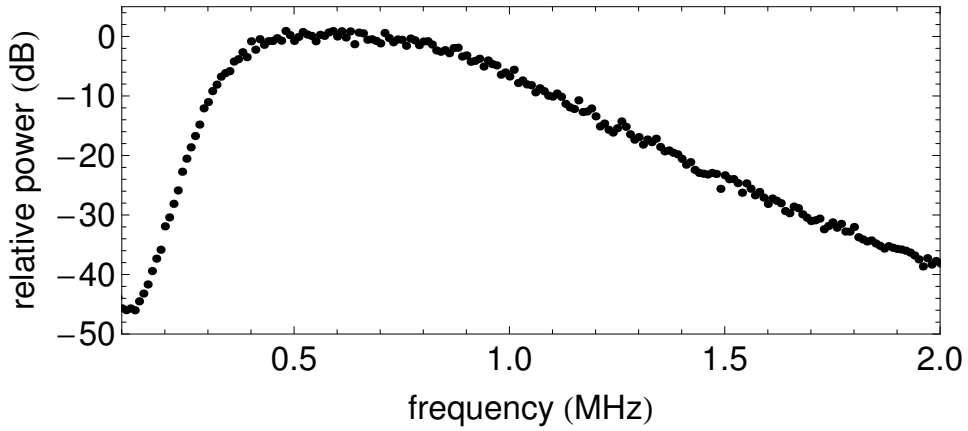

Figure 7.6: Transmitted power of white noise through the Chebyshev band-pass filter. The 3 dB points are designed to be 300 kHz and 1 MHz.

7.2.1 Noise Drives

The SRS DS345 frequency generator can output a white noise spectrum between 0 and 10 MHz. As shown in Fig. 7.5, frequency components above ≈ 1 MHz do not interact with $\overline{\mathrm{p}}$ COM frequencies at any energy, and instead broadcast power into the cryogenic environment and deposit unwanted heat. Conversely, low-frequency components below ≈ 300 kHz can excite $\overline{\mathrm{p}}$ too high in energy, and are unwanted as well.

Accordingly, we insert a filter between the frequency generator and the trap electrode, with a frequency response shown in Fig. 7.6. A fifth-order high-pass and a third-order low pass Chebyshev filter restrict the passband to be between 300 kHz and 1 MHz (at 3 dB attenuation). The filter sits at room temperature to block undesirable frequencies from propagating down to the low-temperature regions of the apparatus.

For all trials, the noise drive is applied for 10 minutes, significantly longer than the equilibration time within the plasma. In steady-state, a sizable percentage of the $\overline{\mathrm{p}}$

plasma overlaps in energy with the e^+ so that $\overline{H}$ may be formed. The long interaction time permits larger numbers of $\overline{H}$ to be created. However, as $\overline{p}$ continue to be driven through the e^+, many $\overline{p}$ follow diverging magnetic field lines into the electrode walls and are lost from the trap. Space-charge depletion of $\overline{p}$ increases the relative barrier height between the two species, leading to an observed suppression of $\overline{H}$ production at times longer than 10 minutes.

The steady-state temperature is determined by the balance between noise-drive heating and embedded e^- cooling. The $\overline{p}$ plasma is excited to higher temperatures when large drive amplitudes are applied, causing a larger fraction to overlap with e^+ energies. Yet, when $\overline{p}$ are injected into the e^+ plasma with large kinetic energies, they may form hot $\overline{H}$ unless e^+ cooling reduces their temperature before $\overline{H}$ recombination occurs. The target drive amplitude is thus one for which only a minority of $\overline{p}$ are excited into the e^+ cloud at any given time. A $\overline{p}$ with just enough energy to surmount the central nested well barrier will enter the e^+ plasma nearly at rest and may form cold, trappable $\overline{H}$.

Fig. 7.7 shows the steady-state $\overline{p}$ distribution while a -9 dBm noise drive is applied. The drive is sufficient to increase the $\overline{p}$ temperature from 30 K to 10^4 K, exciting approximately 20% of the $\overline{p}$ into the e^+ energy range. The figure also highlights a potential drawback of the noise drive method, namely that a majority of $\overline{p}$ never have the opportunity to interact with e^+ and form $\overline{H}$. This property remains true even for much stronger drives, since the plasma thermalizes through $\overline{p}$-$\overline{p}$ collisions and since the Maxwell-Boltzmann distribution has a finite population at low energy. As we will see next, chirped drives circumvent this difficulty and more allow many

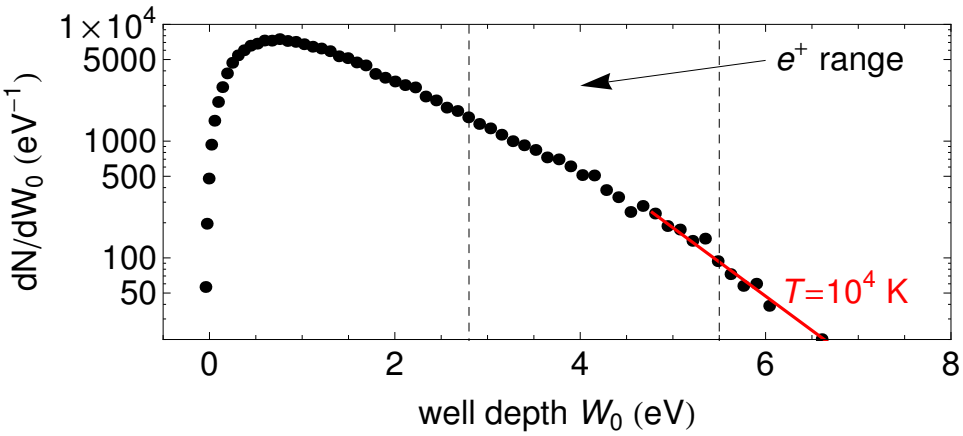

Figure 7.7: The $\overline{\mathrm{p}}$ distribution is significantly broadened by the application of a noise drive. In this example, $\approx 20\%$ of the $\overline{\mathrm{p}}$ overlap the e^+ distribution in energy. A $\overline{\mathrm{p}}$ temperature of 10^4 K is extracted by the methods presented in Sec. 6.1.

more $\overline{\mathrm{p}}$ to participate in $\overline{\mathrm{H}}$ creation.

7.2.2 Coherent Chirped Drives

The SRS DS345 frequency generator can also be made to output a frequency that varies from an initial value f_i to a final value f_f in a time t_{drive}. In contrast to noise drives, such chirped drives seek to excite the $\overline{\mathrm{p}}$ while remaining in resonance with their decreasing COM frequency [4, 149]. If the drive is of sufficient amplitude, the entire $\overline{\mathrm{p}}$ plasma acts like a single particle and may be excited coherently [177]. Ideally, the $\overline{\mathrm{p}}$ energy can be increased (i.e. oscillation amplitude made larger) without raising the $\overline{\mathrm{p}}$ temperature.

The time t_{drive} is optimized when the relation $1/f_{COM} \ll t_{drive} \ll 1/\nu_c$ is satisfied, where $1/f_{COM}$ is the $\overline{\mathrm{p}}$ axial oscillation period and $1/\nu_c$ is the $\overline{\mathrm{p}}$-$\overline{\mathrm{p}}$ collision time. Short drive times (compared with the axial bounce period) should be avoided since they can no longer be considered adiabatic and may lose phase lock with the $\overline{\mathrm{p}}$ plasma.

In the opposite limit, $\overline{\text{p}}$-$\overline{\text{p}}$ collisions are a source of decoherence, so the chirp should conclude before collisions restore a Maxwell-Boltzmann energy distribution. For the typical $\overline{\text{p}}$ plasma parameters used in these trials ($N = 10^6$, $n = 10^6$ cm^{-3}), we find $1/f_{COM} = 1.5$ μs and $1/\nu_c = 5$ ms, setting experimentally reasonable bounds for t_{drive}.

Accordingly, we investigated the $\overline{\text{p}}$ distribution after setting $t_{drive} = 2$ ms - nearly the shortest chirp time allowable by the SRS DS345 frequency generator. Empirically, we have found that the $\overline{\text{p}}$ may be excited by drive frequencies up to 900 kHz and begin overlapping with e^+ energies when the COM frequency is approximately 600 kHz. The observed deviation from the frequencies calculated in Fig. 7.5 is not well understood. It is possible that the applied frequency must always be blue detuned from the resonant frequency to ensure that the $\overline{\text{p}}$ are driven preferentially to lower frequencies (and higher excitation energies). It may also be possible that contributions from the off-axis $\overline{\text{p}}$ (in deeper confining wells with larger concavity and axial bounce frequency) cannot be entirely neglected.

The $\overline{\text{p}}$ distributions after applying a 2 ms chirped drive are shown in Fig. 7.8. Surprisingly, no coherent excitation was observed. The width of the distribution has become slightly larger (compared with Fig. 7.4), but a significant population remains at low energy, and only a small fraction of $\overline{\text{p}}$ reach the e^+ energy range. Marginally more $\overline{\text{p}}$ can be excited when the final frequency f_f is decreased to 600 kHz (compared with 700 kHz), though the large general features do not change. The situation was not improved by changing the drive amplitude, since larger amplitudes led to significant $\overline{\text{p}}$ losses, while smaller amplitudes gave hardly any excitation at all.

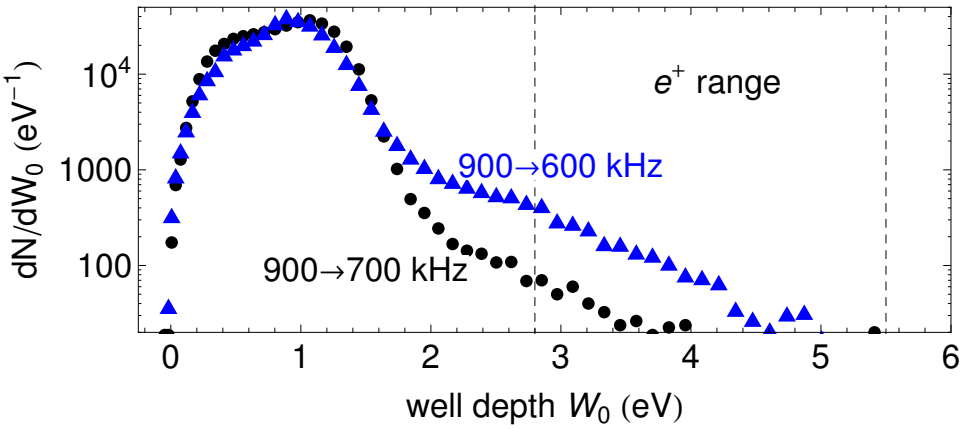

Figure 7.8: $\overline{\text{p}}$ distributions after applying a 2 ms chirped drive from 900 → 700 kHz (black circles) and from 900 → 600 kHz (blue triangles). Only a small fraction of $\overline{\text{p}}$ energies overlap with the e^+, and a large fraction remain unexcited.

When the same experiment is performed without the Ioffe trap energized, nearly half of the $\overline{\text{p}}$ are excited coherently by the drive. We now believe that the strong radial gradient of the quadrupole Ioffe field makes coherent excitation impossible. Driving coherently presupposes that the $\overline{\text{p}}$ COM mode is narrow and well-defined, so that the bulk plasma behaves like a single particle [177]. However, diverging magnetic field lines within the Ioffe trap cause the $\overline{\text{p}}$ "axial" motion to have $\hat{x}, \hat{y}$, and $\hat{z}$ components. The COM oscillation - purely along $\hat{z}$ - is thus strongly coupled to higher-order plasma modes. Exciting the COM mode with a resonant drive no longer guarantees that the axial oscillation amplitude (and energy) will increase, since the absorbed energy can be shared among a large number of coupled modes. We anticipate more success in the future, when we will be able to apply coherent drives in the low-gradient field of a Ioffe octupole trap (currently under construction).

7.2.3 Slow Chirped Drives

In contrast to the coherent chirped drive method above, we have developed an excitation scheme that purposefully proceeds slowly compared to the $\overline{\text{p}}$ equilibration rate. As before, the drive is still chirped from f_i to $f_f < f_i$ in a time t_{drive}. However, t_{drive} is increased to be as long as 15 minutes (compared with 2 ms previously), and collisions play an important role in shaping the final distribution. By choosing f_i and f_f appropriately, up to 97% of the $\overline{\text{p}}$ may be excited to elevated energies.

Consider a fixed-frequency drive applied to a $\overline{\text{p}}$ plasma that is in resonance with the COM oscillation. Though the energy absorbed in the COM mode is shared with many other modes, the plasma as a whole steadily gains energy under continued application of the fixed drive until it moves out of resonance. Ordinarily (as is the case with noise drives), $\overline{\text{p}}$-$\overline{\text{p}}$ collisions will then broaden the energy distribution over time until a Maxwell-Boltzmann equilibrium is achieved. However, with the fixed-frequency drive still applied, $\overline{\text{p}}$ that lose energy in collisions fall back into resonance with the drive and may be re-excited. The equilibrium state of the plasma is thus similar to a Boltzmann distribution, but translated to higher energy. Of course, $\overline{\text{p}}$ that gain energy in collisions will remain unaffected by the drive and populate the high-energy tail of the Boltzmann-like distribution.

With such an equilibrium established, the process can be repeated by stepping the drive frequency downwards by a small amount. In response, the $\overline{\text{p}}$ plasma gains slightly more energy and rethermalizes to a new truncated Boltzmann distribution. Progressively decreasing the drive frequency in small steps is analogous to chirping the drive frequency downwards, provided the drive time is made long compared to

the thermalization time.

For the slow chirp drive to be fully successful, it is imperative that the initial frequency f_i be below the initial COM resonance. Fig. 7.9 shows the $\overline{\mathrm{p}}$ distributions after three different drives, with different initial frequencies f_i and the same final frequency $f_f = 700$ kHz. For each trial, the drive is applied for 10 minutes with a 0.06 Vpp amplitude. When f_i is set too low, as in Fig. 7.9a, a sizable portion of the distribution remains unexcited. Increasing f_i to 800 kHz addresses more $\overline{\mathrm{p}}$ at low energy, and setting $f_i = 900$ kHz excites as many as 97% of the $\overline{\mathrm{p}}$.

Tuning f_f affords control over the final $\overline{\mathrm{p}}$ excitation energy. The final frequency $f_f = 700$ kHz in Fig. 7.9 was specifically chosen to excite $\overline{\mathrm{p}}$ just below the e^+ energy range. If f_f is set lower (say, to 600 kHz), nearly all of the $\overline{\mathrm{p}}$ will pass through the e^+ plasma. Compared to noise-drive techniques, the slow chirped drive method can be used to match the $\overline{\mathrm{p}}$ and e^+ energy ranges much more efficiently. By tuning f_f, $\overline{\mathrm{p}}$ can be made to enter the e^+ cloud with a minimum of longitudinal energy. Due to the improved control over the final $\overline{\mathrm{p}}$ energies, the slow chirp technique serves as a workhorse of our trapped $\overline{\mathrm{H}}$ searches.

7.2.4 Chirped Drives with Positron Well Sweep

We explored one final method to mix $\overline{\mathrm{p}}$ and e^+ that builds off of the slow chirp drive technique. First, $\overline{\mathrm{p}}$ are slowly excited to an energy just below that of the e^+. As shown in Fig. 7.9c, this creates an energy gap between the lowest-energy $\overline{\mathrm{p}}$ and the bottom of the well. After excitation, the voltage applied to the e^+ well is swept upwards adiabatically in a time t_{sweep} until the well is inverted. During the sweep,

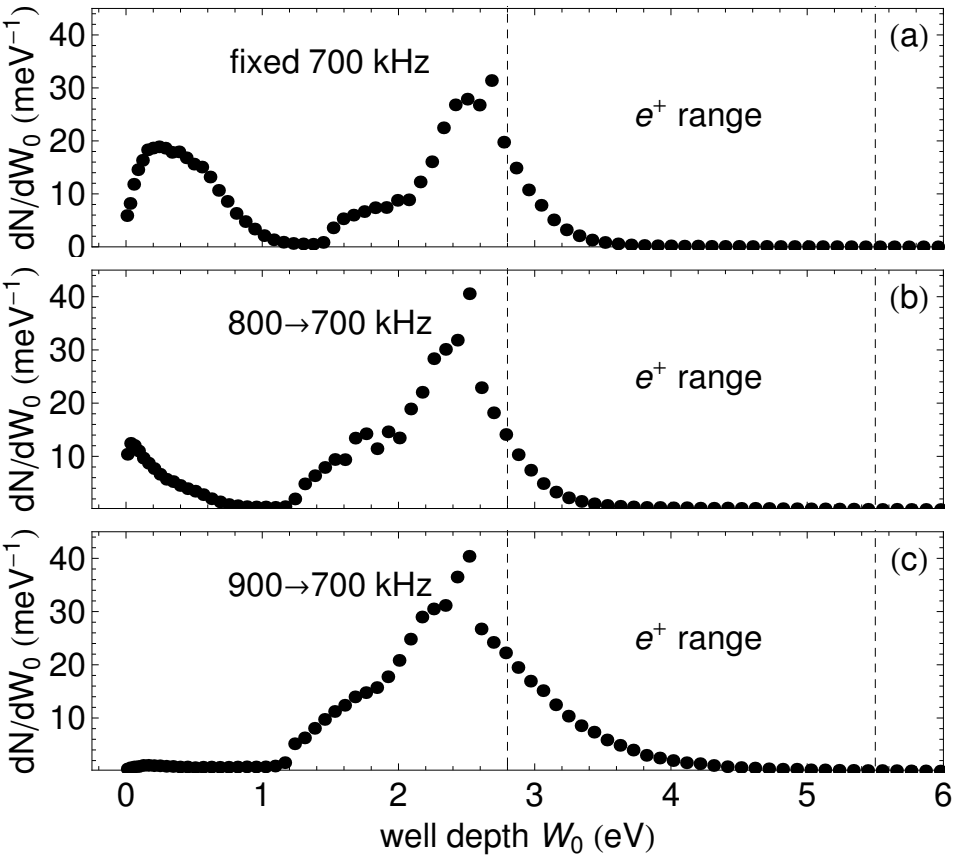

Figure 7.9: $\overline{\mathrm{p}}$ distributions after applying a 10 minute fixed drive at 700 kHz (a) and 10 minute chirped drives from 800 − 700 kHz (b) and 900 − 700 kHz (c). As the starting frequency is made higher, a larger fraction of $\overline{\mathrm{p}}$ are excited. The average energy of the excited $\overline{\mathrm{p}}$ remains constant in all cases and is set by the 700 kHz final frequency.

all of the $\overline{\mathrm{p}}$ have an opportunity to pass through the e^+ before the e^+ are ejected.

Let us first consider the process in the simpler case of a thermal $\overline{\mathrm{p}}$ distribution that fills the well down to zero energy. The $\overline{\mathrm{p}}$ sit below the e^+ energy range, and the two species do not yet interact. As we begin to lower the e^+ well depth, there comes a point at which the top of the e^+ and $\overline{\mathrm{p}}$ space-charge distributions are matched in energy (see Fig. 7.10a). At this point, the total potential through the e^+ and $\overline{\mathrm{p}}$ wells is flat, allowing particles of both types to escape through each other (Fig. 7.10b).

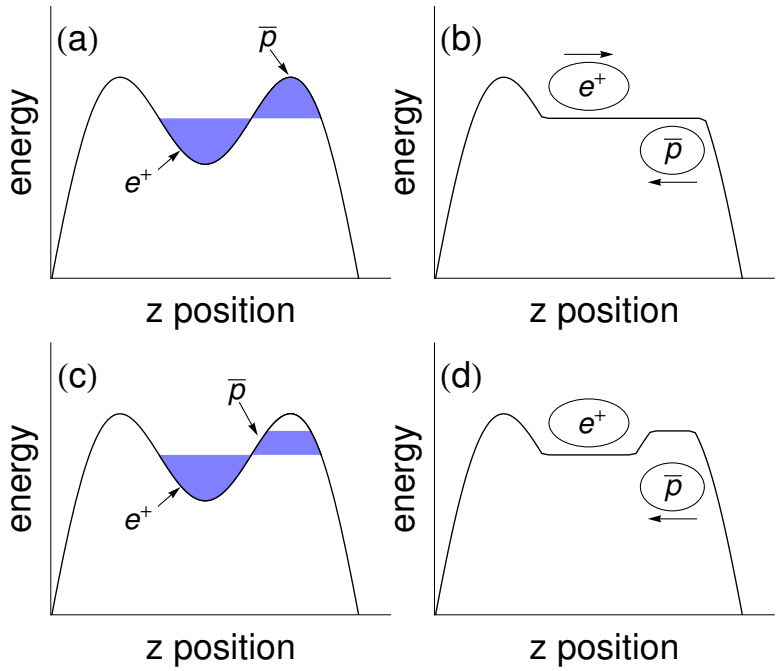

Figure 7.10: The on-axis potential (a) and total potential (b) when the e^+ and $\overline{p}$ space-charge potentials fill to the same level. Both species are no longer confined in their initial wells. When the $\overline{p}$ are excited above the bottom of their well (c), the total potential remains confining for e^+, but the $\overline{p}$ have enough energy to enter the e^+ plasma (d).

Particle loss soon depletes the space-charge width of both species and creates a new energy gap, suppressing the mixing process. However, the e^+ well depth may be lowered once more to restart the interaction. The process repeats until the e^+ well is completely inverted.

Though this technique has synthesized $\overline{H}$ in the past [57], two disadvantages may be identified. First, on account of their much lower mass and higher axial oscillation frequency, the e^+ escape at a much faster rate than the $\overline{p}$. Resultingly, only a reduced fraction of $\overline{p}$ are able to participate in $\overline{H}$ formation before the e^+ plasma is entirely depleted. Second, the $\overline{p}$ that do enter the e^+ plasma are almost invariably too hot to form trappable $\overline{H}$. Suppose a $\overline{p}$ is well-matched to the e^+ space-charge level, so that

it may enter with only a small amount of longitudinal energy. If the $\overline{\mathrm{p}}$ undergoes a collision before it forms $\overline{\mathrm{H}}$ (which is likely since $\nu_c > \nu_{tbr}$), it will either lose energy and fall out of contact with the e^+, or gain energy and continue traversing the e^+ plasma with a high kinetic energy. For trappable $\overline{\mathrm{H}}$ to be formed, the e^+ must hence re-cool the $\overline{\mathrm{p}}$ at a faster rate than recombination can take place. Comparisons of the calculated three-body rate [178] and the e^+ cooling rate [179] show that cooling of $\overline{\mathrm{p}}$ below approximately 8 K is not expected [66].

Now consider sweeping the e^+ well depth downwards after the $\overline{\mathrm{p}}$ have been excited using a slow chirped drive. As before, there will come a time during the sweep when the highest-energy $\overline{\mathrm{p}}$ and e^+ will overlap (Fig. 7.10c). However, since the $\overline{\mathrm{p}}$ distribution does not extend to the bottom of the well, the $\overline{\mathrm{p}}$ space-charge does not completely cancel out the applied potential (Fig. 7.10d). As a result, the e^+ remain confined, with a total well depth approximately equal to the energy gap between the lowest-energy $\overline{\mathrm{p}}$ and the bottom of the $\overline{\mathrm{p}}$ well. The $\overline{\mathrm{p}}$ must of course surmount a barrier of the same height to enter the e^+ cloud, but the slow chirped drive has given them precisely enough energy to do so.

Unlike the previous example, nearly all $\overline{\mathrm{p}}$ have an opportunity to mix with the full e^+ plasma as the e^+ well is swept upwards. The e^+ may only begin to escape once the well depth is decreased by the barrier height shown schematically in Fig. 7.10d. By this point, the e^+ have overlapped in energy with almost the entire width of the $\overline{\mathrm{p}}$ distribution, allowing for many more opportunities to form $\overline{\mathrm{H}}$.

The e^+ well sweep rate Γ_{sweep} is an important tunable parameter during experimental trials. The problem of collisions creating energetic $\overline{\mathrm{p}}$ may be avoided if the

sweep rate is set fast enough. For the calculated collision time $1/\nu_c \approx 0.01$ s, the 3 eV space-charge width of the $\overline{\mathrm{p}}$ determines a minimum sweep rate of $\Gamma_{sweep} > 300$ eV/s. Though it is possible to sweep slower than 300 eV/s and still form cold $\overline{\mathrm{H}}$, collisions will increasingly begin to effect the energy with which the $\overline{\mathrm{p}}$ enter the e^+ plasma.

Conversely, sweeping the e^+ well too quickly can also be detrimental to creating cold $\overline{\mathrm{H}}$. Ideally, the depth of the e^+ well should change by no more than 375 mK ($= 32$ μeV) during a single $\overline{\mathrm{p}}$ axial bounce period (≈ 2 μs). As the sweep rate is made faster than $\sim$ 16 eV/s, $\overline{\mathrm{p}}$ become increasingly likely to enter the e^+ cloud with more energy than the Ioffe trap depth of $k_B \times 375$ mK. Clearly, both desired limits $\Gamma_{sweep} > 300$ eV/s and $\Gamma_{sweep} < 16$ eV/s cannot be simultaneously satisfied, so a compromise must be made. Accordingly, we have varied the sweep rate from 0.10 eV/s to 3500 eV/s (corresponding to sweep times of 300 s to 9 ms) in the search for the optimal $\overline{\mathrm{H}}$ trapping parameters.

Chapter 8

Mirror-Trapped Antiprotons

During trapped $\overline{\mathrm{H}}$ searches, we are unable to discriminate between $\overline{\mathrm{H}}$ annihilations and annihilation signals from bare $\overline{\mathrm{p}}$. Although we apply a strong electric field to clear away charged particles after $\overline{\mathrm{p}}$-e^+ mixing, $\overline{\mathrm{p}}$ can remain directly "mirror-trapped" by the axial field of the Ioffe trap if their cyclotron energy is large enough. Here we consider the mirror-trapping mechanism and the $\overline{\mathrm{p}}$ energies required, and we argue that no identifiable process can provide a $\overline{\mathrm{p}}$ with even a sizable fraction of the energy required for it to remain mirror-trapped.

The ALPHA collaboration was similarly concerned about mirror-trapped $\overline{\mathrm{p}}$ corrupting their trapped $\overline{\mathrm{H}}$ experiments [180, 181]. Their simulations predicted that no $\overline{\mathrm{p}}$ could be energetic enough to remain mirror-trapped in their apparatus after an electric clearing field was applied, a result confirmed by their experimental observations. Compared with the ALPHA apparatus, the smaller fractional change in Ioffe field strength within the BTRAP apparatus places an even more stringent limit on the minimum energy of mirror-trapped $\overline{\mathrm{p}}$. Since we calculate a negligible probability

for mirror-traping to occur, and since no mirror-trapped $\overline{\mathrm{p}}$ were observed even in conditions substantially less favorable than our own, we conclude that mirror-trapped $\overline{\mathrm{p}}$ cannot influence our trapped $\overline{\mathrm{H}}$ measurements.

8.1 Mechanism

A bare $\overline{\mathrm{p}}$ moving in the fields of a Penning-Ioffe trap executes a modified cyclotron, axial, and magnetron motion compared to the simple Penning trap [53]. Adiabatic invariants [85] may be identified for each of these motions, provided that the magnetic field changes slowly along the $\overline{\mathrm{p}}$ trajectory (a condition easily satisfied within the trap). For a $\overline{\mathrm{p}}$ with cyclotron energy E_c, its magnetic moment $\mu_{\overline{\mathrm{p}}} = E_c/|\vec{B}|$ is an adiabatic invariant of the cyclotron motion. As $|\vec{B}|$ increases, E_c also increases to keep $\mu_{\overline{\mathrm{p}}}$ fixed.

The total energy of the $\overline{\mathrm{p}}$, given by the sum of the cyclotron energy E_c and the translational kinetic energy E_T, also remains fixed. Thus as a $\overline{\mathrm{p}}$ moves from a region of weak $|\vec{B}|$ to strong $|\vec{B}|$, E_c increases to keep $\mu_{\overline{\mathrm{p}}}$ invariant, and E_T decreases to keep the total energy constant. If the $\overline{\mathrm{p}}$ moves into a field with $|\vec{B}|$ so large as to cause $E_T = 0$, the $\overline{\mathrm{p}}$ will have reached a turning point, reverse its trajectory, and remain "mirror-trapped". In our apparatus, annihilations of mirror-trapped $\overline{\mathrm{p}}$ are indistinguishable from annihilations of trapped $\overline{\mathrm{H}}$, so it is critical to investigate whether any mirror-trapped $\overline{\mathrm{p}}$ could survive.

By equating the total energies for a $\overline{\mathrm{p}}$ starting its motion in a field $|\vec{B}| = B_0$ with kinetic energy E_T and reaching a turning point at $|\vec{B}| = B > B_0$, we can find the minimum E_T necessary to ensure that a $\overline{\mathrm{p}}$ with an initial cyclotron energy E_c will

not be mirror-trapped

$$E_T \geq E_c \left(\frac{B}{B_0} - 1 \right) \tag{8.1}$$

Substituting $B_0 = 2.15$ T and $B_{max} = 2.71$ T for our Ioffe trap (as seen in Fig. 7.2c), a $\overline{\mathrm{p}}$ must have a kinetic energy $E_T \geq 0.26 E_c$ to avoid being mirror-trapped. In a thermalized plasma of 4 K $\overline{\mathrm{p}}$, about 8% would not satisfy this condition, which is an unacceptably large fraction.

It is for this reason that we apply the strong clearing electric potential described in Sec. 7.1. When the potential Φ is applied, an additional term $-q\Phi$ must be added to the total energy. Equating the total energy at the center of the trap, where $|\vec{B}| = B_0$ and $\Phi = \Phi_0$, to the energy at some other point parameterized by B and Φ, our condition becomes

$$E_T \geq E_c \left(\frac{B}{B_0} - 1 \right) - q \left(\Phi - \Phi_0 \right) \tag{8.2}$$

Unlike Eqn. 8.1, it is possible to satisfy Eqn. 8.2 for any E_c and B, even when $E_T = 0$, if Φ is made large enough. Note that since $(B/B_0 - 1) = 0.26$ in BTRAP, compared with $(B/B_0 - 1) = 1.0$ in the ALPHA apparatus, we may tolerate a markedly larger value of E_c while still satisfying Eqn. 8.2 (for fixed E_T and Φ).

8.2 Mirror-Trapping On-Axis

To determine whether a $\overline{\mathrm{p}}$ with a given E_c will remain mirror-trapped with the clearing potential applied, we consider the most restrictive case of a $\overline{\mathrm{p}}$ with $E_T = 0$. The right-hand side of Eqn. 8.2 can then be treated as a pseudopotential through which the $\overline{\mathrm{p}}$ moves. A $\overline{\mathrm{p}}$ will only remain mirror-trapped if it remains in a local min-

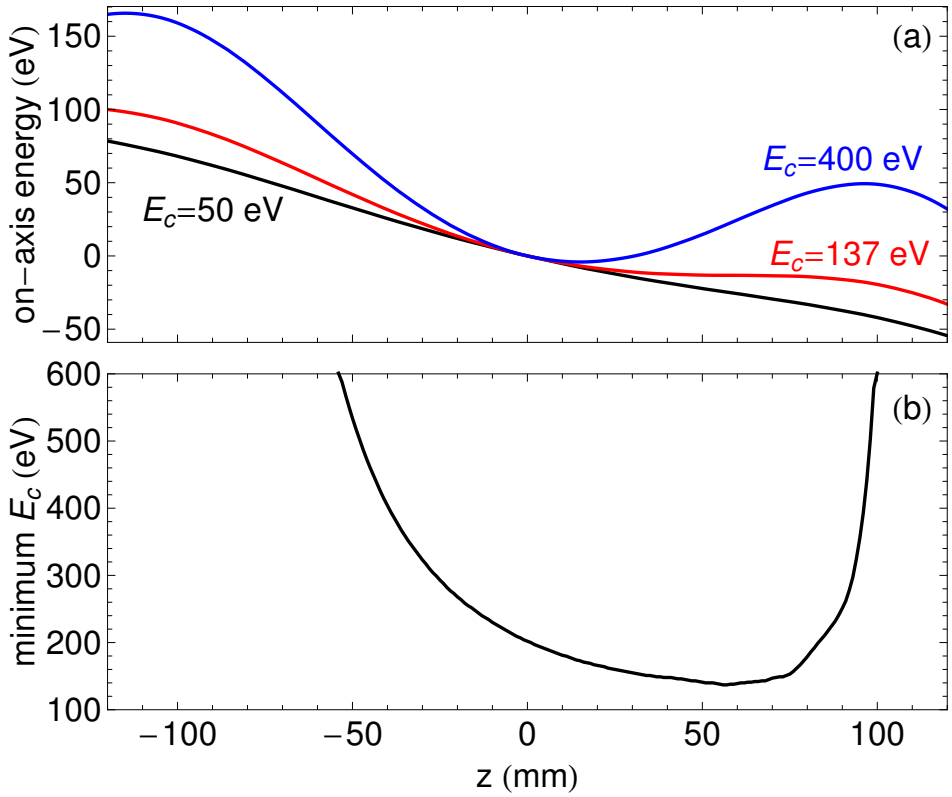

Figure 8.1: (a) The pseudopotential on-axis is plotted for 3 different values of $\overline{\text{p}}$ cyclotron energy E_c when an electric clearing field of 0.5 V/mm is applied. At E_c = 137 eV, the pseudopotential just begins to show a local minimum. (b) Minimum value E_c a $\overline{\text{p}}$ would need to remain mirror-trapped when starting at different axial positions z.

imum of the pseudopotential as it bounces axially and magnetron drifts azimuthally along its trajectory.

The trajectory of a $\overline{\text{p}}$ starting on the trap axis with $E_T = 0$ is constrained to move along $\hat{z}$. Since the on-axis potential $\Phi(z)$ is known (dashed line, Fig. 7.2d) as well as the on-axis magnetic field strength $B(z)$ (Fig. 7.2c), we can directly calculate the on-axis pseudopotential energy for various choices of E_c. If the pseudopotential exhibits a local minimum, then a $\overline{\text{p}}$ with that E_c could remain mirror-trapped.

Fig. 8.1a plots the on-axis pseudopotential energy as a function of axial position

for three values of E_c. With the ≈ 0.5 V/mm electric clearing field applied, the pseudopotential contains no local minimum until $E_c > 137$ eV. Thus, any $\overline{\mathrm{p}}$ on-axis with $E_c < 137$ eV will be swept away by the clearing potential, while those with $E_c > 137$ eV can remain mirror-trapped if they are localized in the pseudopotential well with too small an energy E_T to escape.

If a $\overline{\mathrm{p}}$ starts with $E_T = 0$ far to the left in Fig. 8.1a, it may still have enough energy to escape even if $E_c > 137$ eV. Fig. 8.1b plots the minimum cyclotron energy a $\overline{\mathrm{p}}$ would need to remain mirror-trapped when starting from different values of z on-axis. As expected, the curve reaches a minimum at 137 eV. Away from the minimum, the curve rises to the left on account of the longer distance over which the clearing potential can accelerate $\overline{\mathrm{p}}$, while the curve rises to the right as $\overline{\mathrm{p}}$ are no longer localized in the confining well of the pseudopotential.

8.3 Mirror-Trapping Off-Axis

The off-axis trajectories for a $\overline{\mathrm{p}}$ in a Penning-Ioffe trap are more complicated due to the presence of the radial Ioffe field. The magnetic field lines, some of which are shown in Fig. 8.2a, no longer point along $\hat{z}$ and diverge exponentially in the planes aligned with the Ioffe current bars. Nonetheless, the pseudopotential along these field lines may be calculated in the same way as above, as shown in Fig. 8.2b.

To determine if any $\overline{\mathrm{p}}$ with $E_c < 137$ eV may be mirror-trapped off-axis, we calculated $\overline{\mathrm{p}}$ trajectories starting from different locations in the trap. To ease calculations, we employ the guiding center approximation, in which the fast cyclotron motion is replaced by the adiabatically invariant magnetic moment $\mu_{\overline{\mathrm{p}}}$ that remains aligned with

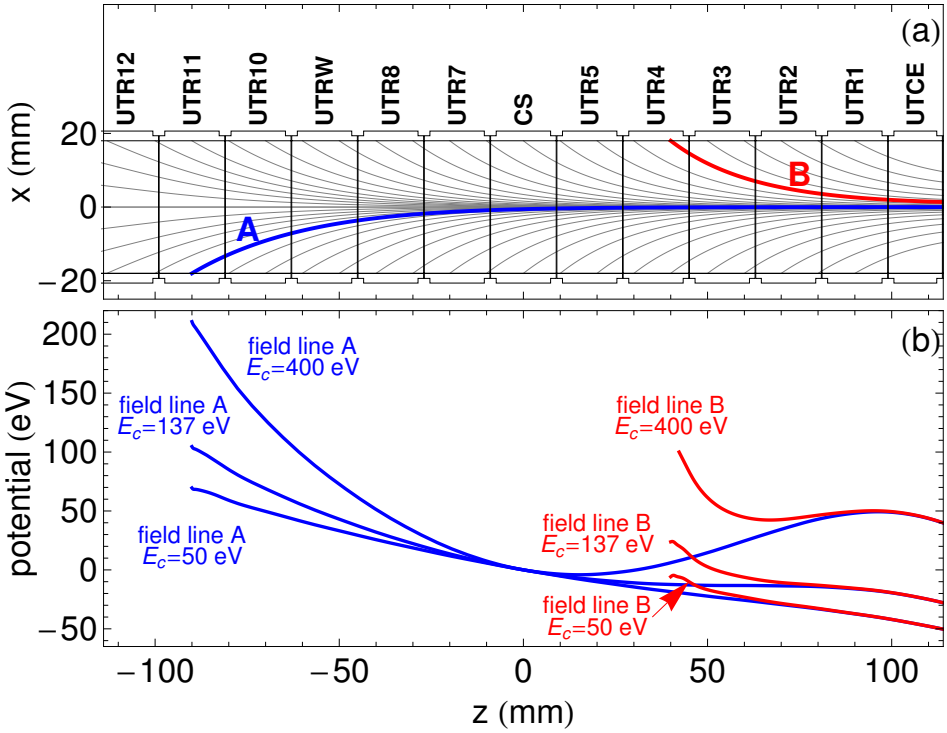

Figure 8.2: (a) A sample of the maximally-divergent magnetic field lines in the Penning-Ioffe trap. For various values of E_c, the pseudopotential along the two indicated field lines is plotted in (b), projected on the z axis.

the local magnetic field. Trajectories for $\overline{\mathrm{p}}$ off-axis are thus axial excursions along a magnetic field line with a slight change in azimuthal angle during each bounce due to the magnetron drift.

A $\overline{\mathrm{p}}$ will only remain mirror-trapped if it stays in a local minimum of the pseudopotential throughout its entire trajectory. For example, consider a $\overline{\mathrm{p}}$ with $E_c = 200$ eV starting at the coordinates $\rho = 10$ mm, $\phi = \pi/2$, and $z = 70$ mm. This $\overline{\mathrm{p}}$ will be mirror-trapped initially, as shown in Fig. 8.3. However, as the $\overline{\mathrm{p}}$ magnetron drift changes the azimuthal angle ϕ, the pseudopotential becomes less confining until, at $\phi = 0.94\pi$, the $\overline{\mathrm{p}}$ escapes. A $\overline{\mathrm{p}}$ is only confined in a stable mirror-trapped trajectory if the pseudopotential is confining for all ϕ.

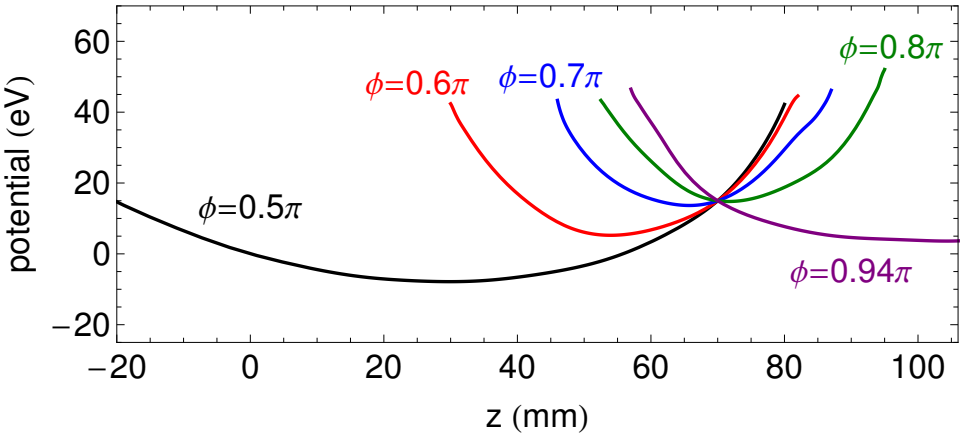

Figure 8.3: The value of the pseudopotential is plotted along magnetic field lines passing through $\rho = 10$ mm, $\phi = \{0.5\pi, 0.6\pi, 0.7\pi, 0.8\pi, 0.94\pi\}$, and $z = 70$ mm for a $\overline{\text{p}}$ with $E_c = 200$ eV. Though the $\overline{\text{p}}$ may be temporarily mirror-trapped when $\phi = 0.5\pi$, magnetron drift allows the $\overline{\text{p}}$ to escape once its azimuthal angle crosses $\phi = 0.94\pi$.

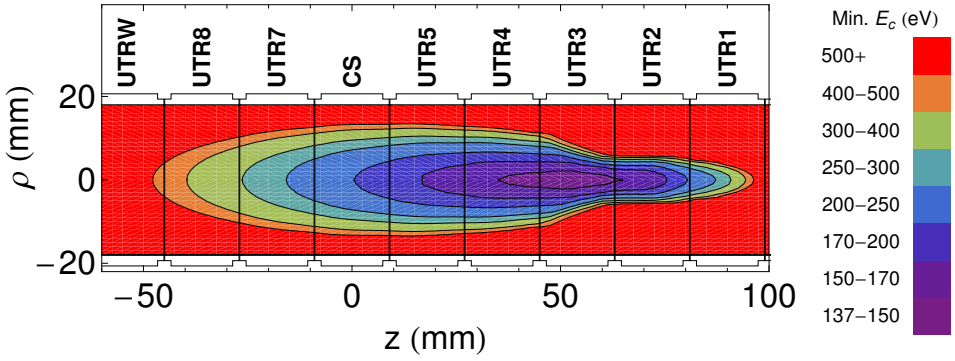

Figure 8.4: The minimum cyclotron energy E_c necessary for a $\overline{\text{p}}$ to remain mirror-trapped as a function of starting position. The global minimum $E_c = 137$ eV falls along the central axis of the trap.

With knowledge of the off-axis pseudopotential and $\overline{\text{p}}$ trajectories, we may determine the global minimum E_c for mirror-trapping. In analogy to the on-axis case presented in Fig. 8.1b, Fig. 8.4 shows the minimum E_c required for a $\overline{\text{p}}$ with $E_T = 0$ starting anywhere in the trap. The result is that no $\overline{\text{p}}$ with $E_c < 137$ eV can remain in the trap – the same result as the on-axis case, but verified everywhere.

8.4 Antiproton Energy Scales

We must now ask whether any mechanisms exist that might create $\overline{\mathrm{p}}$ with cyclotron energies larger than 137 eV. Both thermal and non-thermal excitations are considered from the time $\overline{\mathrm{p}}$ are initially loaded through the time at which they are cleared away. However, we can identify no process through which a $\overline{\mathrm{p}}$ may gain even a substantial fraction of the 137 eV necessary for it to remain mirror-trapped.

We first consider the $\overline{\mathrm{p}}$ distribution before $\overline{\mathrm{H}}$ formation takes place. After catching, cooling, and transferring $\overline{\mathrm{p}}$ to the nested well, their temperature has been directly measured to be 31 K before adiabatic cooling [163]. For a $\overline{\mathrm{p}}$ density of $\approx 10^6$ cm^{-3}, the isotropization rate between axial and cyclotron energy is 330 Hz [108], which is fast enough to assure that the axial and cyclotron temperatures are in thermal equilibrium with each other. For a thermal distribution of cyclotron energies centered around $E_c = 31$ K $= 2.7$ meV, the probability of having $E_c > 137$ eV is $\approx e^{-50000}$, a factor that overwhelmingly rules out any mirror-trappable $\overline{\mathrm{p}}$ at this stage.

In principle, there may also be a small non-thermal component of $\overline{\mathrm{p}}$ in the nested well before $\overline{\mathrm{H}}$ is formed. These $\overline{\mathrm{p}}$ may be confined at large radii, avoiding thermalizing collisions with the bulk of the $\overline{\mathrm{p}}$ plasma. However, we find that the thermalized $\overline{\mathrm{p}}$ plasma has a radius just inside the cutoff radius of the quadrupole Ioffe trap; any $\overline{\mathrm{p}}$ at larger radii will necessarily be ballistically lost from the trap as they follow diverging magnetic field lines into the electrode walls.

To excite $\overline{\mathrm{p}}$ into the e^+ plasma, we apply drives in which the applied frequency is either chirped or broadened by noise. The $\overline{\mathrm{p}}$ cyclotron energy is not directly excited, since both types of drives are cylindrically symmetric. Instead, the $\overline{\mathrm{p}}$ gain axial

energy, and collisions equilibrate the axial and cyclotron motions, leaving them both in a thermal distribution at the same temperature.

For every set of drive parameters, the axial $\overline{\mathrm{p}}$ temperature has been measured following their excitation. In the most extreme case, when the strongest noise-broadened drive was applied for 10 minutes, the $\overline{\mathrm{p}}$ axial (and hence cyclotron) energy was found to be 1 eV. For a thermal distribution at this energy, only a single $\overline{\mathrm{p}}$ out of 10^6 has a cyclotron energy larger than 15 eV. Since all $\overline{\mathrm{p}}$ with $E_c < 137$ eV are ejected by the clearing electric field, the probability that a single $\overline{\mathrm{p}}$ could remain mirror-trapped falls to $\approx 10^{-53}$.

The $\overline{\mathrm{p}}$ temperature is measured only after the conclusion of the excitation, and we therefore lack a direct measurement during application of the drive. However, we may set upper bounds on the axial energy by observing $\overline{\mathrm{p}}$ loss rates. Approximately 500 out of 10^6 $\overline{\mathrm{p}}$ in a 3 eV thermal distribution would have enough axial energy to escape the 27 eV deep nested well. Since such loss is not observed, the $\overline{\mathrm{p}}$ energy must always be less than 3 eV (consistent with our direct measurements). Even more stringent bounds may be placed by observing the number of $\overline{\mathrm{p}}$ escaping over the 5 eV central nested well barrier. In all cases, the probability of creating a mirror-trappable $\overline{\mathrm{p}}$ during the drive is negligible.

As the $\overline{\mathrm{p}}$ mix with e^+ to form $\overline{\mathrm{H}}$, they are likely to lose cyclotron energy since the two species equilibrate at a rate faster than the recombination rate. The e^+ cooling of $\overline{\mathrm{p}}$ has long been demonstrated [46], with a collisional cooling rate of approximately 100 s^{-1} for a e^+ plasma with a density of 5×10^7 cm^{-3} in a 2.2 T magnetic field [179]. At the 31 K e^+ temperature, the three-body recombination rate is nearly two orders

of magnitude smaller than the collisional cooling rate [141], which affords sufficient time for any $\overline{\mathrm{p}}$ with large amounts of cyclotron energy to equilibrate with the e^+.

During the mixing of $\overline{\mathrm{p}}$ and e^+, $\overline{\mathrm{H}}$ atoms are formed with a temperature dominated by the temperature of the recombining $\overline{\mathrm{p}}$. The newly-formed $\overline{\mathrm{H}}$ may be ionized by electric fields within the trap, leaving a bare $\overline{\mathrm{p}}$ with some axial and cyclotron energy. Although the above arguments already demonstrate that $\overline{\mathrm{p}}$ created through this process cannot posses a significant cyclotron energy, knowledge of the trap electric and magnetic fields may be used to set an independently stringent upper bound.

The largest electric field within the trap volume is 55 V/mm, located near the gap between two independently-biased electrodes. In the rare case that an $\overline{\mathrm{H}}$ traverses this region, it will be ionized if its principal quantum number $n > 27$. However, no high-velocity $\overline{\mathrm{H}}$ can make it to large radii. Due to its motion through a magnetic field, an $\overline{\mathrm{H}}$ atom "sees" a Lorentz-transformed transverse electric field of strength vB_0, which may also cause ionization.

Three possibilities thus exist for an $\overline{\mathrm{H}}$ atom. First, $\overline{\mathrm{H}}$ may be produced with a large velocity, whereupon it will immediately ionize due to the motional electric field and rethermalize with the e^+. Second, it may be produced with a low velocity and be ionized by the static electric fields within the trap. The maximum $\overline{\mathrm{H}}$ velocity at which this may occur is $v_{max} = |\vec{E}|/B_0$, which corresponds in the worst case to only 3 eV. Finally, an $\overline{\mathrm{H}}$ may be moving too slowly or be too deeply bound to be ionized at all, in which case it will either remain trapped or annihilate upon the electrode walls. In no case can a bare $\overline{\mathrm{p}}$ be created with a cyclotron energy comparable to 137 eV.

If an $\overline{\mathrm{H}}$ atom is ionized at a place in the trap with a deeper potential than the

place at which it was formed, the bare $\overline{\mathrm{p}}$ will gain the difference in potential energy. At most, this process could create a $\overline{\mathrm{p}}$ with 40 eV of axial energy if the ionization took place just inside the electrode wall and if the $\overline{\mathrm{p}}$ avoided annihilation with the electrode surface. Collisions would thus be required to both convert axial into cyclotron energy as well as boost the cyclotron energy above 137 eV. If a $\overline{\mathrm{p}}$ formed by ionization collides with the bulk of the thermalized $\overline{\mathrm{p}}$ or e^+ plasma, it would quickly lose energy until it attains thermal equilibrium. Collisions with similarly-ionized $\overline{\mathrm{p}}$ could broaden the distribution of cyclotron energies in principle, but such collisions are exceedingly rare; we very conservatively estimate the collision rate to be only 2×10^{-5} Hz, which is negligibly slow compared with our $\overline{\mathrm{H}}$ formation times.

Considering that $\overline{\mathrm{p}}$ cannot start with and cannot gain enough energy to become mirror trapped before, during, and after $\overline{\mathrm{H}}$ formation, we conclude that mirror-trapped $\overline{\mathrm{p}}$ cannot generate a false trapped $\overline{\mathrm{H}}$ signal. One final technical reason further supports this argument: only the radial Ioffe field is de-energized to allow trapped $\overline{\mathrm{H}}$ to escape. With the mirror-coils still at full-field, any mirror-trapped $\overline{\mathrm{p}}$ (should they exist) would remain confined and not produce an annihilation signal as the quadrupole field is reduced.

Chapter 9

Trapped Antihydrogen: Event Detection and Findings

With concerns that mirror-trapped $\overline{\mathrm{p}}$ could be confused with signatures of trapped $\overline{\mathrm{H}}$ dispelled, we begin this chapter by discussing the $\overline{\mathrm{H}}$ event detection and classification protocols. Taking the 20 trials performed in 2011 together, we find a signal corresponding to a total of 105 ± 21 $\overline{\mathrm{H}}$ atoms trapped for 15 to 1000 s, which we argue is long enough to ensure that they have reached their ground state. Finally, we are able to set a crude limit on the strength of the gravitational acceleration of antimatter using our trapped $\overline{\mathrm{H}}$ result.

9.1 Event Detection

As described in Sec. 2.7, scintillating fibers (two straight and two helical layers) and paddles (one inner and outer layer) surround the Penning-Ioffe trap. These

scintillators detect the desired $\overline{\mathrm{H}}$ annihilation signals (when the $\overline{\mathrm{p}}$ nucleus annihilates) in addition to the undesired signals from cosmic rays. Observing a small number of $\overline{\mathrm{H}}$ annihilation counts hidden within the cosmic ray background noise thus poses a significant challenge during the search for trapped $\overline{\mathrm{H}}$. Coincidencing between the fibers and paddles significantly reduces the background count rate from 500 Hz to 41 Hz (and the detection efficiency from 75% to 54%), but this rate is still too large for small numbers of $\overline{\mathrm{H}}$ to be seen during the 1 s quench of the Ioffe trap.

Differences in the specific subset of scintillators which fire in the presence of a $\overline{\mathrm{p}}$ annihilation or a cosmic ray allow us to further discriminate between signal and noise. Below, we describe the 12 different tests applied to events so that the distinctions between $\overline{\mathrm{p}}$ and cosmic rays may be amplified. We then describe how event classification can markedly improve the signal to noise ratio and present a Monte-Carlo simulation for determining the optimum trade-off between low background and high detection efficiency.

9.1.1 Event Classification

Before the Ioffe trap is quenched to release trapped $\overline{\mathrm{H}}$, we begin recording the timestamp, energy deposition, and set of triggered fibers and paddles for each scintillation event. The detector system continues acquiring events at a rate of up to 10^3 per second (much higher than needed for the observed count rate), until long after the Ioffe trap has reached zero field. This permits a direct comparison of the number of counts observed during the 1 s quench of the Ioffe trap with the number of counts observed beforehand and afterwards.

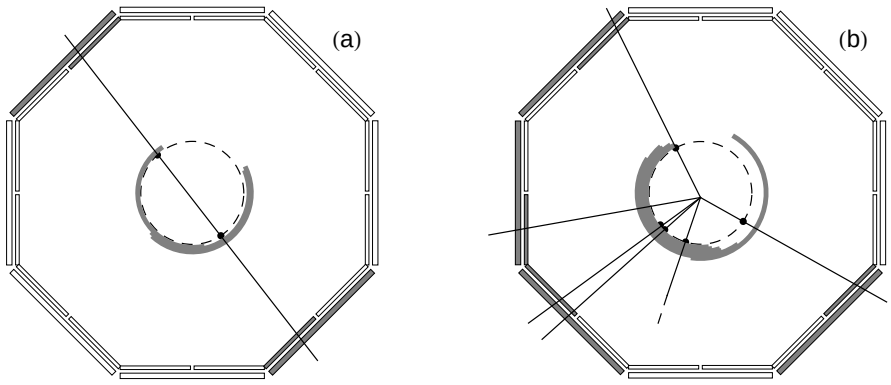

Figure 9.1: Events recorded by the detector system corresponding to (a) a cosmic ray traveling in a straight-line trajectory, and (b) a $\overline{\mathrm{p}}$ annihilation that cannot be reconciled with a single straight-line trajectory.

Each recorded event - be it a $\overline{\mathrm{p}}$ annihilation or cosmic ray - triggers at least two of the 808 scintillating detectors surrounding the apparatus. Since the position of each triggered detector is logged, we can reconstruct whether the trigger pattern is consistent with a straight-line trajectory (indicating a cosmic ray), or multiple non-colinear detector hits (indicating a $\overline{\mathrm{p}}$ annihilation). Fig. 9.1 shows the detector geometry and an example of the scintillators which may be triggered in the presence of both a cosmic ray and a $\overline{\mathrm{p}}$.

To objectively analyze the more than 3×10^4 events in our recent $\overline{\mathrm{H}}$ trapping experiments, we developed a set of criteria to preferentially identify $\overline{\mathrm{p}}$ compared with cosmic rays. An automated routine first characterizes the trigger pattern of each event. Nearest-neighbor and next-nearest-neighbor fibers that are simultaneously triggered are grouped together into "clusters," since a single high-energy particle can easily be responsible for multiple nearby hits. Clusters with at least 2 fibers are referred to as "multiplicity-2" and are less likely to have been caused by electrical

noise. We investigate whether clusters are separated by more than $\pi/8$ radians, indicating that they are caused by the passage of more than one high-energy particle. The number and position of paddle coincidences (an inner paddle along with its corresponding outer paddle) is also determined. Finally, the analysis code checks if the trigger pattern can be reconciled with a straight-line trajectory.

With this characterization complete, we test the trigger pattern of each event against 12 criteria developed by McConnell [66] and repeated here:

1. ≥ 1 paddle coincidence
2. ≥ 3 helical fiber clusters
3. ≥ 3 straight fiber clusters
4. ≥ 3 non-neighboring paddle coincidences
5. ≥ 5 helical fiber clusters and/or straight fiber clusters
6. ≥ 3 multiplicity-2 helical fiber clusters separated by more than $\pi/8$ rad., OR ≥ 4 multiplicity-2 helical fiber clusters, OR ≥ 4 helical fiber clusters separated by more than $\pi/8$ rad., OR ≥ 5 helical fiber clusters of any kind
7. ≥ 3 multiplicity-2 straight fiber clusters separated by more than $\pi/8$ rad., OR ≥ 4 multiplicity-2 straight fiber clusters, OR ≥ 4 straight fiber clusters separated by more than $\pi/8$ rad., OR ≥ 5 straight fiber clusters
8. ≥ 2 helical fiber clusters AND ≥ 1 paddle coincidence or straight fiber. The helical fiber clusters and the paddle coincidence/straight fiber must not be colinear.

9. ≥ 2 straight fiber clusters AND ≥ 1 paddle coincidence or helical fiber. The straight fiber clusters and the paddle coincidence/helical fiber must not be colinear.

10. ≥ 2 paddle coincidences AND ≥ 1 fiber of any type. The paddle coincidences and the fiber must not be colinear.

11. ≥ 2 multiplicity-2 helical fiber clusters separated by more than $\pi/8$ rad. A straight line through the helical fiber clusters must be more than $\pi/8$ rad. away from either a paddle coincidence or 2 straight fiber clusters.

12. ≥ 2 multiplicity-2 straight fiber clusters separated by more than $\pi/8$ rad. A straight line through the straight fiber clusters must be more than $\pi/8$ rad. away from either a paddle coincidence or 2 helical fiber clusters.

The results of each test may be either true or false, giving a total of $2^{12} = 4096$ different classes into which any event may fall. Ideally, $\overline{\text{p}}$ events would exclusively occupy some classes, and cosmics others, making discrimination between the two trivial. An unknown test event could then easily be identified as a $\overline{\text{p}}$ or cosmic depending upon the class into which it falls. In practice, most occupied classes are comprised of both $\overline{\text{p}}$ and cosmic ray events, so we are unable to say with 100% certainty whether an unknown event is caused by a $\overline{\text{p}}$ annihilation or not.

9.1.2 Data Thresholding

To further improve our sensitivity to small numbers of $\overline{\text{p}}$ annihilations, we may consider only those detector events that are reasonably likely to have been caused by

a $\overline{\mathrm{p}}$. This determination is made by first calibrating the detector with large numbers of $\overline{\mathrm{p}}$ and cosmic rays to find the relative proportion of each event type that fall into each of the 4096 classes. The class into which an unknown event is assigned is then compared to the calibration data to asses the likelihood $\mathcal{L}$ that the event was caused by a $\overline{\mathrm{p}}$. We then identify a threshold by the methods outlined in Sec. 9.1.3, and only include events in our analysis for which the $\overline{\mathrm{p}}$ likelihood $\mathcal{L}$ is larger than the threshold.

We calibrate our detector by assigning annihilation events from 3×10^5 $\overline{\mathrm{p}}$ spilled radially and 3.5×10^5 cosmic ray events into one of the 4096 classes. We then count the number of $\overline{\mathrm{p}}$ and cosmic rays, $N_{\overline{\mathrm{p}}}$ and N_{cos}, assigned to each class, and for each class calculate the fractions $f_{\overline{\mathrm{p}}} = N_{\overline{\mathrm{p}}}/(3 \times 10^5)$ and $f_{cos} = N_{cos}/(3.5 \times 10^5)$. If a new event to be analyzed falls into a given class, the likelihood that it is a $\overline{\mathrm{p}}$ can then be expressed as $\mathcal{L} = f_{\overline{\mathrm{p}}}/(f_{\overline{\mathrm{p}}} + f_{\mathrm{cos}})$. By selecting only those events that fall into classes for which $\mathcal{L}$ surpasses some threshold, a large reduction in the cosmic background count rate is obtained, at the expense of a small decrease in $\overline{\mathrm{p}}$ detection efficiency.

Fig. 9.2a shows the $\overline{\mathrm{p}}$ likelihood $\mathcal{L}$ determined from the calibration data for each of the 4096 classes. $\mathcal{L}$ spans the full range between 0 and 1, indicating that some classes have not been populated by a single $\overline{\mathrm{p}}$ out of 3×10^5, while others have not been populated by any of the 3.5×10^5 cosmic rays used in the calibration set. The optimized threshold $\mathcal{L} = 0.82$ determined by a Monte Carlo calculation described in Sec. 9.1.3 is shown for comparison. The $\overline{\mathrm{p}}$ preferentially occupy only ≈ 300 of the 4096 possible classes, and 256 classes have $\mathcal{L} \geq 0.82$.

We naturally desire low noise for our $\overline{\mathrm{p}}$ event detection. As shown in Fig. 9.2b, the

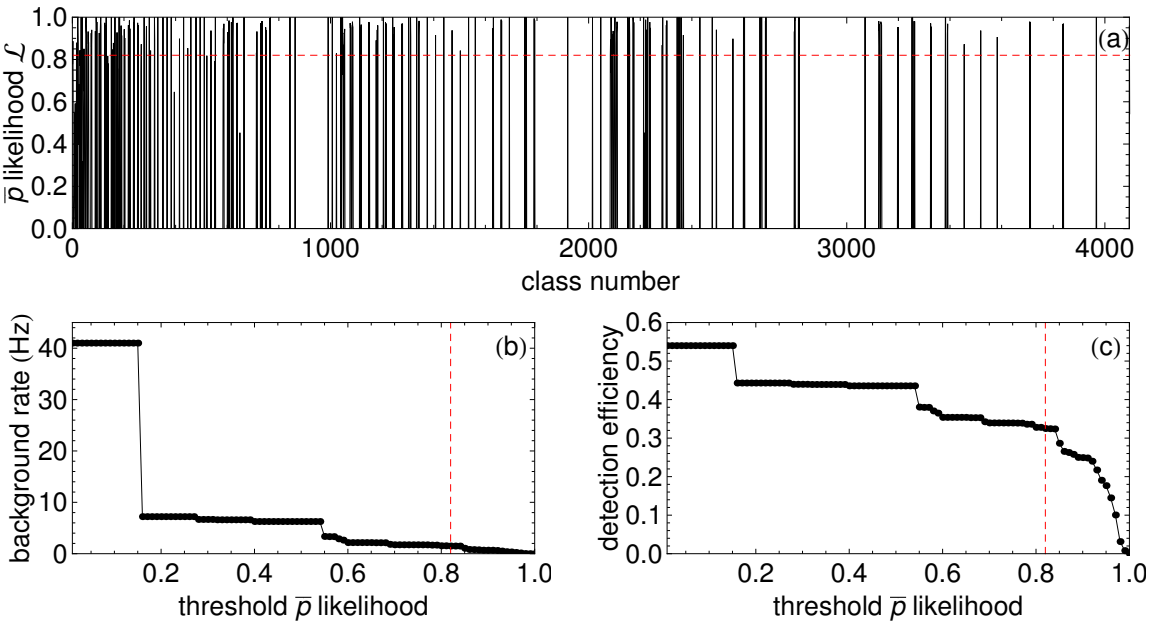

Figure 9.2: (a) The $\overline{\text{p}}$ likelihood $\mathcal{L}$ is plotted for each of the 4096 event classes. The red dashed line indicates the optimum threshold $\mathcal{L} = 0.82$ determined from a Monte Carlo simulation. The cosmic ray background rate (b) and $\overline{\text{p}}$ detection efficiency (c) both fall as $\mathcal{L}$ is increased.

cosmic ray background rate can be reduced by increasing the threshold value for $\mathcal{L}$. The decrease in background rate with increasing threshold is not necessarily smooth, since sudden jumps downward may occur when large numbers of cosmics fall into the same event class. For instance, 80% of all cosmics are found to occupy the class in which the first 3 of the 12 criteria (but no others) in Sec. 9.1.1 are satisfied. Once this single event class is eliminated (by increasing the threshold above $\mathcal{L} = 0.16$), the background rate accordingly drops by 80%.

Although increasing the threshold leads to a lower background rate, it also decreases the $\overline{\text{p}}$ detection efficiency (and hence signal size), as shown in Fig. 9.2c. For an infinitely large data set, small detector efficiencies are inconsequential since even the rarest events will be well-represented within the population. For our finite data

set, however, we cannot afford to miss too many signal events. If the threshold is set too high, the statistical uncertainty in the small number of remaining counts can become large compared with the number of counts itself. For example, if the data set contains 100 $\overline{\mathrm{p}}$ annihilation events, only 3 (or fewer) would survive a threshold set at $\mathcal{L} = 0.98$ (or above), with an uncertainty large enough to obscure any meaningful result. We therefore seek an intermediate threshold value that strikes a proper balance between a low background rate and a high detection efficiency.

There is an inherent danger in choosing the threshold for $\mathcal{L}$ based on the data set to be analyzed. For each threshold level, the number of surviving $\overline{\mathrm{p}}$ and cosmic events are subject to trial-to-trial statistical fluctuations. By selecting a threshold that maximizes the observed signal to noise ratio, it is impossible to distinguish whether the selection is inherently optimal or has fallen victim to the vagaries of statistical variation. More often than not, such a selection process will systematically overstate the statistical significance of any result. Therefore, we determine the optimal threshold for $\mathcal{L}$ by performing a Monte Carlo simulation to remove this source of bias in the analysis.

9.1.3 Monte Carlo Simulation

The Monte Carlo simulation to determine the optimum threshold consists of 20,000 repeated runs in which we "quench" the Ioffe trap to release trapped $\overline{\mathrm{H}}$ 20 times, and then sum the results. For each simulated run, 21 seconds of Poisson-distributed background (from $t = -10$ s to $t = +11$ s) are generated with a mean rate of 20×41 Hz (to match our measured rate for the sum of 20 trials), and 100 $\overline{\mathrm{p}}$ are

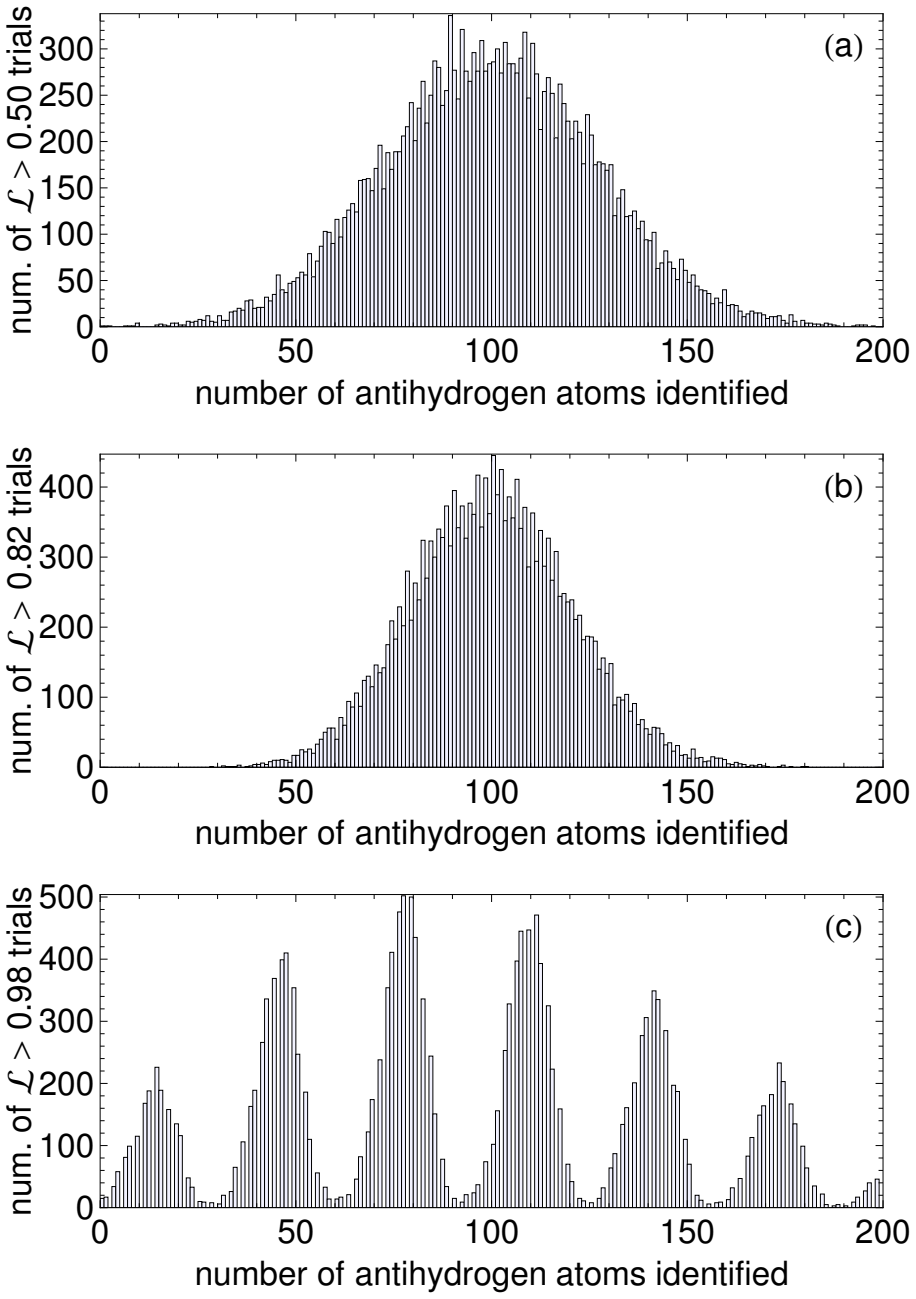

Figure 9.3: Distribution of the number of $\overline{\mathrm{H}}$ detected for various thresholds of $\overline{\mathrm{p}}$ likelihood $\mathcal{L}$ after 20,000 simulated trials. The widths of the distributions for too low (a) and too high (c) thresholds are broadened by statistical fluctuations in either the background or the signal. An intermediate threshold (b) minimizes the width.

added between $t = 0$ s and $t = 1$ s. Every $\overline{\mathrm{p}}$ and cosmic ray in the simulation is randomly assigned into one of the 4096 classes, with weightings given by $f_{\overline{\mathrm{p}}}$ and f_{cos} from the calibration data. For all simulated runs, 99 "cuts" are applied to the results by allowing the threshold for $\mathcal{L}$ to vary from 0.01 to 0.99 in increments of 0.01. As the threshold is increased, the number of events that survive the cuts decreases, while those which do survive are increasingly likely to have been caused by $\overline{\mathrm{p}}$ annihilations.

Fig. 9.3 shows the distribution of detected $\overline{\mathrm{H}}$ for three different threshold values applied to the simulated data. As expected, all cuts find a mean of 100 $\overline{\mathrm{p}}$ within the simulated data set. The optimal cut is the one that minimizes the width of the distribution about the mean (Fig. 9.3b), thereby maximizing the probability that the correct number of $\overline{\mathrm{p}}$ is returned in any single trial. When the threshold value for $\mathcal{L}$ is set too low (Fig. 9.3a), the size of Poissonian fluctuations in the background approaches the size of the signal, broadening the distribution. When the threshold value for $\mathcal{L}$ is too high (Fig. 9.3c), only a few events survive the cut, and Poissonian fluctuations in the signal also may broaden the distribution (and in some cases, lead to a distinct discretization).

Calculating the standard deviation of each Monte Carlo distribution allows determination of the optimal threshold, $\mathcal{L} = 0.82$. As shown in Fig. 9.4, taking only those events for which $\mathcal{L} > 0.82$ minimizes the distribution width (and fractional uncertainty). The 20% minimum uncertainty indicates that when the optimal threshold is used, 68% of experiments may expect to observe between 80 and 120 $\overline{\mathrm{H}}$ atoms if 100 are truly present. The simulation shows that the threshold choice need not be overly precise, since nearly identical widths are found when the threshold $\mathcal{L}$ is set

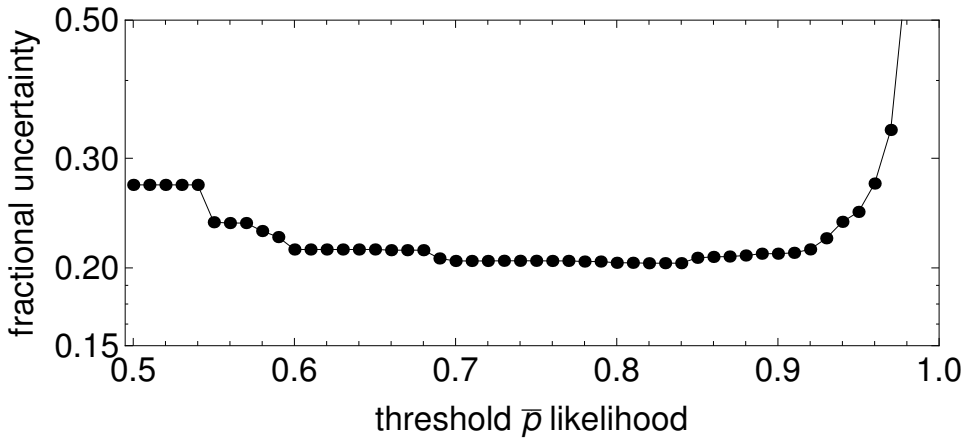

Figure 9.4: The width of the distributions determined by the Monte Carlo simulation is minimized when the threshold $\overline{\mathrm{p}}$ likelihood $\mathcal{L} = 0.82$.

between 0.80 and 0.84. Indeed, applying this range of threshold values to the experimental data set yields comparable numbers of detected $\overline{\mathrm{H}}$ atoms, in agreement with the simulation prediction. The optimized choice of $\mathcal{L} = 0.82$ results in a new cosmic ray background rate of 1.7 Hz (reduced from 41 Hz) and a slightly lower $\overline{\mathrm{p}}$ detection efficiency of 33% (compared with 54% previously).

9.2 Demonstration of Trapped Antihydrogen

With the $\overline{\mathrm{H}}$ experimental protocol and event detection procedures now explicated, we present the results of the 20 trapping trials performed in 2011. Though the methods used to make $\overline{\mathrm{p}}$ and e^+ interact are varied from trial to trial, a total of 105 ± 21 $\overline{\mathrm{H}}$ atoms were observed to be trapped in the 375 mK quadrupole Ioffe trap. This corresponds to an average of 5 ± 1 simultaneously trapped $\overline{\mathrm{H}}$ per trial, stored in the trap for between 15 and 1000 s. We begin with the observations from each of the individual trials, then sum the detector counts for all 20 trials to average down the

background and allow a small trapped $\overline{\mathrm{H}}$ signal to become visible. We conclude the section with arguments that the $\overline{\mathrm{H}}$ has been trapped long enough to be in its ground state, a crucial precursor to performing precision spectroscopy and laser cooling of $\overline{\mathrm{H}}$ atoms.

9.2.1 Individual Trials

The drive parameters for each of the 20 individual $\overline{\mathrm{H}}$ trapping trials, along with the results, are shown in Tables 9.1 and 9.2, respectively. Only two of the 20 trials show a signal with more than 3σ significance, and many are consistent with background. Most, however, fall between 1 and 2 standard deviations above background, suggesting that a variety of different methods may produce trapped $\overline{\mathrm{H}}$.

No clear favorite has yet emerged among the $\overline{\mathrm{H}}$ production methods, since the interaction of plasmas varies noticeably even for trials intended to be identical. Both $\overline{\mathrm{p}}$ and e^+ plasmas are radially compressed using a rotating wall, though trial-to-trial variations in the radius may be as large as 10-20%. The number of $\overline{\mathrm{p}}$ and e^+ used in each trial may vary by up to 10% depending upon the shot-to-shot performance of the AD and the reproducibility of our radial compression. Both factors effect differences in the $\overline{\mathrm{p}}$ and e^+ plasma shapes and space-charge potentials, leading to observable dissimilarities in the $\overline{\mathrm{H}}$ formation rate, $\overline{\mathrm{p}}$ temperature, and the rate at which particles escape the nested trap.

The best of the 20 $\overline{\mathrm{H}}$ trials illustrates current challenges and future possibilities. The background count rate before and after the Ioffe trap is quenched is consistent with other trials and Poisson-distributed. However, the number of counts observed

Trial	Type	Amplitude	f_i	f_f	t_{drive}	e^+ sweep?	t_{sweep}
1	Noise	-9 dBm	300 kHz	1 MHz	600 s	No	–
2	Noise	-10 dBm	300 kHz	1 MHz	600 s	No	–
3	Noise	-12 dBm	300 kHz	1 MHz	600 s	No	–
4	Noise	-12 dBm	300 kHz	1 MHz	600 s	No	–
5	Noise	-12 dBm	300 kHz	1 MHz	600 s	No	–
6	Noise	-12 dBm	300 kHz	1 MHz	600 s	No	–
7	Chirp	0.10 Vpp	1.3 MHz	100 kHz	2.4 s	No	–
8	Chirp	0.10 Vpp	1.3 MHz	100 kHz	2.4 s	No	–
9	Chirp	0.06 Vpp	900 kHz	600 kHz	900 s	No	–
10	Chirp	0.06 Vpp	900 kHz	600 kHz	900 s	No	–
11	Chirp	0.06 Vpp	900 kHz	600 kHz	900 s	No	–
12	Chirp	0.06 Vpp	900 kHz	600 kHz	900 s	No	–
13	Chirp	0.06 Vpp	900 kHz	700 kHz	600 s	Yes	300 s
14	Chirp	0.06 Vpp	900 kHz	700 kHz	600 s	Yes	150 s
15	Chirp	0.06 Vpp	900 kHz	700 kHz	600 s	Yes	1.8 s
16	Chirp	0.06 Vpp	900 kHz	700 kHz	600 s	Yes	1.8 s
17	Chirp	0.06 Vpp	900 kHz	700 kHz	600 s	Yes	0.54 s
18	Chirp	0.06 Vpp	900 kHz	700 kHz	450 s	Yes	2.1 s
19	Chirp	1.00 Vpp	900 kHz	700 kHz	0.002 s	Yes	0.009 s
20	Chirp	1.00 Vpp	900 kHz	700 kHz	0.002 s	Yes	0.030 s

Table 9.1: Summary of the 20 trials searching for signals of trapped $\overline{\mathrm{H}}$. Noise drives are white noise within the frequency band 300 kHz to 1 MHz. Chirp drives are reduced linearly from an initial frequency f_i to a final frequency f_f in the indicated time.

Trial	Raw Cts.	Cts. above Bkgrd.	$\overline{\mathrm{H}}$ above Bkgrd.	Significance (σ)
1	2	0.3	0.9	0.2
2	0	-1.7	-5.1	-1.3
3	15	13.3	40.0	10.2
4	3	1.3	3.9	1.0
5	3	1.3	3.9	1.0
6	1	-0.7	-2.1	-0.5
7	3	1.3	3.9	1.0
8	4	2.3	6.9	1.8
9	6	4.3	13.0	3.3
10	2	0.3	0.9	0.2
11	2	0.3	0.9	0.2
12	3	1.3	3.9	1.0
13	4	2.3	6.9	1.8
14	3	1.3	3.9	1.0
15	2	0.3	0.9	0.2
16	2	0.3	0.9	0.2
17	3	1.3	3.9	1.0
18	4	2.3	6.9	1.8
19	4	2.3	6.9	1.8
20	3	1.3	3.9	1.0
Total	69	35	105	6.0

Table 9.2: Summary of the results of 20 trials searching for signals of trapped $\overline{\mathrm{H}}$. The trial numbers correspond to those used in Table 9.1.

during the 1 s quench of the Ioffe trap corresponds to 40 ± 8 $\overline{\mathrm{H}}$ atoms (when the detection efficiency is included), much larger than average. Sometimes we produce more $\overline{\mathrm{H}}$ atoms and sometimes fewer, owing to our inability to precisely control the interaction of the $\overline{\mathrm{p}}$ and e^+, even in "identical" trials. Improvements in plasma control should enable much more reproducible trials, perhaps allowing for this large number of trapped $\overline{\mathrm{H}}$ to become the new baseline standard.

9.2.2 Combined Signal

Since very few of the 20 trials individually show a trapped $\overline{\mathrm{H}}$ signal with large statistical significance, we sum the signals from all trials together to improve the contrast over noise from cosmic rays. Although it is tempting to discard the trials consistent with or below background as unsuccessful, we nevertheless keep them to avoid selection bias. This conservative approach thus likely understates the statistical significance that would be found if only successful trials were included in the sum.

Fig. 9.5a shows the sum of the detector counts for the 20 trials in 1 s intervals. The central bin (dark blue) marks the 1 s in which the Ioffe trap is quenched to release trapped $\overline{\mathrm{H}}$, while surrounding bins (light blue) show the background before and after the quench. When divided by the detector efficiency of 0.33, the pronounced peak corresponds to 105 ± 21 trapped $\overline{\mathrm{H}}$ atoms, or 5 ± 1 atoms per trial on average. This signal is 6 standard deviations above the average number of background counts (right vertical scale in Fig. 9.5a), indicating that there is only 1 chance in 10^7 that the signal in the central channel is a fluctuation of the cosmic background (Fig. 9.5b). The counts in the 1 s intervals before and after the central bin are consistent with

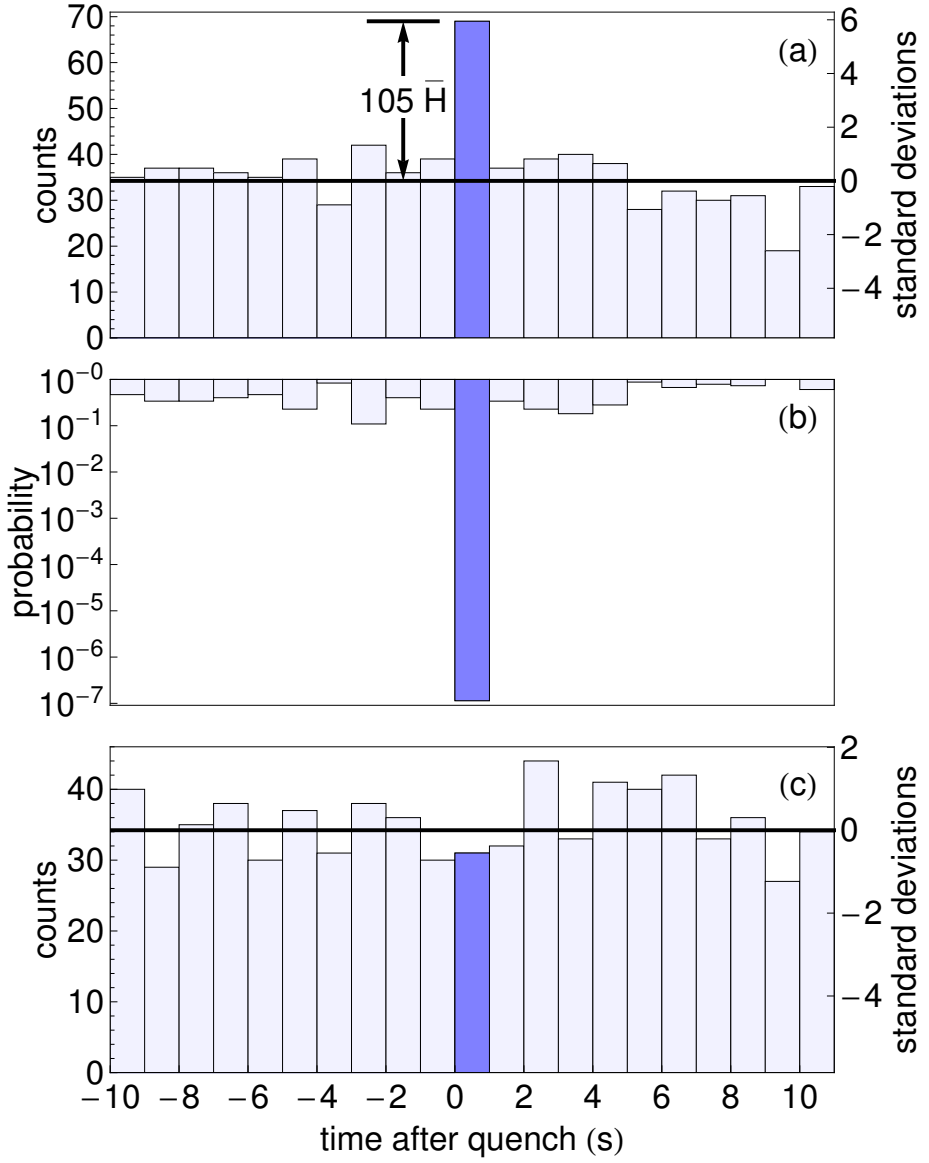

Figure 9.5: (a) Detector counts in 1 s intervals for the sum of 20 trials. The radial Ioffe trap field turns off and releases trapped $\overline{\text{H}}$ between $t = 0$ and $t = 1$ s. The counts in this interval above the average cosmic ray background counts (solid line) correspond to 105 trapped $\overline{\text{H}}$ for our detection efficiency. (b) Probability that cosmic rays produce the observed number of counts or more. (c) Quenching the Ioffe trap generates no false signals in 20 control trials.

the measured Poisson-distributed background.

We have separately analyzed our trials with the best one excluded (though we have no justification for discarding it) to ensure that the result is still statistically significant. The average number of simultaneously trapped $\overline{\mathrm{H}}$ in the remaining 19 trials is 3.5 ± 0.7, consistent with the result from all 20 trials (5 ± 1 per trial). The statistical significance without the best trial is still 4 standard deviations above the expected background, giving a probability of less than 3×10^{-4} that the signal is caused by fluctuations in the background rate.

One may worry that the sudden change in magnetic field as the Ioffe trap quenches induces voltage signals in our detectors that may be confused with trapped $\overline{\mathrm{H}}$. We therefore performed 20 control trials in which we quenched the Ioffe trap when no $\overline{\mathrm{H}}$ are present. Fig. 9.5 shows that the sudden flux change does not create signals that could be misinterpreted as $\overline{\mathrm{H}}$ atoms, since the number of counts before, during, and after the Ioffe trap quench are all consistent with the expected cosmic ray background.

9.2.3 Ground-State Antihydrogen

To realize the long-term goal of precise $\overline{\mathrm{H}}$ spectroscopy [1], the $\overline{\mathrm{H}}$ atoms must be in their ground state. However, essentially all of the $\overline{\mathrm{H}}$ atoms formed by three-body recombination when $\overline{\mathrm{p}}$ and e^+ mix in a nested Penning trap are in highly excited Rydberg states [3]. These atoms radiatively decay to the ground state, and stay trapped only if they remain in low-field seeking states. Simulations [150, 151] show that this process happens in $\sim$ 100 ms, with the low-field seeking character of the $\overline{\mathrm{H}}$ presumably preserved since the angular momentum quantum number m does not

change on average, and since $\Delta m = \pm 1$ in a single radiative decay. Though the simulations already calculate a decay time short compared with the 15 to 1000 s that $\overline{\mathrm{H}}$ is confined within our Ioffe trap, we present a conservative analytical calculation showing that the trapped $\overline{\mathrm{H}}$ atoms reach their ground state in less than 250 ms.

When ATRAP first probed the distribution of $\overline{\mathrm{H}}$ atoms formed by three-body recombination, many were found to be large-n guiding-center atoms [148], which overwhelmingly occupy high-field seeking states and cannot be trapped. The trapped atoms must therefore come from the small $\overline{\mathrm{H}}$ fraction produced in non-guiding-center states. Earlier field ionization measurements have identified more deeply-bound $\overline{\mathrm{H}}$ atoms with chaotic e^+ orbits, owing to comparable strengths of the nonlinear Coulomb and magnetic forces on the e^+ [182]. Such atoms are produced with radii smaller than 0.14 μm, corresponding to $n \approx 50$ (though energy levels are highly mixed in the strong magnetic field). Some are formed in weak-field seeking states, which are then trapped via diamagnetic forces that are large for large B.

An overestimate of the time required for an $n = 50$ $\overline{\mathrm{H}}$ atom to decay to the ground state is the slowest possible radiation path, that from one circular state ($n - 1 = \ell$) to another. The Einstein A coefficient defines the decay rate from the state $|n, \ell\rangle = |n, n-1\rangle$ to the state $|n', \ell'\rangle = |n-1, n-2\rangle$ [183]

$$A_{n\ell,n'\ell'} = \frac{4}{3}\frac{\alpha}{c^2}\omega^3_{n\ell,n'\ell'}\frac{\ell}{2\ell+1}\left|\langle n'\ell'|\, r\, |n\ell\rangle\right|^2 \tag{9.1}$$

where α is the fine structure constant, c is the speed of light (in cgs units), and $\omega_{n\ell,n'\ell'}$ is the frequency difference between $|n, \ell\rangle$ and $|n', \ell'\rangle$. Since in the large-n limit $\omega_{n\ell,n'\ell'} \propto 1/n^3$ and $\langle r\rangle \propto n^2$ [184], and since $\ell = n - 1$ in circular states, Eqn. 9.1

may be simplified to give [152]

$$A_{n\ell,n'\ell'} = (1.1 \times 10^{10}) n^{-5} \text{ s}^{-1} \tag{9.2}$$

The decay time to the ground state $\tau_{n\ell}$ is then calculated by summing $A_{n\ell,n'\ell'}$ over all lower states $|n', \ell'\rangle$

$$\frac{1}{\tau_{n\ell}} = \sum_{n',\ell'} A_{n\ell,n'\ell'} \tag{9.3}$$

Finally, substituting Eqn. 9.2 into Eqn. 9.3 yields a total radiative decay time of $\tau_{n\ell} = 250$ ms starting from the $n = 50$ circular state. The actual cascade time is shorter given that fields and collisions mix in states with lower ℓ quantum numbers that radiate at a rate $\propto n^{-3}$, much faster than the $\propto n^{-5}$ rate for circular states. Thus, $\overline{\text{H}}$ detected after a 15-1000 s storage time are in their ground state.

9.3 Antimatter Gravity

Trapped $\overline{\text{H}}$ makes it possible to compare the gravitational force on antimatter κmg to the more familiar gravitational force mg [34]. $\overline{\text{H}}$ atoms created at the center of the Ioffe trap gain κmgh of energy in free fall to the magnetic maximum of the trap, with $h = 10.6$ cm. The total trapping potential is thus reduced from a $k_B \times 375$ mK depth to $(k_B \times 375 \text{ mK}) - \kappa mgh$. Fig. 9.6 shows the effect of setting $\kappa = 200$ on the total confining potential for $\overline{\text{H}}$ atoms. The symmetric, 375 mK Ioffe trap depth (solid) is altered by the presence of the linear gravitational potential to give an asymmetric well with a 350 mK depth.

As described in Sec. 9.1.1, we record the times at which $\overline{\text{H}}$ released from the Ioffe trap annihilate on the trap walls. In the sum of the 20 trials, a 2σ trapped $\overline{\text{H}}$ signal is

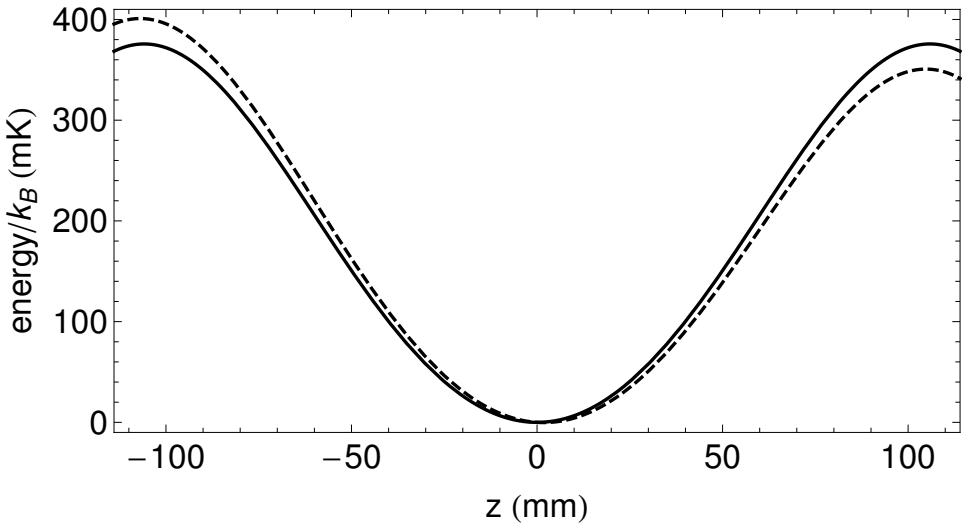

Figure 9.6: The Ioffe trap depth is reduced from 375 mK (solid) to 350 mK (dashed) if the gravitational force on $\overline{\mathrm{H}}$ is 200 times stronger than the force on H.

observed within 0.16 s after the quench, when the Ioffe trap depth has been reduced from 375 mK to 350 mK. However, if the gravitational force on antimatter were truly 200 times stronger than the force on matter, then no $\overline{\mathrm{H}}$ atoms with more 350 mK of energy could remain trapped, and no signal would be observed. Our observation therefore establishes the crude limit $|\kappa| < 200$. Improved limits should be possible when larger numbers of trapped $\overline{\mathrm{H}}$ and laser cooling allow for probing of the spatial $\overline{\mathrm{H}}$ distribution [34]. Eventually, it may be possible to exceed the limit $|\kappa - 1| < 1 \times 10^6$ set by the consistency to better than 1 part in 10^{10} of $\overline{\mathrm{p}}$ and p cyclotron clocks [23], which would have different gravitational redshifts if the gravitational force differs by a factor of κ for $\overline{\mathrm{p}}$ and p [37].

9.4 Summary and Discussion

The previous three chapters have shown that large $\overline{\mathrm{p}}$ and e^+ plasmas can be used to create more simultaneously trapped $\overline{\mathrm{H}}$ atoms than previously demonstrated, despite the ongoing difficulties of controlling the interactions of large plasmas in a stable and reproducible way. We observed 105 $\overline{\mathrm{H}}$ atoms trapped in a 375 mK Ioffe trap, corresponding to an average of 5 simultaneously trapped atoms per trial. These $\overline{\mathrm{H}}$ were stored for between 15-1000 s before their release, which is long enough to ensure that they reached their ground state.

Our observation of trapped $\overline{\mathrm{H}}$ atoms was made possible by many factors working in concert. Control over the $\overline{\mathrm{p}}$ and e^+ plasma number, geometry, and temperature (as described in Chapters 4-6) are crucial for preparing the constituent particles for mixing. Variations on old methods and development of new methods to make $\overline{\mathrm{p}}$ and e^+ interact allow for the creation of cold, trappable $\overline{\mathrm{H}}$. Performing more trials in a single year than ever before permits the data to be summed and the background averaged down. Improved detector characterization and event classification procedures greatly increase the sensitivity to small numbers of trapped atoms. Finally, elimination of mirror-trapped $\overline{\mathrm{p}}$ or induced voltages during the Ioffe trap quench as possible sources of spurious signals further boosts confidence in our results.

We are optimistic that additional increases in the number of simultaneously trapped $\overline{\mathrm{H}}$ atoms are coming. Further progress in manipulating the large and cold $\overline{\mathrm{p}}$ and e^+ plasmas seems likely to continue. It seems feasible to adapt these methods to make use of the 10 times more $\overline{\mathrm{p}}$ currently available, while the ELENA upgrade to the AD promises still many more. Implementation of an octupole Ioffe trap currently under

construction should allow for $\overline{\mathrm{p}}$ and e^+ to interact more efficiently in the low-gradient radial field. In the years ahead, we look forward to trapping many more atoms and making the first attempts at $\overline{\mathrm{H}}$ laser cooling and spectroscopy.

Chapter 10

Electrode Fabrication for an Improved Penning-Ioffe Trap

With the milestone of trapped $\overline{\mathrm{H}}$ achieved [59], future studies will seek to confine larger numbers of $\overline{\mathrm{H}}$ atoms for laser cooling and spectroscopy [1]. To this end, we are constructing a new apparatus for $\overline{\mathrm{H}}$ trapping. The design is centered around an improved Ioffe trap, described briefly below and in further detail in Ref. [65], and a novel Penning trap, which is the main focus of this chapter.

The new Ioffe trap promises three significant advantages over the one used in BTRAP. First, radial confinement can be provided by either a quadrupole or an octupole field. We expect more efficient $\overline{\mathrm{H}}$ production and trapping within the octupole field on account of the smaller radial gradient. Ballistic particle losses during mixing would be greatly suppressed (allowing more particles to participate in $\overline{\mathrm{H}}$ formation), and coherent chirped drives can excite a larger fraction of $\overline{\mathrm{p}}$ into the e^+ cloud. However, the octupole field does not provide the tight spatial confinement (desirable for

$\overline{\text{H}}$ spectroscopy) that a quadrupole can. Having both sets of windings allows us the flexibility to tailor the trap fields based on the desired experiment.

Second, the trap depths for the octupole (510 mK) and quadrupole (790 mK) are significantly deeper than the 375 mK trap depth used in this work, practically assuring that larger numbers of $\overline{\text{H}}$ atoms can be trapped. Since the low-energy tail of the Boltzmann distribution $\propto T^{3/2}$, one may expect up to a factor of 3 boost in the number of simultaneously trapped $\overline{\text{H}}$ per trial. Finally, the inductance of the new magnet has been significantly reduced, giving a turn-off time of only 10 ms (compared with 1 s currently). Given the cosmic ray background rate, this short de-energization time should provide sensitivity to a single trapped $\overline{\text{H}}$ atom, greatly accelerating the search for and development of optimized experimental parameters for trapping $\overline{\text{H}}$.

Fig. 10.1 shows a schematic of the new apparatus and Ioffe trap. The new Ioffe trap sits in the same location as in BTRAP and surrounds the upper Penning trap electrodes. Four NbTi superconducting coils are wound into groves cut into a G10 form, then wrapped with fiberglass cloth and vacuum impregnated with epoxy [185]. Currents of 680 A (500 A) applied to the octupole (quadrupole) coils generate a maximum radial trap depth of 0.78 T (1.20 T). The axial field is produced by applying up to 390 A and 340 A to the pinch and bucking coils, respectively. Retractable vapor-cooled current leads limit the heat load on the cryogenic environment.

As in BTRAP, four side ports provide radial access to the central axis of the trap. As before, two opposing ports will be used for mounting and monitoring the Cs source for double-charge exchange formation of $\overline{\text{H}}$ [66]. The remaining ports provide a conduit for lasers and microwaves to interrogate and address $\overline{\text{H}}$ atoms within the

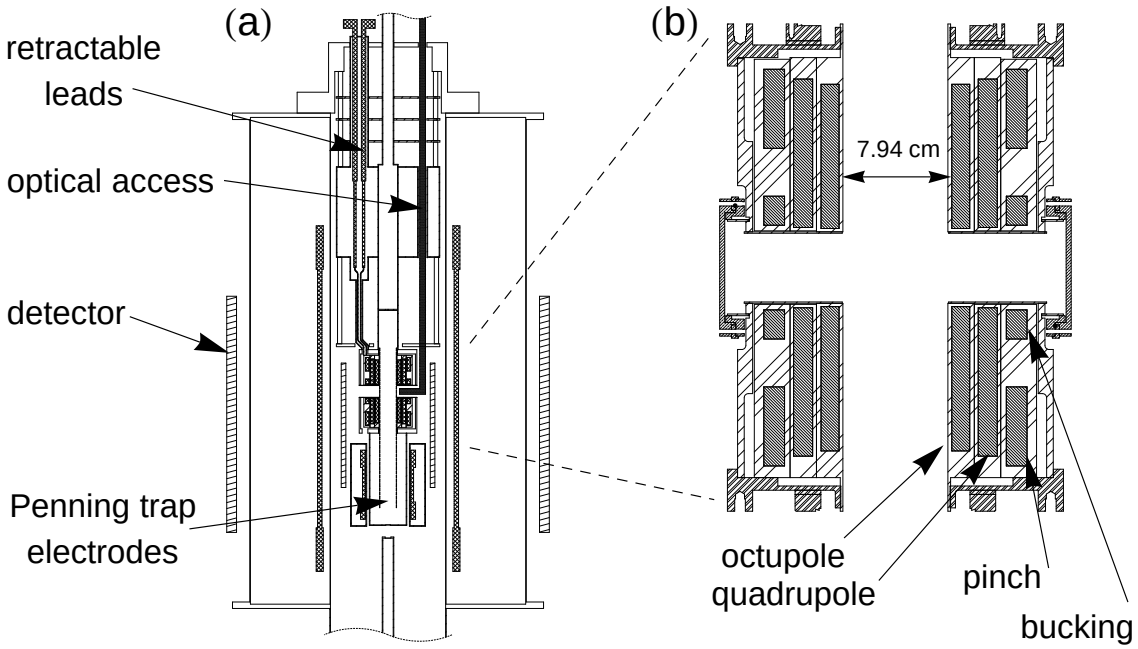

Figure 10.1: Schematic of the Ioffe trap position within the new apparatus (a) along with a detail cross-section view (b). The four superconducting coils are indicated, along with the 7.94 cm bore surrounding the Penning trap electrodes.

trap.

The cylindrical Penning trap electrode stack fits within the central 7.94 cm bore of the Ioffe trap. As we will see in the next section, the strength of the radial octupole field climbs steeply ($\propto \rho^3$) with radius, requiring large-radius electrodes to make full use of the octupole trap depth. This design constraint, along with several others to be described, demanded a re-engineering of our standard electrode fabrication process. Here we discuss the electrode design parameters, construction of the electrodes themselves (along with their support structures), and the final implementation and assembly within the new apparatus.

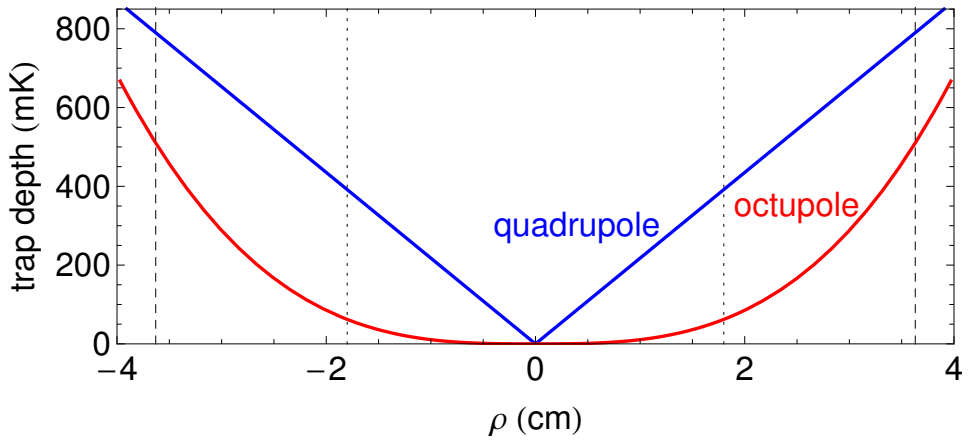

Figure 10.2: The trap depth for ground-state $\overline{\mathrm{H}}$ atoms is plotted as a function of radius for a quadrupole and an octupole field. The inner radius of the BTRAP electrodes (1.8 cm, dotted) and the new electrodes (3.63 cm, dashed) are shown for comparison.

10.1 Electrode Design Constraints

10.1.1 Octupole Field Profile

As derived in Sec. 2.2.1, the magnitude of the radial component of the Ioffe trap magnetic field grows as $\rho^{\ell-1}$, where ℓ is the multipole order. For a quadrupole, for which $\ell = 2$, we have already seen in Fig. 2.11a that the radial magnetic field grows linearly. For an octupole ($\ell = 4$), the radial field strength increases $\sim \rho^3$, providing only a small perturbation to the axial field near the center of the trap while increasing steeply near the windings. Fig. 10.2 compares the radial field strength of an octupole and a quadrupole within the Ioffe trap.

To maximize the trap depth, the inner electrode radius should be made as large as possible, demanding that the electrode thickness be as small as possible. This design principle becomes crucial for the case of the octupole, which would only provide a ≈ 60 mK trap depth for ground-state $\overline{\mathrm{H}}$ if the BTRAP electrode radius of 1.8 cm was

maintained. Doubling the radius to 3.63 cm (the largest we could reasonably achieve) yields a factor of 8 improvement in the trap depth.

10.1.2 Induced Currents

When the Ioffe magnetic field is de-energized in 10 ms to release trapped $\overline{\mathrm{H}}$ atoms, currents may be induced in the cylindrical Penning trap electrodes. Lenz's Law tells us that current will flow in order to oppose the change in magnetic flux, while Faraday's Law predicts an emf proportional to the rate at which the magnetic flux changes. The induced emf will be particularly large in our apparatus on account of the several-Tesla magnetic fields, large-diameter cylindrical electrodes, and short magnetic rampdown times.

The induced current continues to propagate through the ring until the energy is dissipated by the resistance of the conductor. Since the electrodes are constructed from high-purity oxygen-free copper (alloy 101), the characteristic decay time may be as long as 100 ms [186]. Thus, efforts to quickly reduce the Ioffe magnetic field and improve the signal-to-noise ratio for small numbers of $\overline{\mathrm{H}}$ atoms may be thwarted by magnetic fields that arise from induced currents.

A secondary effect of induced currents is resistive heating of the electrodes. Integrating the I^2R power loss during current decay leads to ≈ 100 J deposited within the copper, potentially increasing the electrode temperature from 1.2 K to over 30 K. In BTRAP, Joule heating effects are visible even with a much slower magnetic field reduction, raising the electrode temperature from 1.2 K to 8 K.

To reduce the effects of induced currents, each electrode contains a vertical slit to

arrest current flow around the ring. The slit is made narrow (400 μm wide) so that the electrostatic properties of the electrode are not significantly altered, and so that charged particles remain well-shielded from dielectric surfaces. This slit geometry is most effective in preventing currents induced by sudden changes in the axial magnetic field. The relatively short electrode heights (preventing large current loops on the surfaces) and the smaller stored field energy make fast changes in the octupole field a smaller concern.

10.1.3 Particle Manipulation

The upper electrode stack in BTRAP is comprised primarily of radius-length electrodes. Keeping radius-length electrodes in the new apparatus, however, would pose several difficulties. First, since the new electrode radius has doubled, the length would double as well. Since the Ioffe trap height has remained unchanged in the new design, only half as many electrodes would thus fit within the trap. We would then have too few tunable voltages to create complex nested well structures or other potential schemes for $\overline{\mathrm{H}}$ formation. Second, very thin-walled copper cylinders become increasingly difficult to machine (while maintaining tight tolerances) as the length increases. We would then have the undesirable choice between looser tolerances (bad for electrostatics and $\overline{\mathrm{p}}/\mathrm{e}^+$ trapping) or thicker electrode walls (bad for maximizing trap depth for $\overline{\mathrm{H}}$ trapping).

The natural choice is to instead construct half-radius length electrodes. Just as many electrodes as in BTRAP can then fit within the Ioffe trap region, at the expense of requiring larger applied voltages to create the same on-axis potential.

Additionally, shorter electrodes improve the adiabatic transfer routine (Sec. 4.5) since the neighboring electrodes used to shape the potential are closer to the well minimum.

As described in Sec. 2.1.2, a harmonic potential on-axis can be made by appropriately biasing a central electrode at V_0, nearest-neighbors at $V_1 = 0.931V_0$, and next-nearest neighbors at $V_2 = 0.706V_0$. However, it is desirable to have an "orthogonalized" Penning trap [76, 73], in which the axial frequency for particles in the harmonic well is independent of the voltage V_1 applied to the nearest-neighbor compensation electrode. Tuning the electrode length to radius ratio provides the free parameter necessary to achieve an orthogonalized trap. Setting $D_2 = 0$ in Eqn. 12a of Ref. [73] gives an orthogonalized electrode length $L = 0.509\rho_0$ - just over half-radius length. We therefore have constructed electrodes with this length to allow for an orthogonalized, harmonic Penning trap to be created anywhere within the upper electrode stack without sacrificing our particle manipulation capabilities.

10.2 Electrode Body

The design for a single Penning trap electrode is shown in Fig. 10.3a. The electrode body - a 1 mm thick copper ring - is epoxied within a G10 support support sleeve. Five distinct steps, most of which were developed specifically for fabricating these electrodes, are required to transform copper tube stock into an electrode ready for mounting.

First, the electrode ring must be machined. We begin with oxygen-free copper tube stock (alloy 101) with an inner diameter of 6.25 cm and an outer diameter of

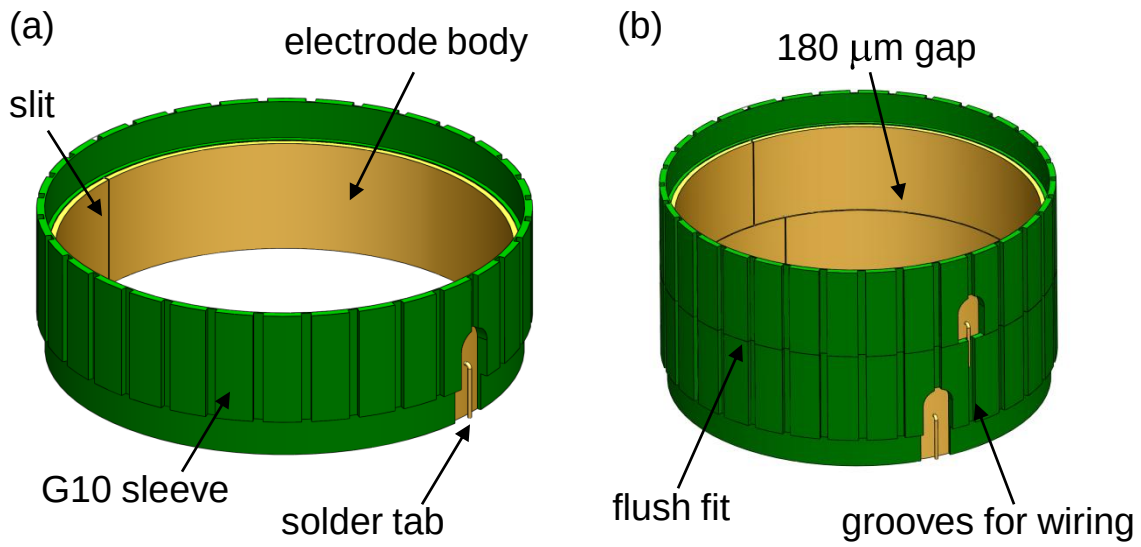

Figure 10.3: (a) Drawing of a single Penning trap electrode, showing the conductor, G10 support sleeve, vertical, slit, and solder tab for attaching the voltage lead. The single-electrode assemblies are stacked (b) to build the complete Penning trap. A 180 μm gap separates the electrodes.

8.75 cm. Though much of this material will be cut away before reaching the $\approx$ 7.5 cm electrode diameter, the extra thickness ensures that mechanical stresses at the center of the copper tube stock are as circumferential as possible. Machining proceeds slowly so that excess heat is not transmitted into the copper, which may cause mechanical relaxation and thermal expansion. A custom-made lathe-mounted jig applies uniform, outwardly directed radial pressure to hold the electrode while the length is machined.

Second, the inner surfaces of the electrodes (facing the particles) must be polished to remove dings and scratches which may detract from cylindrical symmetry and cause particle instabilities. The electrode is mounted into a custom-made lathe collet to apply uniform inward pressure, providing access to the inner surface without distorting the ring out-of-round. With the electrode spinning at 3000 rpm, polishing begins by removing any large scratches with 600-grit sandpaper. We then switch to

3M Wet-or-Dry polishing paper, starting from a 30 μm grade, followed by 15 μm, 9 μm, and 3 μm.

Third, a solder tab is connected to the electrode body to allow a voltage lead to be connected during assembly of the full trap. Soldering a wire directly to the electrode is difficult since the thermal mass (and good thermal conductivity) of the copper requires more heat than a standard soldering iron can provide. Additionally, the electrode cannot be significantly heated once it is epoxied within the G10 sleeve without damaging the epoxy or the G10. A 20 mm long, 1.6 mm wide, 0.25 mm thick OFE copper strip is clamped onto the outer electrode surface in a custom-made jig, then soft-soldered by heating the assembly with a heat gun. We have found that the standard technique of brazing in a hydrogen furnace anneals the thin-walled copper, allowing internal stresses to relax and deform the electrode.

Fourth, the electrode is gold-plated to prevent the copper surface from oxidizing. Exposure to air between polishing and gold plating, especially at the elevated temperatures during the soldering in step 3 (above), leaves a noticeable oxide layer which must be removed before plating. This process is readily accomplished by submerging the electrode in a 4 : 1 mixture of deionized water to hydrochloric acid for 30 seconds, then cleaning immediately in an ultrasonic bath of isopropyl alcohol. To gold-plate, the electrode is placed in a 3 : 1 mixture of deionized water and TG25 gold-plating solution (Technic, Inc.) held at 55° C, along with a platinized anode wand. With the cathode connected to the electrode itself, a current of 200 mA is passed through the solution for 30 seconds while agitating vigorously with a magnetic stirrer. The electrode is then flipped, plated for 30 seconds further, then cleaned immediately in

isopropyl alcohol.

Finally, the narrow slit is cut into the side of the electrode wall. The electrode is held on-end within a custom-made clamp that prevents the copper from springing open once the slit has been made. Once secured in the clamp, the electrode is mounted sideways on an end-mill and a 400 μm slitting saw is used to make the cut in a single pass. The electrode remains in the clamp until it is securely epoxied into the G10 support sheath.

10.3 Electrode Support Structure

The electrode support structure, shown in Fig. 10.3, is comprised of a G10 sleeve with a thickness that varies between 1 mm and 2 mm along its length. The sleeves are epoxied to the electrode body to make a modular assembly of electrodes which may then be stacked to form the cylindrical Penning trap. During the cooldown to cryogenic temperatures, the thermal contraction of the copper and thin-walled G10 are well-matched [187], with the copper contracting by only 0.06% more. Vertical grooves cut into the outer faces of the G10 sleeve provide a path for 0.86 mm diameter micro-coax cables to carry voltages to each electrode.

The electrode body is mounted within the G10 sleeve using Stycast 2850 epoxy, which has a thermal contraction coefficient comparable to that of copper and G10 and stays flexible at cryogenic temperatures. After pumping on the epoxy to remove any trapped air, the epoxy is applied along cutouts in the G10 sleeve that expose the outer surface of the copper electrode. It is crucial that the G10 sleeve and copper electrode rest on a level, dust-free surface during gluing since only a 180 μm gap

separates neighboring electrodes. The G10-copper assembly becomes rigid within approximately 2 hours, though 24 hours is needed for the epoxy to cure completely.

10.4 Penning Trap Assembly

The full Penning trap assembly is shown in Fig. 10.4. The lower electrode stack (below the HV electrode) is identical to the one used in BTRAP, so the e^- loading and $\overline{p}$ catching parameters should remain unchanged. Above the HV electrode, a long electrode with a conical bore provides a smooth transition between the 1.8 cm radius electrodes in the lower stack and the 3.63 cm radius electrodes in the upper stack. Numerical relaxation methods [76] of the type discussed in Sec. 2.1.2 are used to find the electrostatic potential within the CONE electrode, which exhibits only a slight linear skew on-axis.

Several "specialty" electrodes are placed in the upper stack near the center of the Ioffe trap. The CS and UV electrodes each have four 5 mm diameter holes aligned with the side-ports in the Ioffe trap to allow Cs atoms and microwave/UV laser radiation to enter the Penning trap. A small titanium plate with six tapped holes is epoxied into the G10 sheath for these electrodes, allowing baffles, collimation optics, or other sub-assemblies to be mounted from and directly aligned with the access hole. As in BTRAP, a rotating wall (UTRW) is included to enable control over the plasma radii. A split electrode (UTSE) sits just below the $\overline{H}$ formation region, and may potentially be used to Stark decelerate Rydberg $\overline{H}$ atoms in flight if the two halves are appropriately biased [188, 189].

As in previous designs, bundles of constantan wire and micro-coax cables carry

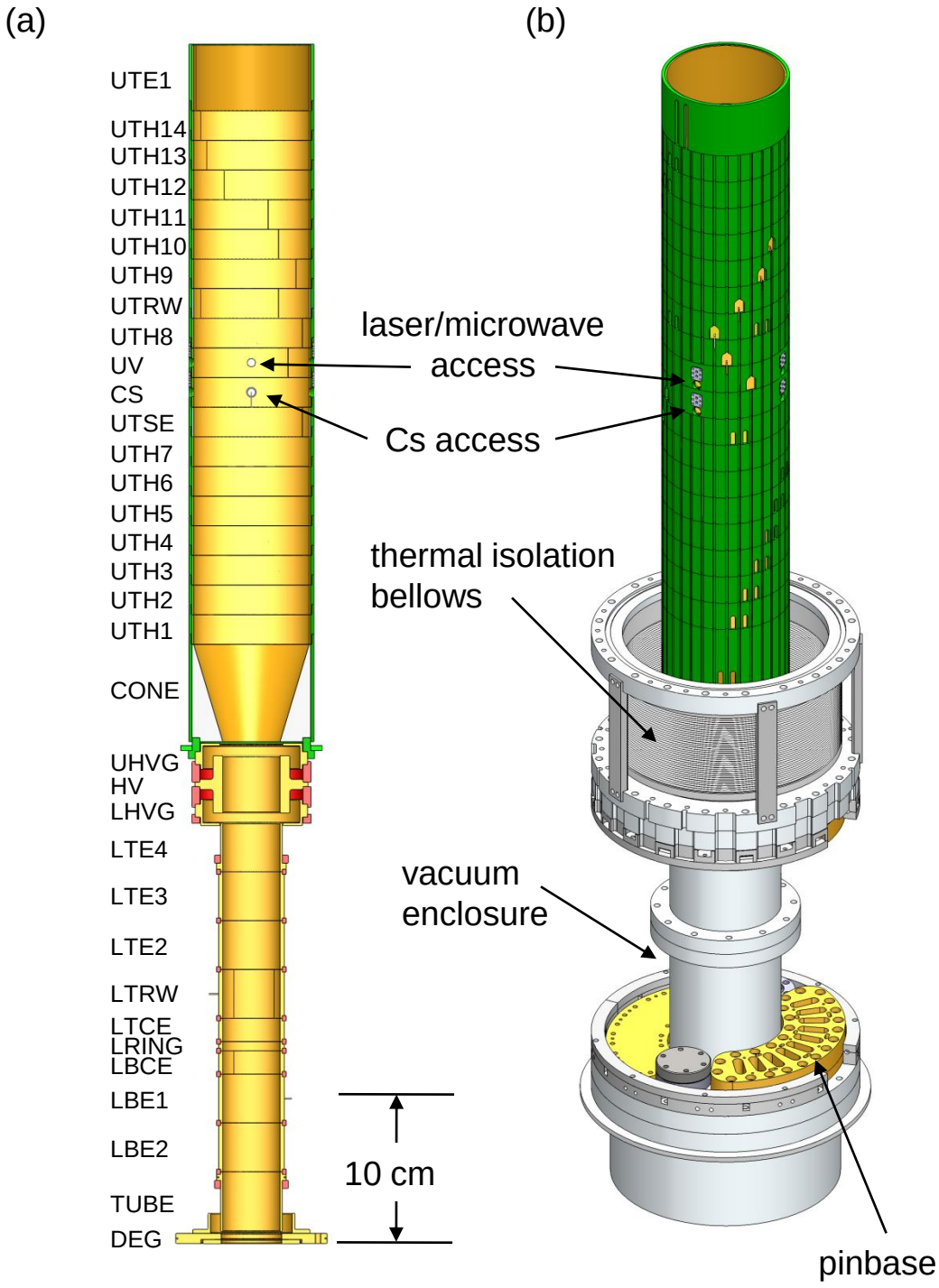

Figure 10.4: Cross-section view of the full Penning trap (a) along with the surrounding vacuum enclosure (b).

DC and rf signals to the electrodes (respectively). The high- and low-pass filters located near the electrical feethrough pinbases remain unchanged. Internal to the vacuum enclosure, however, space constraints force the voltage leads to pass within 1 mm of the copper electrodes, potentially leading to large capacitive couplings. To mitigate this effect, the internal connections are made with micro-coax to shield the signal from crosstalk.

In order to maximize the electrode radius, a radial gap of only 380 μm separates the outer diameter of the G10 sleeve and the inner bore of the Ioffe trap. Hence, it is important not only for the tight machining tolerances to be met, but also for each sleeve to sit flush against the supporting electrode below. Great care has been taken to remove traces of dust, copper filings, and burrs so that each electrode is properly seated and electrically isolated from its neighbors. After assembly, a theodolite is used to confirm that no deviations from perpendicularity are present, and the stack may be shimmed if any tilts are discovered. We are pleased that the final stack assembly was measured to be straight (to better than 3 arcminutes), and was inserted into the central bore of the Ioffe trap with no difficulties.

Chapter 11

Conclusion

Trapping $\overline{\mathrm{H}}$ atoms has been the primary goal of this work. Five years ago, $\overline{\mathrm{H}}$ production within a quadrupole Ioffe field had yet to be demonstrated, and $\overline{\mathrm{H}}$ trapping was a distant vision. Our recent observations of 5 trapped $\overline{\mathrm{H}}$ atoms per trial (on average) thus marks substantial progress towards the goal of performing precise spectroscopic measurements on $\overline{\mathrm{H}}$ for studies of fundamental symmetries [1] and antimatter gravity [34].

Following the confinement of $\overline{\mathrm{p}}$ and e^+ in the field of a quadrupole Ioffe trap for hundreds of seconds [56], ATRAP created the first $\overline{\mathrm{H}}$ atoms within a Penning-Ioffe trap [57]. This result served as a necessary stepping stone towards trapped $\overline{\mathrm{H}}$ and demonstrated the feasibility of using quadrupole traps for $\overline{\mathrm{H}}$ formation and confinement. However, no trapped atoms were observed at the time, likely due to relatively small numbers of $\overline{\mathrm{p}}$ and e^+, uncontrolled plasma geometries, elevated temperatures, a limited number of trials, and a low detection efficiency.

ATRAP systematically set about improving each of these impediments, with a

focus towards creating more atoms rather than detecting fewer. Over the past three years, the number of $\overline{\mathrm{p}}$ accumulated and available for use in $\overline{\mathrm{H}}$ experiments has grown from 7×10^5 to 1×10^7, a factor of 14 increase. Two developments have enabled this advancement. First, a field-boosting solenoid was installed so that the local magnetic field could be increased from 1 T to 3.7 T during $\overline{\mathrm{p}}$ loading, and then reduced back to 1 T, so that $\overline{\mathrm{p}}$ could be transferred into the Ioffe trap. The higher field yields a factor of 5 improvement in $\overline{\mathrm{p}}$ capture efficiency, allowing for up to 2×10^5 $\overline{\mathrm{p}}$ to be caught per AD shot. Second, development and implementation of a rotating-wall electric field [115] permits radial compression of the $\overline{\mathrm{p}}$ plasma. Since plasmas expand by a factor of $\sqrt{B_0/B}$ as the magnetic field is reduced from B_0 to B, compressing the radius of the $\overline{\mathrm{p}}$ plasma before local magnetic field is reduced from 3.7 T to 1 T ensures that $\overline{\mathrm{p}}$ will not annihilate on the electrode walls during the rampdown of the field-boosting solenoid. The accumulation of e^+ is also greatly aided by regular applications of a rotating wall drive. Despite a perpetually decaying radioactive source, up to 4×10^9 e^+ may now be accumulated and stored within our Penning trap, compared to 2×10^8 previously.

Rotating wall drives, combined with a non-destructive method to determine plasma oscillation frequencies, allowed for a level of control and characterization of our plasma geometries that was formerly unachievable. Measurements of the center-of-mass and quadrupole modes within a plasma, along with knowledge of the plasma number, uniquely describe the plasma shape within ideal [101] and non-ideal Penning traps [102]. Using these mode measurement techniques, we directly observe the expected responses in plasma axial length and radius when the trap electric and magnetic fields

are changed. Additionally, we can measure the final radii of plasmas compressed by the rotating wall drive. Such manipulations facilitated the first observation of centrifugal separation between $\overline{\mathrm{p}}$ and the e^- that cool them [158], indicating a low-temperature, high-density $\overline{\mathrm{p}}$ plasma.

In addition to plasma number and geometry, plasma temperatures must be sufficiently low to allow for the creation of cold, trappable $\overline{\mathrm{H}}$. We implemented a robust and accurate method [165] to measure low $\overline{\mathrm{p}}$ temperatures for the first time within our apparatus. With this diagnostic in hand, we demonstrated a two-stage cooling process to reduce the temperature of up to 3×10^7 $\overline{\mathrm{p}}$ to 3.5 K or below - more $\overline{\mathrm{p}}$ at colder temperatures than ever before [163]. We begin with embedded e^- cooling, in which only $\sim 10^3$ e^- are kept with the $\overline{\mathrm{p}}$ to serve as a slow but effective cooling mechanism. Heat transferred to the $\overline{\mathrm{p}}$ during pulsed e^- ejection and particle transfer is radiated away by the embedded e^-, with $\overline{\mathrm{p}}$ and e^- equilibrating to a temperature of ≈ 30 K. Following embedded e^- cooling, adiabatic cooling allows for at least another factor of 10 reduction in the $\overline{\mathrm{p}}$ temperature. The plasma volume is adiabatically expanded by reducing the axial confining potential, with larger expansions giving greater cooling. Both embedded e^- and adiabatic cooling are lossless processes, a significant advantage for a rare particle species like $\overline{\mathrm{p}}$.

With improved control over our $\overline{\mathrm{p}}$ and e^+ plasma numbers, geometries, and temperatures, we were in a much better position to create and search for evidence of trapped $\overline{\mathrm{H}}$. During the 2011 beam run, a total of 20 trials were performed in which $\overline{\mathrm{p}}$ were excited into the e^+ plasma by frequency drives, $\overline{\mathrm{H}}$ formed via three-body recombination, and the Ioffe trap was quickly de-energized (by quenching) to release

trapped atoms. Improvements in detector characterization and event classification, along with summing the data from all 20 trials together, allowed the observation of 105 trapped $\overline{\mathrm{H}}$ atoms, or approximately 5 atoms per trial on average [59]. These atoms were stored in the Ioffe trap for between 15 and 1000 s, long enough to ensure that they were in their ground state. In addition, we were able to set a crude limit on the size of the gravitational acceleration of antimatter by observing the trap depths at which $\overline{\mathrm{H}}$ atoms escape.

The direct focus of future work will be to further increase the number of simultaneously trapped $\overline{\mathrm{H}}$ atoms so that the long-term goal of precise $\overline{\mathrm{H}}$ spectroscopy may be realized [1]. A new experimental apparatus currently under construction, featuring improved Ioffe and Penning traps, promises significant improvements in $\overline{\mathrm{H}}$ trapping and detection sensitivity. Though known and unknown challenges lie ahead, performing precision measurements on large numbers of trapped $\overline{\mathrm{H}}$ atoms is not so far beyond the horizon. ATRAP stands on the cusp of significantly increasing the number of simultaneously trapped atoms, and it is not irrationally optimistic to predict that laser cooling and spectroscopy will follow within several years. The resulting comparisons between matter and antimatter may allow us to find the answers to some of nature's most difficult and fundamental questions.

Bibliography

[1] G. Gabrielse, in *Fundamental Symmetries*, edited by P. Bloch, P. Pavlopoulos, and R. Klapisch (Plenum, New York, 1987), pp. 59–75.

[2] G. Baur, G. Boero, S. Brauksiepe, A. Buzzo, W. Eyrich, R. Geyer, D. Grzonka, J. Hauffe, K. Kilian, M. Lo Vetere, M. Macri, M. Moosburger, R. Nellen, W. Oelert, S. Passagio, A. Pozzo, K. Rohrich, K. Sachs, G. Schepers, T. Sefzick, R. S. Simon, R. Stratmann, F. Stinzing, and M. Wolke, Phys. Lett. B **368**, 251 (1996).

[3] G. Gabrielse, N. S. Bowden, P. Oxley, A. Speck, C. H. Storry, J. N. Tan, M. Wessels, D. Grzonka, W. Oelert, G. Schepers, T. Sefzick, J. Walz, H. Pittner, T. W. Hänsch, and E. A. Hessels, Phys. Rev. Lett. **89**, 213401 (2002).

[4] G. Gabrielse, N. S. Bowden, P. Oxley, A. Speck, C. H. Storry, J. N. Tan, M. Wessels, D. Grzonka, W. Oelert, G. Schepers, T. Sefzick, J. Walz, H. Pittner, T. W. Hänsch, and E. A. Hessels, Phys. Rev. Lett. **89**, 233401 (2002).

[5] M. Amoretti *et al.* (ATHENA Collaboration), Nature **419**, 456 (2002).

[6] G. Gabrielse, H. Kalinowsky, W. Jhe, T. W. Hänsch, C. Zimmerman, J. Walraven, T. Hijmans, W. Oelert, W. D. Phillips, S. L. Rolston, and D. Wineland, CERN SPSLC **96-23**, I211 (1996).

[7] G. Gabrielse, T. Roach, J. Estrada, D. Hall, P. Yesley, H. Kalinowsky, T. W. Hänsch, K. Eikema, J. Walz, W. Oelert, D. Grzonka, T. Sefzick, T. Hijmans, W. D. Phillips, S. L. Rolston, J. Walraven, W. Jhe, D. Wineland, and J. Bollinger, CERN SPSLC **97-8**, P306 (1997).

[8] G. Lüders, Ann. Phys. **2**, 1 (1957).

[9] T. D. Lee and C. N. Yang, Phys. Rev. **104**, 254 (1956).

[10] R. L. Garwin, L. M. Lederman, and M. Weinrich, Phys. Rev. **105**, 1415 (1957).

[11] J. I. Friedman and V. L. Telegdi, Phys. Rev. **106**, 1290 (1957).

[12] D. Griffiths, *Introduction to Elementary Particles* (Wiley-VCH, Weinheim, 2008).

[13] L. D. Landau, Nucl. Phys. **3**, 127 (1957).

[14] M. Gell-Mann and A. Pais, Phys. Rev. **97**, 1387 (1955).

[15] J. H. Christenson, J. W. Cronin, V. L. Fitch, and R. Turlay, Phys. Rev. Lett. **13**, 138 (1964).

[16] A. Alavi-Harati *et al.* (KTeV Collaboration), Phys. Rev. Lett. **83**, 22 (1999).

[17] V. Fanti *et al.* (NA48 Collaboration), Phys. Lett. B **465**, 335 (1999).

[18] B. Aubert *et al.* (BaBar Collaboration), Phys. Rev. Lett. **93**, 131801 (2004).

[19] Y. Chao *et al.* (Belle Collaboration), Phys. Rev. D **71**, 031502 (2005).

[20] M. Niering, R. Holzwarth, J. Reichert, P. Pokasov, Th. Udem, M. Weitz, T. W. Hänsch, P. Lemonde, G. Santarelli, M. Abgrall, P. Laurent, C. Salomon, and A. Clairon, Phys. Rev. Lett. **84**, 5496 (2000).

[21] S. Eidelman, et al., Phys. Lett. B **592**, 1 (2004).

[22] R. S. Van Dyck, Jr., P. B. Schwinberg, and H. G. Dehmelt, Phys. Rev. Lett. **59**, 26 (1987).

[23] G. Gabrielse, A. Khabbaz, D. S. Hall, C. Heimann, H. Kalinowsky, and W. Jhe, Phys. Rev. Lett. **82**, 3198 (1999).

[24] R. Carosi *et al.*, Phys. Lett. B **237**, 303 (1990).

[25] A. D. Sakharov, J. of Exp. and Th. Phys. **5**, 24 (1967).

[26] O. Bertolami, D. Colladay, V. A. Kostelecký, and R. Potting, Phys. Lett. B **395**, 178 (1997).

[27] A. D. Dolgov and Ya. B. Zeldovich, Rev. Mod. Phys. **53**, 1 (1981).

[28] C. L. Cesar, D. G. Fried, T. C. Killian, A. D. Polcyn, J. C. Sandberg, I. A. Yu, T. J. Greytak, D. Kleppner, and J. M. Doyle, Phys. Rev. Lett. **77**, 255 (1996).

[29] C. Zimmerman and T. W. Hänsch, Hyperfine Interact. **76**, 47 (1993).

[30] D. Colladay and V. A. Kostelecký, Phys. Rev. D **55**, 6760 (1997).

[31] R. Bluhm, V. A. Kostelecký, and N. Russell, Phys. Rev. Lett. **82**, 2254 (1999).

[32] J. DiSciacca and G. Gabrielse, Phys. Rev. Lett. **108**, 153001 (2012).

[33] S. Ulmer, K. Blaum, H. Kracke, A. Mooser, W. Quint, C. C. Rodegheri, and J. Walz, Phys. Rev. Lett. **107**, 103002 (2011).

[34] G. Gabrielse, Hyperfine Interact. **44**, 349 (1988).

[35] G. Yu Drobychev *et al.* (AEGIS Collaboration), CERN SPSC **2007-017**, P334 (2007).

[36] W. D. Phillips, S. L. Rolston, P. D. Lett, I. McIlrath, N. Vansteenkiste, and C. I. Westbrook, Hyperfine Interact. **76**, 265 (1993).

[37] R. J. Hughes and M. H. Holzscheiter, Phys. Rev. Lett. **66**, 854 (1991).

[38] P. A. M. Dirac, Proc. Roy. Soc. A **133**, 62 (1931).

[39] O. Chamberlain, E. Segrè, C. Wiegand, and T. Ypsilantis, Phys. Rev. **100**, 947 (1955).

[40] G. Gabrielse, X. Fei, K. Helmerson, S. L. Rolston, R. L. Tjoelker, T. A. Trainor, H. Kalinowsky, J. Haas, and W. Kells, Phys. Rev. Lett. **57**, 2504 (1986).

[41] G. Gabrielse, S. L. Rolston, L. Haarsma, and W. Kells, Hyperfine Int. **44**, 287 (1988).

[42] G. Gabrielse, X. Fei, L. A. Orozco, S. L. Rolston, R. L. Tjoelker, T. A. Trainor, J. Haas, H. Kalinowsky, and W. Kells, Phys. Rev. A **40**, 481 (1989).

[43] G. Gabrielse, X. Fei, L. A. Orozco, R. L. Tjoelker, J. Haas, H. Kalinowsky, T. A. Trainor, and W. Kells, Phys. Rev. Lett. **63**, 1360 (1989).

[44] G. Blanford, D. C. Christian, K. Gollwitzer, M. Mandelkern, C. T. Munger, J. Schultz, and G. Zioulas, Phys. Rev. Lett. **80**, 3037 (1998).

[45] G. Gabrielse, D. S. Hall, T. Roach, P. Yesley, A. Khabbaz, J. Estrada, C. Heimann, and H. Kalinowsky, Phys. Lett. B **455**, 311 (1999).

[46] G. Gabrielse, J. Estrada, J. N. Tan, P. Yesley, N. S. Bowden, P. Oxley, T. Roach, C. H. Storry, M. Wessels, J. Tan, D. Grzonka, W. Oelert, G. Scheppers, T. Sefsick, W. Breunlich, M. Carngelli, H. Fuhrmann, R. King, R. Ursin, H. Zmeskal, H. Kalinowsky, C. Wesdorp, J. Walz, K. S. E. Eikema, and T. Hänsch, Phys. Lett. B **507**, 1 (2001).

[47] G. Gabrielse, N. S. Bowden, P. Oxley, A. Speck, C. H. Storry, J. N. Tan, M. Wessels, D. Grzonka, W. Oelert, G. Schepers, T. Sefzick, J. Walz, H. Pittner, and E. A. Hessels, Phys. Lett. B **548**, 140 (2002).

[48] G. Gabrielse, A. Speck, C. H. Storry, D. Le Sage, N. Guise, D. Grzonka, W. Oelert, G. Schepers, T. Sefzick, H. Pittner, J. Walz, T. W. Hänsch, D. Comeau, and E. A. Hessels, Phys. Rev. Lett. **93**, 073401 (2004).

[49] E. A. Hessels, D. M. Homan, and M. J. Cavagnero, Phys. Rev. A **57**, 1668 (1998).

[50] A. Speck, C. H. Storry, E.A. Hessels, and G. Gabrielse, Phys. Lett. B **597**, 257 (2004).

[51] C. H. Storry, A. Speck, D. Le Sage, N. Guise, G. Gabrielse, D. Grzonka, W. Oelert, G. Scheppers, T. Sefzick, J. Walz, H. Pittner, M. Herrmann, T. W. Hänsch, D. Comeau, and E. A. Hessels, Phys. Rev. Lett. **93**, 263401 (2004).

[52] D. E. Pritchard, Phys. Rev. Lett. **51**, 1336 (1983).

[53] T. M. Squires, P. Yesley, and G. Gabrielse, Phys. Rev. Lett. **86**, 5266 (2001).

[54] E. P. Gilson and J. Fajans, Phys. Rev. Lett. **90**, 015001 (2003).

[55] J. Fajans, W. Bertsche, K. Burke, S. F. Chapman, and D. P. van der Werf, Phys. Rev. Lett. **95**, 155001 (2005).

[56] G. Gabrielse, P. Larochelle, D. Le Sage, B. Levitt, W. S. Kolthammer, I. Kuljanishvili, R. McConnell, J. Wrubel, F. M. Esser, H. Glückler, D. Grzonka, G. Hansen, S. Martin, W. Oelert, J. Schillings, M. Schmitt, T. Sefzick, H. Soltner, Z. Zhang, D. Comeau, M. C. George, E. A. Hessels, C. H. Storry, M. Weel, A. Speck, F. Nillius, J. Walz, and T. W. Hänsch, Phys. Rev. Lett. **98**, 113002 (2007).

[57] G. Gabrielse, P. Larochelle, D. Le Sage, B. Levitt, W. S. Kolthammer, R. McConnell, P. Richerme, J. Wrubel, A. Speck, M. C. George, D. Grzonka, W. Oelert, T. Sefzick, Z. Zhang, A. Carew, D. Comeau, E. A. Hessels, C. H. Storry, M. Weel, and J. Walz, Phys. Rev. Lett. **100**, 113001 (2008).

[58] G. B. Andresen *et al.* (ALPHA Collaboration), Nature **468**, 673 (2010).

[59] G. Gabrielse, R. Kalra, W. S. Kolthammer, R. McConnell, P. Richerme, D. Grzonka, W. Oelert, T. Sefzick, M. Zielinski, D. W. Fitzakerley, M. C. George, E. A. Hessels, C. H. Storry, M. Weel, A. Müllers, and J. Walz, Phys. Rev. Lett. **108**, 113002 (2012).

[60] G. B. Andresen *et al.* (ALPHA Collaboration), Nature Physics **7**, 558 (2011).

[61] J. Alsner *et al.* (AD User Community), CERN SPSC **2009-026**, P338 (2009).

[62] A. Speck, Ph.D. thesis, Harvard University, 2005.

[63] D. Le Sage, Ph.D. thesis, Harvard University, 2008.

[64] P. Larochelle, Ph.D. thesis, Harvard University, 2009.

[65] W. S. Kolthammer, Ph.D. thesis, Harvard University, 2011.

[66] R. McConnell, Ph.D. thesis, Harvard University, 2011.

[67] G. Gabrielse, X. Fei, L. A. Orozco, R. L. Tjoelker, J. Haas, H. Kalinowsky, T. A. Trainor, and W. Kells, Phys. Rev. Lett. **65**, 1317 (1990).

[68] S. Maury, Hyperfine Int. **109**, 43 (1997).

[69] L. S. Brown and G. Gabrielse, Rev. Mod. Phys. **58**, 233 (1986).

[70] H. Dehmelt, "Autobiography for the 1989 Nobel Prize in Physics" in *Les Priz Nobel* (1990).

[71] G. Gabrielse and F. Colin MacKintosh, Intl. J. of Mass Spec. and Ion Proc. **57**, 1 (1984).

[72] J. N. Tan and G. Gabrielse, Appl. Phys. Lett. **55**, 2144 (1989).

[73] G. Gabrielse, L. Haarsma, and S. L. Rolston, Intl. J. of Mass Spec. and Ion Proc. **88**, 319 (1989), ibid. **93**, 121 (1989).

[74] J. D. Jackson, *Classical Electrodynamics*, 3rd ed. (John Wiley & Sons, Hoboken, 1999).

[75] D. Hanneke, S. Fogwell, and G. Gabrielse, Phys. Rev. Lett. **100**, 120801 (2008).

[76] G. Gabrielse, Phys. Rev. A **27**, 2277 (1983).

[77] W. Press, B. Flannery, S. Teukolsky, and W. Vetterling, *Numerical Recipes in C* (Cambridge University Press, New York, 1988).

[78] H. J. Metcalf and P. van der Straten, *Laser Cooling and Trapping* (Springer, New York, 1999).

[79] W. D. Phillips, Rev. Mod. Phys. **70**, 721 (1998).

[80] C. Cohen-Tannoudji, B. Diu, and F. Laloë, *Quantum Mechanics* (John Wiley and Sons, New York, 1977).

[81] W. H. Wing, Prog. Quant. Electr. **8**, 181 (1984).

[82] E. Majorana, Nuovo Cimento **9**, 43 (1932).

[83] T. Bergman, G. Erez, and H. Metcalf, Phys. Rev. A **35**, 1535 (1987).

[84] M. N. Wilson, *Superconducting Magnets* (Oxford University Press, Oxford, 1983).

[85] T. Northrop, *"The Adiabatic Motion of Charged Particles"* (Wiley, New York, 1963).

[86] E. Gilson and J. Fajans, in *Non-neutral Plasma Physics III*, edited by J. J. Bollinger, R. Spencer, and R. C. Davidson (AIP, New York, 1999), pp. 250 – 255.

[87] J. Wrubel, G. Gabrielse, W.S. Kolthammer, P. Larochelle, R. McConnell, P. Richerme, D. Grzonka, W. Oelert, T. Sefzick, M. Zielinski, J.S. Borbely, M.C. George, E.A. Hessels, C.H. Storry, M. Weel, A. Müllers, J. Walz, and A. Speck, Nuc. Inst. and Meth. A **640**, 232 (2011).

[88] S. Agostinelli *et al.*, Nuc. Inst. and Meth. A **506**, 250 (2003).

[89] R. C. Davidson, *Physics of Non-Neutral Plasmas* (Imperial College Press, London, 2001).

[90] D. H. E. Dubin and T. M. O'Neil, Rev. Mod. Phys. **71**, 87 (1999).

[91] H. Goldstein, C. Poole, and J. Safko, *Classical Mechanics*, 3rd ed. (Addison Wesley, Reading, MA, 2002).

[92] L. D. Landau and E. M. Lifshitz, *Mechanics*, 3rd ed. (Pergamon Press, New York, 1976).

[93] R. C. Davidson and N. A. Krall, Phys. Fluids **13**, 1543 (1970).

[94] S. A. Prasad and T. M. O'Neil, Phys. Fluids **22**, 278 (1979).

[95] J. J. Bollinger and D. J. Wineland, Phys. Rev. Lett. **53**, 348 (1984).

[96] L. Turner, Phys. Fluids **30**, 3196 (1987).

[97] D. H. E Dubin, Phys. of Fluids B **5**, 295 (1993).

[98] R. L. Spencer, S. N. Rasband, and R. R. Vanfleet, Phys. Fluids B **5**, 4267 (1993).

[99] T. M. O'Neil and C. F. Driscoll, Phys. Fluids **22**, 266 (1979).

[100] D. H. E. Dubin, Phys. Rev. Lett. **66**, 2076 (1991).

[101] M. D. Tinkle, R. G. Greaves, C. M. Surko, R. L. Spencer, and G. W. Mason, Phys. Rev. Lett. **72**, 352 (1994).

[102] J. K. Jennings, R. L. Spencer, and K. C. Hansen, Phys. Plasmas **2**, 2630 (1995).

[103] J. D. Huba, *NRL Plasma Formulary* (Naval Research Laboratory, Washington, D. C., 2009).

[104] L. Spitzer, Jr., *Physics of Fully Ionized Gases* (Dover, New York, 1962).

[105] S. Ichimaru and M. N. Rosenbluth, Phys. Fluids **13**, 2778 (1970).

[106] D. Montgomery, G. Joyce, and L. Turner, Phys. Fluids **17**, 2201 (1974).

[107] T. M. O'Neil and P. G. Hjorth, Phys Fluids **28**, 3241 (1985).

[108] M. E. Glinsky, T. M. O'Neil, M. N. Rosenbluth, K. Tsurula, and S. Ichimaru, Phys. Fluids **4**, 1156 (1992).

[109] J. H. Malmberg and J. S. deGrassie, Phys. Rev. Lett. **35**, 577 (1975).

[110] D. J. Heinzen, J. J. Bollinger, F. L. Moore, W. M. Itano, and D. J. Wineland, Phys. Rev. Lett. **66**, 2080 (1991).

[111] J. J. Bollinger, D. J. Heinzen, F. L. Moore, W. M. Itano, D. J. Wineland, and D. H. E. Dubin, Phys. Rev. A **48**, 525 (1993).

[112] C. S. Weimer, J. J. Bollinger, F. L. Moore, and D. J. Wineland, Phys. Rev. A **49**, 3842 (1994).

[113] A. Speck, G. Gabrielse, P. Larochelle, D. Le Sage, B. Levitt, W. S. Kolthammer, R. McConnell, J. Wrubel, D. Grzonka, W. Oelert, T. Sefzick, Z. Zhang, D. Comeau, M. C. George, E. A. Hessels, C. H. Storry, M. Weel, and J. Walz, Phys. Lett. B **650**, 119 (2007).

[114] M. Amoretti, *et al.* (ATHENA Collaboration), Phys. Rev. Lett. **91**, 55001 (2003).

[115] X. P. Huang, F. Anderegg, E. M. Hollmann, C. F. Driscoll, and T. M. O'Neil, Phys. Rev. Lett. **78**, 875 (1997).

[116] F. Anderegg, E. M. Hollmann, and C. F. Driscoll, Phys. Rev. Lett. **81**, 4875 (1998).

[117] E. M. Hollmann, F. Anderegg, and C. F. Driscoll, Phys. Plasmas **7**, 2776 (2000).

[118] R. G. Greaves and C. M. Surko, Phys. Rev. Lett. **85**, 1883 (2000).

[119] A. W. Trivelpiece and R. W. Gould, J. Appl. Phys. **30**, 1784 (1959).

[120] C. F. Driscoll, K. S. Fine, and J. H. Malmberg, Phys. Fluids **29**, 2015 (1986).

[121] J. R. Danielson and C. M. Surko, Phys. Rev. Lett. **94**, 035001 (2005).

[122] J. R. Danielson and C. M. Surko, Phys. Plasmas **13**, 055706 (2006).

[123] J. R. Danielson and C. M. Surko, in *Non-Neutral Plasma Physics VI*, edited by M. Drewson, U. Uggerhøj, and H. Knudsen (American Institute Of Physics, New York, 2006), p. 19.

[124] L. H. Haarsma, K. Abdullah, and G. Gabrielse, Phys. Rev. Lett. **75**, 806 (1995).

[125] H. Stelzer, Nucl. Instrum. Meth. **133**, 409 (1976).

[126] J. F. Ziegler, M. D. Ziegler, and J. P. Biersack, Nuc. Inst. and Meth. B **268**, 1818 (2010).

[127] W. H. Barkas, W. Birnbaum, and F. M. Smith, Phys. Rev. **101**, 778 (1956).

[128] X. Fei, R. Davisson, and G. Gabrielse, Rev. Sci. Instrum. **58**, 2197 (1987).

[129] A. Einstein, Ann. der Physik **17**, 132 (1905).

[130] B. Levitt, G. Gabrielse, P. Larochelle, D. Le Sage, W. S. Kolthammer, R. McConnell, J. Wrubel, A. Speck, D. Grzonka, W. Oelert, T. Sefzick, Z. Zhang, D. Comeau, M. C. George, E. A. Hessels, C. H. Storry, M. Weel, and J. Walz, Phys. Lett. B **656**, 25 (2007).

[131] R. D. Dixon and L. A. Lott, J. Appl. Phys. **40**, 4938 (1969).

[132] S. L. Rolston and G. Gabrielse, Hyperfine Interact. **44**, 233 (1988).

[133] G. B. Andresen *et al.* (ALPHA Collaboration), Phys. Rev. Lett. **100**, 203401 (2008).

[134] A. Mills and E. Gullikson, Appl. Phys. Lett. **49**, 1121 (1986).

[135] C. M. Surko, M. Leventhal, and A. Passner, Phys. Rev. Lett. **62**, 901 (1989).

[136] J. Estrada, T. Roach, J. N. Tan, P. Yesley, and G. Gabrielse, Phys. Rev. Lett. **84**, 859 (2000).

[137] D. Comeau, A. Dror, D. W. Fitzakerley, M. C. George, E. A. Hessels, C. H. Storry, M. Weel, D. Grzonka, W. Oelert, G. Gabrielse, R. Kalra, W. S. Kolthammer, R. McConnell, P. Richerme, A. Müllers, and J. Walz, New J. Phys. **14**, 045006 (2012).

[138] W. K. Hensinger, S. Olmschenk, D. Stick, D. Hucul, M. Yeo, M. Acton, L. Deslauriers, C. Monroe, and J. Rabchuk, Appl. Phys. Lett. **88**, 034101 (2006).

[139] S. Schulz, U. Poschinger, K. Singer, and F. Schmidt-Kaler, Fortschr. Phys. **54**, 648 (2006).

[140] D. R. Bates and A. Dalgarno, in *Atomic and Molecular Processes*, edited by D. R. Bates (Academic Press, New York, 1962), pp. 245–271.

[141] G. Gabrielse, S. L. Rolston, L. Haarsma, and W. Kells, Phys. Lett. A **129**, 38 (1988).

[142] L. K. Richerme, Music Educators Journal **98**, 35 (2011).

[143] R. Neumann, H. Poth, A. Winnackker, and A. Wolf, Z. Phys. A **313**, 253 (1983).

[144] M. Amoretti *et al.* (ATHENA Collaboration), Phys. Rev. Lett. **97**, 213401 (2006).

[145] M. L. Wall, C. S. Norton, and F. Robicheaux, Phys. Rev. A **72**, 52702 (2005).

[146] P. Mansbach and J. Keck, Phys. Rev. **181**, 275 (1969).

[147] B. Makin and J. C. Keck, Phys. Rev. Lett. **11**, 281 (1963).

[148] M. Glinsky and T. O'Neil, Phys. Fluids B **3**, 1279 (1991).

[149] G. B. Andresen *et al.* (ALPHA Collaboration), Phys. Rev. Lett. **106**, 025002 (2011).

[150] T. Pohl, H. R. Sadeghpour, Y. Nagata, and Y. Yamazaki, Phys. Rev. Lett. **97**, 213001 (2006).

[151] F. Robicheaux, Phys. Rev. A **73**, 33401 (2006).

[152] M. R. Flannery and D. Vrinceanu, Phys. Rev. A **68**, 030502 (2003).

[153] T. O'Neil, Phys. Fluids **24**, 1447 (1981).

[154] D. J. Larson, J. C. Bergquist, J. J. Bollinger, W. M. Itano, and D. J. Wineland, Phys. Rev. Lett. **57**, 70 (1986).

[155] D. J. Wineland, C. S. Weimer, and J. J. Bollinger, Hyperfine Interact. **76**, 115 (1993).

[156] H. Imajo, K. Hayasaka, R. Ohmukai, U. Tanaka, M. Watanabe, and S. Urabe, Phys. Rev. A **55**, 1276 (1997).

[157] B. M. Jelenkovic, A. S. Newbury, J. J. Bollinger, W. M. Itano, and T. B. Mitchell, Phys. Rev. A **67**, 063406 (2003).

[158] G. Gabrielse, W. S. Kolthammer, R. McConnell, P. Richerme, J. Wrubel, R. Kalra, E. Novitski, D. Grzonka, W. Oelert, T. Sefzick, M. Zielinski, J. S. Borbely, D. Fitzakerley, M. C. George, E. A. Hessels, C. H. Storry, M. Weel, A. Müllers, J. Walz, and A. Speck, Phys. Rev. Lett. **105**, 213002 (2010).

[159] N. Kuroda, H. A. Torii, K. Y. Franzen, Z. Wang, S. Yoneda, M. Inoue, M. Hori, B. Juhász, D. Horváth, H. Higaki, A. Mohri, J. Eades, K. Komaki, and Y. Yamazaki, Phys. Rev. Lett. **94**, 023401 (2005).

[160] G. B. Andresen *et al.* (ALPHA Collaboration), Phys. Rev. Lett. **106**, 145001 (2011).

[161] M. Geva, M. Krishnan, and J. L. Hirshfield, J. Appl. Phys. **56**, 1398 (1984).

[162] R. L Spencer, (private communication).

[163] G. Gabrielse, W. S. Kolthammer, R. McConnell, P. Richerme, R. Kalra, E. Novitski, D. Grzonka, W. Oelert, T. Sefzick, M. Zielinski, D. Fitzakerley, M. C. George, E. A. Hessels, C. H. Storry, M. Weel, A. Müllers, and J. Walz, Phys. Rev. Lett. **106**, 073002 (2011).

[164] G. B. Andresen *et al.* (ALPHA Collaboration), Phys. Rev. Lett. **105**, 013003 (2010).

[165] D. L. Eggleston, C. F. Driscoll, B. R. Beck, A. W. Hyatt, and J. H. Malmberg, Phys. Fluids B **4**, 3432 (1992).

[166] W. Ketterle and N. J. Van Druten, Adv. At. Mol. Opt. Phys. **37**, 181 (1996).

[167] S. X. Hu, D. Vrinceanu, S. Mazevet, and L. A. Collins, Phys. Rev. Lett. **95**, 163402 (2005).

[168] M. V. Gorshkov, C. D. Masselon, G. A. Anderson, H. R. Udseth, R. Harkewicz, and R. D. Smith, J. Am. Soc. Mass Spectrom. **12**, 1169 (2001).

[169] A. Sommerfeld, *Atombau und Spektrallinien* (Vieweg und Sohn, Braunschweig, 1919).

[170] D. ter Haar, *The Old Quantum Theory* (Pergamon, Oxford, 1967).

[171] A. Einstein, in *La Theorie du Rayonnement et les Quanta: rapports et discussions de la reunion tenue a Bruxelles, du 30 octobre au 3 novembre 1911*, edited by P Langevin and M. de Broglie (Gauthier-Villars, Paris, 1912).

[172] J. Mehra and H. Rechenberg, *The Historical Development of Quantum Theory* (Springer-Verlag, New York, 2001), p. 235.

[173] G. Z. Li, R. Poggiani, G. Testera, and G. Werth, Hyperfine Interact. **76**, 281 (1993).

[174] T. M. O'Neil and D. H. E. Dubin, Phys. Plas. **5**, 2163 (1998).

[175] F. Reif, *Fundamentals of Statistical and Thermal Physics* (McGraw-Hill, New York, 1965).

[176] G. Z. Li, R. Poggiani, G. Testera, and G. Werth, Z. Phys. D **22**, 375 (1991).

[177] I. Barth, L. Friedland, E. Sarid, and A. G. Shagalov, Phys. Rev. Lett. **103**, 155001 (2009).

[178] F. Robicheaux and J. D. Hanson, Phys. Rev. A **69**, 010701 (2004).

[179] J. L. Hurt, P. T. Carpenter, C. L. Taylor, and F. Robicheaux, J. Phys. B **41**, 165206 (2008).

[180] G. B. Andresen *et al.* (ALPHA Collaboration), Phys. Lett. B **695**, 95 (2011).

[181] C. Amole *et al.* (ALPHA Collaboration), New J. Phys. **14**, 015010 (2011).

[182] G. Gabrielse, Adv. At. Mol. Opt. Phys. **50**, 155 (2005).

[183] H. A. Bethe and E. E. Salpeter, *Quantum Mechanics of One- and Two-Electron Atoms*, 2nd ed. (Plenum, New York, 1977).

[184] T. F. Gallagher, *Rydberg Atoms* (Cambridge Univ. Press, Cambridge, 1994).

[185] R. B. Meinke, C. Goodzeit, W. Hinson, C. Gung, J. Minervini, A. Radovinsky, J. Schultz, B. Smith, R. Camille, and L. Myatt, in *Proc. 2001 Particle Accelerator Conf.* (IEEE, Washington, D.C., 2001), Vol. 5, p. 3436.

[186] H. E. Knoepfel, *Magnetic Fields* (Wiley, New York, 2000).

[187] L. F. Goodrich, S. L. Bray, and T. C. Stauffer, IEEE Trans. Magnetics **25**, 2375 (1989).

[188] E. Vliegen and F. Merkt, J. Phys. B **39**, L241 (2006).

[189] E. Vliegen, S. D. Hogan, H. Schmutz, and F. Merkt, Phys. Rev. A **76**, 023405 (2007).